Polystyrene blends: a rheological and solid-state study of the role of molecular weight distribution



Andrea Sánchez Valencia
B.Eng, MSc

Faculty of Engineering

University of Nottingham

Thesis submitted to the University of Nottingham for the degree of

Doctor of Philosophy

January 2018

Acknowledgements

I would like to express my sincere gratitude to my supervisor Dr. Davide De Focatiis for the opportunity of enrolling in this project, and for his invaluable support, guidance, inspiration and encouragement. His true concern about teaching and guiding new polymer scientists is exceptional. I am grateful for his never ending patience, particularly when technical obstacles and challenges got in the way. Without his motivation and quest for excellence, this work would have never been a reality. I would also like to acknowledge the invaluable input, and support of my co-supervisor Dr. Richard Graham; lab partners Dr. Gabriel Choong, Dr. Vanessa Fernandes, Mike Ward, Magdalena Tomczynska, Dr. Silvio Curia and Dr. Alex Ilchev, and external collaborators Dr. Olga Smerdova and Prof. Lian Hutchings.

A great deal of appreciation goes to the University of Nottingham, the Institute of Mineral, Materials and Minning (IOM3), Royal Society of Chemistry (RSC) and the EPSRC, for investing in this research and without whom the realisation and dissemination of this work would otherwise not have been possible.

To my friends and family, who provided the external motivation and unconditional trust in that I could pursue the end of this journey. Finally and foremost, I would like to express my love and admiration to my devoted husband who shared the long nights, the extra-hours at the office, and the microwave food when time did not seem to be enough. Special recognition goes to his admirable and restless capacity of providing endless cups of freshly brewed coffee. You are my super-star, I love you to bits.

Abstract

Commercial polymers are typically classified according to their melt flow indices, measures of their viscosities. These properties are known to depend on a material's molar mass distribution, on its averages and its degree of polydispersity. In determining a polymer's performance, both the molar mass distribution and the the process employed to produce the part are highly relevant, since the balance in the mass fractions from its distribution will determine the flow characteristics in the mould, and influence the material's performance. The compromise polymer manufacturers have to make is to maintain the mechanical properties known to improve with increased molar mass at the same time as a sufficiently low viscosity, known to reduce with decreasing molar mass, to enable part production. This is often achieved by judicious blending of homopolymers. This thesis examines how varying molar mass and distribution in blends leads to changes in the thermal, rheological, and mechanical properties in polystyrene, and discusses and develops physical models to capturing the observed experimental responses.

Chromatographic and calorimetric studies were carried out on monodisperse, bimodal blends of monodisperse, polydisperse, and blends of polydisperse polystyrenes. They revealed that changes in molar mass distributions and glass transition temperatures, T_g, could be directly attributed to the blending procedure of choice. In polydisperse blends, higher contents of low molar mass fractions, and corresponding lower T_gs were observed in the blends produced using a melt mixing method compared with solution-blended equivalents. Thermal degradation, accelerated by the large number of chain ends,

was suggested as the cause for the increase in low molar mass fractions in the melt-mixed blends. The filtration and precipitation stages characteristic of solution blending instead promoted oligomer loss and evaporation, resulting in reductions in the low molar mass tails of the distributions.

Craze initiation stress was measured in 3-point bending isochronal creep tests on the same polymers and blends, and was found to increase rapidly with additions of a higher molar mass component, reaching a plateau at 20 wt%. A simple model based on a weighted addition of the crazing stress contributions of individual weight fractions was developed from an established piecewise linear crazing law in order to enable predictions of the crazing stress in the blends, using a power law exponent of 2.59 (90% CI [1.75 17.34]). In highly polydisperse systems, where short unentangled chains dilute the polymer, it was necessary to include dynamic tube dilution theory. Dilution leads to a change in the entanglement length and hence in the molar mass at which transitions in the crazing mechanisms (disentanglement and chain scission) occur. With the improved model, crazing stress could be predicted even for highly polydisperse blends with wide and bimodal distributions.

Linear and non-linear rheological measurements were carried out in shear and extensions on the same materials. Existing rheological models for linear viscoelasticity including Likhtman-McLeish (L-M), Rubinstein-Colby (R-C) and polydisperse double reptation (pDR) theory were applied to the linear experimental data, exposing some of the fundamental difficulties of modelling the structure of systems where multiple chain-lengths interact. R-C was found applicable to bimodal blends of monodisperse, whereas pDR was better able to model broad polydisperse blends. New non-linear shear and extensional rheology was recorded experimentally on all polymers and blends, and should enable future non-linear theories to be compared to experiment.

Publications

The contents of this thesis have been published as a scientific article in the following journal:

Sánchez-Valencia, A.; Smerdova, O.; Hutchings, L.; De Focatiis, D. S. A. The Roles of Blending and of Molecular Weight Distribution on Craze Initiation. *Macromolecules* 2017; 50(23), 9507-9514.

Similarly, the contents of this thesis have been presented and documented in the form of conference proceedings at:

Sánchez-Valencia, A; and De Focatiis, D. S. A., 2015. *Craze initation of glassy polymers: the effect of molar mass distribution of homopolymer bimodal and multimodal polystyrene blends*, presented at the 16th International Conference on the Deformation, Yield and Fracture of Polymers, 29 March - 2 April 2015, Kerkrade, The Netherlands.

Sánchez-Valencia, A; Graham, R.S.; and De Focatiis, D. S. A., 2016. *Assessment of linear and non-linear rheological theories using monodisperse, bimodal and polydisperse polystyrene systems*, The XVIIth International Congress on Rheology, Aug 8-13 2016, Kyoto, Japan.

Contents

Contents v

List of Figures ix

Nomenclature xxiv

1 Introduction 1

1.1 Overview 1

2 Literature Review 4

2.1 The concept of molar mass 4

2.2 Molecular entanglements in polymers 11

2.3 Review on viscoelasticity 12

2.4 Mechanical constitutive models 14

2.5 LVE and NLVE: a rheological approach 20

2.5.1 LVE models 22

2.5.2 NLVE models 31

2.6 Birefringence 37

2.7 Crazing 41

2.7.1 Craze grow and micromechanics 42

2.7.2 Crazing and the entanglement network 45

2.7.3 Temperature effect on crazing 50

2.7.4 Modelling of crazing 52

2.7.5 Crazing and birefringence 58

2.8 Summary and objectives 60

3 Materials and Methods **65**
3.1 Materials . . . 65
3.2 Size Exclusion Chromatography (SEC) . . . 67
3.2.1 MMDs: MatLab analysis . . . 71
3.3 Differential Scanning Calorimetry (DSC) . . . 75
3.3.1 Equipment validation . . . 77
3.3.2 Test profile . . . 77
3.3.3 DSC data Analysis . . . 79
3.4 Compression moulding . . . 80
3.5 Crazing . . . 81
3.5.1 Miniature specimen preparation . . . 81
3.5.1.1 Laser cutting specimens . . . 83
3.5.2 Crazing stress measurements . . . 87
3.5.3 Miniature crazing rig . . . 89
3.5.4 Quantification of the crazed region . . . 93
3.6 Birefringence . . . 94
3.6.1 Manufacture of oriented specimens . . . 94
3.6.2 Birefringence measurements . . . 96
3.7 Rheology . . . 97
3.7.1 Linear rheology . . . 98
3.7.2 Non-linear rheology . . . 100
3.7.3 Extensional rheology . . . 100
3.7.4 Rheological Data Analysis . . . 103

4 Molar Mass Analysis **105**
4.1 Prelude . . . 105
4.2 SEC data . . . 106
4.2.1 SEC: Monodisperse and blends . . . 106
4.2.2 SEC: Polydisperse and blends . . . 109
4.2.3 Molar mass simulations . . . 114
4.2.3.1 Monodisperse blends . . . 114
4.2.3.2 Polydisperse blends . . . 118
4.3 DSC data . . . 124

4.3.1 Monodisperse and blends . . . 124
4.3.2 Polydisperse and blends . . . 127
4.3.3 Tg simulations . . . 129
4.4 Conclusions . . . 137

5 Crazing Analysis **139**
5.1 Prelude . . . 139
5.2 Crazing: monodisperse blends . . . 140
5.3 Blending model for CIS . . . 146
5.4 Monte Carlo simulation . . . 152
5.5 CIS model in polydisperse materials . . . 154
5.6 Hybrid CIS-DTD model . . . 160
5.6.1 Hybrid CIS-DTD model: polydisperse blends . . . 165
5.7 Birefringence and crazing . . . 172
5.7.1 Birefringence and orientation . . . 172
5.7.2 Crazes in oriented specimens . . . 177
5.8 Conclusions . . . 181

6 Rheological Analysis **185**
6.1 Prelude . . . 185
6.2 Validation of LVE configuration . . . 186
6.3 LVE monodisperse material parameters . . . 188
6.4 PS materials LVE master curves . . . 191
6.4.1 Monodisperse blends . . . 191
6.4.2 Polydisperse and blends . . . 191
6.5 REPTATE LVE simulations . . . 198
6.5.1 Polydisperse materials: pDR theory . . . 198
6.5.2 Blends: R-C and pDR theories . . . 201
6.5.2.1 Monodisperse blends . . . 201
6.5.2.2 Polydisperse blends . . . 207
6.6 Non-linear Viscoelasticity . . . 211
6.6.1 Monodisperse materials . . . 212
6.6.2 Polydisperse materials . . . 217

6.6.3 Monodisperse blends 220
6.6.4 Polydisperse blends 227
6.7 Conclusions 235

7 Conclusions **237**
7.1 Prelude 237
7.2 Key findings 237
7.2.1 Molar Mass Analysis 238
7.2.2 Crazing Analysis 238
7.2.3 Rheological Analysis 239
7.3 Summary 240
7.4 Concluding remarks and further work 245

Appendix A: Crazing rigs **246**

Appendix B: CIS correction **250**

References **255**

List of Figures

2.1 Representative molar mass distribution plots of (a) monodisperse, (b) polydisperse and (c) bimodal blend systems. 7
2.2 Young's Modulus vs. temperature for a range of monodisperse PS and their corresponding blends from [1]. 9
2.3 Ultimate elongation of PVC plotted against $\overline{M}_n$, $\overline{M}_w$, $\overline{M}_z$ from [2]. 10
2.4 G' and G" parts of the LVE complex shear modulus for PS as predicted using the GR model in the glassy regime from [3]. . . . 17
2.5 M dependence on σ_y as reported by [3]. 18
2.6 M dependence on T_g as reported by [4]. 19
2.7 The molecular weight dependence of the recoverable compliance for nearly monodisperse polyisoprenes, extracted from [5]. 21
2.8 Master curve of (a) monodisperse PBD and (b) binary PBD blend of 5%410 kDa and 90%100 kDa at $T_0 = 40\,^{\circ}\mathrm{C}$ from [6]. 24
2.9 L-M best fit theory for dynamic moduli of PS from [7]. 27
2.10 Experimental and predicted data from [8], for a diluted monodisperse PS ($\overline{M}_w = 820\,\mathrm{kg/mol}$) with 95wt% styrene oligomers ($\overline{M}_w = 8.8\,\mathrm{kg/mol}$). 30
2.11 ROLIEPOLY best fit theory for the transient data of Kahvand for PS/TCP [9]. 33
2.12 De Focatiis GM stress-strain curves predictions against experimental data for materials AF, AG and R. Modified from [10]. 35
2.13 De Focatiis GM model as published for material AG in [10]. . . . 36
2.14 PS interaction with refractive indices, $n1$ and $n2$, from [11]. 37

2.15 Birefringence simulations for a range of drawing temperatures in oriented PS samples [12]. 40
2.16 Mechanism for the formation of crazes adapted from [13]. 41
2.17 Craze/bulk interface microstructure, adapted from [14]. 43
2.18 Craze surface stress profiles in monodisperse, polydisperse and bimodal blend of polystyrene adapted from[15]. 45
2.19 Craze stress as a function of $\overline{M}_n$ in PS, from [16]. 46
2.20 Craze fibril extension ratio as a function of M_e in various polymer systems, adapted from [17]. 48
2.21 Entanglement loss process in crazes, adapted from [18]. 49
2.22 Craze fibril extension ratio as a function of M_e in various polymer systems, adapted from [19]. 51
2.23 Predicted surface tension, T_s, curves for two PS systems at $\dot{\epsilon} = 4x10^{-6}\text{s}^{-1}$, adapted from[18]. 54
2.24 Craze initiation stress for monodisperse and branched PS systems, adapted from[20]. 55
2.25 Calculated craze initiation stresses for the data of De Focatiis and Han [20], exhibiting the disentanglement and crazing regimes. . . 57
2.26 Measurement of average crazing stress as a function of melt-drawing temperature for materials AF, AG and R[21]. 59
2.27 Crazing stresses of drawn samples relative to that of isotropic specimens, plotted versus the birefringence [21]. 60

3.1 Conventional column calibration plot for a series of PS standards ranging from 580 Da-1112 kDa. 69
3.2 Processed GPC data, showing the original baseline (black), and the optimised baseline (red) using MatLab's code linear regression. 73

3.3 SEC data processing using the MatLab script through the definition of a number of standard deviations (continuous blue line) from the baseline (dashed blue line) to determine the distribution. Trimming limits are defined as a function of the standard deviation chosen by the user. The intersection of the blue line with the black and red lines shows the molar mass distribution data considered for the analysis. 74
3.4 Molar Mass Distribution of material BJ as processed using the MatLab code. Molar mass averages $\overline{M}_n$, $\overline{M}_w$, and $\overline{M}_z$ are shown as thick black lines. 75
3.5 Normalised Molar Mass Distribution as processed using the MatLab code. Molar mass averages $\overline{M}_n$, $\overline{M}_w$, and $\overline{M}_z$ are shown as thick black lines. 76
3.6 Linear correlation between the Q-10 and the Linkam enquipment in the melting points of the chosen standard materials. Literature data [22] is shown in small symbols for reference 78
3.7 Temperature test profile for the DSC analysis of PS samples. . . . 79
3.8 T_g for material BI as processed by TA DSC data anaylsis software. 80
3.9 Heated press moulding procedure. Adapted from [23]. 82
3.10 Temperature profile of disc moulding process. Average cooling rate temperatures are shown for reference for both recorded trials. . . 83
3.11 Laser cutting set ups explored for the production of miniature crazing and extensional rheology specimens. 85
3.12 Difference between mechanical and laser cutting of miniature crazing specimens. 86
3.13 3D profile of manually cut miniature specimen. 87
3.14 3D profile of laser cut miniature specimen. 88
3.15 Schematic diagram of the distribution of load determined from the bending moment and moment of inertia of a beam subjected to symmetric 3-point bending. The extent of the crazed region is shown by L_c, and the craze iniation stress that can be calculated at the edge of this area is labelled as σ_c. Adapted from [24]. . . . 90

3.16 Photograph of the custom-made crazing rig for isochronal three point bending creep of miniature specimens. 91
3.17 Details of the experimental set-up of miniature crazing specimens in three point bending creep custom made crazing rig. 92
3.18 Schematic representation for the optical microscopy technique of craze measurement through light refraction, adapted from [24]. . . 93
3.19 Experimental setup for the measurement of crazing through light reflection under optical microscopy. 94
3.20 Schematic diagram of the craze measurement quantification protocol. The crazes in the specimen are measured at five longitudinal lines (c1-c5). Each individual length is measured by correlation with the eyepiece micrometer, which has been calibrated with the aid of a calibration graticule. 95
3.21 Micrograph of the craze measurements in a real specimen. Values for each measurement line (C1-C5) are shown, and will be used to obtain the average craze length, L_c, to be used in calculations. . . 96
3.22 Illustration of a polarized microscope configuration from [25]. . . . 97
3.23 Parallel-plate and cone-and-plate geometries for rheological tests, from [26; 27]. 98
3.24 Velocity profile for a parallel plate configuration in shear. 100
3.25 Experimental setup for oscillatory and transient shear rheology in an Anton Paar MCR-302 rheometer. 101
3.26 Configuration of a SER system from [27; 28]. 102
3.27 Experimental setup for extensional rheology of an Anton Paar MCR-302 rheometer. 103

4.1 Data comparison for the (a) $\overline{M}_n$, and (b) $\overline{M}_w$ averages, as obtained from ASTRA and processed using MatLab. All materials have been colour coded. Polydisperse blends have been colour coded to refer to their blending ratio (e.g. molar mass), and distinguished by square symbols to refer to the blends obtained by solution blending, and diamonds to refer to the blends obtained through melt-mixing. 107

4.2 Molar mass distributions of (a) monodisperse materials, and (b) their corresponding blends obtained using MatLab. 108
4.3 Molar mass distributions of (a) polydisperse materials and (b) their corresponding *mm*-blends and *sb*-blends obtained using MatLab. . 111
4.4 Trimming limits I, II , III for the computation of $\overline{M}_{n,p1}$, $\overline{M}_{w,p1}$, $\overline{M}_{n,p2}$, $\overline{M}_{w,p2}$, $\overline{M}_{n,p3}$, and $\overline{M}_{w,p3}$ in the bimodal monodisperse blends BI, BJ, BK, and BL. 116
4.5 $\Delta\%$ between the simulated blends (-*th*) and the experimental data when defining M_{peak} at (a) $\log M = 5.15$ / $\log M = 5.35$, (b) $\log M = 5.20$ / $\log M = 5.40$, and (c) $\log M = 5.25$ / $\log M = 5.45$. 117
4.6 Trimming limits I, II, III for the computation of $\overline{M}_{n,p1}$, $\overline{M}_{w,p1}$, $\overline{M}_{n,p2}$ and $\overline{M}_{w,p2}$ in the bimodal polydisperse blends CA-CD. . . . 119
4.7 $\Delta\%$ between the simulated blends (-*th*) and the experimental data when defining M_{peak} at (a)/(d) $\log M = 3.8$, (b)/(e) $\log M = 3.9$, (c)/(f) $\log M = 4.0$, for the solution blended (squares) and melt-mixed materials (diamonds), respectively. 120
4.8 DSC results for (a) monodisperse materials and (b) their corresponding blends. 125
4.9 DSC results for (a) polydisperse materials and (b) their corresponding blends. 128
4.10 Effective glass transition temperatures for BX/BY blends using the Lodge and McLeish T_g^{eff} model [29]. Solution blends are shown in squares, while melt-mixed materials are shown as diamonds. . . . 136

5.1 Rate of change of craze initiation stress with log time as a function of molar mass for materials BG and BH and for literature data from ref [20]. 143
5.2 CIS of monodisperse materials BF and BG, and their corresponding blends as a function of % BG by weight. 144
5.3 CIS of monodisperse materials BF and BH, and their corresponding blend as a function of % BH by weight. 145

5.4 Calculation of the rms between the predicted CIS, and the experimental CIS, as a function of parameter θ. Lowest error margin found at $\theta = 3.78$. 149
5.5 Predictions for the calculated CIS when solving for θ are presented against the experimental data, at (a) $\theta = 1$, (b) $\theta = 2$, and (c) best rms fit at $\theta = 3.78$. 150
5.6 $\overline{M}_z$ and $\overline{M}_{\theta=3.78}$ averages plotted in reference to their location within the GPC distributions of monodisperse blends: (a)BI, (b)BJ, (c)BK and (d)BL. 151
5.7 Probability plot of the MC analysis of θ. The calculated MC probability function for θ is shown against the pdf and cdf to establish a confidence interval at 90%. 153
5.8 Predictions for the calculated CIS when solving for θ =2.59 and a 90% CI [1.75,17.34], represented by vertical error bars. 154
5.9 3-linear step model for CIS for monodisperse materials as proposed by [20]. 156
5.10 3-linear step model [20] for CIS alongside MMDs of polydisperse materials. 158
5.11 Experimental vs predictions of CIS at θ=2.59 90% CI [1.75,17.34] for polydisperse materials R,BX and BY. 159
5.12 SEC distribution of material BX as a function of Z; along with the 3-linear step crazing limits. 164
5.13 Micrographs of polydisperse blends (a) CB_{sb}, (b) CC_{sb} and (c) CD_{sb} at 300s. Crazes are pointed with arrows. 167
5.14 CIS of polydisperse bimodal blends of materials BX and BY, as a function of %BY by weight 168
5.15 Experimental vs. prediction of CIS in the melt-mixed materials at θ =2.59 90% CI [1.75, 17.34] (a) without and (b) with the inclusion of the DTD effect. 170
5.16 Experimental vs. prediction of CIS in the solution blended materials at θ =2.59 90% CI [1.75, 17.34] (a) without and (b) with the inclusion of the DTD effect. 171

5.17 -Δn as a function of molar mass, M, and drawing temperature: (a) 106°C, (b) 116°C, (c) 126°C, and (d) 136°C. 175
5.18 Measurements of the birefringence vs. drawing temperature for monodisperse materials BF, BG and BH. Also illustrated are the temperatures at which Weissenberg numbers are equal to unity. . 176
5.19 Measurements of the birefringence vs. drawing temperature for monodisperse blends BI, BJ BK and BL. Also illustrated are the temperatures at which Weissenberg numbers are equal to unity. . 177
5.20 Micrographs of crazing pattern of oriented monodisperse blend BI at different drawing temperatures: (a) 106 °C, (b) 116 °C, (c) 126 °C, and (d) 136 °C. 179
5.21 Measurements of the crazing stress vs. drawing temperature for monodisperse materials BF, BG and BH. 180
5.22 Measurements of the crazing stress vs. drawing temperature for monodisperse blends BI-BL. 181
5.23 Measurements of the increase in crazing stress relative to that of isotropic specimens in monodisperse systems BF, BG and BH, plotted versus the birefringence, $-\Delta n$, measured directly on the crazing test specimens. Dashed line represents the limit for linearity of the stress-optical rule, while solid line represents De Focatiis [21] birefringence linear prediction for monodisperse materials. 182
5.24 Measurements of the increase in crazing stress relative to that of isotropic specimens in bimodal blends of monodisperse systems BI, BJ, BK and BL, plotted versus the birefringence, $-\Delta n$, measured directly on the crazing test specimens. Dashed line represents the limit for linearity of the stress-optical rule, while solid line represents De Focatiis [21] birefringence linear prediction for monodisperse materials. 183

6.1 G' and G" moduli at 170∘C using TTS, for polymer R: using parallel plate (pp), using cone and plate (cp) and reported by De Focatiis[10]. 187

6.2 Master curve plots for monodisperse materials BF, BG and BH (symbols), plotted against REPTATE simulations using the L-M theory (lines), and obtained fitting parameters M_e, G_e, τ_e. 189
6.3 Master curves of monodisperse materials BF and BG, and their corresponding blends. 192
6.4 Master curves of monodisperse materials BF and BH, and their corresponding blend. 193
6.5 T_g dependence on $1/\overline{M}_n$. 195
6.6 Master curves of polydisperse materials BX and BY, and their corresponding blends obtained by solution blending. 196
6.7 Master curves of polydisperse materials BX and BY, and their corresponding blends obtained through melt mixing. 197
6.8 Master curve plots for polydisperse materials R, BX and BY (symbols), plotted against REPTATE simulations using the pDR theory (lines). 200
6.9 Master curve plots for monodisperse blends BI, BJ and BK (symbols), plotted against REPTATE simulations using the R-C (lines) and pDR (dashed) theories. 203
6.10 Master curve plots for monodisperse blend BL (symbols), plotted against REPTATE simulations using the R-C (lines) and pDR (dashed) theories. 204
6.11 Master curve plots for solution blended polydisperse blends (symbols), plotted against REPTATE simulations using the R-C (lines) and pDR (dashed) theories. 208
6.12 Master curve plots for melt-mixed polydisperse blends (symbols), plotted against REPTATE simulations using the R-C (lines) and pDR (dashed) theories. 209
6.13 Ten Maxwell modes (filled diamonds) are fitted to the mastercurve of material BH at 170 °C. The obtained predictions are shown with continuous black lines, while the experimental data is presented with blank symbols. 213

6.14 Extensional and transient shear viscosity for material BF. The linear envelope is presented as a continuous black line. The applied shear rate is indicated alongside corresponding data. 214
6.15 Extensional and transient shear viscosity for material BG. The linear envelope is presented as a continuous black line. The applied shear rate is indicated alongside corresponding data. 215
6.16 Extensional and transient shear viscosity for material BH. The linear envelope is presented as a continuous black line. The applied shear rate is indicated alongside corresponding data. 216
6.17 Transient shear viscosity for material BX. The linear envelope is presented as a continuous black line. The applied shear rate is indicated alongside corresponding data. 218
6.18 Extensional and transient shear viscosity for material BY. The linear envelope is presented as a continuous black line. The applied shear rate is indicated alongside corresponding data. 219
6.19 Extensional and transient shear viscosity for material BI. The linear envelope is presented as a continuous black line. The applied shear rate is indicated alongside corresponding data. 221
6.20 Extensional and transient shear viscosity for material BJ. The linear envelope is presented as a continuous black line. The applied shear rate is indicated alongside corresponding data. 222
6.21 Extensional and transient shear viscosity for material BK. The linear envelope is presented as a continuous black line. The applied shear rate is indicated alongside corresponding data. 223
6.22 Extensional and transient shear viscosity for material BL. The linear envelope is presented as a continuous black line. The applied shear rate is indicated alongside corresponding data. 224
6.23 Comparative transient data at 170 °C for blends of materials BF and BG at varying strain rates: (a) $0.01\,s^{-1}$; (b) $0.03\,s^{-1}$; and (c) $0.3\,s^{-1}$. Linear envelopes are shown as continuous lines, while data is presented as symbols. 225

6.24 Comparative transient data at 170 °C for the blend of materials BF and BH at varying strain rates: (a) 0.01 s^{-1}; (b) 0.03 s^{-1}; and (c) 0.1 s^{-1}. Linear envelopes are shown as continuous lines, while data is presented as symbols. 226
6.25 Transient shear viscosity for material CA; plots of: (a) solution blended and (b) melt-mixed samples have been identified with the corresponding subscripts ($-_{sb}$ and $-_{mm}$). The linear envelope is presented as a continuous black line. The applied shear rate is indicated alongside corresponding data. 228
6.26 Transient shear viscosity for material CB; plots of: (a) solution blended and (b) melt-mixed samples have been identified with the corresponding subscripts ($-_{sb}$ and $-_{mm}$). The linear envelope is presented as a continuous black line. The applied shear rate is indicated alongside corresponding data. 229
6.27 Extensional and transient shear viscosity for material CC; plots of: (a) solution blended and (b) melt-mixed samples have been identified with the corresponding subscripts ($-_{sb}$ and $-_{mm}$). The linear envelope is presented as a continuous black line. The applied shear rate is indicated alongside corresponding data. 230
6.28 Extensional and transient shear viscosity for material CD; plots of: (a) solution blended and (b) melt-mixed samples have been identified with the corresponding subscripts ($-_{sb}$ and $-_{mm}$). The linear envelope is presented as a continuous black line. The applied shear rate is indicated alongside corresponding data. 231
6.29 Comparative transient data at 170 °C for the solution blends of materials BX and BY at varying strain rates: (a) 0.03 s^{-1}; (b) 0.1 s^{-1}; and (c) 1 s^{-1}. Linear envelopes are shown as continuous lines, while data is presented as symbols. 233
6.30 Comparative transient data at 170 °C for the melt-mixed blends of materials BX and BY at varying strain rates: (a) 0.03 s^{-1}; (b) 0.1 s^{-1}; and (c) 1 s^{-1}. Linear envelopes are shown as continuous lines, while data is presented as symbols. 234

1 Exploted view of new crazing tool CAD drawings; elements have been labelled and numbered for production purposes. 247
2 Detail image of new crazing rig as manufactured from CAD drawings shown in figure 1. 248
3 Image of the two sets of crazing rigs produced. 249
4 Craze initiation stress for polymer R in DEG, as reported in this study compared to [24]. 251
5 CIS as measured for monodisperse materials BF, BG and BH. Data has been plotted against the monodisperse data and fitting limits for the mechanisms of crazing as reported by [20]. 252
6 Micrographs showing the radii (R) difference of the edges in the specimen support plates used in this study and by De Focatiis[20; 24]. 253
7 CIS of monodisperse materials using the radii correction, and new modified crazing limits. 254

Nomenclature

Roman Symbols

cdf	Cumultative Density Function
CI	Confidence Interval
E	Young's Modulus
MC	Monte Carlo
G'	Storage modulus
G''	Loss modulus
G_e	Entanglement Modulus
G_N^0	Plateau Modulus
$G(t)$	Stress-relaxation Modulus
$I_{rectangle}$	Moment of inertia for a rectangular prism
J_e^0	Steady-state shear compliance
$J(t)$	Creep Compliance
M	Bending Moment
M_e	Molecular weight between entanglements
M_e'	Effective Molecular Weight between Entanglements

$\overline{M}_n$	Number Average Molecular Weight
$\overline{M}_w$	Weight Average Molecular Weight
$\overline{M}_z$	Z-Average Molecular Weight
P	Laser Power
pdf	Probability Density Function
PPI	Laser Resolution
r	Retardation
$R\theta$	Excess Rayleigh Proportionality
$S(x)$	Stress Profile
T_g	Glass Transition Temperature
v	Laser speed
Wi	Weissenberg Number
Wi_d	Weissenberg Number Reptation timescale
Wi_e	Weissenberg Number entanglement timescale
Wi_R	Weissenberg Number Rouse timescale
Z	Number of entanglements
Z'	Effective Number of entanglements

Greek Symbols

Δn	Birefringence
Δ_n	Normalised difference number average
Δ_w	Normalised difference weight average
η_0	Zero-shear Viscosity

$\dot{\gamma}$ Shear Strain rate

$\dot{\gamma}_{cp}$ Shear Strain Rate for cone and plate

$\dot{\gamma}_{pp}$ Shear Strain Rate for parallel-plate

λ_{max} Finite Extensibility

$\phi_\theta(M)$ Molar Mass Fraction parameter

ω Angular Frequency

σ Standard Deviation

σ_{cn} New corrected craze initiation stress

σ_c Craze initiation stress

$\dot{\epsilon}$ Strain rate

σ_M Standard Error

τ_d Reptation time

τ_e Relaxation time

τ_R Rouse time

τ_{cp} Shear Stress for cone and plate

θ Power Law Molar Mass parameter

τ_{pp} Shear Stress for parallel-plate

Acronyms

CCR Convective Constraint Release

CIS Craze Initiation Stress

CLF Contour Length Fluctuations

CR Constraint Release

DSC Differential Scanning Calorimetry

DEG Diethylene Glycol

DTD Dynamic Tube Dilution

ESC Environmental Stress Crazing

FE Finite Extensibility

GPC Gel Permeation Chromatography

GE Kramer's Geometrically Entanglement loss theory

GM Glass-Melt Model

GR Glass-Rubber Model

$L-M$ Likhtman-McLeish

LVE Linear Viscoelasticity

$MALS$ Multi Angle Light Scattering

mm Melt-mixing

MMD Molar Mass Distribution

MWD Molecular Weight Distribution

$NEMD$ Non equilibrium molecular dynamic simulations

$NLVE$ Non-linear Viscoelasticity

PDI Polydispersity Index

pDR Polydisperse Double Reptation theory

PS Polystyrene

PVC Polyvinyl Chloride

$R-C$ Rubinstein-Colby

$REPTATE$ Rheology of Entangled Polymers: Toolkit for Analysis of Theory and Experiment

sb Solution blending

SEC Size Exclusion Chromatography

SER Sentmanat Extensional Rheometer

TEM Transmission Electron Microscopy

th Theoretical or predicted data

THF Tetrahydrofuran

TTS Time-temperature Superposition

WLF William-Landel-Ferry equation

Chapter 1

Introduction

1.1 Overview

Ever since the development of synthetic polymers in the early 1900s, the macromolecular nature of these materials has led science into developing a range of fundamental characterisation techniques to understand the segmental and collective motions that occur in their diffusive responses to applied stimuli. The development of gel permeation chromatography (GPC), the refinement of polymerisation processes and the maturity of rheological instruments, have all contributed to recognise that both the melt and solid state properties of polymer systems are dependent of two major aspects: their macromolecular characteristics, defined by the polymer's monomeric unit, architecture and molar mass; and secondly, the interaction of these molecules during flow at the segmental and collective levels.

From a commercial perspective, the recognition of how polymer synthesis can be fine-tuned to obtain specific mechanical properties represents a very lucrative and cost-effective path for industrialisation. Polymer blending is carried for a variety of reasons: to enhance mechanical properties, improve processing, lower costs, promote adhesion, stability, or surface properties. What makes blending such a resourceful approach is that mixing of different polymer systems offers the potential of combining the attractive features of each constituent component while at the same time reducing their deficient characteristics. In the case of

industrial high-volume manufacturers of polymer products, blending of miscible materials is a common practice for achieving a fuller control over the final properties of a polymer system. The usual process entails finding the right equilibrium between the end mechanical (i.e. dictated by customer specifications) and flow (i.e. defined by processing equipment) characteristics of a polymer system. This is usually achieved by blending of lower molar mass polymers to secure low processing temperatures, and higher molecular weight materials to improve tensile, impact and fracture performance. Traditionally the easiest way to optimise polymer powder mixing operations has been to leverage previous experience coupled with manufacturer knowledge about the equipment and to perform a series of pilot -and/or production- scale test runs [30]. This trial-and-error approach is not only time-consuming and costly, but it also deviates the attention to the fundamental understanding of the risks and consequences associated with the molar mass characteristics of the blend constituents and the blending method of choice.

Ever since the first viscoelastic models for rubbers and polymers were developed, mainly by Treloar [31] and Ferry [32], polymer science has focused on understanding how synthesis of these materials, and subsequent blending, can lead to specific and desirable processing and mechanical properties. This stream of research can be split into various fields: mechanical constitutive models near the glass transition [33; 34; 35; 36], experimental validation for elastic and inelastic deformation [3; 15; 37; 38], and rheological theories for polymer solutions and melts [39].

In this thesis a generation of physical and constitutive theories are tested and scrutinised through their correlation with mechanical and rheological experiments. The literature review on the first chapter, gives particular attention into the analysis of the effect molar mass and molar mass distribution exert in the crazing, birefringence and rheological behaviour of polystyrene. The bulk of this research is divided into 5 chapters. In the third chapter, an introduction to the materials and experimental methods used is provided. This thesis examines a total of 18 PS materials, with a range of varying molar mass, and levels of polydispersity. In a further fourth chapter, experimental chromatographic and calorimetry data is provided to further understand the manifestations of molar mass and molar mass distribution in the physical properties of the studied poly-

mers.

Chapters 5 and 6 are devoted to the analysis of experimental evidence of the changes in the solid-state and melt responses of the various PS systems. The experimental data is then used to compare the relevant available theories to evaluate their validity, accuracy and limitations. This is done with particular emphasis on the role of molar mass distributions by examination of inherently different molar mass systems: bimodal blends of monodisperse homopolymers, polydisperse polymers and blends of polydisperse polymers. This study makes use of the novel experimental data to further lengthen and improve existing models, particularly by coupling physical polymer models with observed mechanical responses in isochronal creep tests.

The study concludes with a summary of the observations on how accurate current crazing and rheological models are to predict solid-state or melt state responses even in complex and challenging polydisperse blends with high degrees of unentangled fractions.

Chapter 2

Literature Review

2.1 The concept of molar mass

Polymers have become popular materials in many industrial processes and consumer products. They are widely used due to their versatility in being manufactured for a specific purpose, often leading to new polymers with differing mechanical properties. Essentially, polymer molecules are a network of many repeating units ("poly", many,"mer",parts). They are synthesised through polymerisation, often resulting in a distribution of molecules of different sizes. Each polymer molecule -or polymer chain-, is defined by its monomeric unit and its degree of polymerisation. Since the monomeric unit has a specific molar mass, it becomes possible to use the terms molar mass and chain length interchangeably when describing the size or length of a polymer molecule. In this study, the term molar mass will be used preferentially.

The vast majority of synthetic polymers are heterogeneous in size, resulting in a spread of molar mass around a mean value, in what is normally known as a molar mass distribution, MMD, or molecular weight distribution, MWD . Measures of this distribution that are easier to quote and compare are needed, and for this purpose it is common to use averages of the distribution. These can be defined in various ways, but the two most commonly used averages are the number average molecular weight, $\overline{M}_n$, and the weight average molecular weight, $\overline{M}_w$ [40; 41; 42].

$$\overline{M}_n = \frac{\sum N_i M_i}{\sum N_i} \tag{2.1}$$

$$\overline{M}_w = \frac{\sum N_i M_i^2}{\sum N_i M_i} \tag{2.2}$$

where N_i defines the number of molecules of specific molar mass M_i.

While $\overline{M}_n$ is more dependent on the total number of molecules, found in the distribution, $\overline{M}_w$ is more influenced by the higher molar mass fractions, through the M_i^2 term in the numerator.

The calculation of molar mass averages is not limited to the number or weight averages, in fact averages such as the Z-average, $\overline{M}_z$ (equation 2.3), and viscosity average, $\overline{M}_v$, are sometimes associated with specific polymer properties that are more strongly affected by distinct moments of the distribution.

$$\overline{M}_z = \frac{\sum N_i M_i^3}{\sum N_i M_i^2} \tag{2.3}$$

Polymer manufacturers have observed specific associations between mechanical properties of polymers and their molar mass averages. For instance, tensile strength and hardness tend to be a function of $\overline{M}_w$, while it has been found that $\overline{M}_n$ is often a sensitive indicator of the brittleness of a polymer. Particularly when adding plasticizers, such as polybutene oil in polystyrene, the polymer is often overload with species of small molecules, hence the number average molecular weight provides a better insight into ultimate product quality [43].

The ratio of $\overline{M}_w/\overline{M}_n$ is a measure of the breadth of the distribution, and is known as the polydispersity index, PDI . Since 2009, the International Union

of pure and applied chemistry has suggested the replacement of the loosely word polydispersity for dispersity, $Đ$ [44]. Although this study acknowledges this differentiation, it preferentially makes use of the former term polydispersity to enable a better correlation with data published before 2009.

Molar mass distributions are helpful in classifying different polymer systems, and it is common to categorise polymers after their PDIs. For instance, when the molar mass is narrowly distributed over a span of molecular weights, the polymer is said to be monodisperse, with the length of each polymer chain scarcely differing the next. Common values for monodisperse systems are in the range of PDI$\approx$ 1. In contrast, a polydisperse polymer is a material whose composition involves a wide distribution of different-sized molecules, or a very large PDI. Finally, when two polymer systems are mixed in a polymer blend, the new material will mainly be constituted of two defined molar mass phases, or peaks in what is commonly recognised as a bimodal or binary blend. Representative plots of molar mass distributions for PS examples of these polymer systems as observed in University of Nottingham Polymer Composites' laboratory are shown in Figure 2.1.

The molar mass details for PS materials (a) monodisperse, (b) polydisperse and (c) a bimodal blend referred to in Figure 2.1 are presented in Table 2.1. Note material (c) was a mixture of material 80 wt% (a) with a 20 wt% of a higher $\overline{M}_w$ molar mass PS component.

Table 2.1: Examples of various PS distributions as analysed at the University of Nottingham.

Code	$\overline{M}_n$ [kDa]	$\overline{M}_w$ [kDa]	$\overline{M}_z$	PDI
(a)	74.7	149.2	293	2.0
(b)	183.6	198.7	213.3	1.08
(c)	502	668.8	806.1	1.33

The challenge with polymers lies in finding a balance between the polymer molecular weight, the flow properties that enable the manufacturing during shape moulding processes, such as extrusion or injection, and the desired material properties of the solid products. Monodisperse materials can be useful in testing out scientific theories, but are time-consuming and expensive to synthesize, requiring

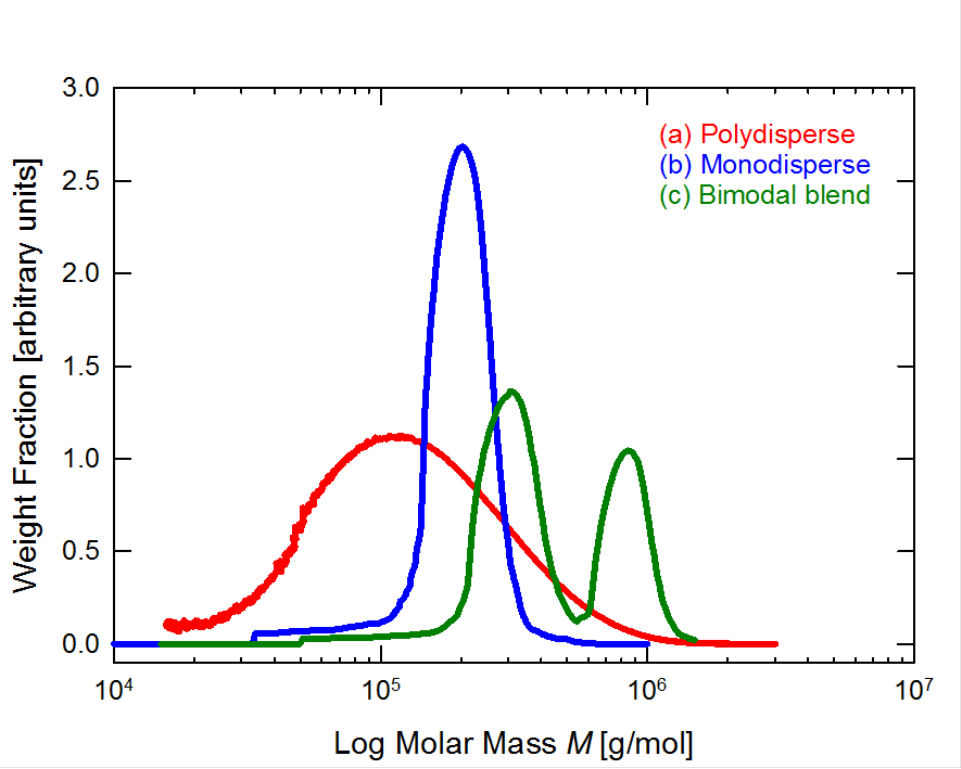


Figure 2.1: Representative molar mass distribution plots of (a) monodisperse, (b) polydisperse and (c) bimodal blend systems.

accurate, expensive and lengthy polymerisation processes. As a result, most commercial grades of polymers are found to be polydisperse to some extent. Hence, the wide molecular weight distributions of commercial polymers makes it challenging to quantify the degree to which molecular weight has an effect on their mechanical properties.

In the 1950s, at the early start of polymer science, it became obvious to polymer scientists that molar mass and molar mass distribution had a profound influence on the mechanical properties of polymers. Foden *et al.* [45] presented clear experimental evidence of how an increase in molecular weight can effectively increase the fatigue life of PS by testing varying molar mass samples in alternating cycles of axial tension and compression. In a different study, Merz *et al.* [1] tested a range of monodisperse polystyrenes (PDI$\leq$1.2) from 128 kDa, to 1500 kDa and their associated blends. The blends were obtained by adding a low molar mass

polymer or bibenzyl to the monodisperse polymers; details for these materials can be found in Table 2.2.

Table 2.2: Range of monodisperse materials and blends analysed by [1].

Code	$\overline{M}_n$ [kDa]	$\overline{M}_w$ [kDa]	PDI
1	1360	1500	1.10
4	1190	992	1.20
9	880	765	1.15
29	266	231	1.15
34	168	146	1.15
Code	$\overline{M}_n$ [kDa]	$\overline{M}_w$ [kDa]	Blend wt %
1b	11.7	650	1.55% Bibenzyl in 660kDa
2b	3.3	623	5.52% Bibenzyl in 660kDa
3b	1.82	594	9.97% Bibenzyl in 660kDa
4b	10.24	263	25% low polymer in 320kDa
5b	5.12	176.9	50% low polymer in 320kDa
6b	5.12	596	50% low polymer in 1190kDa

The materials were examined through dynamic tests to obtain the change in the dynamic Young's modulus, E, as a function of temperature. The results are presented in Figure 2.2.

Already in this early data, it is possible to see how E drops more rapidly in the blends compared to the monodisperse materials. It is equally possible to see that even though the $\overline{M}_w$ of blends 1b, 2b and 3b is similar, their dynamic response is very different, with material 3b showing the lowest young modulus at high temperature as a result of the higher addition of bibenzyl.

In the 1980s, Nunes *et al.* [2], presented an extensive experimental portfolio of studies to showcase how various mechanical properties of polymers depended on molar mass and molar mass distribution. The general observation made was that the mechanical properties of polymers increase with molar mass, until a limiting critical value of molar mass where the properties seem to level off. One particular study performed by Deanin *et al.* [2] analysed how higher molar mass fractions were in fact the controlling factor for the ultimate elongation in a range of commercial and broad MWD blends of plasticized polyvinyl chloride (PVC).

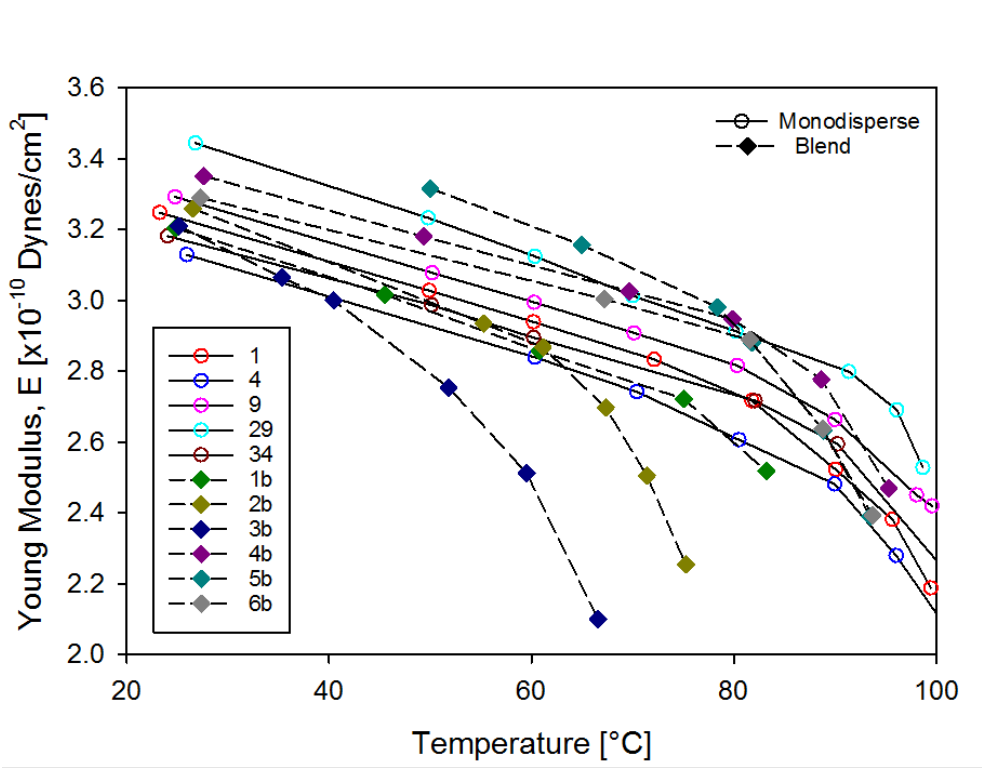


Figure 2.2: Young's Modulus vs. temperature for a range of monodisperse PS and their corresponding blends from [1].

In Figure 2.3 it is possible to see that when the elongation is plotted against the different molar mass averages, the correlation improves with the higher the moment of the distribution. This suggests that ultimate elongation for both sets of materials is more closely related to the higher molar mass fractions in the distributions, captured by the $Z-$molar mass average, rather than simply by differences in polydispersity. As reported by Cazes [43], it is known that several pragmatic associations have been developed between specific M-averages and polymer properties. In the case of the M_z average, this is often reported to be a good measure of the flex life and stiffness of polymer materials.

One of the main problems when trying to associate mechanical properties with specific molecular weight averages is the inability to produce a universal molar mass-derived parameter to correlate with any shape of molar mass distribution. Bersted and Anderson [46] tried to address this issue by experimentally analysing

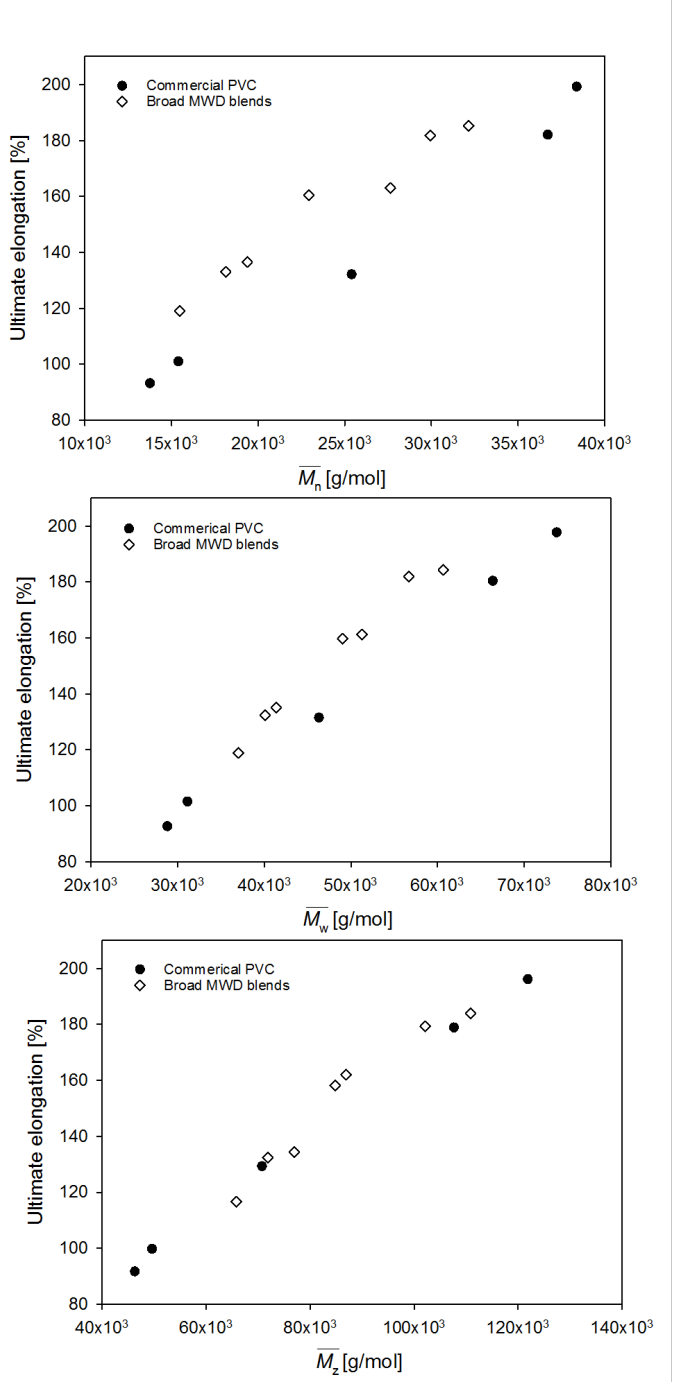


Figure 2.3: Ultimate elongation of PVC plotted against $\overline{M}_n$, $\overline{M}_w$, $\overline{M}_z$ from [2].

the influence of MMDs on tensile properties of monodisperse and polydisperse polystyrenes. Their argument was to develop a parameter to describe the tensile strength of both narrow and broad distributions of polymers. They suggested the failure property parameter, M_T, of the form $\phi(1 - M_T/\overline{M}_n*)$ by considering that only the entangled molecules ($\geq$ 60 kDa) could make an effective contribution to the tensile strength of the polymer network. Although M_T showed marginal success in producing predictions that could capture the tensile behaviour of both narrow and broad distributions, this still needs to be expanded into other mechanical phenomenon observed in polymers such as strain hardening, crazing or physical ageing.

2.2 Molecular entanglements in polymers

Entanglements in polymers can be defined as physical interactions that arise between polymer molecules due to their topology. Entanglements can act as temporary anchoring points restricting the movement of the interacting chains. Unlike cross-links, entanglements change and relax over time, which poses additional challenges in the modelling of polymer diffusive responses.

When a polymer distorts, its interconnecting molecules elongate with limited extensibility due to movement restrictions imposed by their entanglements with adjacent chains. Once the stress is removed these molecules move back to a state of equilibrium at a timescale representative of their ability to diffuse through their active entanglements. Because the probability of molecules entangling with one another depends on their length if the chains are too short, i.e. consisting only of a couple repeating monomeric units, entanglements cannot occur. The overall observation is that when molecules become longer than a critical molecular weight, M_c, the probability of entanglements to occur becomes larger and this serves the network to develop better stress dissipation characteristics, rendering the material with improved tensile strength, and other mechanical properties [47]. Similarly, if the chains become too long, the system becomes saturated and the molecules are unable to flow or slip pass one another, at which point the further lengthening of the chain does not make much difference to increase mechanical

properties (as observed in [2]).

Polymer chain dynamics have found meaning of these observations in the core principles established by polymer physical models, such as those developed for polymer viscoelasticity and polymer rheology, as will be discussed in the subsequent sections.

2.3 Review on viscoelasticity

A distinctive feature of the mechanical behaviour of polymers is the way in which their response to an applied stress or strain depends upon the rate or time of loading. Contrary to metals and ceramics that behave as elastic solids, -and as such obey Hooke's law-, polymers depict stress-strain characteristics both of elastic solids, and viscous liquids, hence the term viscoelastic. While at low temperatures and high strain rates polymers display elastic behaviour, at high temperatures and low rates of strain they are seen to behave in a viscous manner, i.e. flowing like a liquid [48].

Viscoelasticity fundamentally controls the mechanical response of polymers to applied stimuli and has been shown to be correlated to their microstructural features, such as molar mass, molar mass distribution, architecture and entanglements [5]. When a polymer undergoes deformation, an energy exchange takes place. In accordance to the second law of thermodynamics, part of the energy imparted is invariably dissipated even when part of it is stored [49]. Under ordinary conditions the material response is time-dependent and composed of both parts: a stored deformational elastic response, and a dissipated viscous response. Materials displaying both elastic and viscous properties are thus referred to as viscoelastic. For instance, liquids above the glass transition temperature, T_g, can relax quickly through Brownian motion, hence structural memory is short and their response is essentially viscous. On the other hand, structural relaxation in a solid is very slow, and at small deformations the response is fundamentally elastic. In polymers, their structural relaxation depends on the heterogeneity their macromolecular dimensions. As a consequence, polymers exhibit a multiplicity of relaxation times, τ [32; 40; 50].

Polymer viscoelasticity can be measured through linear viscoelastic tests: creep-recovery, $J(t)$, stress-relaxation, $G(t)$, and dynamic measurements, $G(\omega)$. The complex shear modulus $G(\omega)$ can be split into: a elastic component, namely the storage modulus G'; and a viscous term: the loss modulus G". The data in these tests is often manipulated to obtain a mastercurve through the application of the time-temperature-superposition principle, TTS, which is well described by the William-Landel-Ferry, WLF , equation 2.4 [32; 51].

$$\log a_T = \frac{-C_1(T - T_0)}{[C_2 + (T - T_0)]} \tag{2.4}$$

where T is the experimental temperature, T_0 the reference temperature, and C_1 and C_2 are empirical constants. In essence superposition enables to associate a range of short-time experiments at different temperatures through a shift parameter, a_T.

The linear theory of viscoelasticity, LVE, provides a mathematical framework for the description of viscoelastic phenomenon. Simple models represent the elastic contribution by Hookean springs, while the viscous parts are described by linear dashpots. These contributions are combined in a series of Maxwell or Voigt models, and integrated into generalised equations that consider spectra of relaxation times. The most widely used is the generalised Maxwell, or generalised Zener model [40; 52; 53]. Equations for $J(t)$, $G(t)$ and $G(\omega)$ can be found in Table 2.3.

The above expressions, are applicable to linear viscoelasticity, LVE, where stress and strain show a linear relationship. As strains become larger, the response of polymers deviates from linearity and enters the non-linear viscoelastic regime, NLVE, where stress and strain rate become time and strain dependent. In a later subsection, mechanical and rheological models for linear and non-linear viscoelasticity are discussed. Particular attention is given to the effect of molar mass and entanglements in the polymer's experimental response and chain relaxation.

Table 2.3: Viscoelastic properties

Property	Basic equation	Generalised equation
$J(t)$	$J(t) = \frac{\epsilon(t)}{\sigma}$	$J(t) = J_e + \int_0^\infty 1 - \exp[-(t/\tau)]J_i(\tau)d\tau$
$G(t)$	$G(t) = \frac{\sigma(t)}{\epsilon}$	$G(t) = G_v + \int_0^\infty \exp[-(t/\tau)]G_i(\tau)d\tau$
$G(\omega)$	$G'(\omega) = (\sigma_0/\epsilon_0)cos\delta$	$G' = G_v + \sum_{i=1}^{n}(G_i\omega^2\tau_i^2/1+\omega^2\tau_i^2)$
	$G"(\omega) = (\sigma_0/\epsilon_0)sin\delta$	$G" = \sum_{i=1}^{n}(G_i\omega\tau_i/1+\omega^2\tau_i^2)$

2.4 Mechanical constitutive models

The concepts of viscoelasticity have evolved into complex physical equations to describe polymer behaviour, -e.g, stress-strain curves, strain-hardening and physical ageing-, through the development of constitutive models. The description of the behaviour of a material is generally considered to be constitutive if the formation does not violate any principles of continuum mechanics [49]. The constants and functions proposed to describe the observed behavior must therefore be material constants and material functions and can contain physical information on the constitution of the material.

Polymer constitutive models can help in the understanding of one crucial issue: the effect molecular deformation history has on the mechanical properties of these materials. The mechanical properties of manufactured polymers are well known to depend on the degree of flow and thermal changes due to production processes (injection, extrusion, drawing), which in turn depend on their inherent molar mass characteristics. Constitutive equations are sets of non-linear equations proposed to mechanistically describe the energetic and deformation processes undergone by polymer macromolecules when a stress is applied [3; 54].

The basis for most current mechanical polymer constitutive models started with the work of Haward and Thackray [55], who modelled the stress-strain properties of polymers through the decomposition of the linear and non-linear viscoelastic components of their behaviour into one dimensional models. They assumed that the behaviour of polymers is an additive contribution of:

- Large-strain elasticity, modelled through a Hookean spring
- Non-linear viscoelasticity, modelled as an Eyring dashpot in series with a linear spring
- Finite extensibility, can be included by the addition of a Langevin chain expression instead of the Hookean spring

Haward and Thackray essentially described two fundamental free energy sources: atomic diffusion, through Eyring viscoelastic flow; and the perturbation of conformational entropy, through a Langevin or Hookean spring. These are the assumptions which form the basis of polymer constitutive models used nowadays.

Boyce [33], Tervoort [36] and Buckley [35], went on to develop these ideas further, accounting for 3D deformation using the principles of continuum mechanics. This study, will focus on the evolution of the Glass-Rubber model, GR , developed by the Oxford group [35], but other models are similar in nature.

Assuming continuity, the polymer changes upon deformation from an initial position $\mathbf{X}$ to a final position x in an Euclidean plane. This displacement is represented through a deformation gradient tensor, $\mathbf{F}$, (the notation used follows convention, where boldface terms indicate tensorial quantities) separated into a volumetric, J, and deviatoric, $\overline{\mathbf{F}}$, parts:

$$J = \det \mathbf{F} \quad \text{and} \quad \overline{\mathbf{F}} = J^{-\frac{1}{3}}\mathbf{F} \tag{2.5}$$

The stress tensor, $\boldsymbol{\sigma}$, is similarly separated into a volumetric, σ_m, and deviatoric, $\boldsymbol{S}$, part

$$\sigma_m = K \ln J = \frac{1}{3} \operatorname{tr} \boldsymbol{\sigma} \quad \text{and} \quad \boldsymbol{S} = \boldsymbol{\sigma} - \sigma_m \boldsymbol{I} \tag{2.6}$$

where K is the bulk modulus. When a polymer is deformed, there are two contributions to the deviatoric stress: bond-stretching stress, $\boldsymbol{S^b}$, and conformational stress, $\boldsymbol{S^c}$; and these are assumed to be additive hence $\boldsymbol{S}=\boldsymbol{S^b}+\boldsymbol{S^c}$. The authors

[3; 56; 57] also derived an expression for the rate of deformation tensor $\overline{\boldsymbol{D}}$, and isochronic velocity gradient tensor $\overline{\boldsymbol{L}}$. The relaxation time associated with the jth glassy mode is referred back to an unstressed relaxation time $\tau^*_{j,0}$, at reference temperature T^*, and structural state T^*_f, through shift factors [3; 35; 57]. The complex modulus is defined in the GR model as,

$$G* = G' + iG" = G^c + G^b \sum_{j=1}^{N} v_j \frac{\omega^2 \tau^2_{j,0}}{1 + \omega^2 \tau^2_{j,0}} + iG^b \sum_{j=1}^{N} v_j \frac{\omega \tau_{j,0}}{1 + \omega^2 \tau^2_{j,0}} \tag{2.7}$$

The model employed a multimode discrete spectrum to predict various aspect of stress relaxation in polymers. Wu *et al.* [3] illustrate this by analysing the relationships between temperature, molar mass and compressive yield stress for a series of monodisperse and bimodal blends of PS. Wu was able to achieve a good quality fit between dynamic experiments from Groves on polydisperse PS (at T=80-200 °C and frequencies of 0.1 s^{-1}-100 s^{-1} in PS), and the GR model prediction across the glass transition. The results for the mastercurve at T=120 °C, are reproduced in Figure 2.4.

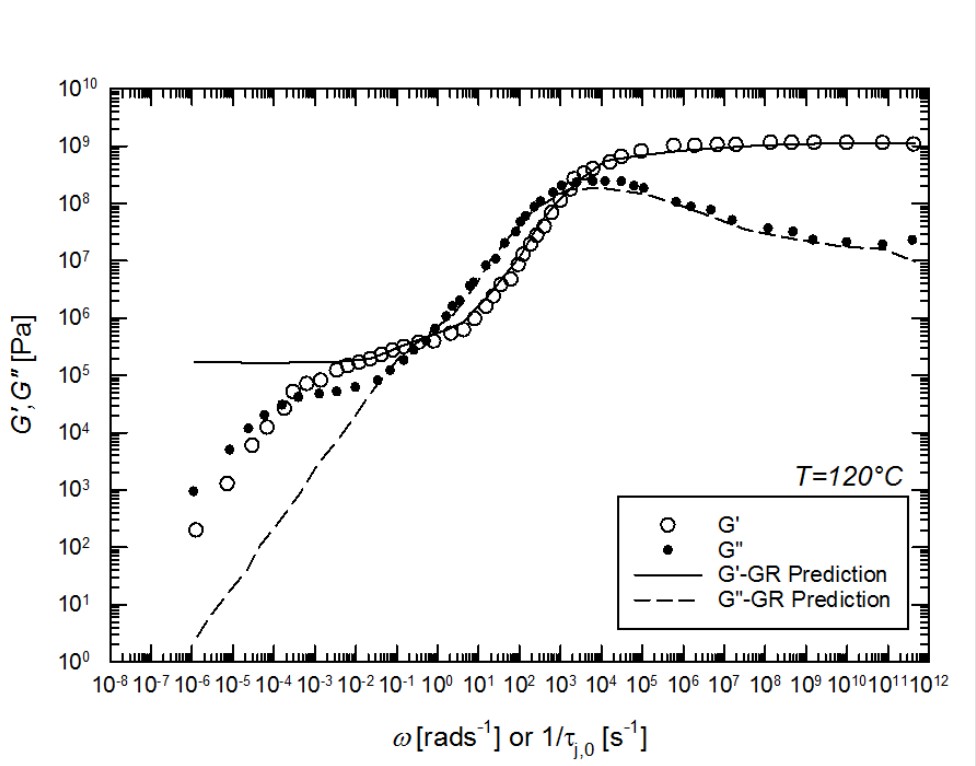


Figure 2.4: G' and G" parts of the LVE complex shear modulus for PS as predicted using the GR model in the glassy regime from [3].

By using a discrete 17-element spectrum, Wu was able to fit Groove's data, but only until the long-time (low frequency) end of the glassy, α-relaxation process. In fact, it was recognised that the state of the GR model was only concerned with the portion of the relaxation spectrum associated with motion on a small length scale, less or equal than a tube diameter in the frame of tube theories. As will be further discussed in section 2.5.1, in the α-relaxation process, relaxation times do not scale with molecular weight, unlike slower modes in the melt regime that involve diffusion along the tube. Nevertheless, in addition to these observations, Wu was able to identify a sensitivity to molecular weight in the compressive yield stress for a range of isotropic monodisperse PS, Figure 2.5.

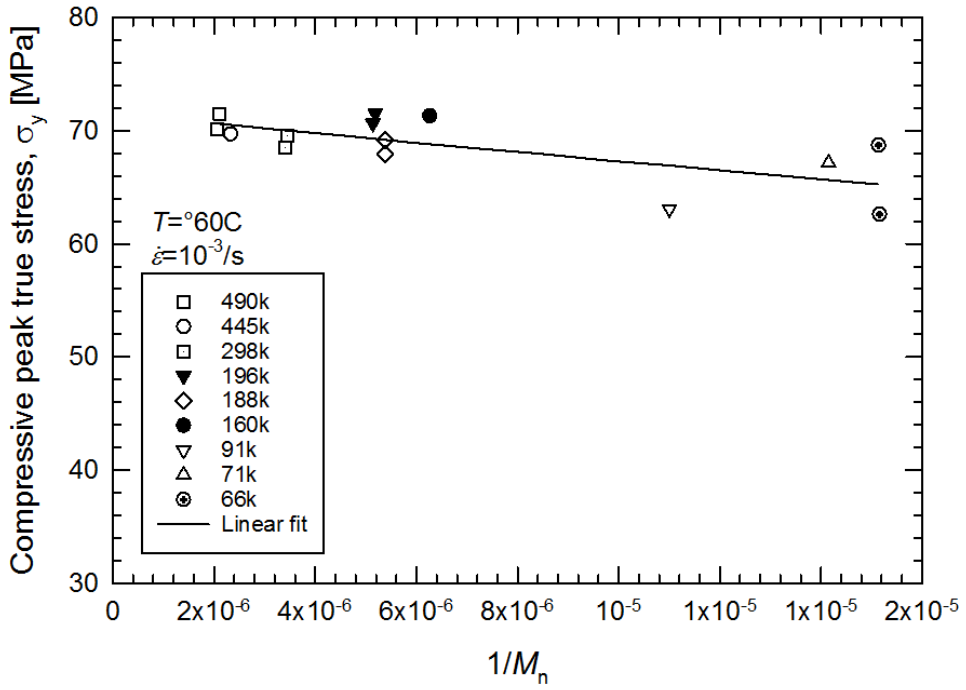


Figure 2.5: M dependence on σ_y as reported by [3].

Although these results are limited to the very narrow range of molar mass analysed by Wu, it was possible to observed an an enhanced mobility in the lower molecular weight samples, attributable to the presence of chain ends. Chain ends introduce local discontinuities, thus increasing the specific volume. This behaviour had been previously reported by Fox and Flory [4] in their dilatometric study for a range of varying molecular weight monodisperse PS, as seen in Figure 2.6.

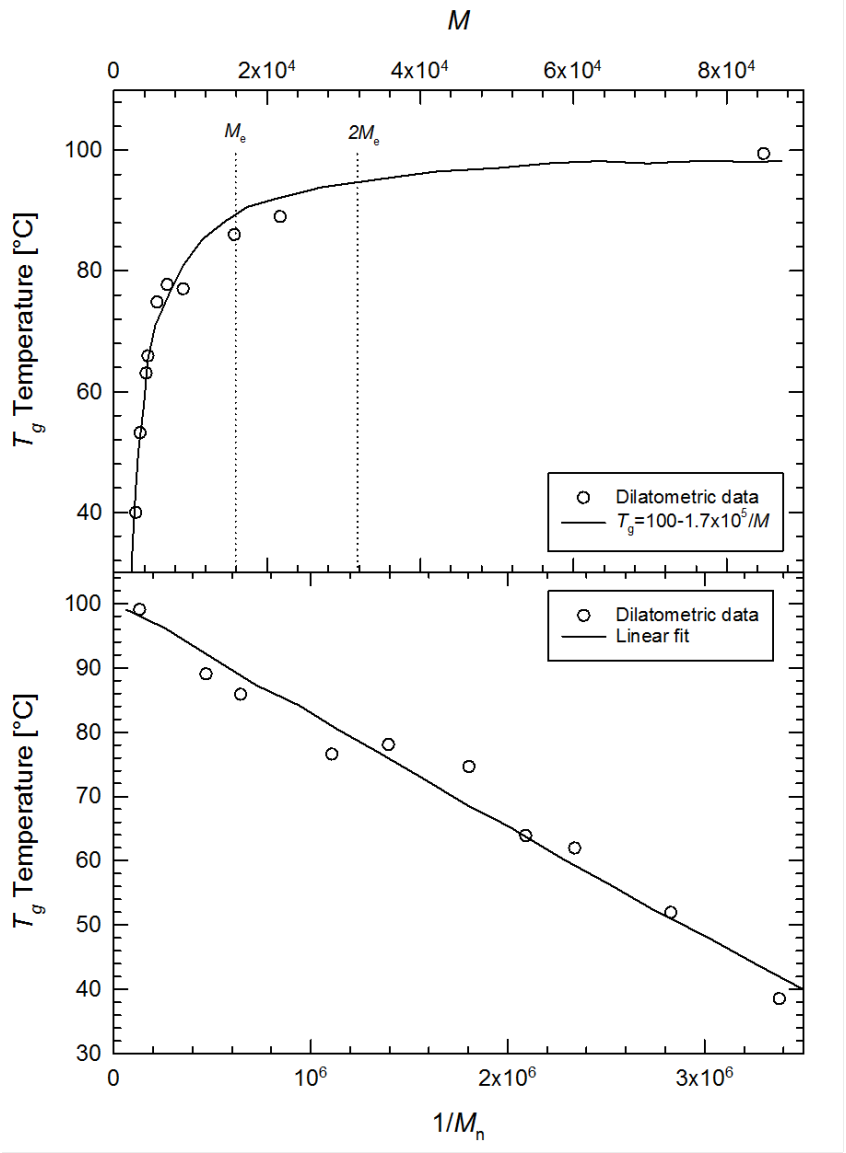


Figure 2.6: M dependence on T_g as reported by [4].

Wu's observation is consistent with the reduction in T_g with increasing chain ends, proportional to $1/\overline{M}_n$. Wu and Buckley concluded that chain ends increase the probability for thermally activated flow events, corresponding to a decrease in the Vogel temperature T_∞. The authors, were able to present quantitative means of accounting for this effect and incorporating it into the GR model.

Similar to the framework presented for the GR model, there is further evidence

by several other authors showcasing different aspects of mechanical constitutive models. Studies by the MIT team [58; 59] have looked at predicting strain hardening [58; 59], while Struik [60; 61] has widely contributed to the understanding of physical ageing. Yet, as highlighted by De Focatiis [10], a lot of these models have been refined using a pheonomenological approach, rather than deriving the corresponding molecular models to account for the consequences of changing molecular structure or chain length. Particularly near and above the glass transition (just in the limits of Wu's example in 2.4), the conformational entropy begins to relax by molecular diffusion within the tube, and the entanglement network becomes elastoviscous. The obvious next step in improving the applicability of these mechanical models is to couple them with melt-state rheology to obtain a full stress relaxation spectrum, for a variety of molar mass distributions and architectures. The upcoming section will provide an insight to the underlying physics and challenges in the modelling of flow dynamics in polymeric systems, and it will emphasize on the latest state-of-the-art molecularly aware models.

2.5 LVE and NLVE: a rheological approach

In addition to the mechanical models used for solid-state predictions, over the past 30 years the theory of linear viscoelasticity has greatly benefited from the reptation [62] and tube model [63; 64] ideas, to interpret the dynamics involved in chain relaxation of polymer flows, in the melt-state and in solutions. The combination of both these theories has coined the fundamental concept for the stress relaxation of polymer molecules along an entanglement network. The tube model essentially describes that a chain is constraint by the topological interactions to surrounding molecules by means of a field called "the tube". The so-called chain is unable to cross another molecule, and is confined to move within a tube of diameter a [6].

The usual method of determining the onset of entanglements is to detect a change in the molecular weight dependence of a viscoelastic constant, such as the zero-shear viscosity, η_0 , or the steady-state shear compliance J_e^0 [65]. Figure 2.7, shows a plot of creep compliance, J_0, against molecular weight for a range of

monodisperse polyisoprenes.

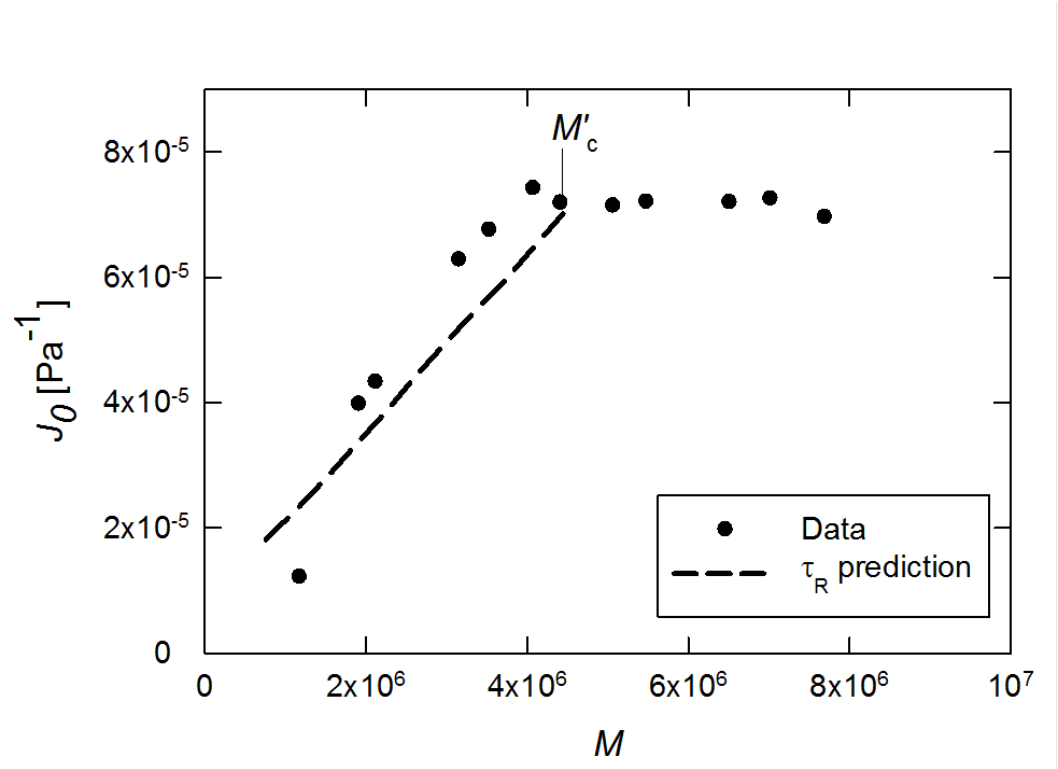


Figure 2.7: The molecular weight dependence of the recoverable compliance for nearly monodisperse polyisoprenes, extracted from [5].

These results show that as the molar mass increases so does the creep compliance up to a critical M_c' value, where it becomes weight independent. Polymer chain dynamics correlate the changes of molar mass with the entanglement theory through considering the entanglement molecular weight, M_e, which is simply an expression for the weight of a chain strand between entanglements,

$$M_e = \frac{\rho RT}{G_e} \tag{2.8}$$

where R, is the ideal gas constant, T is the absolute temperature, and G_e entanglement modulus [5; 7; 66] (as it will be discussed, the entanglement modulus is

obtained from rheological data, as per section 2.5.1).

The standard agreement is that $M_c \approx 2M_e$ [65; 67]. Through the concepts of M_e and M_c, it has been possible to define the relaxation times of polymer chains based on their entanglement networks. Particularly in the field of polymer rheology, timescales for chain deformation such as the Rouse time, τ_R , and the reptation time, τ_d , are used in the prediction of chain relaxation in polymers.

The development and maturity of rheological instruments has in fact made it possible to analyse and document polymers' linear and non-linear behaviour at a range of temperatures and across a wide frequency range. An account of the models proposed to interpret the experimental data is presented in the subsections below.

2.5.1 LVE models

Dynamic tests have gained wide acceptance to evaluate the LVE behaviour of polymers, as $G', G"$ plots accurately reflect on the distribution of relaxation times associated with molar mass and MMD.

In a well compiled review [6], van Ruymbeke discusses the differences between the rheological traits on the linear viscoelastic mastercurves of a monodisperse polybutadiene, PBD, (100 kDa, PDI=1.01), against those of a binary blend of two monodisperse PBD: 5%-410 kDa and 95%-100 kDa PBD. The data was measured at temperatures -80 °C to 100 °C, at ω=0.1 s^{-1}-100 s^{-1}, and plotted using TTS at T_0=40 °C. The results are provided in Figure 2.8.

The rheological data for the monodisperse case is illustrated in Figure 2.8(a). The image shows the plateau modulus G^0_N has been determined by locating the value of G' where the minimum value of $G"$ is reached in the rubbery plateau. The relaxation time τ_e, or equilibration time for a segment between entanglements, is approximated through the $G' - G"$ crossover; and the slope for J^0_e is represented by the intersection of the terminal $G', G"$ slopes. J^0_e, and η_0 can be determined by extrapolation, through the limiting laws $G'(\omega) = J^0_e \eta_0^2 \omega^2$ and $G"(\omega) = \eta_0 \omega$. It can be seen that the slopes are quite well defined, with the characteristic 2 and 1 gradients for G' and $G"$, respectively.

In the case of the binary blend (Figure 2.8(b)), $(J^0_e)_M$ is sensitive to the 5%

higher molar mass component. In the terminal region, shoulders are visible on the moduli of the blend compared to the monodisperse system. This clearly evidences the change in the distribution of relaxation times attributed to the presence of the higher molar mass component, even though this only represents 5% of the total mass. Similarly, from the intersection of G' and G" with G_N^0 determined by the slopes, it can be seen that J_e^0=0.04 MPa for the blend, compared to 0.5 MPa for the monodisperse sample, which translates into a 10-fold broadening of the distribution of relaxation times. This clear sensitivity in the low frequency response to a small high molecular weight tail in the polymer's MMD is due to the very strong molecular weight scaling of relaxation times [6], and thus becomes experimental evidence of the effect that molar mass and molar mass distribution have on the viscoelastic properties of polymers.

Since G_N^0 is considered a constant material parameter that can be calculated in combination with M_e in equation 2.8. For some theories, the value of G_N^0 is often referred to as G_e. J_e^0 is often the variable of choice to be associated with the width of the relaxation times distribution, and polydispersity of the polymer. Ferry [32] and Soo Cho *et al.* [65] have reported that η_0 shows a sharper transition to entanglement than J_e^0, while J_e^0 appears to be more responsive to molecular weight distribution than η_0.

The above results can be understood in the frame of a tube model. The tube represents a temporary space constraint resulting from the presence of other surrounding chains. The test chain, i.e. observed chain, is able to move and relax the stress within these tube boundaries. Although, there are other models available, both are useful in understanding the effect entanglements have on the relaxation spectra of polymers. Most models nowadays use the following approach: for chains that are too short to entangle ($M < M_e$), relaxation times are brief enough to be described using the Rouse model, where τ_R is defined through

$$\tau_R(M) = \tau_e * Z^2 \tag{2.9}$$

where Z is the number of entanglements, obtained from M/M_e.

At times larger than τ_e, chains start to interact topologically and their motion

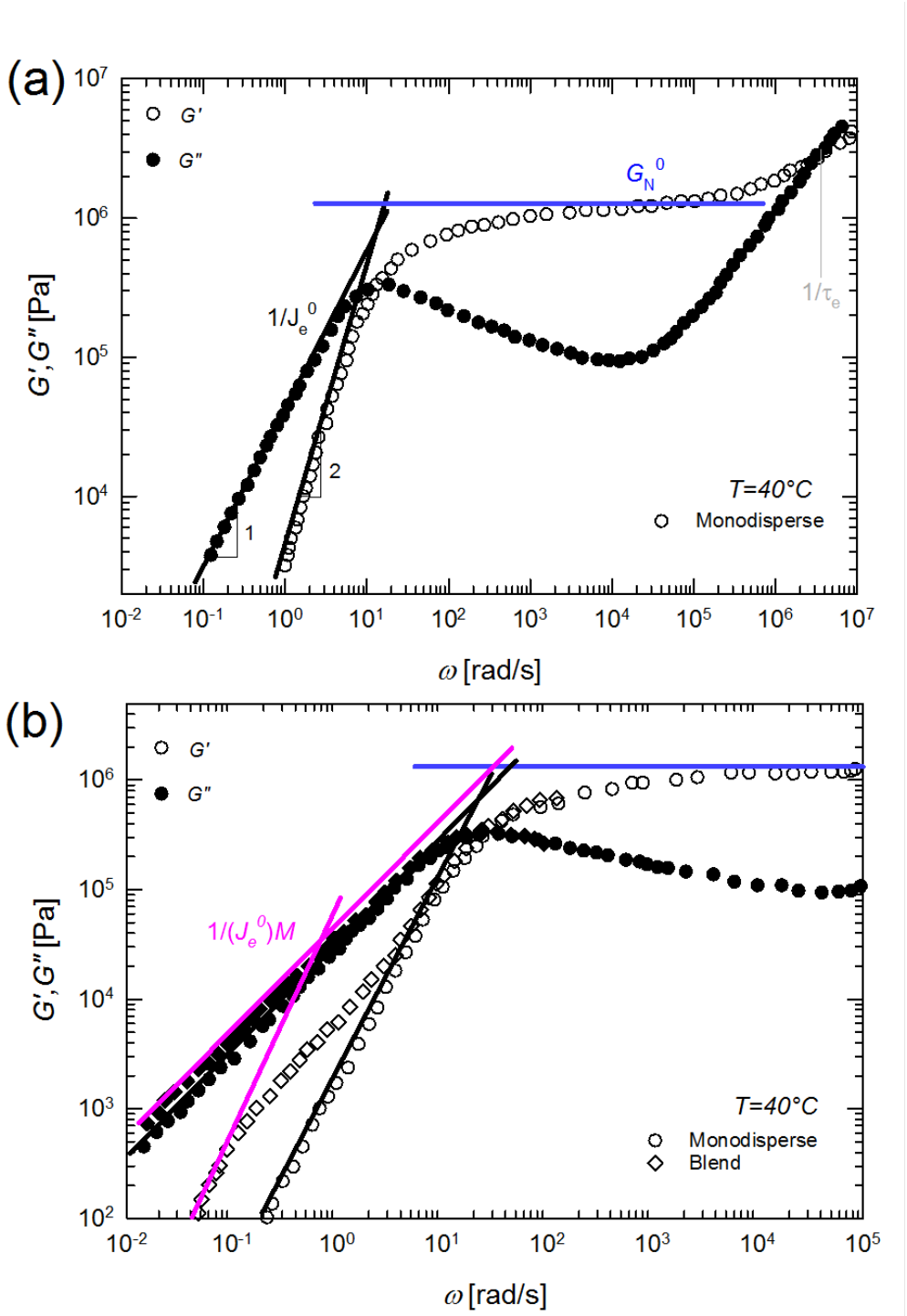


Figure 2.8: Master curve of (a) monodisperse PBD and (b) binary PBD blend of 5%410 kDa and 90%100 kDa at $T_0 = 40\,°C$ from [6].

is influenced by the entanglement network. This can be modelled by means of reptation in a surrounding tube of diameter a. In this model, the chain relaxes from the outer to the inner segments, and the reptation time, τ_d, is defined by

$$\tau_d(M) = 3\tau_e Z^3 = \frac{L_{eq}^2}{\pi^2 D_c} \propto \frac{M^2}{M^{-1}} = M^3 \tag{2.10}$$

where D_c is the curvilinear diffusion coefficient ($kT/N\zeta_0$, where ζ_0 is the monomeric friction coefficient), and L_{eq} is the primitive path length.

Various authors have examined the shifting relaxation mechanisms in polymers associated with a distribution of chain lengths. In a series of studies of monodisperse PS systems and binary blends, Watanabe *et. al* [68; 69; 70] propose a phenomenological molecular weight criterion. They observed that the relaxation of PS blends was associated with the onset of entanglements of the short and long chains within the systems. In a dilute system, i.e. where the weight fraction of the short chains was smaller than a critical weight fraction value, w_c, the relaxation of the short chains took place first, and at longer times, the entanglements of the long chains appeared to be dissolved by the short chains. In concentrated blends, where the weight fraction was above w_c, the relaxation of the long chains appears to occur at times closer to the relaxation times characteristic of the longer chains.

Experimental observations have in fact shown that the anticipated M^3 dependence predicted by pure reptation does not fully capture the viscosity behaviour of entangled polymer melts, and it is in fact closer to a $M^{3.4}$ as reported by [71; 72]. This has introduced the recognition of additional motion mechanisms such as the free movement of chain ends, contour length fluctuations, (CLF) along the tube, and constraint release, (CR) a mechanism whereby constraints are lost by the movement of neighbouring chain ends. By incorporating these concepts into the reptation and tube models it has been possible to increase the accuracy of LVE predictions for the behaviour of polymer melts and solutions. This in itself opens a range of possibilities for polymer scientists and manufacturers, as it enables to anticipate the LVE of a specific polymer formulation

based on its molar mass distribution characteristics, or viceversa. Likhtman and McLeish [7] presented a convincing quantitative theory for the prediction of dynamics in linear monodisperse materials. They address the problem of including CLF and CR, by seeking to incorporate all Rouse modes resulting from CLF through the improvement of the ideas for single time approximation of Doi [71], and time-dependent one-dimensional diffusion from des Cloizeaux [39], to provide an algorithm that accounts for the quantitative calculation of the full relaxation function $G(t)$, through the treatment of single chain relaxation $\mu(t)$. In their theory, Likhtman and McLeish, (L-M), also introduced the numerical parameter c_v, to describe the number of chains needed to create one entanglement. This parameter, is associated with the "strength" of the CR mechanism, i.e., $c_v = 0$, means no constraint, while $c_v = 1$ assumes that one CR event leads to an effective jump of another chain's tube by distance a. The validity of this theory was compared to previous publications [39; 73], presenting improved predictions, particularly for the relaxation of short chains. Figure 2.9 shows the L-M prediction for a series of monodisperse PS of varying molar mass, using a single set of material constants.

In tube theories, the relaxation is thus modelled by means of three fundamental parameters: G_N^0, M_e and τ_e. G_N^0 and M_e can be connected through,

$$G_N^0 = \frac{4}{5}\frac{\rho RT}{M_e} \tag{2.11}$$

where G_N^0 is the entanglement modulus, ρ is the polymer density, M_e is the entanglement molecular weight. The prefactor 4/5 is included to account for the longitudinal motion along the tube. In the L-M theory, G_N^0 is in fact substituted by G_e, the entanglement modulus, which defines the stress before the relaxation of the longitudinal modes, and is linked to M_e through equation 2.8.

Other authors have successfully built upon the idea of tube models to assess the validity of more complex molecular dynamics scenarios. Rubinstein and Colby [74], (R-C), focused their work on testing the validity of reptation theories on binary mixtures of two monodisperse linear chains. In a similar at-

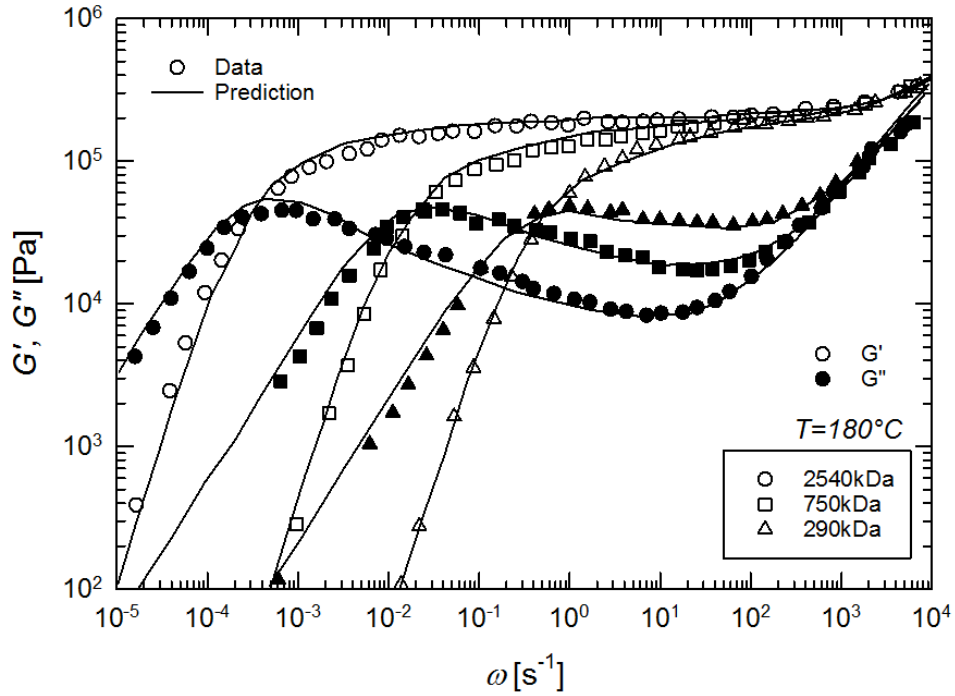


Figure 2.9: L-M best fit theory for dynamic moduli of PS from [7].

tempt, des Cloizeaux [39] proposes to address the problem through the analysis of stress points formed by the entanglement between two chains of different lengths. Tsenoglou [75], on the other hand, worked on the idea of a double reptation mechanism, by which the entanglements between molecules of different lengths occur randomly and proportionally to the volumetric fraction of the components in the mixture. His results are used in the form of derivated blending laws and additivity rules to calculate the relaxation modulus of binary blends and polydisperse distributions. One of the issues with the double reptation model is that it assumes that an entanglement relaxes when one of the chains diffuses away, ignoring CR effects. Therefore, this argument can only be valid when the relaxation times between the two chains are not too different, and in consequence remains unable to describe polydisperse blends, for example. Most recently, van Ruymbeke [76] extended the double reptation model to include the prediction of broad polydisperse systems by combining the Doi and Edwards relaxation function, with

des Cloizeaux time-dependent diffusion presenting convincing quantitative LVE data for polystyrene (PS), high-density polyethylene (HDPE) and polycarbonate (PC).

Although most of these models reflect upon observable mechanisms in molecular dynamics, the attempt to achieve the full universality of fitting parameters seems to fail. Some of the ongoing problems raised by van Ruymbeke [6] are the quantitative relationship between G_N^0 and M_e, particularly when including even more challenging features, such as the dynamic tube dilution, (DTD), or the constraint release Rouse regime. Another topic is the value of the dilution exponent, α, which serves to describe DTD through the effect of relaxed polymer fractions in the remaining unrelaxed chains, and whose value normally oscillates between 1-1.3. In a novel study, Shahid *et. al* [8] aim at addressing this issue by looking at the effect different-sized molecules (e.g. long polymer chains diluted in a matrix of very short chains), have in the relaxation of polymer solutions. To explore this, the authors used a range of monodisperse PS systems of varying molar mass, and diluted them with styrene oligomers to achieve different levels of concentration. As a starting point, Shahid *et al.* refer to Marrucci's [77] concept of dynamic tube dilution; they suggest that the effective tube diameter, a, that constrains a polymer molecule by its vicinity with surrounding chains, increases if the polymer concentration is reduced, thus increasing the space for lateral motion. In other words, a polymer molecule experiences more freedom to move, and relaxes quicker if the concentration is reduced. This was reflected in Marrucci's initial expression for M_e considering DTD, where he argues that the effective tube diameter depends on the unrelaxed fraction of the polymer, $\Phi(t)$ as:

$$M_e(t) = \frac{M_e(0)}{\Phi(t)^\alpha} \tag{2.12}$$

where $M_e(0)$ refers to the initial value of M_e. This argument, as emphasized by van Ruymbeke [6], forces the recognition that the tube diameter must be taken as an increasing function of time during relaxation. One important remark made by Shahid is that $M_e(t)$ is not only a function of fraction Φ, but also of the

concentration, c, within the system, as per equation 2.13,

$$M_e(t) = \frac{M_{(e,0,melt)}}{(c \cdot \Phi(t))^{\alpha}} \tag{2.13}$$

where $M_{e,0,melt}$ is the average molar mass between two entanglements in the melt state at time $t = 0$. As a consequence of rescaling M_e, Shahid proposes a corresponding effect on the G_N^0,

$$G_N^0 = \frac{\rho RT}{M_e} = \frac{c\rho_0 RT}{\frac{M_{e,0,melt}}{c^{\alpha}}} = G_{N,melt}^0 c^{\alpha+1} \Phi(t)^{\alpha+1} \tag{2.14}$$

where ρ_0 and $G_{N,melt}^0$ are the density and plateau modulus of the corresponding melt. Under these expressions, the reptation time of the melt is also affected, and scaled by c and α through $\tau_d(M) = \tau_{d,0,melt}(M)(c \cdot \Phi(t))^{\alpha}$. It is important to note that as M_e in the melt becomes larger, so does τ_e. Z, is consequently decreasing (since $Z = M/M_e$). In systems where short and long chains interact, the relaxation time of the smaller component can speed up the relaxation of the longer chain, consequently lowering G_N^0. Even more so, the short chains can be compared to a solvent, except for the fact that they introduce some extra friction. In his treatment of relaxation behaviour of diluted systems, Shahid recognises two processes: the first process occurring at high frequencies, where both short, and long chains relax (e.g. fast Rouse modes, τ_R); this relaxation is note to occur in strands within the chains that are shorter than the oligomers, $M < M_s$. The second process is associated with the relaxation of the long chains in polymer strands of masses between M_s and $M_{e,0,melt}/v_2$, where v_2 is simply the volume fraction of the long chains. This second frequency is interpreted by Shahid as being governed by Rouse relaxation, and hence calls for the consideration of the constraint release Rouse modes of long chains if any accurate predictions are to be made. This process describes the transition of the long chains from the initial tube into the dilated tube. Figure 2.10 presents the experimental data of this study for a monodisperse PS, $\overline{M}_w = 820\,\mathrm{kg/mol}$, diluted with 95wt% styrene

oligomers $\overline{M}_w = 8.8\,\text{kg/mol}$. It is possible to see that the dynamic response of the polymer is in fact a combination of both the relaxation of the short and long chains. To help elucidate on the differences and contributions of the relaxation processes involved, the authors provide a series of relaxation predictions: the full model (shown in pink); the oligomers (shown in blue); and the long chains, considering CRR (shown in black) and without it (shown in green).

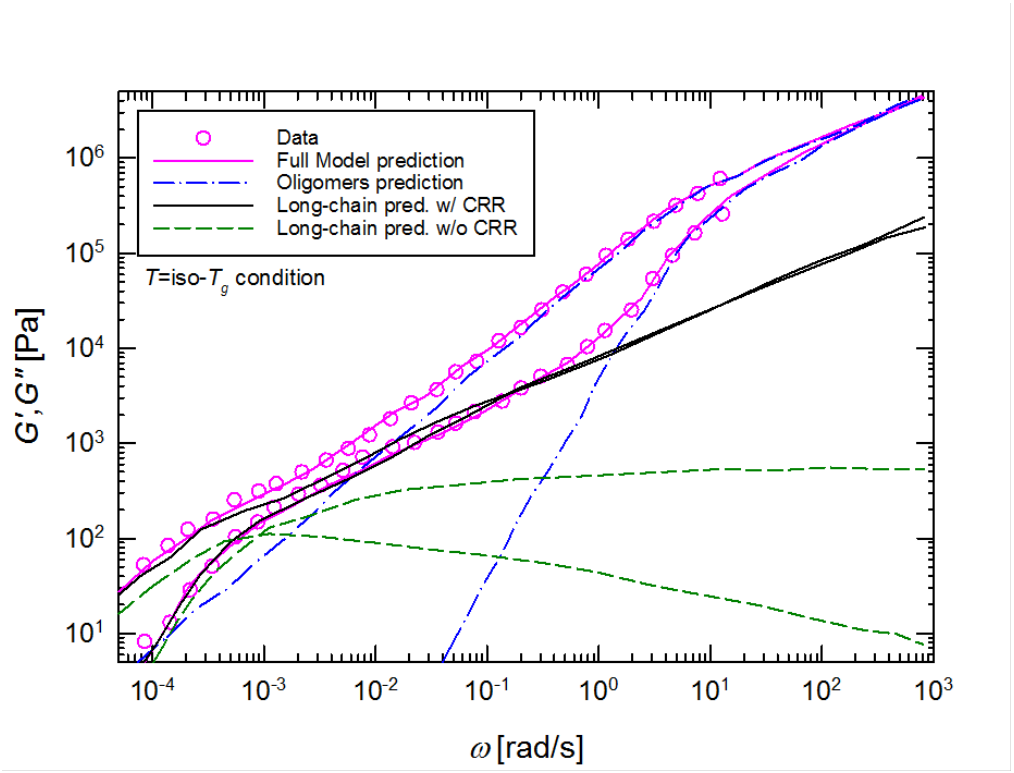


Figure 2.10: Experimental and predicted data from [8], for a diluted monodisperse PS ($\overline{M}_w = 820\,\text{kg/mol}$) with 95wt% styrene oligomers ($\overline{M}_w = 8.8\,\text{kg/mol}$).

Shahid reports that the polymer system needs at least a concentration of 10wt% of the 820 kg/mol monodisperse component for a rubbery plateau to be actually visible. In at the dilute 5wt% state in figure 2.10, the system only contains an average of 2.7 entanglement segments per chain, which is near the limit of the entangled state. This study was able to determine specific viscoelastic associations between G_N^0 and M_e and the polymer concentration in diluted polymer systems by using the DTD theory as a first principle. They presented

novel mathematical derivations to account for the fluctuations in the value of α. Furthermore, they managed to identify and predict relaxation limits and interactions between different-sized molecules. Nevertheless, some of the limitations of the model are: its deviation at high frequency, due to the contribution of the glassy relaxation at this terminal tail, which is not accounted for; and the discrepancy for the scaling of $G_{N,0,melt}$ with $c^{2.3}$ rather than c^2 in semi-dilute solutions, compared to the dilute systems shown. This is suggested to arise from the difference in cooperativity between the long chains, oligomers and small-molecule solvent.

Although the field of polymer rheological models keeps evolving, there are still questions today about the underlying physics governing the behaviour of more complex systems; for instance: in the case of highly polydisperse bimodal blends, below which molar mass can short chains be considered a real solvent?

2.5.2 NLVE models

Non-linear viscoelasticity is observable in large strain experiments. Marrucci [78] argues that when a polymer melt undergoes a fast (transient) flow, the relaxation occurs by two mechanisms: one of them is diffusion due to thermal motion (which occurs also in the absence of flow); the second is a convective mechanism, where the topological constraints, are renewed through the relative motion of chains due to flow. This mechanism of relaxation in the NLVE regime is known as convective constraint release, CCR . In nonlinear flows, as chains retract the constraint release rate is increased; hence, as the release rate grows with the convection rate, the tube constraints are thus removed by convection, through the CCR mechanism.

In the field of NLVE, Likhtman and Graham [9; 79] proposed major refinements to the Doi-Edwards approach. They followed Marcucci's initial postulates to model NLVE, particularly at the limit where the shear rate, $\dot{\gamma}$, approaches $1/\tau_d$ and the Doi theory fails. The authors proposed new arguments to describe the experimental behaviour in transient shear. Firstly, they recognised the contributions of CR by using the c_v parameter previously introduced in [7; 80]; secondly, they propose a new parameter R_s that optimizes the decoupling approximation of the

chains through their retractive motions. They named their model ROLIEPOLY (ROuse Linear Entangled POLYmers). The model requires five parameters: G_e, M_e, τ_e, c_v and R_s. While the first three are obtained by linear rheology fitting the L-M theory, the remaining two are dimensionless prefactors for the constraint release and retraction, respectively. Through this model, Likhtman and Graham were able to predict non-linear flows by incorporating the relevant terms for chain stretch and constraint release in their stochastic equation,

$$\begin{aligned}\frac{d\boldsymbol{\sigma}}{dt} &= \boldsymbol{\kappa}\cdot\boldsymbol{\sigma}+\boldsymbol{\sigma}\cdot\boldsymbol{\kappa}^T-\frac{1}{\tau_d}(\boldsymbol{\sigma}-1)\\ &\quad -\frac{2(1-\sqrt{(3/\operatorname{tr}\boldsymbol{\sigma})})}{\tau_R}\left(\boldsymbol{\sigma}+\beta\left(\frac{\operatorname{tr}\boldsymbol{\sigma}}{3}\right)^{\delta}(\boldsymbol{\sigma}-1)\right)\end{aligned} \tag{2.15}$$

where the conformational changes are defined through the stress tensor $\boldsymbol{\sigma}$. In Figure 2.11, Graham fitted $c_v = 0.1$ and $R_s = 2$ to obtain non-linear predictions for PS/TCP (tricresyl phosphate) data from Kahvand at a wide range of shear rates,

Graham was able to show good agreement between theory and experimental data not only for PS, but also for a range of PBD. In fact, the model has been so well received it has been used in the treatment of polymer elastic instabilities in shear and extension-dominated scenarios. Reis *et al.* [81] investigated the role of chain relaxation and orientation in the flow responses of polymer melts. They did so by studying the flow characteristic of polymeric fluids through: a) a shear dominated array of half-cylinders placed on channel walls (e.g. bumpy wall flow), and the extension dominated contraction/expansion slit geometry. Reis *et al.* correlated the molecular expressions in the ROLIEPOLY model to their own interpretation of reptation, CCR and chain retraction, and the corresponding stress associations via Wi_e, Wi_R and Wi_d, the Weissenberg numbers based on τ_e, τ_R and τ_d, respectively. The effect of the molecular weight of a polymer melt was considered through the model's association with the entanglement number, Z ($Z = \tau_d/3\tau_R$). They argued that in polymeric fluids where the Wi_R is small, the molecules disentangle and the fluid exhibits shear-thinning, thus reducing the base

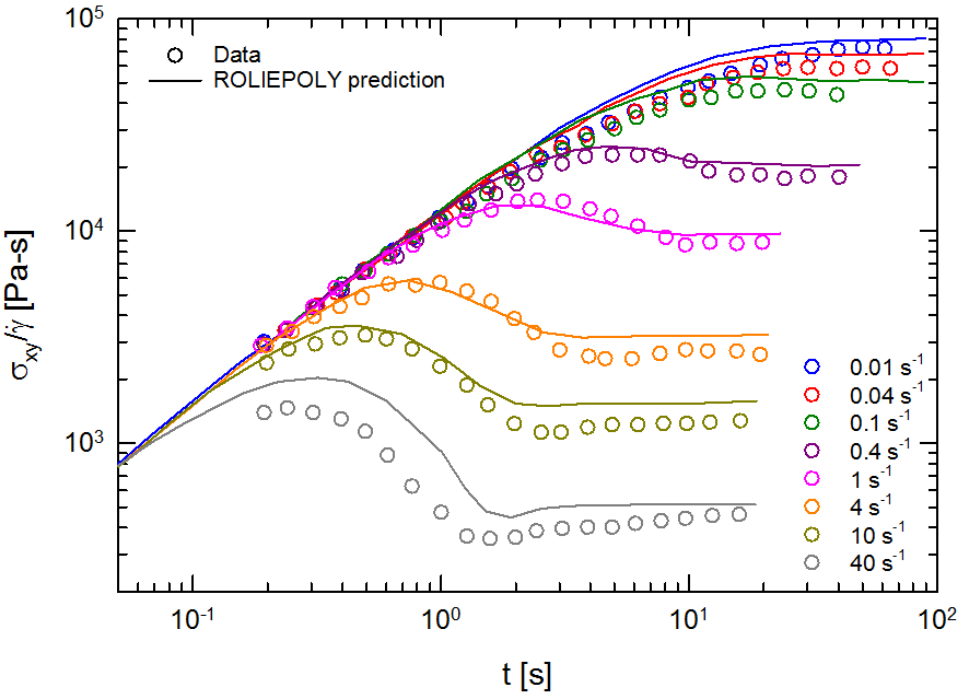


Figure 2.11: ROLIEPOLY best fit theory for the transient data of Kahvand for PS/TCP [9].

flow stresses and producing a more stable flow. This is not the case in fluids with higher molecular weight, where entanglements minimise shear-thinning, hence increasing base flow stresses and elastic instability.

The ultimate goal for all the discussed models is to be able to anticipate the final mechanical properties of polymers through the physical understanding of the molecular dynamics. The mechanical properties of solid polymers can differ as a result of two main factors: 1) their processing parameters, or rheological history; and 2) their microstructural characteristics (e.g. molar mass, distribution, architecture). Consequently, polymer engineers have to be aware of the need for comprehensive constitutive models that can capture both these criteria.

De Focatiis [10] proposed a model that extended the range of the ROLIEPOLY model up to the glassy regime, in an attempt to provide a constitutive equation capable of predicting both solid and melt states, termed the Glass-Melt model,

GM . Coupling of the ROLIEPOLY with Oxfords's GR model allowed him to analyse relaxation through the modelling of conformational entropy using a modified version of the ROLIEPOLY equation accounting for finite chain extensibility, FE , while integrating a multi-mode deformation in the glassy state through the GR model. One of the advantages of De Focatiis' model is its molecular awareness. The physical terms derived accurately describe chain-length dimensions, and hence are sensitive to molar mass and molecular characteristics. One clear example of this, is their expression for FE, λ_{max} ,

$$\lambda_{max} = \sqrt{\frac{n_b}{C_\infty}} \sin(\theta_b/2) \tag{2.16}$$

where n_b is the number of bonds between entanglements, $C_\infty = 10$, the characteristic ratio for PS, and θ_b is the carbon-carbon backbone bond angle (109.28 ° for PS). The inclusion of this term allows the model to explore the effect of high degrees of stretch and limited relaxation, such as in the case of sub-T_g stress-strain tests in melt-oriented specimens. The experiments were conducted on two monodisperse (AF,AG) and one polydisperse (R) grades of amorphous PS. Molar mass details of such materials are provided for reference in Table 2.4.

Table 2.4: SEC Molar Mass Measurements and T_g Measurements using DSC for PS samples as studied by [10].

Code	$\overline{M}_n$ [kDa]	PDI	T_g [°C]
AF	262	1.05	105.7±1.3
AG	518	1.15	107.5±0.9
R	216	2.54	104.7±0.7

Figure 2.12 illustrates the measured stresses of materials AF,AG and R, in De Focatiis' study, in bars drawn at a temperature of 115°C, and stretch, $\lambda = 4$. The simulations for the stress-strain response at the same temperature have been plotted for reference in dashed lines. Although the fit to data is only qualitative in nature, the ability to capture the strain-hardening behaviour at the end of the curve is a clear contribution of the FE effect in chain stretching and orientation.

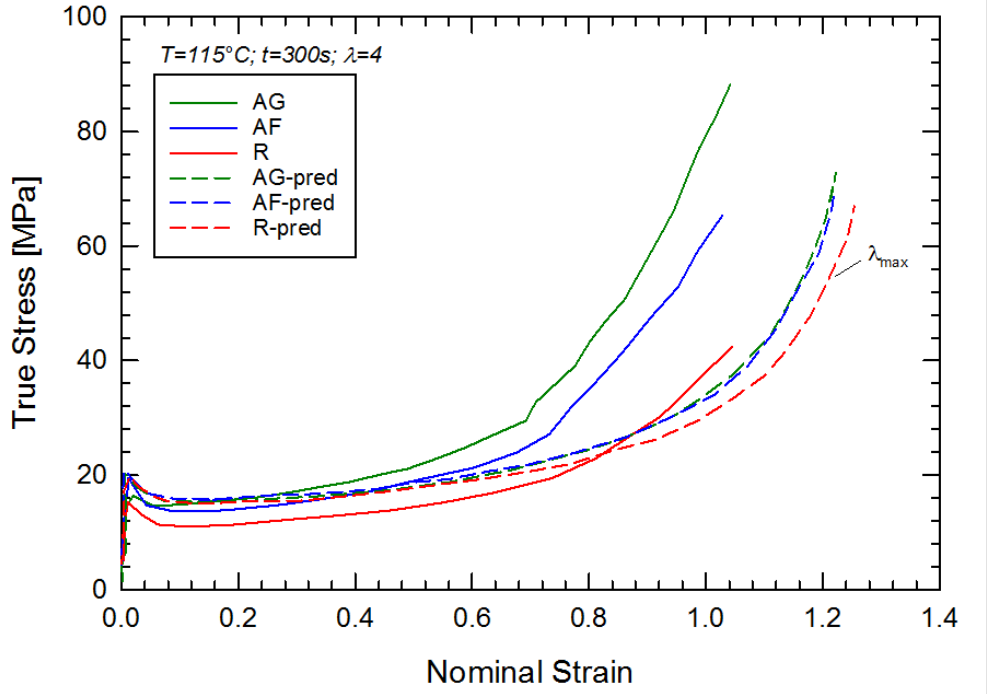


Figure 2.12: De Focatiis GM stress-strain curves predictions against experimental data for materials AF, AG and R. Modified from [10].

The materials were characterised in terms of their rheological behaviour through oscillatory, transient and extensional rheology. An example of the prediction of discrete spectrums for both G' and G" is shown for material AG in Figure 2.13. The corresponding τ_d, τ_R and τ_e are provided for reference, as so the fitting modes. It can be observed that at τ_e, the model partitions from the ROLIEPOLY into the glassy modes.

The model showed remarkable agreement of measurements in isotropic materials deep in the glassy and melt states. One of the most powerful features of this model is its ability to describe rheological behaviour through the entanglement physics derived in [7; 9; 79], and as such is sensitive to microstructural features (M_e, G_e). In the stretched samples, the model was capable of capturing the effects of molecular orientation on length-scales greater than an entanglement. Nevertheless, the model fails to capture the orientation of molecular segments

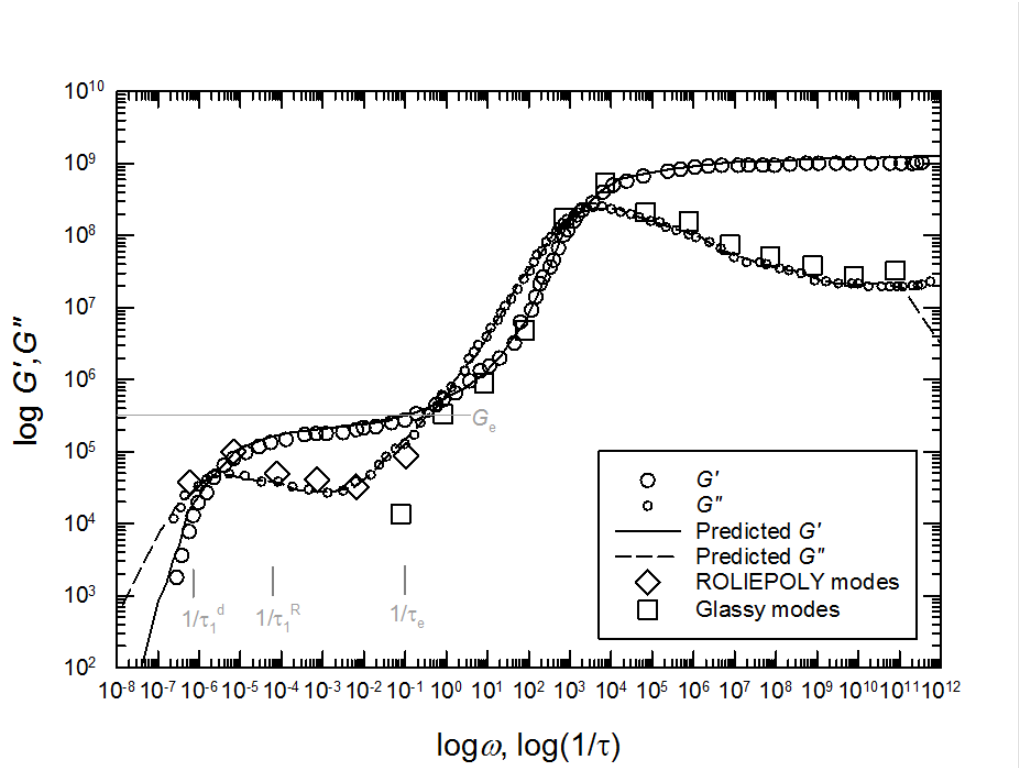


Figure 2.13: De Focatiis GM model as published for material AG in [10].

on a sub-entanglement level, where sub-entanglement orientation appears to be leading to more anisotropy in the yield stress than is accounted for by the conformational stress limits of the model.

Understanding the effect of orientation in these coupled viscoelastic models is essential since frozen-in orientation is a common consequence of manufacturing processes (e.g. injection, or extrusion), where polymer molecules flow and quench in anisotropic states. Frozen-in molecular orientation is essentially a combination of two factors: (a) the strain rate at which the molecules are deformed, and (b) the relaxation time of the polymer. An alternative way of validating these models is through the study of birefringence, and its connection with melt-stretching histories. A review on birefringence modelling is given in the following section.

2.6 Birefringence

Birefringence is an optical property of a material that can be defined through the concept of refractive index, n,

$$n = \frac{c}{v} \tag{2.17}$$

where c is the speed of light in vacuo, and v is the speed of light in the sample [11]. For polymers, it is two orthogonal indices that are usually relevant. In a phenyl polymer such as PS, optical birefringence has two distinct sources: (1) birefringence arising from bond stretching, e.g. carbon-carbon backbone, and (2) birefringence arising from molecular alignment, e.g. conformations of the phenyl side group. Hence, the ortogonal refractive indices n_1 and n_2 interact with the PS monomer as per Figure 2.14.

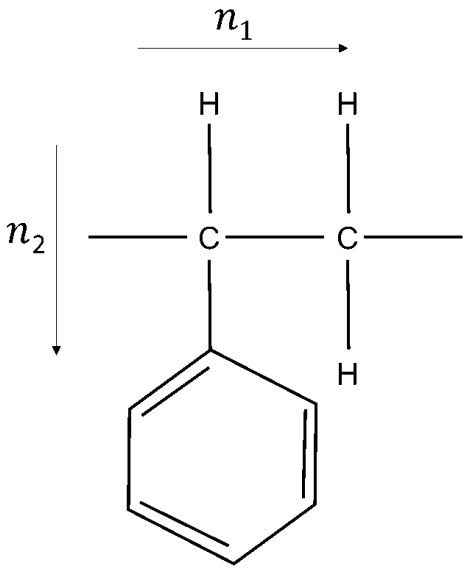


Figure 2.14: PS interaction with refractive indices, $n1$ and $n2$, from [11].

The birefringence $\Delta n'$ is defined as the difference between the refractive indices for light plane-polarized parallel to two of the optic axes.

$$\Delta n' = n_1 - n_2 \tag{2.18}$$

In the case of PS, the birefringence is negative, since the orientation is mainly dominated by the benzyl group (e.g. n_2). For other polymers, the orientation is more a result of the conformation in the carbon-back chain (e.g. n_1), representative of a positive birefringence.

Characterising birefringence in polymers is relevant to understand the level of frozen-in molecular alignment that is captured by quenching the structure before full relaxation can occur. It is known that orientation can alter the mechanical properties of glassy polymers. Parallel to the direction of orientation, elastic modulus and yield stress are reported to increase [82], while these appear to decrease in the perpendicular direction. For example, Landel *et al.* [83] have reported that the Young's moduli of highly oriented fibers is about an order of magnitude greater than than of unoriented polymers. This increase in modulus parallel to the direction of orientation arises because the applied stress largely acts on strong covalent bonds. Perpendicular to the orientation, the force is applied mostly to van der Waals forces between molecules. One other consequence of orientation is that birefringence can often hinder the transparency of some polymer products which rely in optical isotropy.

De Focatiis made a successful attempt at lengthening the boundaries of his GM model to provide a constitutive expression for describing birefringence [12]. His first assumption was to describe the bond-stretching, b, and conformational, c, sources of birefringence through a deviatoric stress state, S, where Δn becomes

$$\Delta n = \Delta n_b + \Delta n_c \tag{2.19}$$

where Δn_b and Δn_c are defined through the stress-optical coefficient C by $C_b \Delta S_b$ and $C_c \Delta S_c$, respectively. In PS, it is the conformational birefringence that dominates molecular orientation, thus $\Delta n \approx \Delta n_c$. This is because of the magnitude

of C_b being too small relative to C_c ($C_c/C_b \approx -5500$) [12]. De Focatiis combined Kuhn and Grun's [84] anisotropy expression for the end-to-end chain vector to derive a polarizability tensor which he combined with his GM multi-mode model to account for the following expression for birefringence

$$\Delta n = C_c G_e \sum_{k=1}^{N} v_k (T_{k,3} - T_{k,1}) \frac{H\left(\frac{\lambda_k}{\lambda_{max}}\right)}{H\left(\frac{1}{\lambda_{max}}\right)} \tag{2.20}$$

where $T_{j,1}$ and $T_{j,3}$ are eigenvalues of the orientation tensor, and $H(x)$ is a three-term approximation. In Figure 2.15 De Focatiis presents birefringence measurements made on the oriented (and subsequently quenched) PS bars as a function of drawing temperature, T. The simulations using the above model are shown for reference. The model uses two versions: one incorporating finite-extensibility, FE, and one without this.

At lower drawing temperatures T >114 °C, ($Wi_e > 1$), the difference in birefringence across the three materials is minimal. Yet, at T <114 °C, the material with the highest molar mass (AG), presents the largest birefringence, indicating the largest orientation. The Weissenberg number essentially defines the relationship between the relaxation time, τ_e and the strain rate, $\dot{\epsilon}$: $W_{ie} = \tau_e * \dot{\epsilon}$. Higher molar mass polymers have longer relaxation times, which at a fixed strain rate will require longer periods to relax orientation. Hence, when compared to similar polymers of lower molar mass, the latter will experience more relaxation, which will translate in less frozen in orientation for a particular time frame.

The model works best at predicting the birefringence of monodisperse materials AF and AG by including FE. This is not the case for polydisperse material R. De Focatiis attributes this to the fact that the ROLIEPOLY equation was developed for monodisperse materials, and in a polydisperse material (such as R), the relaxation times are arbitrarily defined by $M = \overline{M}_w$. This leads to the overprediction on the short relaxation times ($Wi_e < 1$), and underprediction at long relaxation times ($Wi_e > 1$). From a modelling perspective, the additional constraint release provided by the relaxation of the short chains in a polydis-

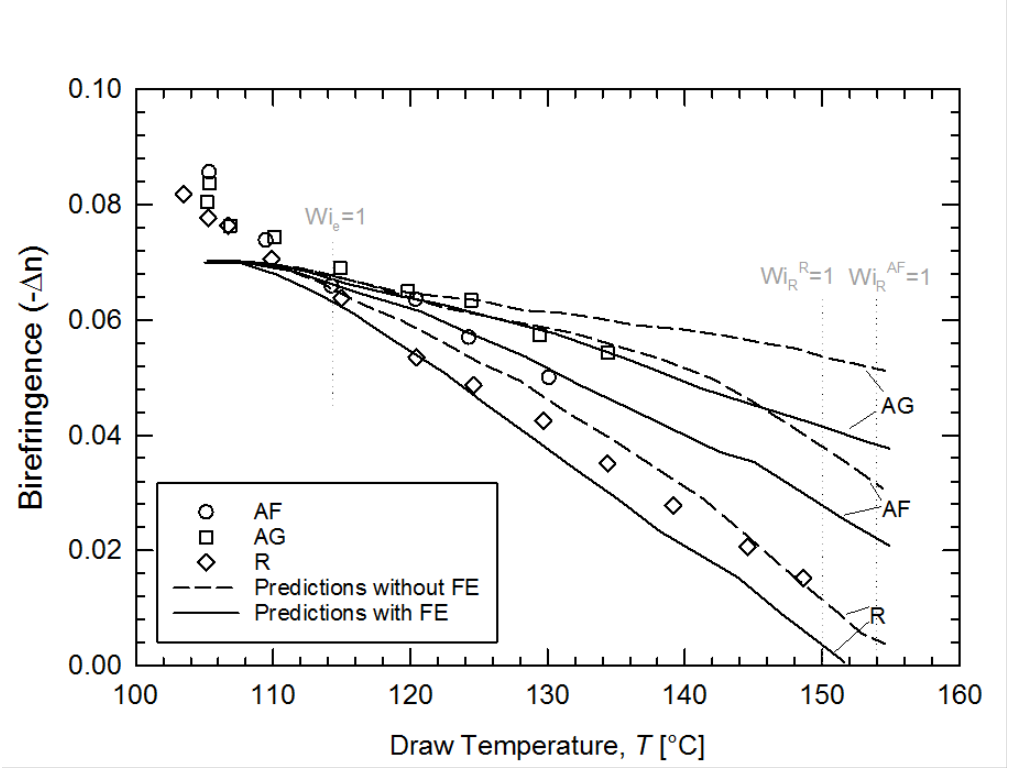


Figure 2.15: Birefringence simulations for a range of drawing temperatures in oriented PS samples [12].

perse distribution at these long relaxation times is thus unaccounted for in the monodisperse constitutive model.

In the case of PS, a whole range of applications rely on good optical transparency, and this can often be hindered by crazing, which impairs visual and optical performance. De Focatiis went one step further at trying to incorporate a crazing prediction capability into his birefringence model by correlating the degree of of stress required to initiate visible crazes to the degree of molecular orientation in PS. His results will be discussed in the next section.

2.7 Crazing

Many polymeric materials (such as PS), generate and propagate stable cracks rather than deforming homogeneously. Both crazing and fracture are controlled by the absorption of energy at the crack tip and this occurs in a relatively small volume of material where large deformations take place [47]. In PS and glassy thermoplastics, the appearance of small crack-like defects is called crazing [15; 40]. Crazes are supported by a network of small load-bearing fibrils -in the range of 3 nm to 5 nm- that spawn through the elongation of polymer chains. Within these crazes, the polymer is highly oriented possessing a different density and refractive index than the surrounding glassy matrix [16]. Figure 2.16 presents a brief visual description of the crazing process. Crazes form as a consequence of void nucleation within the polymer bulk/film under an applied load over time (steps A-B). When the applied stress is increased, the void sites are able to grow and interconnect with the surrounding polymer network (step C). As the voids continue to develop, the adjacent polymer ligaments between the voids start to exhibit strain hardening, causing the voids to stabilise, and the neighbouring polymer molecules to become highly oriented (step D). As the fibrils are drawn further, the craze structure collapses (step E) failing either through disentanglement or chain scission, as suggested by Kramer [15].

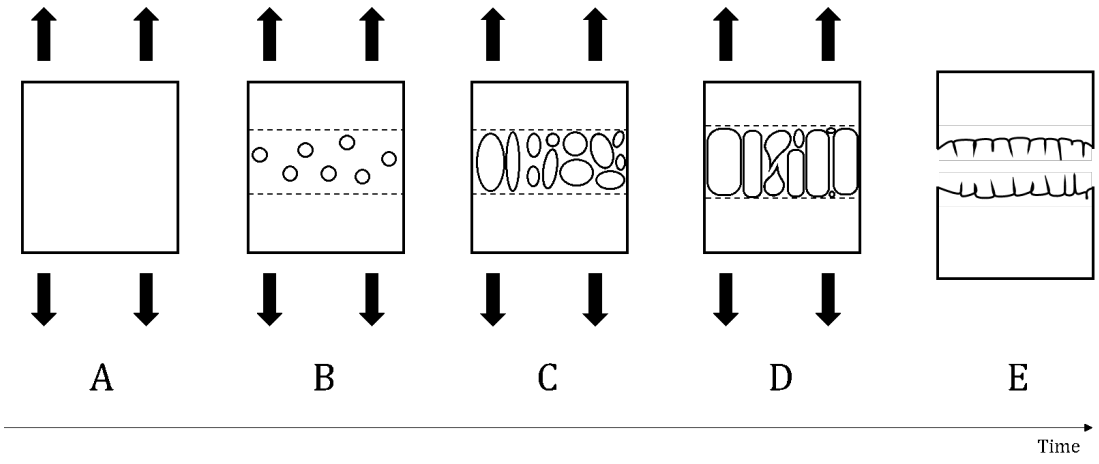


Figure 2.16: Mechanism for the formation of crazes adapted from [13].

In the absence of voids or defect sites, Argon and Hannoosh [85] found that

the stress required for craze initiation substantially increased, with the samples preferentially shear yielding and necking in tension before displaying any crazing. Yet Deblieck [86], argues that shearing deformation may preferentially take place if thermal activation or strain rates favour the yield stress over the craze stress.

Understanding crazing is of great relevance for polymer glasses as it constitutes the precedent mechanism to fracture in these systems, which means that by understanding craze formation it is possible to predict the ultimate failure of these materials. The mechanics of crazing were comprehensively studied from the 1970s to the 1990s. Kramer and his team researched and tested some of the fundamental mechanical and energetic processes involved in craze formation, and a good review can be found in [15].

The nature of crazes is complex in the sense that while the formation of crazes may lead to fracture failure of the glassy polymer, they can also act as load bearing structures aiding the material to sustain substantial macroscopic plastic strain and dissipate energy, such as in the case of rubber-modified PS. In order for crazes to form in a given time, a critical stress must be reached, and this must have a tensile hydrostatic component [15]. Crazing has also seen to be dependent on temperature and environmental conditions [24]. While various authors have reported the formation of crazes in air, others have focused in the analysis of environmentally crazed polymers where an agent is used to accelerate the rate of craze formation, and to achieve more well-defined fibrils for optical analysis. A time-delay between the application of stress and the visual appearance of crazes has been reported [20; 37]. This delay time, according to Kramer is evidence of a barrier to craze nucleation. Although these factors all contribute to the development of crazes in glassy polymers, it was found easier to tackle one aspect at a time, hence a review covering specific features of crazing is presented in the subsections below.

2.7.1 Craze grow and micromechanics

In terms of crazing micromechanics, crazes are reported to grow by the combination of two mechanisms: the craze tip, which extends the periphery of the craze; and craze thickening, that lengthens the craze fibril distance. The first mecha-

nism suggests that the craze tip advances through a zone of plastically deformed and strain softened polymer that is formed ahead the craze tip; craze fibrils form by the deformation of the polymer webs between the tip. The growth of the craze tip will not occur until the stress is sufficiently high as to overcome the surface energy of the surrounding area, often recognised as the active deformation zone, DZ.

The second mechanism, considers that fibrils lengthen through the surface drawing of adjacent polymer material. As suggested by Kramer [15], as the craze fibril elongates, it draws surrounding polymer in an analogous way to cold drawing for polymer fibres. In this sense, the increase in length of the craze fibril is accompanied by a reinforcement of new material being drawn, providing the stability to sustain further extension. A simple diagram showing the microstructure within the craze/bulk interface is presented in Figure 2.17. Microstructrual features such as the mean craze fibril diameter, D, the mean craze fibril spacing D_0 are given for reference.

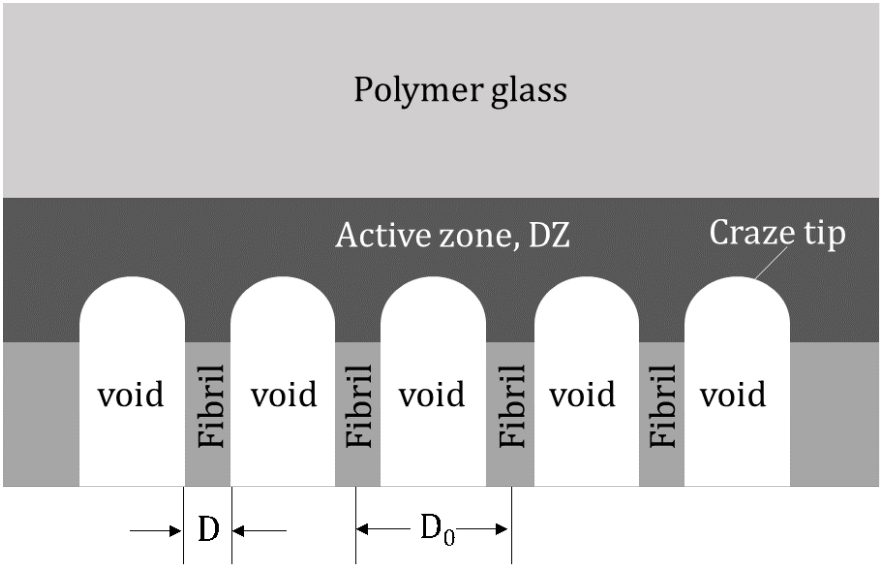


Figure 2.17: Craze/bulk interface microstructure, adapted from [14].

A useful route to understanding craze micromechanics is through the determination of the stresses at which these are formed. A substantial fraction of published studies, mainly lead by Kramer and his team, were able to experimen-

tally characterise the craze surface displacement profile, $w(x)$, along the craze to compute a stress profile, $S(x)$. Their approach consisted of a film characterisation method where polymer films were attached to copper grids through a solvent/water bath and subsequently strained in tension to promote craze formation. Isolated crazes were individually analysed and measured using transmission electron microscopy, TEM , to calculate $S(x)$ as,

$$S(x) = \Delta S(x) + \sigma_\infty \tag{2.21}$$

where σ_∞ is the far-field applied tensile stress along the craze fibril direction and $\Delta S(x)$ is the stress applied to the craze-bulk interfaces to produce the displacement, $w(x)$, between them.

Figure 2.18 reports the determined surface stress profiles found in isolated crazes in polystyrene as reported in [15]. The samples are illustrative of monodisperse, polydisperse and bimodal blend ($5\%\overline{M}_w = 4,000\,\text{g/mol}$ and $95\%\overline{M}_w = 200,000\,\text{g/mol}$) PS systems, and molar mass data can be found in Table 2.5.

Table 2.5: Molar mass averages for PS materials used in Figure 2.18.

System	$\overline{M}_n$ [g/mol]	$\overline{M}_w$ [g/mol]	PDI	σ_∞ [MPa]
Monodisperse	189,000	200,000	1.06	25
Polydisperse	113,000	300,000	2.65	24.5
Bimodal blend	58,000	190,000	-	26

The peak on the data is the stress at the craze tip, which drops over a certain distance to a value similar to the applied stress, σ_∞. The presence, and further dissipation of a peak stress evidences the load-bearing character of crazes. Also interesting is the very sudden increase and drop in stress for the monodisperse material, in contrast to a more subtle transition for the polydisperse material. The bimodal blend system shows an intermediate behaviour between the two. Kramer attributed this observation to be a result of the effect of molecular entanglements in craze micromechanics and microstructure. His remark hints at an effect of dilution of the molecular entanglement network of long chains by polymer chains too short to entangle.

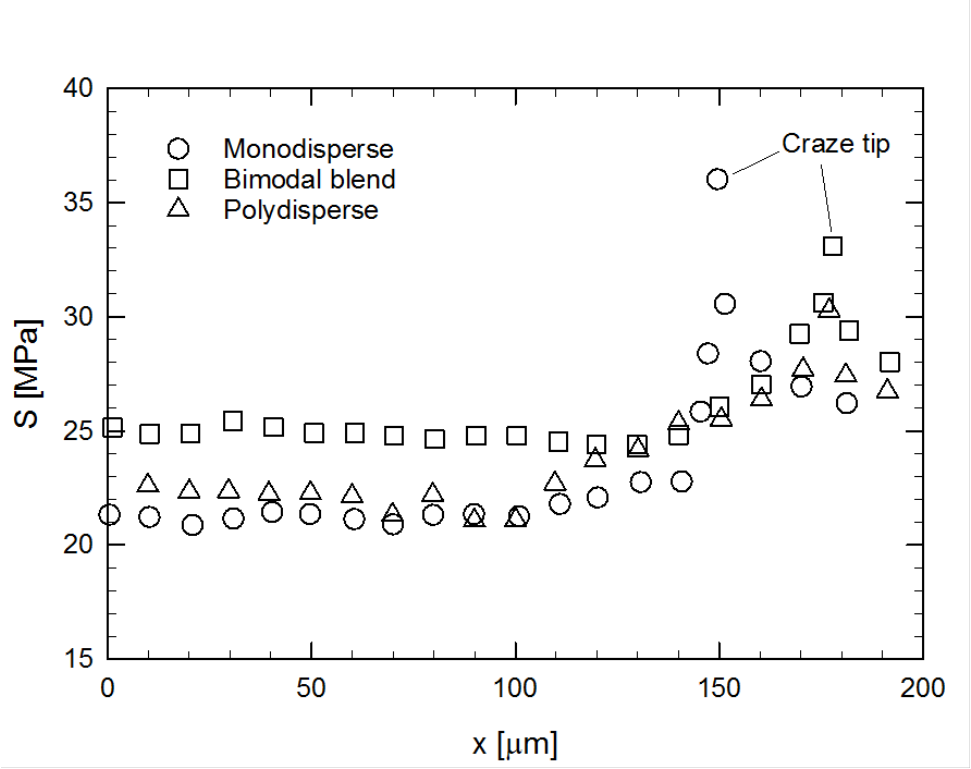


Figure 2.18: Craze surface stress profiles in monodisperse, polydisperse and bimodal blend of polystyrene adapted from[15].

2.7.2 Crazing and the entanglement network

One of the first pieces of evidence to study the effects of molar mass on the initiation of visible crazes is found in the work of Fellers and Kee [16]. They used a series of injection moulded PS, polymerised with different carbon side-groups, for tensile testing and to promote the formation of crazes. The samples were carefully chosen in terms of their molar mass and distribution criteria, as well as closely monitored to try to suppress the orientation effects of injection moulding by chosing the highest melting temperature and lowest flow rate. Craze initiation was detected by relying on the light reflective properties of crazes; the differences in the path of the light beam as it passed through the crazes were captured by a photoresistor. In their observations, Fellers and Kee noted that crazes were impossible to form in the the lower molecular weights samples, some of them even

fracturing while setting these in the jaws of the testing machine. However, stable and prominent crazes were observed in the higher molecular weight polymers. Figure 2.19 presents the breaking and crazing stresses in polystyrene as a function of $\overline{M}_n$ reported by [16]. Molar mass data is provided in Table 2.6 for reference.

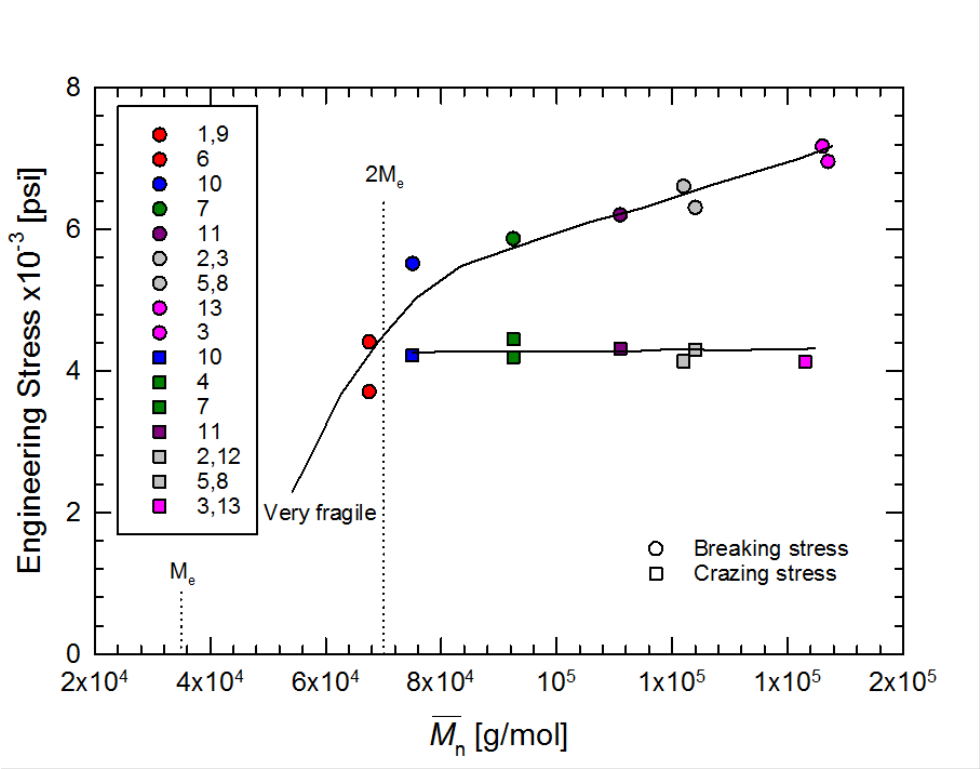


Figure 2.19: Craze stress as a function of $\overline{M}_n$ in PS, from [16].

The main observation from figure 2.19 is that when $M \leq 2M_e$ stable crazes could not be formed, while for $M > 2M_e$ craze initiation seems to be independent of molecular weight. This argument holds valid since a polymer is only considered to be fully entangled if this is constricted at both chain ends, hence two entanglements, or $2M_e$. The authors offered the plausible explanation that void or flaws (where crazes tent to initiate), act as stress concentrators. Hence, at these points the stress level is raised above the resistance barrier to plastic flow, and consequently suppresses the molecular weight dependence of plastic events that are observed in other deformation processes (e.g. strain to break, strain

Table 2.6: Data for PS materials used in figure 2.19.

ID	Endgroup	$\overline{M}_n$x10^3 [g/mol]	PDI	T_g °C
1	Cyclohexanate	67.5	2.39	86
2	Cyclohexanate	122	2.58	102
3	Cyclohexanate	147	2.36	105
4	Eicosonate	92.5	3.11	95
5	Eicosonate	124	3.51	101
6	Rubidium ion	67.5	2.39	87
7	Rubidium ion	92.5	3.11	93
8	Rubidium ion	124	3.51	102
9	2-Methyl propionitrile	68	2.64	88
10	2-Methyl propionitrile	75	2.78	89
11	2-Methyl propionitrile	111	3.20	101
12	2-Methyl propionitrile	123	2.71	100
13	2-Methyl propionitrile	146	2.81	107

hardening). If one was to convert Fellers data into $\overline{M}_w$, it is possible to see that the lowest molar mass materials analysed by Fellers reports a $\overline{M}_w = 161.3\,\text{kDa}$, which as will be reported in the upcoming sections is representative of a highly entangled system whose crazing dynamics will lean more towards a chain scission behaviour. Although early days, the significance of Fellers data is that it provides a starting point to: first, recognise that crazing is different to a solely plastic deformation event, and secondly, that the propagation of crazes requires a minimum molar mass for these to be fully visible.

Another interesting remark of this study is the effect that molecular weight exerts on the crazing pattern. Crazes were seen to be more numerous, longer and finer in texture in higher molecular weight samples, compared to the coarse, scarce and shorter crazes that were observed in specimens where $\overline{M}_n < 70,000\,\text{g/mol}$.

Donald and Kramer [17] followed up on the idea of entanglements and craze microstructure. Their study examined the assumption that a semipermanent entanglement network is retained even after plastic deformation (e.g. recovery upon annealing). And as such, the length of the entanglements will define the endurance of the network itself. Donald's premise is that the extension ratio, λ to which a polymer molecule can be extended is dependent on the length between

entanglements, l_e, and the mesh size (or approximate number of entanglements in the network), d_e, through: $\lambda_{max} = l_e/d_e$. Therefore, as l_e decreases, so does λ_{max} or λ_{craze}, and one can expect to see a decrease, or ultimate suppression of crazing, following the ideas established by Fellers and Kee. To test this, Donald crazed a range of polymeric materials using Kramer's copper grid technique. The samples were analysed using TEM and λ was calculated through the determination of the volume fraction, v_f of the craze in the electron images (assuming $\lambda = 1/v_f$). The entanglement length was calculated from the value of M_e obtained by melt elasticity measurements through: $l_e = (M_e/M_0)l_0$. Their results are plotted as a function of the extension ratio, λ against M_e in Figure 2.20.

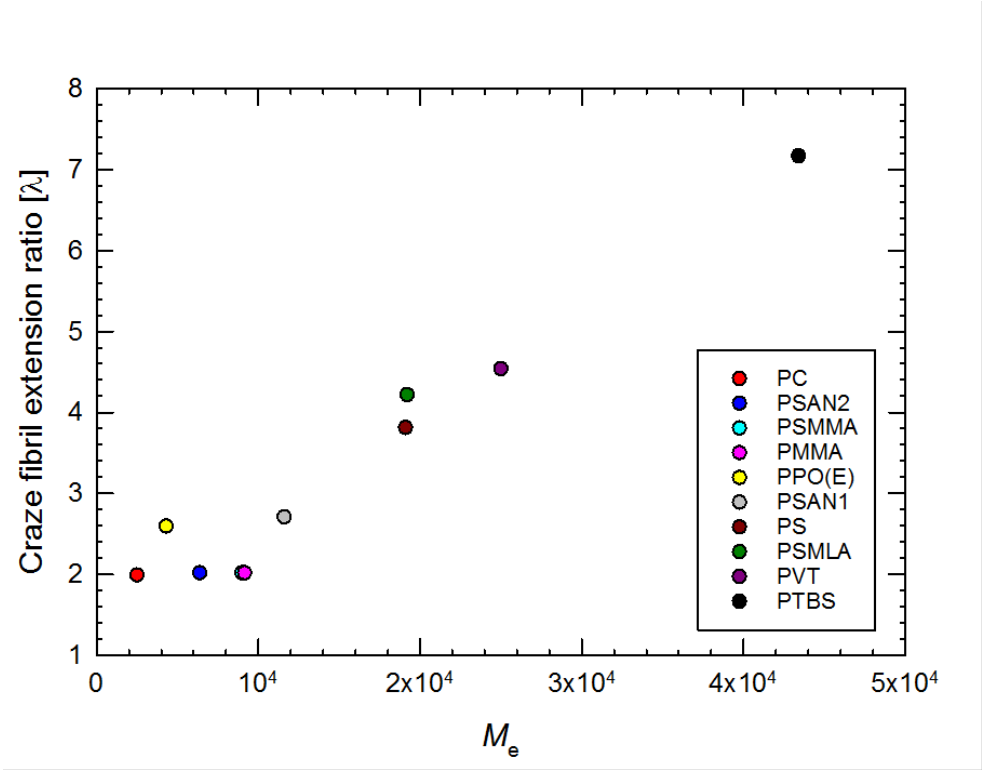


Figure 2.20: Craze fibril extension ratio as a function of M_e in various polymer systems, adapted from [17].

The authors reported a good correlation between M_e (alternatively, l_e), and the observed craze fibril extension ratio, where polymers with larger M_e values presented a correspondingly high value of λ. Similarly, higher fibril stresses should

exist in crazes with higher λ. The fibril stress, therefore becomes the stress parameter controlling the rates of movement within the drawn polymer molecules (e.g. reptative motion). Donald and Kramer, suggest that as the fibril stress reaches a critical value, σ_f, the fibrils can fail by two breakdown processes: a) continuation of the chain reptation, i.e. disentanglement, or b) chain scission.

Berger [14] continued the study of the effect entanglement length, l_e, and density, v_e, exerted in craze microstructure. His research focused on the application of a low-angle electron diffraction, LAED, method to obtain specific information about the nature of crazes, namely: the mean craze fibril diameter, D, the mean craze fibril spacing D_0, and the orientation, φ. The results showed that for a variety of polymers there is a correlation between D, D_0, and φ with v_e. The fibrils' associated parameters were seen to increase as a function of an increase in entanglement density. Both Donald and Berger's results served to support what will become known as Kramer's geometrically entanglement loss theory (GE), due to his well-known premise that states that for crazes to occur "there needs to be a geometrically necessary entanglement loss" [15].

Imagine two chains A and B, that are constrained by an entanglement point, C, as illustrated in Figure 2.21. In order for A and B to move and extend the fibril, they must overcome this constraint, hence producing and entanglement loss (i.e. disentangling) by diffusive motion, see Figure 2.21 (b)). If the chains are indeed longer than $2M_e$, they comply with this constraint requirement.

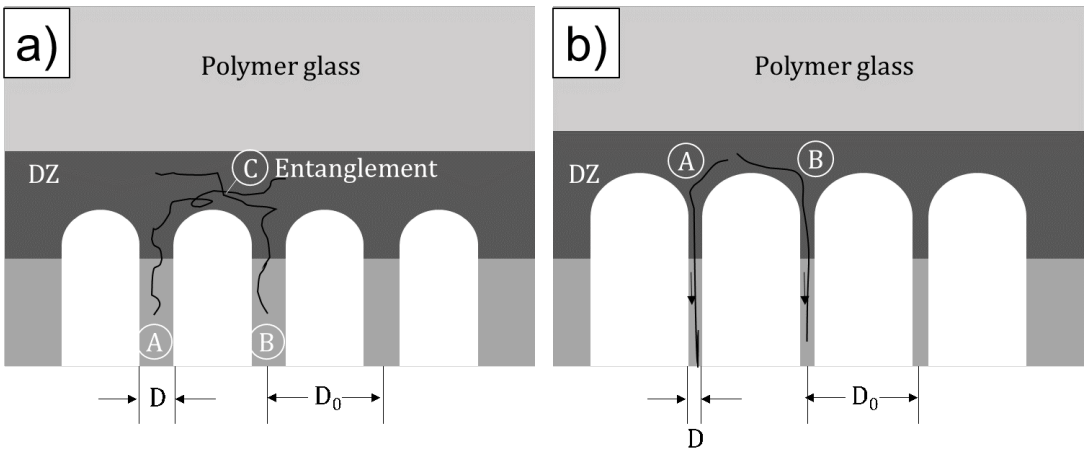


Figure 2.21: Entanglement loss process in crazes, adapted from [18].

An additional observation made by Kramer and Donald was that as polymer molecules become longer and longer, the strands crossing the surface in the active deformation zone of the fibril diameter, D, were assumed to break rather than failing through disentangling. This was presumed on the basis that as the entanglement density is increased, the stress to propagate a scission-mediated craze will increase relative to the stress to propagate the deformation active zone, DZ. Consequently, shear deformation becomes the dominant mode of deformation rather than disentanglement in relatively high v_e materials [18]. In his book, Kinloch [87] states that the mechanical endurance of polymers is a result of structure and morphology, where the overriding factor appears to be molecular anchorage. During chain scission, the anchored molecules tend to be severed, while in disentanglement these are seen to be pulled out if not held strongly enough. In amorphous thermoplastics, the anchorage comes as a result of the number of physical entanglements.

2.7.3 Temperature effect on crazing

Donald [88] and Berger [19] studied the effect of temperature on the initiation and formation of crazes. Their results showed that the temperature at which the transition from crazing to shear deformation occurred decreased with increasing molecular weight. In his study, Berger presented evidence for this in a series of monodisperse PS. His results showed an increase in the craze extension ratio as a function of increasing temperature, which drops in relation to an increasing molecular weight, as per Figure 2.22.

The data demonstrates that λ is dependent on molecular weight at elevated temperatures. Berger explains the increase in craze extension at higher temperatures as being driven by a chain disentanglement mechanism that is dependent on molecular weight through a disentanglement time associated with chain diffusion dynamics. To account for this, Berger assumes that the disentanglement process follows the reptation model, where the diffusion coefficient can be traced to equation 2.10. Similarly, the existence of a void surface in the craze active zone can exert a higher mobility on the adjacent chains as it serves to relax the constraints on the chain's segments. Another important remark of this study was the effect

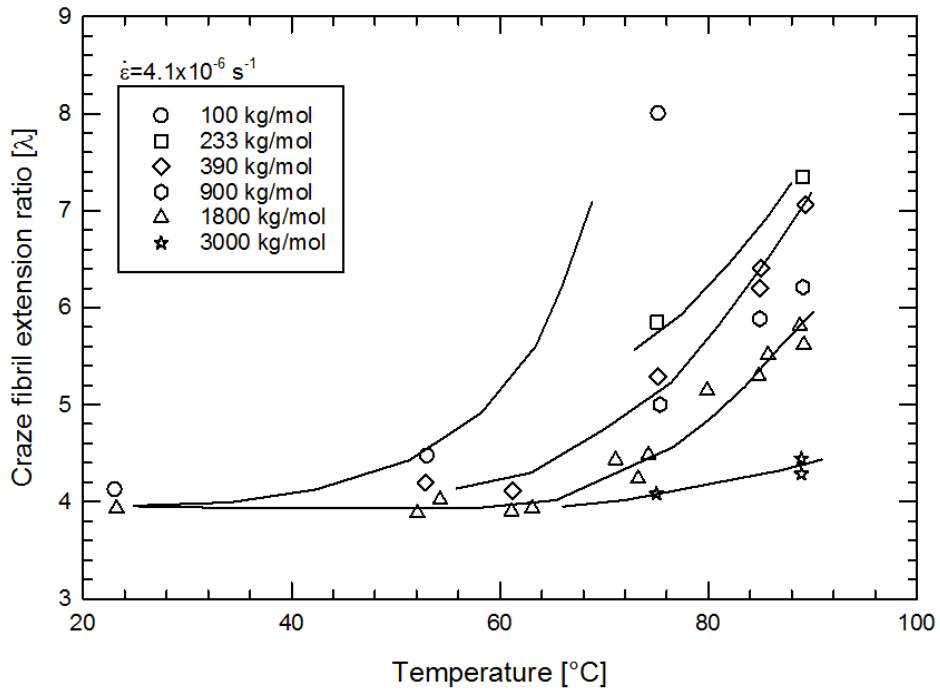


Figure 2.22: Craze fibril extension ratio as a function of M_e in various polymer systems, adapted from [19].

of strain rates: at high strain rates and lower temperatures a scission crazing mechanism was favoured, which was also independent of molecular weight.

In his analysis of failure mechanisms for polyolefines, Deblieck [86] extensively compares Kramer and Argor models to arrive at the following conclusions:

1. At low temperatures and high strain rates the characteristic time for disentangling a chain becomes long with respect to the time scale of the experiment and surface will be created as the chains will tend to break (e.g. chain scission).

2. At elevated temperatures and low strain rates, chain relaxation becomes relatively faster compared to the time scale of the deformation process, and new surface will predominantly be formed by intermolecular separation and chain disentangling (e.g. disentanglement).

Various authors [89; 90; 91] have commented upon these arguments, supporting their validity.

2.7.4 Modelling of crazing

Kramer and his team [14; 17], discussed two different mechanisms over which crazes form: disentanglement and chain-scission. Plummer [18], provided a detailed account of the surface energy and material drawing mechanical considerations involved in both these processes. The first distinction made by Plummer and Donald was on the nature of the the entanglement network. Contrary to previous studies [92], Plummer considered entanglements as moving points in the case of in-plane deformation, and he stated that contrary to Kramer and Berger's assumptions, the probability of a chain to cross adjacent molecules is greater than one. As a first approach to the development of his model, Plummer evokes Kramer's definition of chain-scission effective surface energy at the void tip as 2.22,

$$\Gamma_s = \Gamma_0 + \frac{U d_e v_e}{4} \tag{2.22}$$

where U is taken to be approximately the bond energy of the chain backbone and Γ_0 the van der Waals surface energy. And then he establishes the following assumptions:

1. For chain scission, the force to break a bond is approximated as: $f_b \approx U/(2a)$, where a is the bond length. Hence, if $f_d < f_b$, Plummer assumes that disentanglement will take place in preference to scission.

2. He assumes McLeish "forced-reptation" model [89] for which chains are anchored at one end and forced to reptate out of their tubes at a rate v.

3. There is a molecular weight associated with each chain crossing M_c that determines its frictional force, δf.

4. He defines a critical molecular weight, M_{crit} at which f_b becomes effective and chain scission dominates.

By defining M_{crit}, Plummer is able to establish the transitioning between the disentanglement process, and the preferential breaking of the chain at a maximum force limit, f_{max}. In this view, Plummer modified the expression for Γ, (equation 2.22), to provide a molar mass relationship to describe the crazing process seen at the disentanglement regime, $M > M_{crit}$, and an expression to account for the chain scission crazing mode at $M \leq M_{crit}$.

Figure 2.23 presents the surface tension curves for a series of monodisperse PS of different molar mass. The predictions capture the drop of Γ_s with temperature, but what is particularly interesting is that at lower temperatures Γ_s seems to be approximately independent of M (i.e. appears very similar in both samples). As the temperature increases, the samples enter the slope of the mixed scission/disentanglement regime, and at higher temperatures (i.e. disentanglement regime exclusively), Γ_s is seen to be strongly dependent on the M characteristics of the PS systems, showing remarkable differences in the behaviour between both systems.

Compared to Kramer and Berger's model [92], Plummer's predictions accounted for a possible molecular weight reduction in the scission/disentanglement slope; and provided a closer agreement between theory and experimental data.

Even though the studies performed by Kramer and his team are fundamental to the understanding of crazing, there are limitations that arise from the use of thin polymer films. For instance, the thickness of a thin film could reach the same order as the craze's thickness, thus imposing conditions of plane stress rather than plane strain. Similarly, the T_g and bulk modulus of thin PS films are lower than those of polymers in the bulk [93]. De Focatiis [24], developed an alternative three-point creep bending method to measure the craze initiation stress, CIS, in miniature bulk polymer specimens, allowing the use of minimum material quantities ($< 10\,\text{mg}$). The technique involves the use of a custom-made miniature three-point creep bending rig that transfers the load to the specimen. The formed crazes are optically analysed and measured by relying on the light reflected by the crazes. To ensure the quality of the crazes is adequate for optical inspection, De Focatiis makes use of a mild-environmental agent to facilitate craze

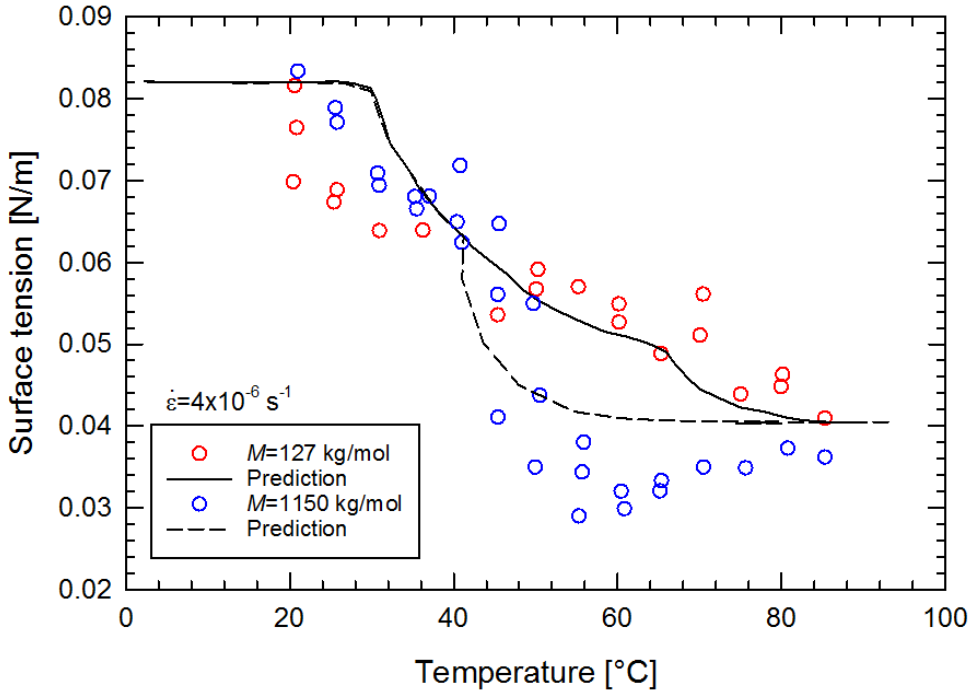


Figure 2.23: Predicted surface tension, T_s, curves for two PS systems at $\dot{\epsilon} = 4x10^{-6}s^{-1}$, adapted from[18].

formation. Agents promote crazing either by a local plasticisation process leading to enhanced mobility or by interfacial tension reduction, without modifying the polymer T_g, as documented for dyethelene glycol, DEG [24].

The method involves the calculation of a CIS, σ_c, namely the stress at which crazes originate in a given creep time, through the assumption that outside the crazed region the tensile stress of the specimen can be described by elementary beam theory. In his first study, De Focatiis was able to validate the accuracy of this technique with the isochronal creep testing of three different PS systems: two monodisperse and one polydisperse. The materials were tested both in air and diethylene glycol, DEG , an environmental crazing agent, at a range of creep times.

In a subsequent study De Focatiis carried out isochronal 300 s CIS measurements for a wide range of monodisperse PS materials of varying molecular weights

, and of branched monodisperse specimens (3-arm and 4-arm stars, and one H-shape). De Focatiis reported difficulties in growing crazes in the monodisperse systems with lowest molecular weight ($M = 68,000\,\mathrm{g/mol}$). The calculated CIS values for the materials above this value are presented in Figure 2.24.

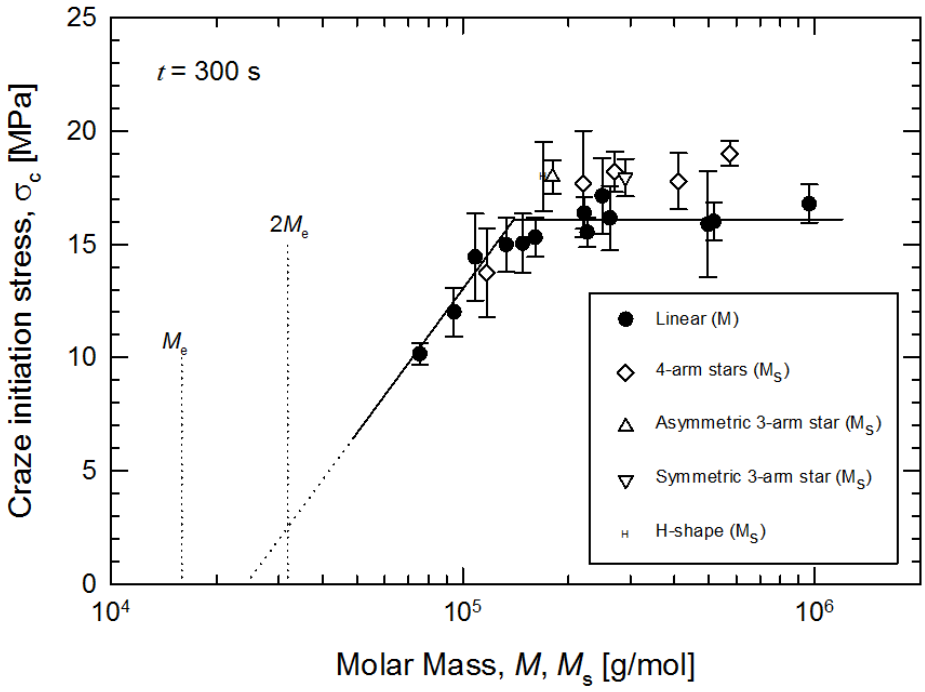


Figure 2.24: Craze initiation stress for monodisperse and branched PS systems, adapted from[20].

For the lower molar mass materials the CIS is seen to increase linearly with $\log M$, as would be expected if disentanglement is the rate-limiting step in craze formation. Nevertheless, at a critical molar mass ($\approx 140,000\,\mathrm{g/mol}$), there is a transition where σ_c becomes independent of M, as suggested for a chain-scission mechanism. The opening premise is based on Kramer's findings that craze formation is indeed driven by entanglement loss. De Focatiis recognised that disentanglement crazing occurs when there is sufficient chain mobility, e.g. in relatively high temperatures or solvents. Yet, when chain mobility is reduced, e.g. in dry environments or low temperatures, crazing is preferentially conveyed through

chain scission.

Craze initiation stresses were also reported for a variety of creep times (t = 12 s,60 s,300 s and 1800 s) for the monodisperse materials. The results confirmed that craze-growth is time-dependent, and the appearance of crazes changed with creep time. Micrographs confirmed that longer times produced wider, more developed craze patterns.

In terms of explaining his results quantitatively, De Focatiis suggests that free surface is the rate-limiting step in craze initiation. This process involves the creation and stretching of a number of craze fibrils per unit area of craze. In order for these fibrils to form, the molecular strands in the free surface surrounding the fibril must disentangle or break. As voids form, fibrils elongate, and thus a displacement normal to the craze plane develops. De Focatiis argue that as this occurs, an additional area A_0 of new surface per surface-crossing strand is created with a free energy cost of ΓA_0, where Γ is the specific surface energy of the fibril. In disentanglement crazing, the surface-crossing strands retract within their tubes, losing their entanglements and allowing the formation of the free surface to form a craze fibril. The rate-limiting step for this process is chain retraction, which De Focatiis attributes to occur on the time scale of the longest Rouse time, τ_R, alternatively defined as $\tau_R = \beta\zeta M^2/T$, where β is a monomer-specific constant, and ζ is the monomeric friction coefficient. The Rouse time is shortened by an Eyring-like acceleration, and the time scale for craze initiation to occur is modelled through equation 2.23

$$\tau_c = \frac{\beta\zeta M^2}{T} \exp\left(\frac{\Gamma A_c - \sigma V_c}{2k_B T}\right) \tag{2.23}$$

where V_c is a craze activation volume, and A_c is a constant associated with craze surface area. De Focatiis introduces an expression for craze initiation stress, σ_c, as:

$$\sigma_c = \frac{2k_B T}{fV_c}[\ln\zeta + 2\ln M - \ln T - \ln t + \ln\beta] + \frac{\Gamma A_c}{fV_c} \tag{2.24}$$

where the square bracket term is simply $\ln(\tau_R/t)$.

A remarkable contribution of De Focatiis' proposed crazing stress model was the capability of validating it against other sets of published data. For comparsion, he made use of the experiments by Han *et. al* [91] on craze initiation strain data in monodisperse PS thin films. The data was processed through the application of an equivalency equation to transform creep time tensile data at constant strain rate to creep-equivalent time per craze initiation stresses for direct comparison. De Focatiis calculated an effective craze activation volume of $fV_c = 1.8 \pm 0.3\text{nm}^3$ from his own data, whilst in Han's data the fV_c value was $1.8 \pm 0.4\text{nm}^3$, remarkably close. Both sets of data are presented in Figure 2.25.

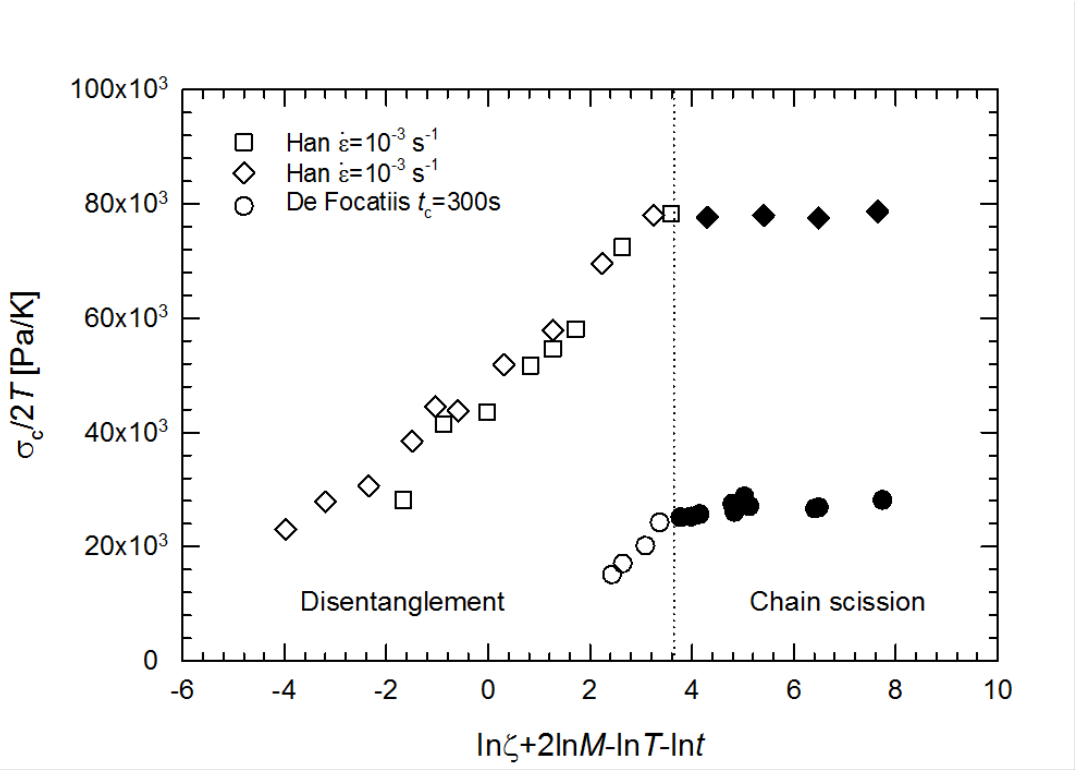


Figure 2.25: Calculated craze initiation stresses for the data of De Focatiis and Han [20], exhibiting the disentanglement and crazing regimes.

It is possible to identify two regimes, one slope and a steady plateau. The slope is the disentanglement mode, where the two data sets show the same gradient, reflected in their agreement in the activation volume. The effect of the crazing

environment (air vs. DEG), is a vertical shift as a result of the solvent reducing the interfacial tension of the polymer. The steady plateau is thought to be crazing by chain scission, and this occurs at a similar transition limit at $\ln\zeta - \ln T + 2\ln M - \ln t \approx 3.7$. The agreement between both sets of data is encouraging, and it provides further experimental evidence that the crazing dynamics modelled by De Focatiis, considering the Rouse time for chain retraction as the rate-limiting step for the formation of crazes, are in fact representative of the observable mechanical crazing phenomenon.

Even though De Focatiis model looks promising for predicting crazing by disentanglement in monodisperse glassy polymers, one of the final observations made was the uncertainty on how to extrapolate this to a polydisperse material.

2.7.5 Crazing and birefringence

The importance of recognising orientation in polymer systems was discussed in section 2.6. Anticipating the onset of crazing in oriented polymer systems provides a route for understanding how anisotropy influences deformation in these glassy systems. In a recent study [21], De Focatiis and Buckley applied Maestrini and Kramer's [94] craze fibril growth model to the experimentally obtained crazing stresses for a series of drawn polymers with known thermomechanical melt-state histories. Monodisperse and polydisperse PS materials were oriented at different temperatures (103 °C to 150 °C), stretch ratios, and with different dwell times prior to quenching. The orientation was characterised through birefringence measurements. De Focatiis reported that in temperatures ≈110 °C, crazes were difficult to induce, as specimens deformed plastically rather than by crazing. At temperatures <105 °C, plastic deformation always occurred over crazing. Nevertheless, at higher temperatures, the crazing stress was seen to decay towards the undrawn (isotropic) state, with increasing temperature, as presented in Figure 2.26.

The relevance of these results lay in the fact that for a given melt deformation (i.e. stretching or orientation), the crazing becomes dependent on the frozen-in orientation. In low drawing temperatures where the material experiences large amounts of frozen-in orientation (or increasing Weissenberg number,

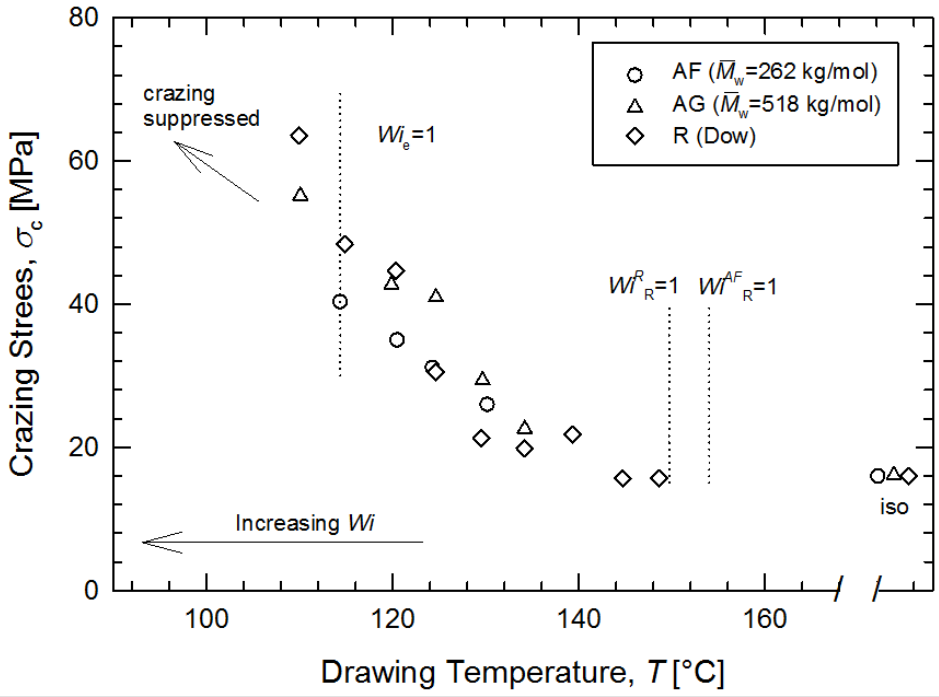


Figure 2.26: Measurement of average crazing stress as a function of melt-drawing temperature for materials AF, AG and R[21].

Wi, $Wi < 1$), the crazing stress becomes larger regardless of the polymer's molar mass characteristics. At high drawing temperatures, the crazing stress decreases with increasing drawing temperature eventually approaching the isotropic region (where $Wi_R \sim 1$).

De Focatiis made used of Maestrini's [94] expression to calculate the crazing stress difference in oriented specimens compared to isotropic ones as a function of the conformational stress, σ_{conf}, equation 2.25.

$$\sigma_c - \sigma_c^{iso} = \frac{\sigma_{conf}}{\beta} \tag{2.25}$$

where σ_{conf} is obtained from the measured birefringence through the stress-optical

coefficient, and β is a proportionality constant. Through the stress-optical rule (2.6) De Focatiis was able to fit the value of β to 0.059±0.002 in the linear regression of their data up to a birefringence limit of 0.0072. The data is available in Figure 2.27.

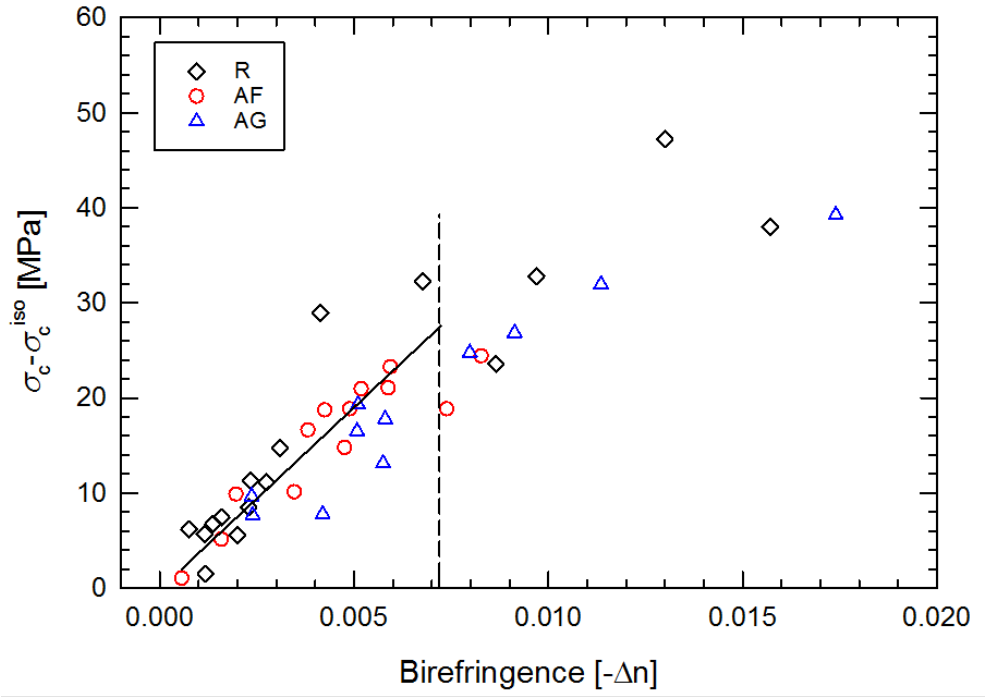


Figure 2.27: Crazing stresses of drawn samples relative to that of isotropic specimens, plotted versus the birefringence [21].

The significance of the above results is that through equation 2.25, and the ROLIEPOLY model for birefringence 2.20, the proposed approach enables predictions of crazing stress from the recognition of the conformational stress.

2.8 Summary and objectives

This review has chronologically analysed experimental manifestations of the effects molar mass and molar mass distribution on the mechanical and rheological

behaviour of polymers, with a focus on PS. The increase in mechanical properties with molar mass was made evident in the first section. Similarly, the limitations in parametrising these with universal molar-mass-derived concepts were explored.

A brief review on viscoelasticity presented some of the fundamental concepts that underpin current constitutive models, both for solid-state and melt-state properties of polymers. The importance of accurately describing the diffusion and relaxation of the entanglement network was recognised as a priority in interpreting the motion mechanisms of chain-distributions in monodisperse, bimodal and polydisperse systems; particularly through the associations of the different relaxation times (τ_R, τ_d, τ_e), with molar mass (M). The GR, ROLIEPOLY and GM models were discussed in the frames of solid-state and melt-state constitutive equations for predicting the behaviour of PS in compression tests, stress-strain curves of drawn specimens with frozen-in molecular orientation, and birefringence. The models proved to be successful at describing the behaviour of monodisperse systems, yet they failed to capture the behaviour of more complex polydisperse systems, where the definition of relaxation modes still requires a non-linear approach to account for the distribution of relaxation-times in materials with wide MMDs. At present, there is not a single model capable of simultaneously predicting both LVE and NLVE for any type of polymer distribution (monodisperse, bimodal or polydisperse). They are found to be exclusive to either system, with evident loss in predicting resolution when these become ever more complex (e.g. binary blends of polydisperse systems).

An added problem is the lack of a basic definition of the interacting limits between short and long molecules in highly heterogeneous distributions. Various questions still remain unresolved, even at defining key transitioning phases, such as: how shorts do chains need to be for them to start acting as a solvent for longer chains? Although there is a phenomenological understanding that this effect is real ($\eta \propto M^{3.4}$), currently, there is a pressing need for an elementary physical interpretation of how and when can one expect this to happen, and what are the relaxation mechanisms involved. The treatment of these questions becomes a priority, particularly when looking at industrially observed time-dependent mechanical phenomena that can affect the life-time of the material, such as crazing in PS.

Crazing in glassy polymers was discussed through an entanglement perspective, trying to associate the molecular dynamics involved in this deformation phenomenon. Studies revealed a correlation between the formation and craze stability, and molecular entanglements (crazes form for $M > 2M_e$). Two mechanisms of craze breakdown were explored: disentanglement and chain scission. These processes were examined through studies in thin film and bulk specimens, and while successful attempts of predicting the behaviour of monodisperse materials were made, the capability of these models still remains limited when applying them on bimodal and highly polydisperse polymer systems.

The current study aims at addressing some of these questions and providing qualitative and quantitative explanations through the careful testing and analysis of the molecular interactions for a series of PS systems, with different inherent levels of heterogeneity in their molar mass distributions. Materials were carefully chosen to cover a wide range of different molar mass polystyrene systems: homopolymer monodisperse materials, bimodal blends of monodisperse homopolymers, polydisperse polymers and blends of polydisperse polymers. PS is a widely used and extensively studied material, offering the possibility of compatible sets of data for theory validation.

Chapters 4, 5 and 6 cover the bulk of the experimental data of this study. In chapter 4, gel permeation chromatography and differential scanning calorimetry are used to achieve the following:

- Characterise and determine the differences in the molar mass averages and distributions of the analysed systems.
- Identify potential side effects in the resulting blends when using melt-mixing and solution blending as two mixing approaches.
- Register the differences in the thermal responses associated with chain length by recording the T_g of the studied materials.
- Interpret available phenomenological blending rules that aim at predicting molar mass related parameters (e.g. T_g of a polymer melt/solution).

In chapter 5, the materials are studied in isochronal 3-point creep to determine their craze initiation stress, following a documented miniature specimen

methodology by De Focatiis [24]. The results will serve to justify the following objectives:

- A piecewise linear rule has been established to predict the craze iniatiation stress of monodisperse materials [20], yet this needs to be extrapolated to enable the prediction for polydisperse systems.
- Previous studies have failed when attempting to craze PS materials below the $M < 2M_e$ limit. This association has only been studied in monodisperse PS systems, and it needs to be clarified whether this limit is also applicable to polydisperse polymers where $\overline{M}_n < 2M_e$, but $\overline{M}_w > 2M_e$. In this study, the analysis and testing of highly polydisperse blends aims to address where this boundary lies.
- The birefringence characterisation and subsequent crazing study in oriented bimodal blends of monodisperse materials will serve to provide experimental evidence for validating the applicability of the current state-of-the-art of De Focatiis model for predicting frozen-in birefringence based on the stress-optical coefficient [21].

Chapter 6, is aimed at comparing rheological simulations as suggested by leading theories in the field, against the data obtained through oscillatory and steady shear experiments. This chapter is set to provide experimental evidence to the following questions:

- What is the state of current rheological models for linear and non-linear viscoelasticity? Is there such thing as a universal model?
- How can current rheological models cope with differences in molar mass distribution and polydispersity? Furthermore, are these capable to account for dilution effects associated with the presence of highly unentangled fractions in polymer systems?
- What are the manifestations of polydispersity, particularly in non-linear data?

The research of the items above, is documented in this thesis, and the overall objective is to use current available models for the interpretation of solid-state and melt properties of polymers, to subsequently scrutinise these based on the collected experimental evidence to identify further improvements in the treatment of molecularly-defined theory parameters.

Chapter 3

Materials and Methods

3.1 Materials

One of the main objectives of this research is to evaluate how the mechanical and rheological characteristics of glassy PS are affected by molar mass and molar mass distribution. Therefore, it was decided to analyse four different sets of materials each of them representative of distinct molar mass distributions:

1. *Monodisperse PS*: three systems representing low, medium and high $\overline{M}_w$ were synthesized at the University of Durham by living anionic polymerisation with benzene as the solvent and *sec*-butyllithium as the initiator using standard high-vacuum techniques [95]. The obtained monodisperse materials are representative of narrow molar mass distributions with PDIs in the range of 1.08-1.14. These materials are labelled BF-BG, and will be reported in chapter 4.

2. *Bimodal blends of monodisperse PS*: four different blends were obtained by combining the above monodisperse materials in a range of blending ratios, from 10% to 50% of the higher molar mass component. The blends were synthesized at the University of Nottingham by chemical blending in a tetrahydrofuran (THF) solution and further precipitated in methanol. The resulting blends were carefully dried in a vacuum oven at constant mass,

following the procedure suggested in [96]. These materials are labelled BI-BL and will be reported in chapter 4.

3. *Polydisperse PS*: three commercial polydisperse materials with wide molar mass distributions were purchased from Dow Chemicals, and Sigma Aldrich, with quoted $\overline{M}_w$ of 216 kDa, 35 kDa and 350 kDa. These are labelled R, BX and BY, respectively and presented in chapter 4.

4. *Bimodal blends of polydisperse PS*: eight bimodal blends were obtained by two different methods: four attained through solution blending and four by melt-mixing the above polydisperse materials in a range of blending ratios ranging from 5% to 50% of the higher molar mass component. These blends were prepared at our Nottingham Laboratory following the methods described below.

   Solution blending: The weighted polymer components were dissolved in THF to give a 5-10 weight% solution. The liquid solution was then left stirring for at least 1 hr prior to precipitation to ensure dispersion. The solution was then precipitated in methanol in a 1:6 ratio. The obtained white solid polymer was collected by vacuum filtration and dried in a vacuum oven to constant mass. Throughout this study the subscript $-sb$ will be used to refer to the solution blended samples used in this research. The blends are labelled CA_{sb}-CD_{sb}, and presented in chapter 4.

   Melt-mixing: The polydisperse components BX-BY were weighted in the corresponding blending ratios (i.e. 5% to 50% of the higher weighted component) and fed into the hopper of a twin screw recirculating extruder HAAKE Mini-Lab II Rheomex CTW 5 fitted with corotating conical screws.The polymer granules were allowed to melt-mix and recirculate through the screws cavity. In this trial, a 50 rpm rotational speed was selected for the mixer rotating screws. The constituent materials were compounded at 200°C for 15min in ambient air at 1 bar. Throughout this study the subscript $-mm$ will be used to refer to the melt-mixed samples used in this research. The blends are labelled CA_{mm}-CD_{mm}, and presented in chapter 4.

A summary for the aforementioned materials is provided in tables 3.2 to 3.4. A further analysis on the molar mass properties for such polymer systems will be provided in sections 4.2.1 and 4.2.2.

Table 3.1: Detail summary for monodisperse materials used in this study.

Code	System	Description
BF	Atatic Monodisperse	Low $\overline{M}_w$-90 kDa
BG		Medium $\overline{M}_w$-250 kDa
BH		High $\overline{M}_w$-500 kDa

Table 3.2: Details summary for bimodal blends of monodisperse PS materials used in this study.

Code	System	Blending composition
BI	Monodisperse blends	90%BF, 10%BG
BJ		80%BF, 10%BG
BK		50%BF, 50%BG
BL		80%BF, 20%BH

Table 3.3: Details summary for polydisperse materials used in this study.

Code	System	Description
R	Atactic Polydisperse	Dow Chemical PS680E $\overline{M}_w$-216 kDa
BX		Sigma Aldrich $\overline{M}_w$-35 kDa
BY		Sigma Aldrich $\overline{M}_w$-350 kDa

3.2 Size Exclusion Chromatography (SEC)

The Molar Mass Distribution (MMDs), of the above materials were analysed using Size Exclusion chromatography, SEC. In SEC, polymer molecules are dissolved in a solvent, and are sorted according to their size through the repeated exchange of the solute molecules with a chromatographic porous-particle column

Table 3.4: Details summary for bimodal blends of polydisperse materials used in this study.

Code	System	Blending composition
CA		95%BX, 5%BY
CB	*Solution blended*:	90%BX, 10%BY
CC	Polydisperse blends	80%BX, 20%BY
CD		50%BX, 50%BY
CA		95%BX, 5%BY
CB	*Melt-mixed*:	90%BX, 10%BY
CC	Polydisperse blends	80%BX, 20%BY
CD		50%BX, 50%BY

packing. The size of the pore packing determines the molecular size range within which separation occurs [97]. Depending on the sort of media used, the technique can be referred to as Gel Permeation Chromatography, GPC, or Gel Filtration Chromatography, GFC. GPC is usually used to refer to analyses employing organic solvents, compared to the aqueous solvents used in GFC. Throughout this thesis, the term GPC will be used preferentially as the SEC technique of choice. The information on the MMD of polymers can be extracted from the molecular size-distribution curve obtained by means of a concentration-sensitive detector. In conventional SEC this detector is usually one which measures the differential refractive index (RI) of the particle size in solution.

At the end of an SEC experiment, the data obtained is a function of retention volume, V_R. The challenge in SEC is to homologise samples obtained using different instruments and experimental conditions. Therefore the elution curves containing the MMD information have to be treated accurately and precisely to remove experimental features that may bias the measured data. The standard way to achieve the reference size or molar mass parameters for a MMD in conventional SEC (e.g. using only a single detector, usually RI) is via a calibration process [98]. The calibration of the SEC equipment is achieved by relating the V_R to the molar mass, $\log M$, of a polymer sample that is used as a standard. Standards are commercially available materials that consist of narrow-MMD, -e.g. monodisperse materials-, in a wide range of molecular weights, i.e. ranging from

30 kDa to 2000 kDa. Common standards are currently available for materials such as polyethylene (PE), polymethyl methacrylate (PMMA) and polystyrene (PS). A calibration curve is constructed by correlating the relative peak position of the polymer standard in the chromatogram with the M value quoted by the manufacturer, in what is commonly known as peak-relative calibration. Figure 3.1 shows a standard calibration curve for PS. The calibration constants are drawn from the slope values for y, in the form of $y = -ax + b$.

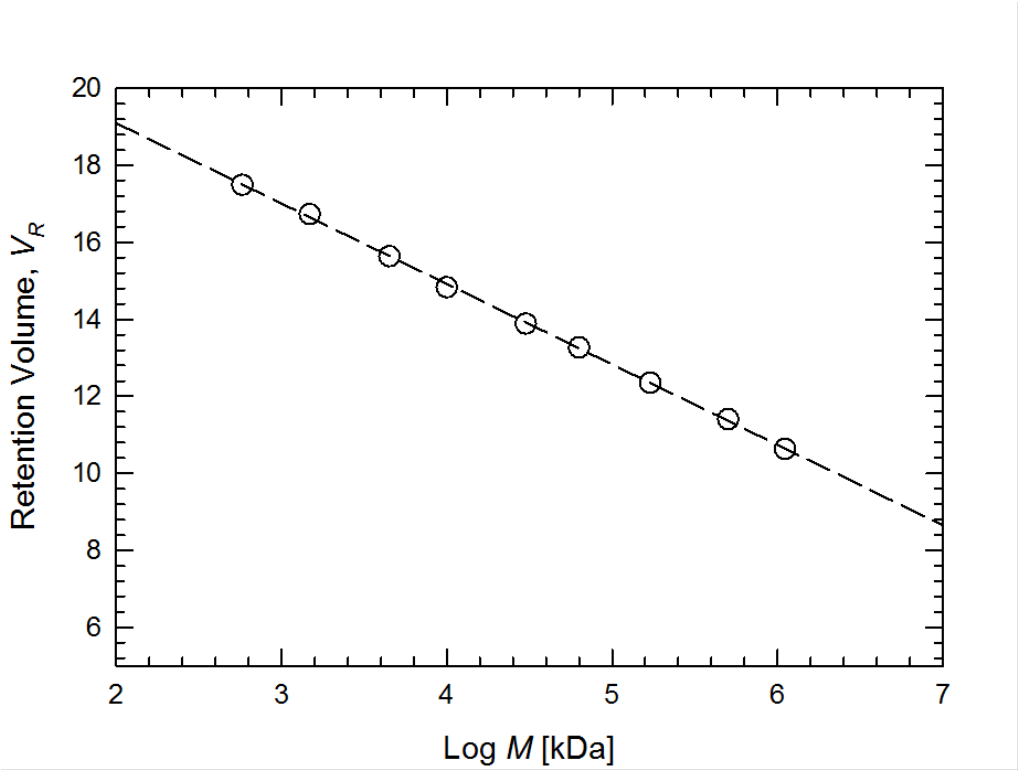


Figure 3.1: Conventional column calibration plot for a series of PS standards ranging from 580 Da-1112 kDa.

M is used instead of the size of the polymers as these can be susceptible to temperature and solvent variations, while M is directly proportional to the contour length of the molecule.

Other additional methods of extracting the absolute molecular weight M, of the polymer molecule involved the use of additional detectors, such as a viscometer. In viscometry, the M data can be extracted from the retention volume signal

through universal calibration, performed by using Einstein's viscosity law, and the Mark-Houwink equation.

In addition to viscometry, the most accurate and precise SEC systems use laser detectors to analyse further phenomena of polymers in dilute solutions such as the thermodynamics, branching, aggregation and conformation, among others. The use of multi angle light scattering methods, MALS , allows to measure the amount of light scattered by a dilute polymer solution at specific angles, θ. In a SEC-MALS experiment, the scattered light is detected at various angles θ, for each slice i eluting from the SEC column. The advantage of using a dual RI/MALS SEC system is that it allows to measure an absolute value of $\overline{M}_w$, that is independent of experimental conditions such as solvent and temperature through its proportionality with the excess Rayleigh ratio,

$$R(\theta) \propto c \times \overline{M}_w \tag{3.1}$$

where c is the concentration. For this reason, light-scattering photometers are recognised as molar-mass-sensitive detectors[97]. By rearranging equation 3.1, $\overline{M}_w \propto \frac{R(\theta)_i}{c}$, which means that for each chromatographic slice i, the ratio of the signals from the MALS photometer $R(\theta)_i$ and the concentration-sensitive detector c_i, is proportional to $M_{w,i}$. Since the slices eluting from the SEC column are sufficiently narrow, for any given slice i, $M_{z,i} \approx M_{w,i} \approx M_{n,i} \approx M_i$. The MMD can then be obtained through the combination of concentration-sensitive and MALS detection of the c_i and M_i at each elution slice. The associated M-averages of the polymer are obtained via,

$$M_\beta = \frac{\sum c_i {M_i}^x}{\sum c_i {M_i}^{x-1}} \quad x = 0, \beta = n; x = 1, \beta = w; x = 2, \beta = z \tag{3.2}$$

The raw-data curve obtained by SEC represents a size distribution in weight concentration type of plot. From SEC, equations 2.1 and 2.2 become, 3.3 and

3.4, respectively

$$\overline{M}_n = \frac{\sum_{i=1}^{N} h_i}{\sum_{i=1}^{N} (h_i/M_i)} \tag{3.3}$$

$$\overline{M}_w = \frac{\sum_{i=1}^{N} (h_i M_i)}{\sum_{i=1}^{N} h_i} \tag{3.4}$$

where h_i is the SEC curve height at the ith volume increment, and M_i is the molar mass of the species eluted at the ith retention volume [97].

The GPC measurements of this study where performed using an Agilent Technologies system, with a Wyatt MALS Dawn multi angle light scattering detector. The equipment was validated using polystyrene standards ranging from 30 kDa to 2000 kDa. The column used was an Agilent PLgel Mixed C column, with a detection range of 0.400-2,000 kDa with THF as a solvent. Column calibration was performed using polystyrene standards and applying peak-relative calibration, a universal calibration without the use of a viscometer was also conducted by applying the Mark-Houwink equation. Finally, peak average molecular weights were also validated using the MALS detector.

The experimental raw-data, obtained in the form of a refractive index signal vs. retention volume, was analysed using ASTRA, the equipment's software to produce a molar mass distribution curve through universal calibration [97; 98], and calculate the corresponding molar mass averages.

3.2.1 MMDs: MatLab analysis

Although automatic and seemingly convenient, the calculation of molar mass averages provided by ASTRA can often be inconsistent, as the fitting of a baseline is dependent on the user's manual determination of left and right trimming limits of the baseline data points. This can lead to inconsistencies as the molar masses of inherently smaller and longer chains, or narrower and wider distributions may

be subjected to differences in their baseline treatment and limits specified. Hence, it was decided that an automated procedure should be created to ensure all the experimentally obtained molar mass distributions are computed using a reproducible data extraction procedure. For this reason, a purpose-defined algorithm was developed and written by the author in MatLab [99]. This sequence allows to use the raw GPC data to establish a baseline by means of a user-defined parameter of a number of standard deviations.

The procedure to use the MatLab script is as follows: first, the raw data from the Agilent GPC is uploaded into MatLab as a text file of V_R versus refractive index, RI. The user manually inputs the area at the ends of the distribution, where there appears to be less noise. Then, the MatLab code interpolates the raw data into a newly fitted distribution accounting for the baseline correction. The new baseline was calculated by performing a linear regression on the original data to obtained an optimised baseline. Figure 3.2, presents the difference between the original baseline as provided by the raw Agilent file (black), compared to the MatLab's code newly regenerated baseline (red).

It is important to assure the baseline is as flat as possible, since the further determination of the molar mass peaks will be susceptible to any skewing of such a reference.

Once the baseline has been established, the code uses the standard deviation, S, as the defining parameter to trim the data of the beginning and the end of the onset of the distribution curve. To achieve this, a parameter for the standard deviation was defined as,

$$S = \sqrt{\frac{1}{N}\sum_{i=1}^{N}(x_i - \mu)} \tag{3.5}$$

where N represents the number of data points in the new corrected baseline, x_i refers to the observed data point, and μ is the mean. In this particular study, a value of $S = 3$ was found acceptable and subsequently applied to obtained the molar mass distributions for the reported materials. The script then uses a search

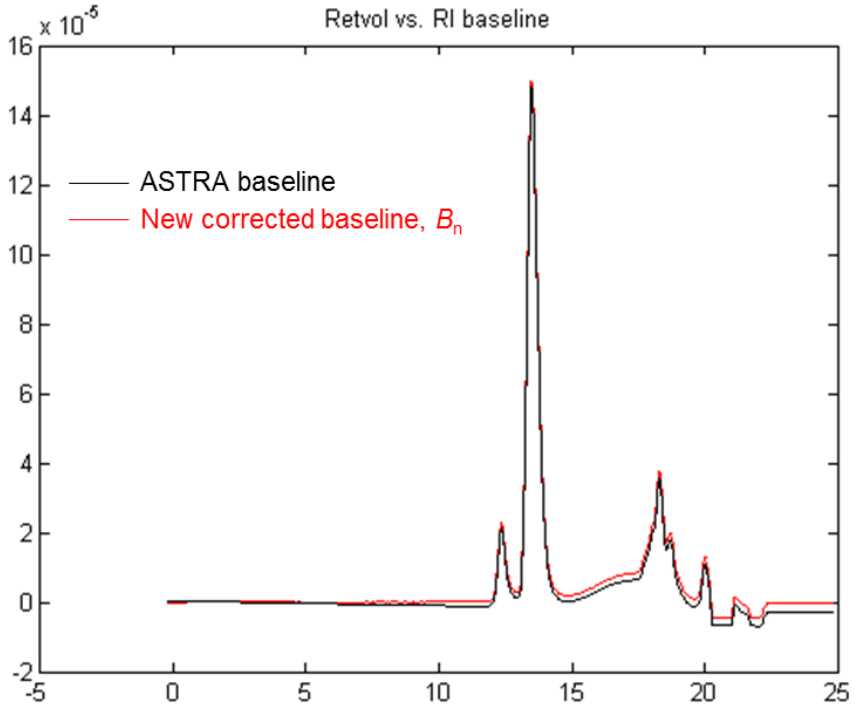


Figure 3.2: Processed GPC data, showing the original baseline (black), and the optimised baseline (red) using MatLab's code linear regression.

min and max points to define the peaks and length of the distribution. Once this is established, the value set for S will be used to establish the trimming points on the left and right of the distribution data set. The limits will then be located at three standard deviations off the baseline value, where in Figure 3.3, this is represented by the intersection of the left and right limits (lines black and red, respectively), with the standard deviation limit (blue line).

Because the number of standard deviations is fixed, it allows the procedure to be repeatable when used in combination the any material's baseline, and ensures the data is handled in the same exact way. Now that the limits of the distribution have been defined, it is necessary to convert the retention volume signal into a molar mass value through its correlation with the calibration constants a and b, as given by $y = -ax + b$. The obtained value will be equal to $\log M$. The RI signal, defines the fraction.

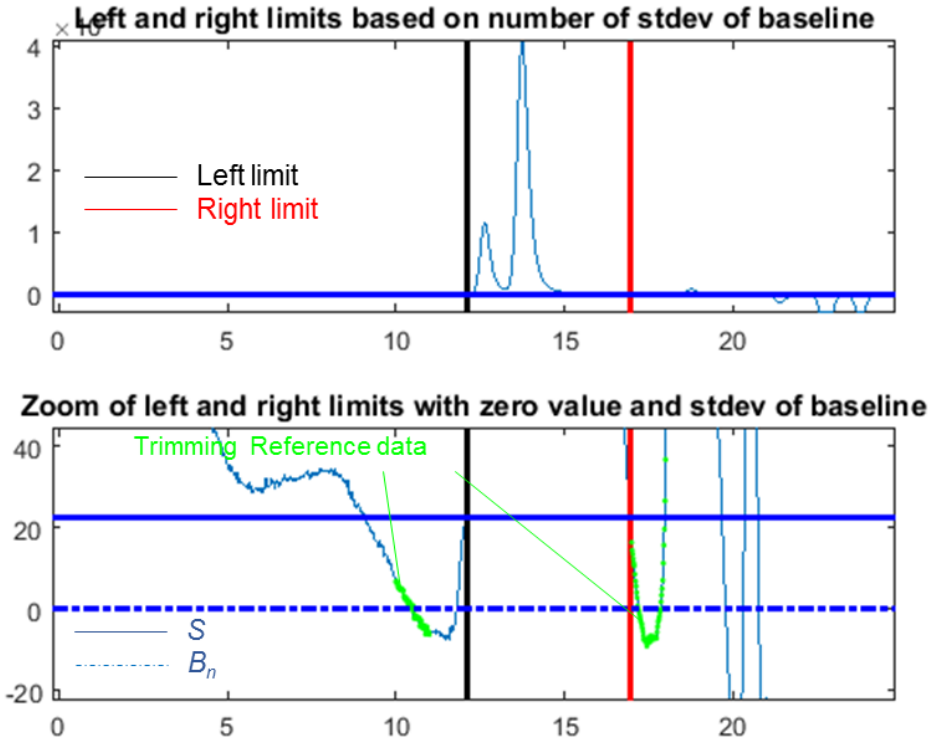


Figure 3.3: SEC data processing using the MatLab script through the definition of a number of standard deviations (continuous blue line) from the baseline (dashed blue line) to determine the distribution. Trimming limits are defined as a function of the standard deviation chosen by the user. The intersection of the blue line with the black and red lines shows the molar mass distribution data considered for the analysis.

Because after this the data is a function of molar mass, M to mass fraction, wi, the code is able to calculate the molar mass averages $\overline{M}_n$ and $\overline{M}_w$, through equations 2.1 and 2.2. Figure 3.4, presents a representative plot of material BJ (80% BF and 20% BG) as processed by the MatLab code for the molar mass distribution of one of the analysed materials. The computed molar mass averages are shown as black thick lines.

The code provides the calculation of three distinct molar mass averages, namely: $\overline{M}_n$, $\overline{M}_w$, and $\overline{M}_z$. The script, also provides the functionality of presenting the distribution as a normalised function (Figure 3.5).

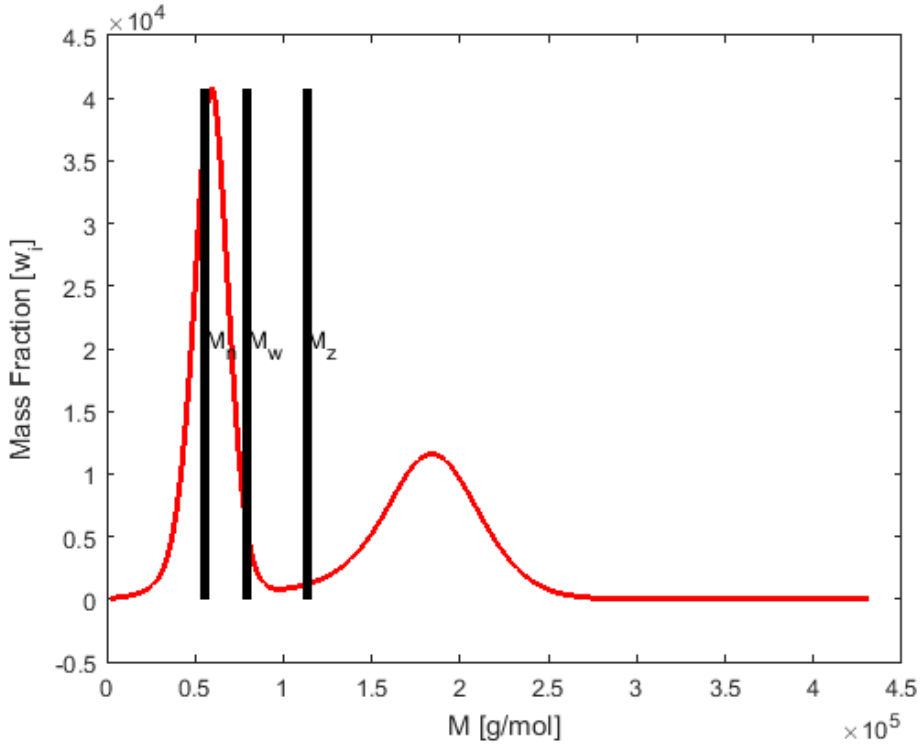


Figure 3.4: Molar Mass Distribution of material BJ as processed using the MatLab code. Molar mass averages $\overline{M}_n$, $\overline{M}_w$, and $\overline{M}_z$ are shown as thick black lines.

All the SEC used in this analysis will be processed using this technique, and will be plotted as a function of normalised weight fraction vs. ln M, molar mass. As will be presented in section 4.2.

3.3 Differential Scanning Calorimetry (DSC)

Differential Scanning Calorimetry, or DSC, is a technique used to identify the heat capacity and glass transition temperature of polymer materials. The glass transition is known to be a material parameter affected by molar mass variations [3; 4; 5]. This based on the fact that polymer systems of lower molar mass have more chain ends, which increase mobility and in turn free volume, θ. T_g and θ

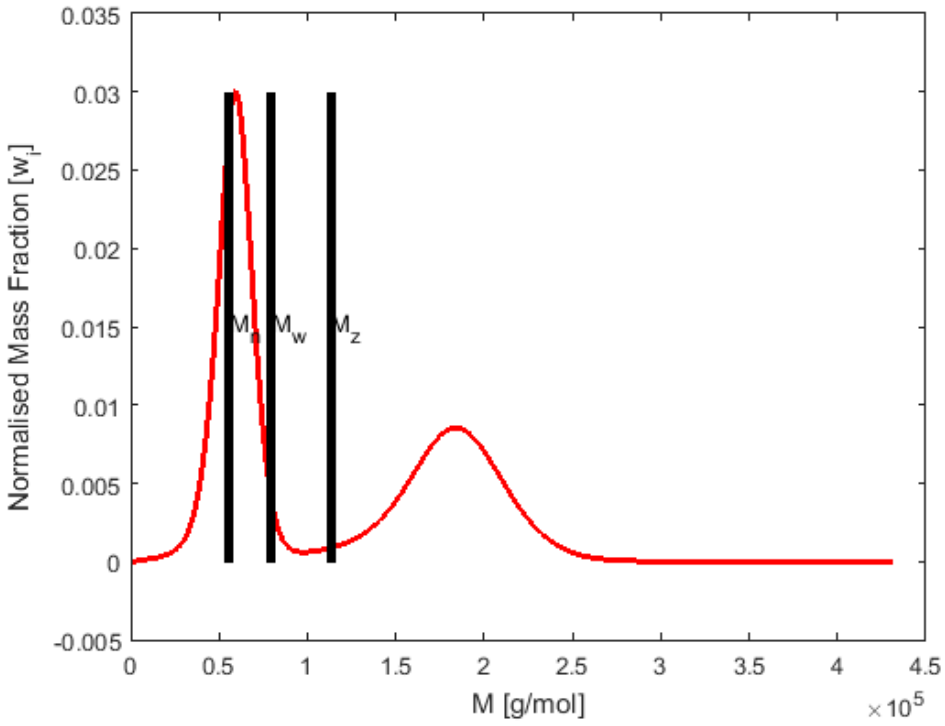


Figure 3.5: Normalised Molar Mass Distribution as processed using the MatLab code. Molar mass averages $\overline{M}_n$, $\overline{M}_w$, and $\overline{M}_z$ are shown as thick black lines.

are correlated through equation 3.6,

$$T_g(M) = T_g(\delta) - 2\frac{\rho\theta N_{av}}{\alpha_f M} \tag{3.6}$$

where $T_g(\delta)$ refers to the glass transition temperature of a polymer at infinite molar mass, ρ is the density, N_{av} is Avogrado's number and α_f is the free volume expansion coefficient. The term $(2\rho\theta N_{av})/\alpha_f$ can be substituted by constant K as suggested by [5].

3.3.1 Equipment validation

DSC tests were performed with the aid of a Q10-QSeries DSC from Thermal Analysis (TA) instruments. Due to time and equipment constraints, some of the final DSC tests had to be performed in an alternative Linkam temperature controller microscopic stage from Linkam Scientific instruments. To validate the differences between the temperature calibration of both sets of equipment, three standards were used to create a correlation plot between the signals obtain in these. Gallium, Indium and Tin were used as standard materials with defined melting points, their recorded values are presented in Table 3.5.

Table 3.5: Comparison of T_g as measured by the Q-10 TA and Linkam instruments.

Material	Q-10 TA [°C]	Linkam [°C]	Literature[22] [°C]
Gallium	25.55	34.4	29.76
Indium	156.50	154.9	156.60
Tin	231.82	215.1	231.93

To enable a correlation between these two sets of data, the melting points for the standards as calculated from the Q-10 TA and Linkam instruments were plotted as a linear function in Figure 3.6. The variation between the values retrieved by both instruments is then assumed to be the calibration offset for the melting points' detection accuracy between the two.

This offset value will be used to homologise both sets of data, and will serve to process the DSC results that will be further discussed in section 4.3.

3.3.2 Test profile

Specimen preparation for both instruments followed a repeatable procedure: pre-pressed fragments of the PS materials were inserted into miniature pans (diameter 4 mm), carefully weighted and subsequently sealed using a manual miniature press. A baseline measurement was done using empty reference plates at the beginning of each sampling round to be used to calibrate the baselines of the

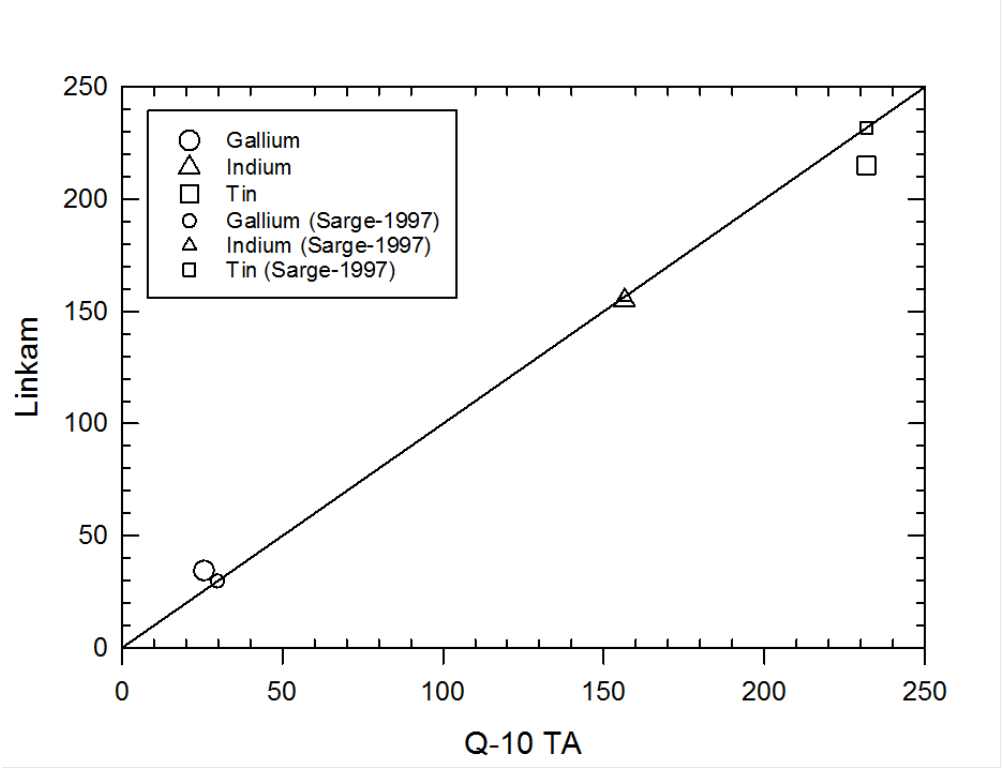


Figure 3.6: Linear correlation between the Q-10 and the Linkam enquipment in the melting points of the chosen standard materials. Literature data [22] is shown in small symbols for reference

measured samples.

The sample was subjected to a temperature profile as follows: the temperature was raised from room temperature ($\sim 20\,^{\circ}\mathrm{C}$) to $200\,^{\circ}\mathrm{C}$ at a rate of $\sim 20\,^{\circ}\mathrm{C/min}$, until reaching $140\,^{\circ}\mathrm{C}$, at that point the temperature was slowly dropped at a rate of $\sim 5\,^{\circ}\mathrm{C/min}$ until reaching $\sim 60\,^{\circ}\mathrm{C}$. Once at $\sim 60\,^{\circ}\mathrm{C}$ the temperature was raised again up to $140\,^{\circ}\mathrm{C}$. The motive behind this, is to have characteristic T_g changes in PS at two different rates, to ensure the changes experienced by the polymer are real and the results are repeatable. The temperature profile for the test can be seen in Figure 3.7.

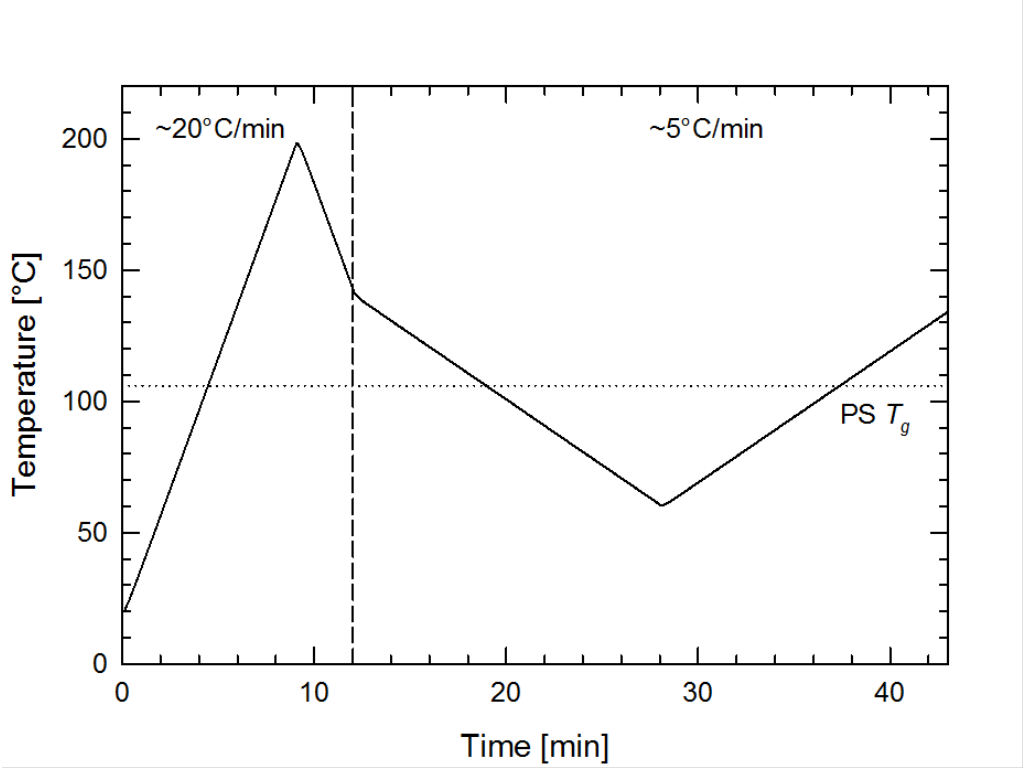


Figure 3.7: Temperature test profile for the DSC analysis of PS samples.

3.3.3 DSC data Analysis

The Q10-QSeries is a differential calorimetry equipment which provides test specimen and reference sample reservoirs that are maintained at nearly the same temperature throughout the experiment. The reference sample is usually an empty pan with no identifiable temperature transitions. The heat capacity and glass transition of the specimen are calculated by subtracting the reference sample's baseline. The Q10-Q DSC instrument uses the TA data analysis software to provide a T_g measurement at the onset, midpoint and end values of the curve. In this study T_g is taken as the temperature at which the specific reached value is midway between the fluid and glassy states. A representative image of the TA's processed data is shown in Figure 3.8.

The data from the Linkam thermal stage was processed using the Linksys 32 software, which enables to subtract a baseline from a experimental library,

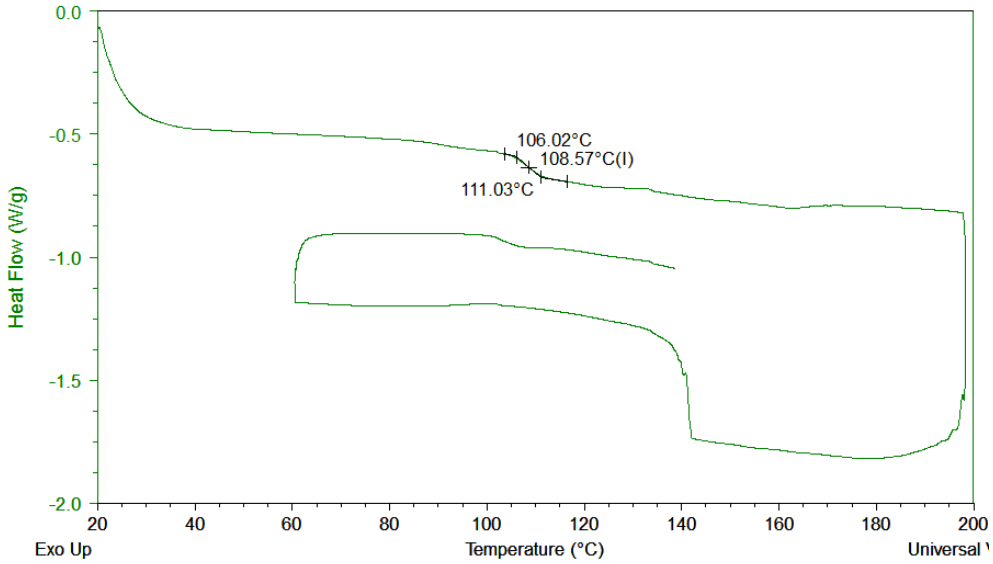


Figure 3.8: T_g for material BI as processed by TA DSC data anaylsis software.

to plot the T_g curves. The T_g was calculated by plotting the peak value of the derivative from the temperature/time plot. Following the format from the Q-10 TA instrument all the quoted T_g values in this research refer to the mid-point of the slope.

3.4 Compression moulding

After the materials were characterised in terms of molar mass distribution and glass transition temperatures, it was required to prepare solid moulded discs for further crazing and rheological analysis. Discs of 0.5 mm in thickness and 25 mm diameter were compression-moulded for all four sets of materials. This was done through a hand-operated Moore hydraulic press with heated platens. Fresh sheets of 0.15 mm thick soft temper 1200 aluminium foil from Multifoil Ltd, were used to cover the top and bottom surfaces of the mould each time to provide a repeatable surface roughness. In order to facilitate the demoulding of the disc samples, the moulds and aluminium foil were sprayed with polytetrafluoroethylene, PTFE. The machine direction of the foil was always aligned with the eventual direction

of the tensile stress, in compliance to the procedure proposed by [100]. Once the mould was prepared it was placed between the pre-heated press platens to undergo the following thermal cycle:

1. *Heating*: The mould was left in between the pre-heated press platens to reach a temperature of approximately 170 °C, for a period of 10 min during which time the platens were slowly closed
2. *Cycling pressure*: Following the gradual heating of the mould, the clamping force was then cycled manually for 5 min to dislodge any trapped bubbles
3. *Hold*: After the pressure cycling, the mould was then held at 170 °C at a moderate pressure for an additional 10 min
4. *Cooling*: Finally, the mould was cooled down through water flow until the mould reached the temperature T_g-20 °C

Figure 3.9 provides a schematic diagram of the moulding temperature-time protocol.

The cooling rate of the material was measured with the aid of embedded thermocouples during moulding. The temperature was monitored and recorded. Moulding temperature curves are shown in Figure 3.10 as obtained in two different PS moulding trials. The average cooling rate was calculated for both trials, and was determined to be 15.3 °C per minute.

The isotropy of the obtained moulded discs was verified by measuring any orientational birefringence using a polarizing microscope as described in section 3.6.

3.5 Crazing

3.5.1 Miniature specimen preparation

The crazing analysis performed in this study used a miniature specimen three-point isochronal creep technique proposed by [23].

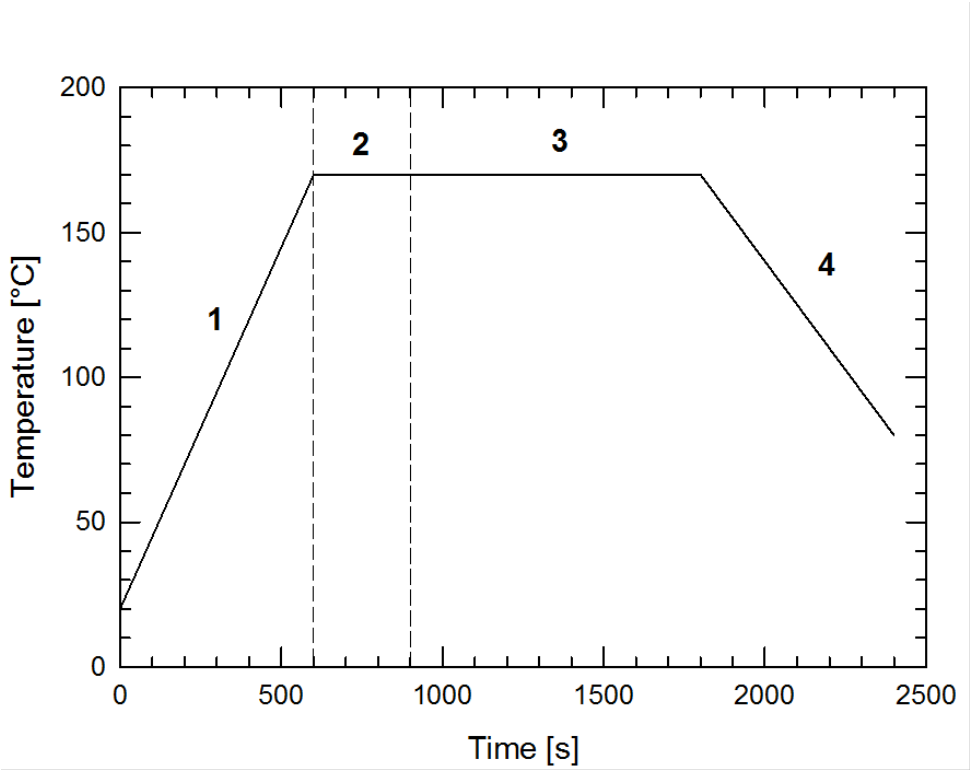


Figure 3.9: Heated press moulding procedure. Adapted from [23].

This technique allows to use minimum material quantities (∼10 mg) and minimise waste, which suited the limited availability of our PS materials. Miniature specimens were prepared by cutting the moulded discs in section 3.4, into parallel-sided strips of material using a custom-made jig with parallel single-bevelled blades. These strips where then trimmed into length to produce prismatic beams typically 0.5 mm x 2 mm x 8 mm in size, with less than 10 mg each. The long axes of the beams were aligned with the rolling direction of the aluminium foil to keep a reproducible surface roughness.

The obtained miniature specimens were immersed in DEG, this mild solvent is useful in crazing analysis, as it promotes environmental stress crazing, ESC [24]. The miniature beams were deposited in a container filled with analytical reagent grade DEG, and left to rest for a minimum of 24 hours prior to testing. Previous liquid uptake of PS in DEG has shown little difference over time as documented elsewhere [24].

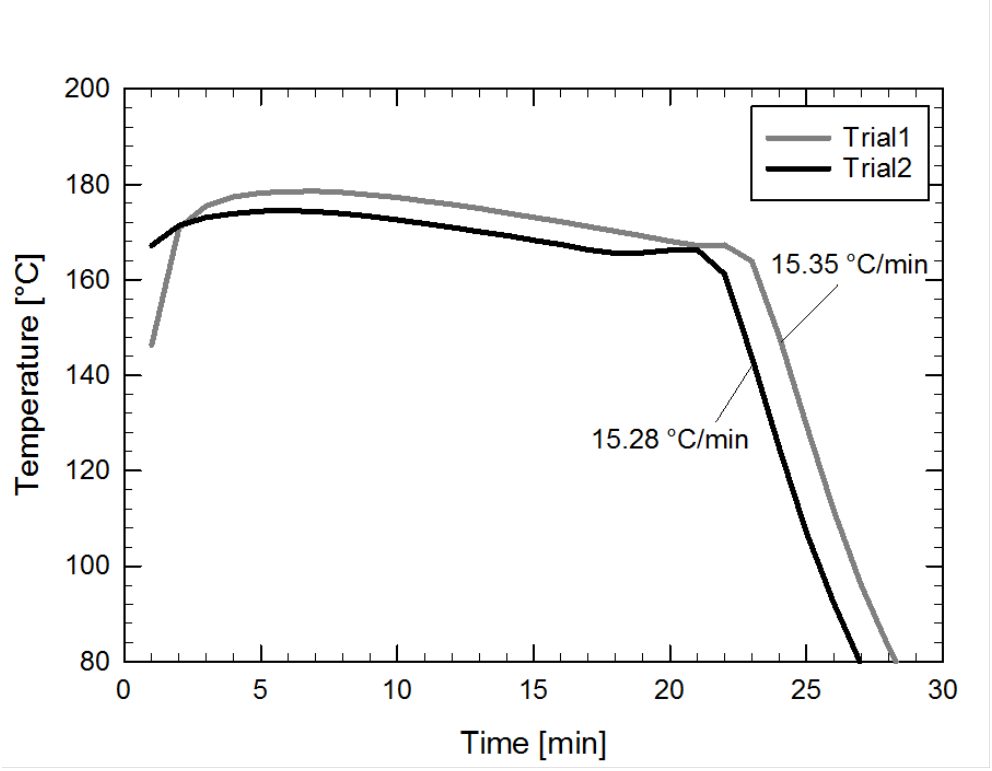


Figure 3.10: Temperature profile of disc moulding process. Average cooling rate temperatures are shown for reference for both recorded trials.

3.5.1.1 Laser cutting specimens

The possibility of finding new alternative methods of producing miniature specimens was explored. The development of precise and adjustable laser cutting tables provides a feasible opportunity to manufacture testing specimens for all sorts of mechanical and rheological tests. Laser cutting instruments rely on the use of a high power focused laser beam that acts as an energy blade to cut materials. The laser moves around a table working space through the use of motor power axes and rotating belts to allow the reproduction of complex geometries. Materials are mainly provided in the form of sheets and are laid on a working table supported with an aluminium honeycomb pattern. The intensity of the laser beam is controlled by two variables: power, P, and laser speed, v.

An experimental assessment was carried out on polymer R, to establish the

laser parameters required to cut miniature crazing specimens, as well as extensional rheological samples. The laser equipment used was a Trotec Speedy 100; films of 6x6 cm and 0.15 mm thickness, -purposely moulded for this assessment-, and discs of $\oslash = 25$ mm and 0.5 mm thickness were moulded following the procedure outlined in section 3.4. The polystyrene films were laid in the honeycomb bed, and were pressed down with squares of acrylic sheets of 3 mm to ensure the films remained flat. The power and speed of the laser were gradually modified to ensure the material was cut and could be demounted off the acrylic support.

Initially the material was layered, as per a sandwich structure, between two layers of 3 mm acrylic to ensure it remained in position. However, it was found that the PS melted together with the acrylic and was unable to be peeled off from the acrylic without breaking. It was then decided to remove the top acrylic layer off to cut the PS material directly with the laser beam. The laser power was decreased to avoid cutting the bottom layer. Unfortunately, this also proved to be challenging as the continuous movement of the laser caused the PS to fly off the acrylic support. It was then decided to use some laser friendly adhesive film to tape the PS to the bottom acrylic layer. This method seem to hold the sample into place, and although it was possible to produce some samples through this method, the obtained specimens were covered in dust from the residues of the melted area where the laser beam went through. Hence, it was decided to cover the whole PS sheet with a layer adhesive film to preserve the cleanliness of the sample. This method was successful in cutting and protecting the sample; after several adjustments the most promising setting for cutting the material without catastrophically fusing this to the bottom acrylic layer was: $P = 70\,\%$, $v = 3$ and laser resolution PPI=1000. With this setting it was possible to cut both miniature crazing (7.5 mmx2 mm) and extensional rheology (20 mmx3 mm) samples, although it was still required to manually remove some of the melted zone surrounding the edge of the specimen with the aid of tweezers. Table 3.6 provides a summary of the different laser cutting parameters used along with complementary observations.

Micrographs were taken of the edges of: (a) a mechanically cut miniature specimen, -in accordance to section 3.5.1-, and (b) a laser cut one. Figure 3.12 clearly shows the appearance of a melt zone at the edge of the laser cut specimen.

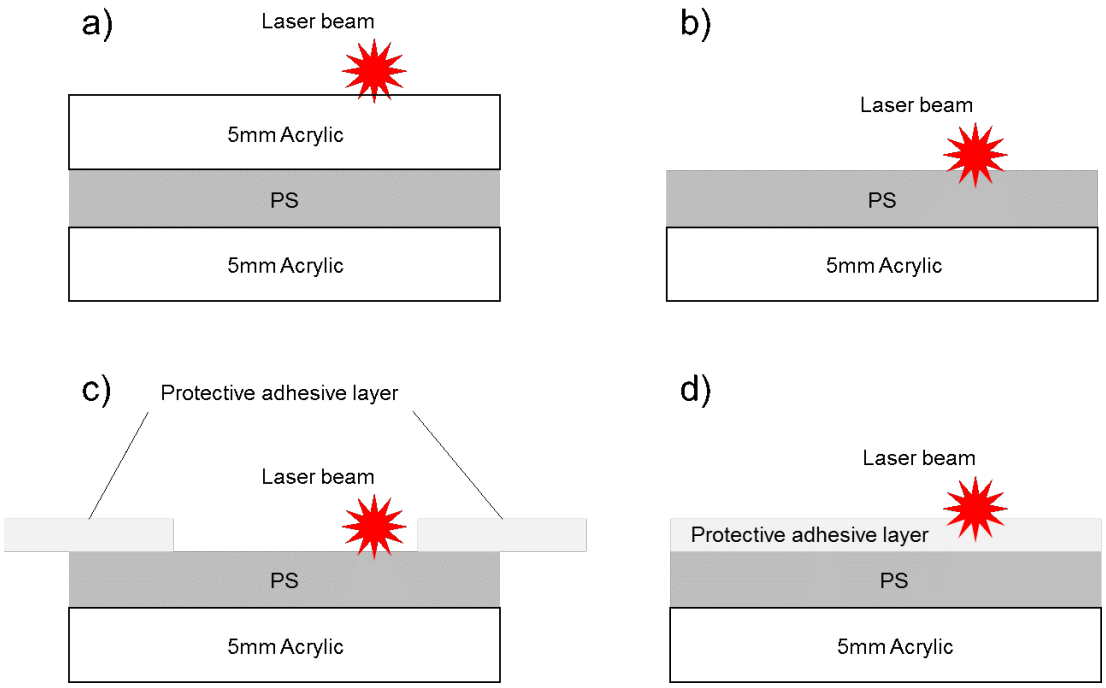


Figure 3.11: Laser cutting set ups explored for the production of miniature crazing and extensional rheology specimens.

Table 3.6: Laser cutting parameters used for cutting PS specimens.

Set up	P [%]	v	PPI	Observations
a	100	0.5	5000	PS melted between acrylic layers. Unable to peel off.
b	60	6	1000	PS flying off acrylic base due to laser head movement.
c	40	6	1000	PS not cut, not melted dust residue left on specimen.
d	40	6	1000	PS not cut, not melted, no dust left on specimen.
d	60	6	1000	PS not cut, not melted; able to peel off acrylic base
d	100	6	1000	Beam too high, PS slightly melted.
d	80	6	1000	Beam still high, PS partially melted.
d	70	5	1000	PS partially cut.
d	70	3	1000	PS cut, but left with surrounding melted zone.

It appears using the laser to cut PS specimens causes the polymer to dramatically melt and flow towards the centre of the creating an uneven cut surface. Bearing in mind the miniature nature of the specimens, the melted area was measured to extend $\sim 0.5\,\text{mm}$ into the sample. This is considerable in samples with a total width of 2 mm.

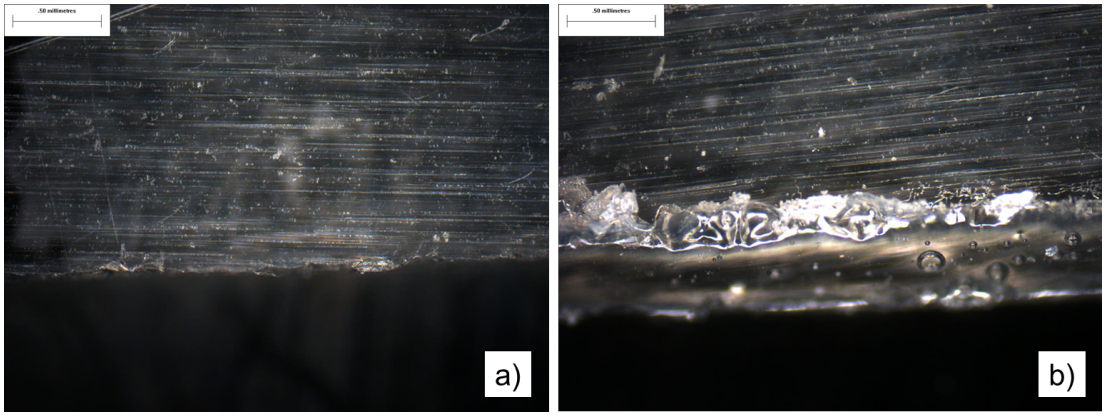


Figure 3.12: Difference between mechanical and laser cutting of miniature crazing specimens.

3D surfaces images of the miniature specimens were obtained by placing a ZeeScan Phase view camera on our Olympus BX51 microscope. This software allows to use fast and precise 3D acquisition without the use of stepper motors or piezo devices. The 3D micrographs of manually cut and laser cut specimens with dimensions of approximately 0.5 mm x 2 mm x 8 mm were processed. The height (z-axis), was measured to provide surface roughness profiles. The image of the manually cut specimen is shown in Figure 3.13, while the image of the laser cut specimen is provided in Figure 3.14.

The most noticeable difference observed when comparing the height profile of Figure 3.13 against that of Figure 3.14 is the profile gradient that is observed in the laser cut sample, that goes from 179 μm closer to the centre of the sample to 20 μm at the edge where the laser has made contact with. The stepped and non-uniform profile is consistent with the edge observed in the micrograph. Since the miniature specimens rely on surface uniformity to promote craze formation, laser cutting was considered an unsuitable method for the production of these sort of samples. Nevertheless, this issue is not observed for extensional rheology specimens, where the uniformity of the sample is not a requirement as the material will effectively be heated above its T_g during the test. Thus, laser cutting can definitely be used for the production of these samples for rheological characterisation as explained in section 3.7.3.

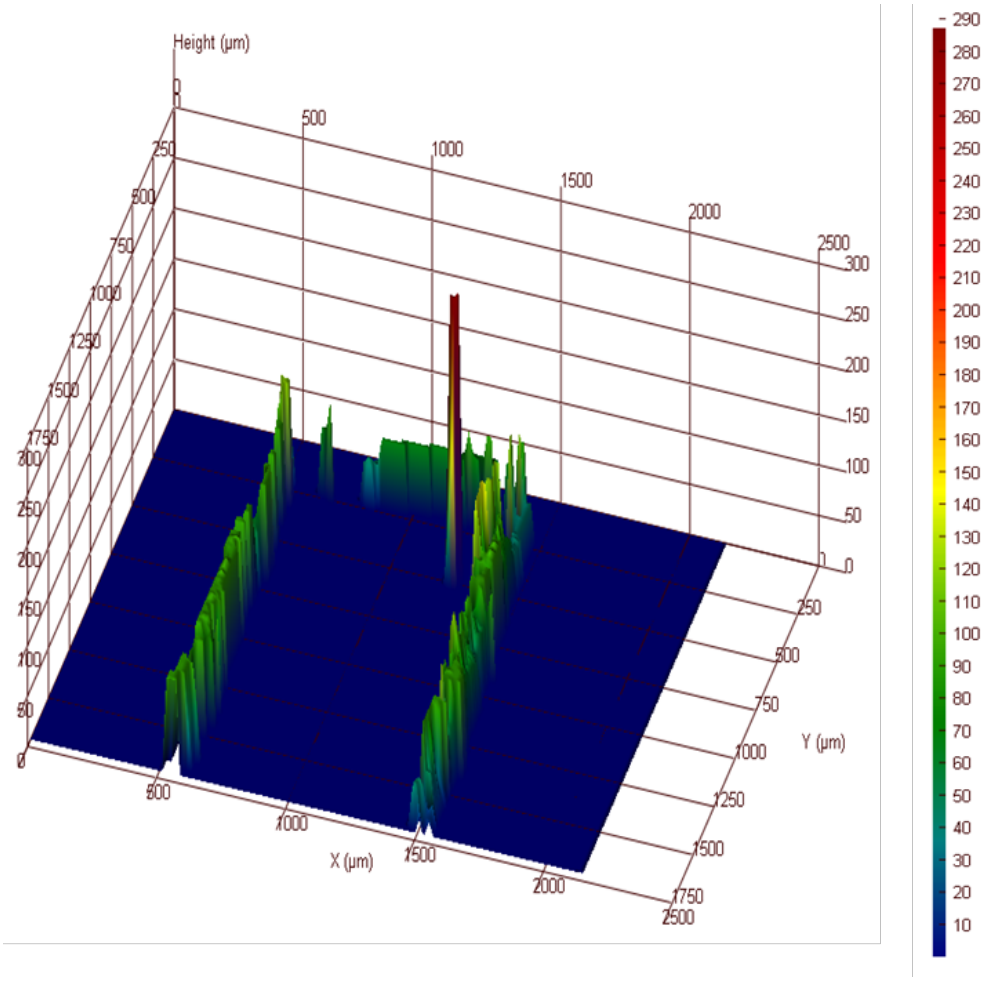


Figure 3.13: 3D profile of manually cut miniature specimen.

3.5.2 Crazing stress measurements

As has been reviewed in section 2.7 many studies have been previously reported concerning the formation of crazes for PS, and a useful review for applied techniques and craze initiation criteria can be found in [101]. This study focuses on the application of a miniature specimen three-point isochronal bending technique developed by De Focatiis *et al.* [24]. In this procedure, miniature polymer specimens are subjected to an applied load for a fixed creep time, leading to the formation of crazes in a region in which the stress is equal to or exceeds the craze initiation stress, CIS. This CIS can be determined from the bending moment, M, and moment of inertia, I, beam. From first principles, for a beam of length

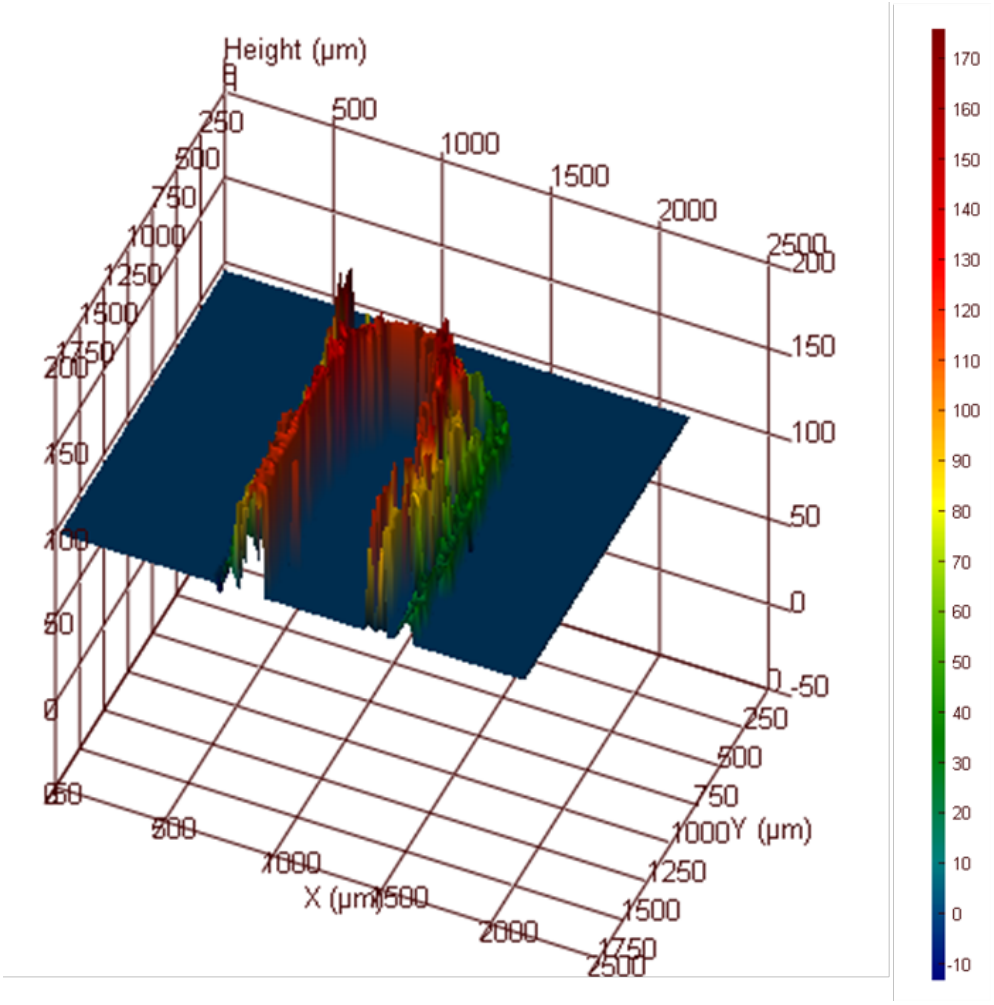


Figure 3.14: 3D profile of laser cut miniature specimen.

L subjected to symmetric 3-point bending with a centred load P, the loading moment M at position x is given by

$$M = \frac{Px}{2} - P[x - \frac{L}{2}] \rightarrow M = \frac{Px}{2} \tag{3.7}$$

The moment of inertia for a rectangular beam of height h and width b is definition of the moment of inertia for a rectangular shaped geometry is

$$I_{rectangle} = \frac{bh^3}{12} \tag{3.8}$$

Outside the craze region, the material can be assumed to follow linear viscoelasticity, and elementary beam theory is obeyed, described through equation 3.9

$$\sigma = \frac{My}{I} \tag{3.9}$$

where y, refers to the distance to the neutral axis.

Hence by measuring the extent of the crazed region it is possible to evaluate the stress at the edge of the crazed region, where in the given creep time the stress was not sufficient for the crazes to form. By combining equations3.7, 3.8 and 3.9 the craze initiation stress, σ_c [24] is given by,

$$\sigma_c = \frac{3}{2}\frac{P(L - L_c)}{bd^2} \tag{3.10}$$

A schematic showing the shear force and bending moment diagrams, is provided in Figure 3.15.

3.5.3 Miniature crazing rig

Craze formation was induced through the use of a custom-made three-point bending crazing rig. Two new rigs were developed and produced at the University of Nottingham as part of this project, and pictures and a CAD explored view can be found in the Appendix A (Figures 1, 2, 3). The crazing rig consists of a loading tray which applies the load onto the specimen beam by means of a sliding tube with a pointed tip at the end. The loading tray tip comes into contact with a lightweight loading plate sliding in PTFE guides. These guides provide location, with minimum friction. The loading plate supports the entirety of the load which will be transferred onto the specimen positioned mid-way between the supports or holders. The loading plate ensures accurate positioning of the load into the miniature beam specimen. A photograph of the miniature crazing rig is given in shown in Figure 3.16.

Each specimen is carefully located between two parallel supports, 5 mm apart

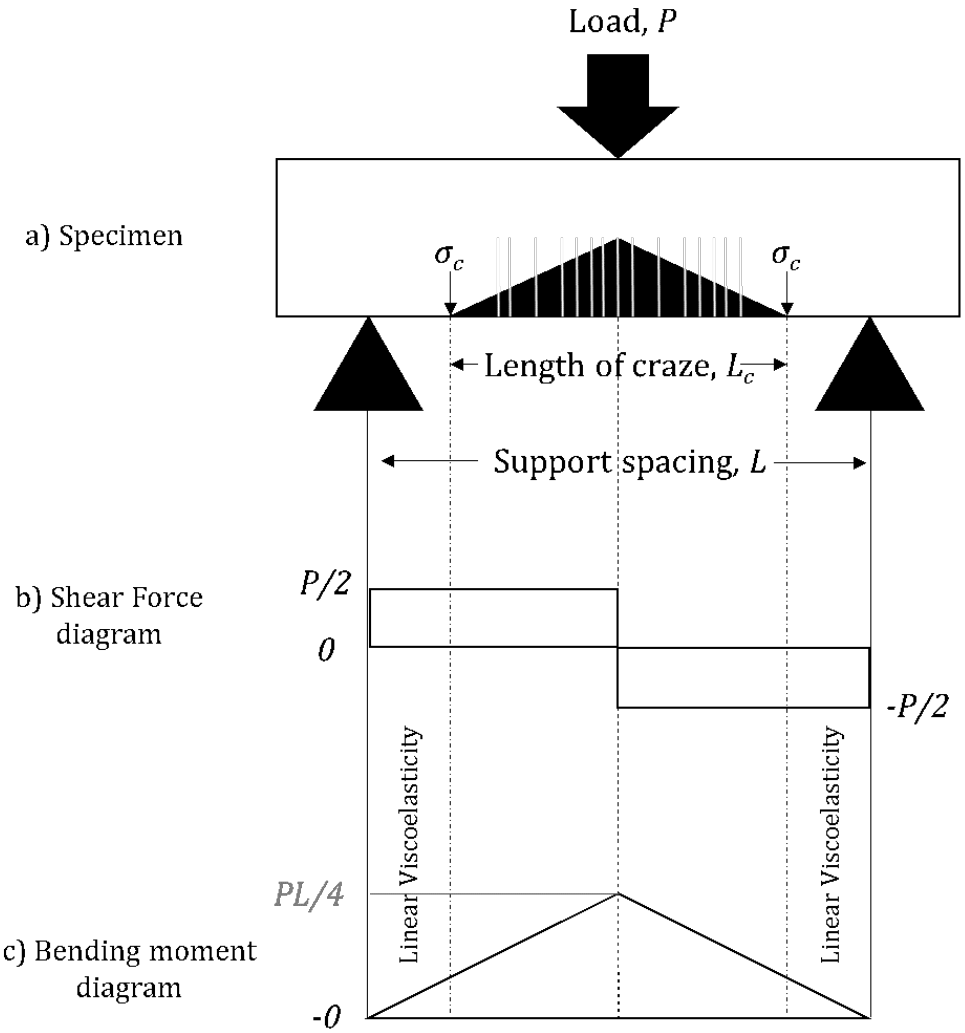


Figure 3.15: Schematic diagram of the distribution of load determined from the bending moment and moment of inertia of a beam subjected to symmetric 3-point bending. The extent of the crazed region is shown by L_c, and the craze iniation stress that can be calculated at the edge of this area is labelled as σ_c. Adapted from [24].

from one another ($L = 5\,\text{mm}$). These supports can be positioned by means of screw holes machined at distances of 4 mm, 5 mm or 6 mm as shown in Figure 3.17(a). The miniature specimen was kept submerged in DEG using a very thin strip of PTFE tape placed between the specimen holders to support the specimen. A few droplets of DEG were put on top of the miniature specimen to wet the

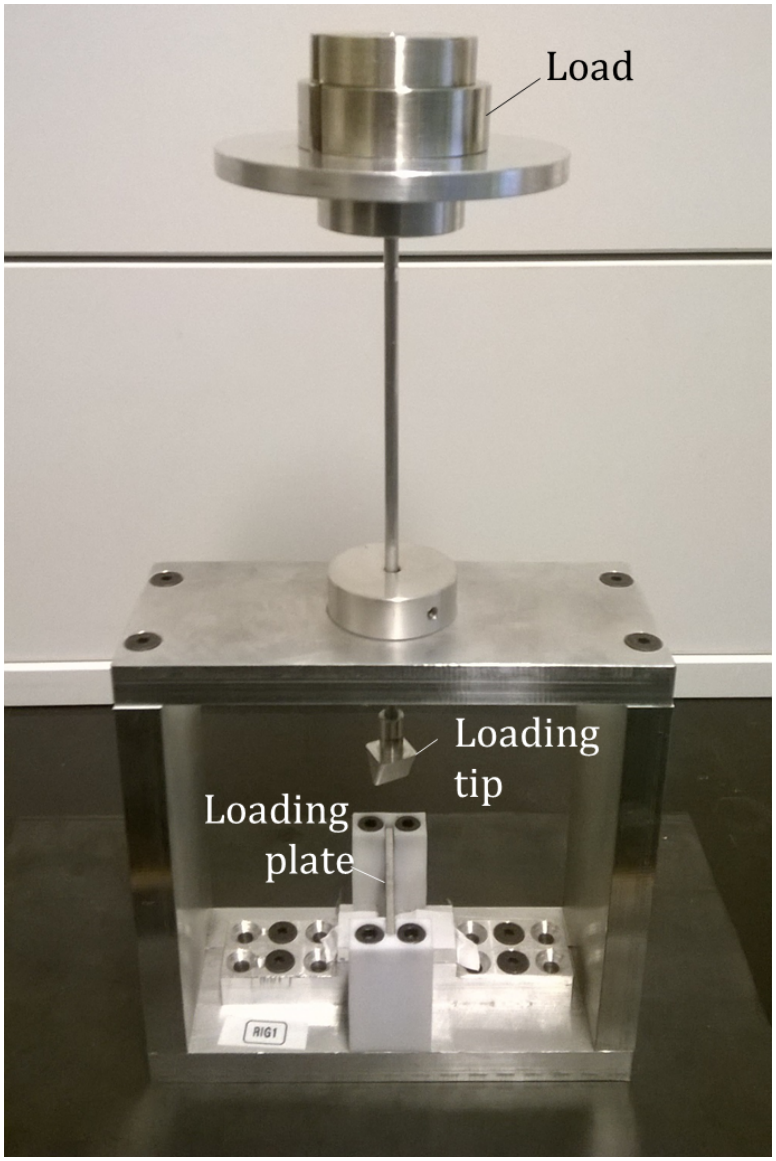


Figure 3.16: Photograph of the custom-made crazing rig for isochronal three point bending creep of miniature specimens.

surface, and the DEG remained in place through surface tension as shown in Figure 3.17(b). Finally, loading plate is placed on the specimen ready for the load to be applied, shown in 3.17(c).

The applied load was left on the sample for a specific creep time, to ensure craze initiation. After the experimental creep time, the load was removed and

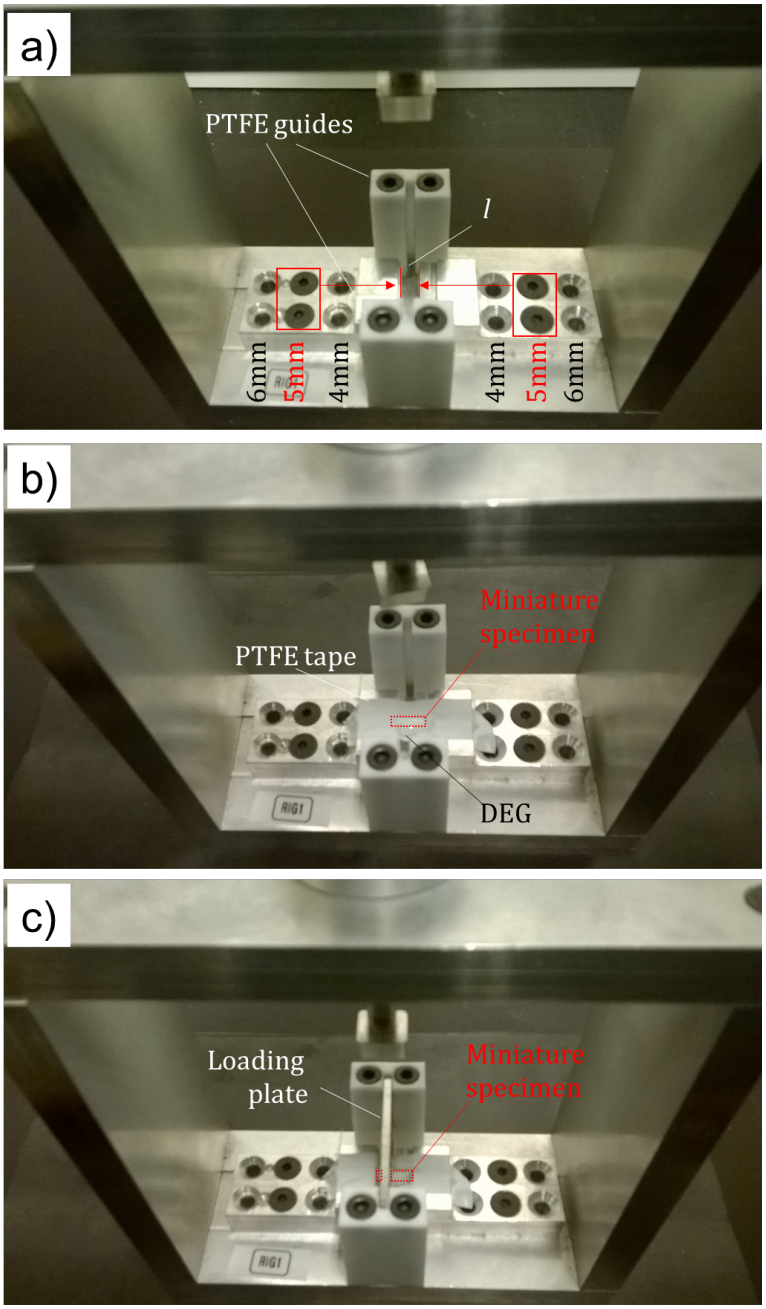


Figure 3.17: Details of the experimental set-up of miniature crazing specimens in three point bending creep custom made crazing rig.

the sample was carefully dried to remove any remaining DEG, and moved to a low power microscope for measurement.

3.5.4 Quantification of the crazed region

To accurately see the crazes, it was necessary to reflect transmitted light from a standard 40W desk lamp, onto the specimen. The craze surfaces are able to reflect the light through and up to the microscope axis for viewing. A more detailed schematic of the interaction between the specimen, light path and optical microscope is shown in Figure 3.18.

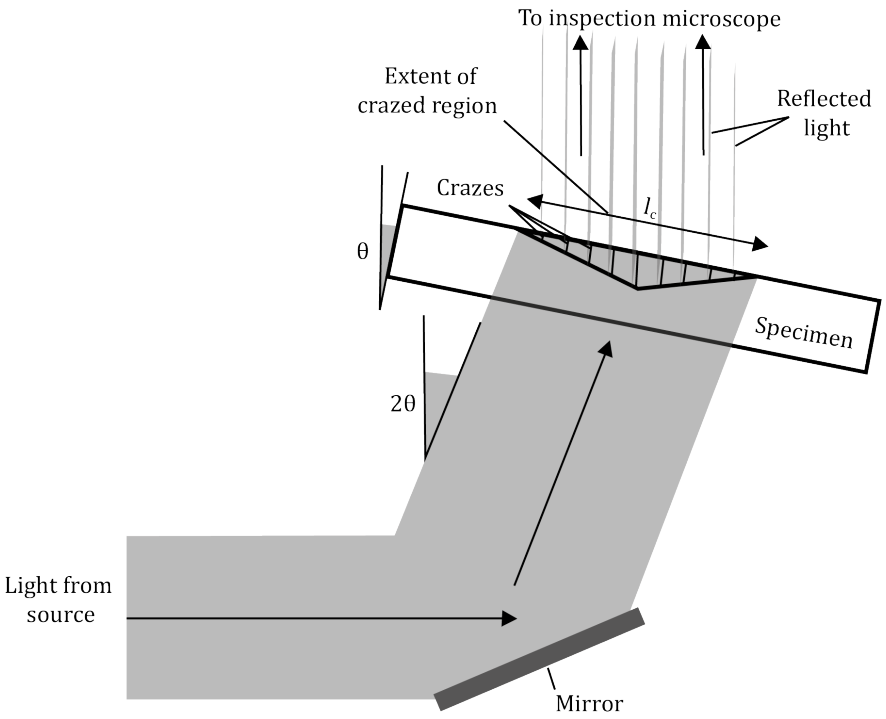


Figure 3.18: Schematic representation for the optical microscopy technique of craze measurement through light refraction, adapted from [24].

To achieve this interaction, it was required to reflect the source beam towards the sample at an angle (2θ) to the vertical. The specimen support plate was tilted by θ, and the reflected beam of white light was reflected by the craze along the microscope axis. The arrangement for this procedure can be found in Figure 3.19.

Once crazes were viewed, it was necessary to quantify the extent of the crazed region to compute the relevant σ_c. This was done by using an eyepiece microme-

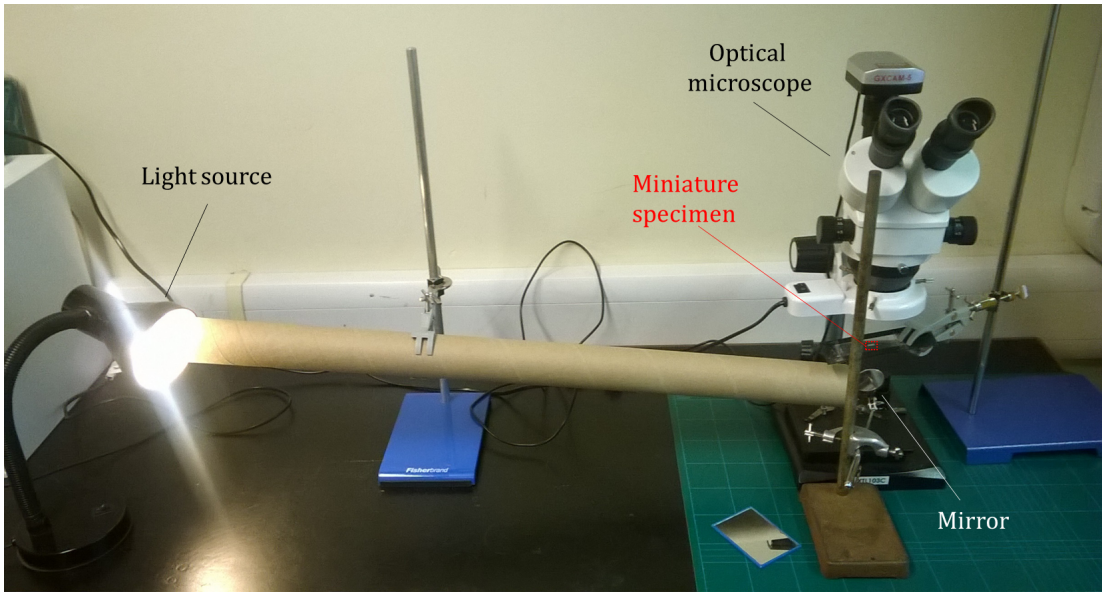


Figure 3.19: Experimental setup for the measurement of crazing through light reflection under optical microscopy.

ter, and a 100 lines per inch graticule for calibration. A calibration measurement was always performed before any craze measurement. After calibration, five separate measurements (c1-c5), were performed of the length of the craze region, L_c, across the width of each specimen as is shown in Figure 3.20.

A micrograph of a typical specimen illustrating the crazes made visible by the incident light is shown in Figure 3.21.

The average of the crazing length values of the five lines was used to obtained the mean length, L_c, to be used in equation 3.10. All measurements were made within one hour of crazing, to limit the effect of craze healing, and where carried out at room temperature of approximately 20±1 °C.

3.6 Birefringence

3.6.1 Manufacture of oriented specimens

The preparation of oriented specimens was done by mechanically stretching rectangular bars at specific temperatures above the glass transition. The orientation

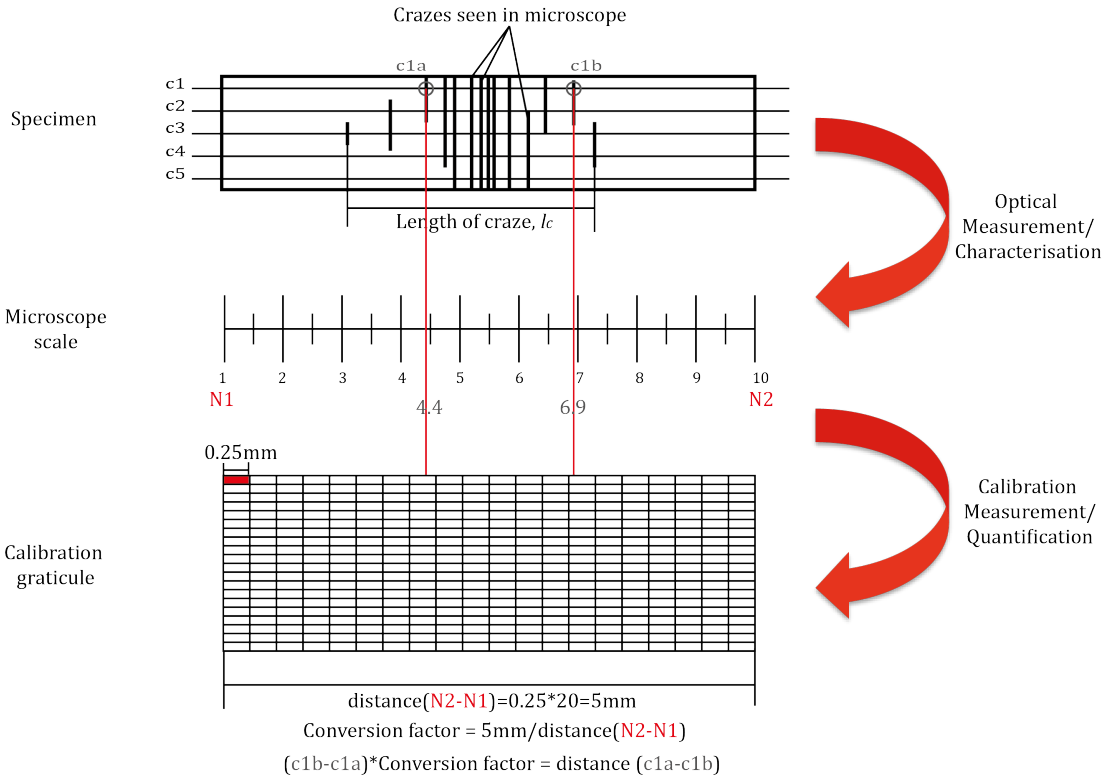


Figure 3.20: Schematic diagram of the craze measurement quantification protocol. The crazes in the specimen are measured at five longitudinal lines (c1-c5). Each individual length is measured by correlation with the eyepiece micrometer, which has been calibrated with the aid of a calibration graticule.

was captured by freezing the structure through rapid cooling before the molecules could relax, with the aid of a freezing spray. The rectangular bars were press-moulded using the same equipment and procedure as described in section 3.4. A rectangular bar-mould was used to make for specimens with a 60 mm x 5 mm x 1.9 mm geometry.

The press-moulded bars were stretched using an Instron 4204 testing machine fitted with an environmental chamber. The drawing of the PS bars was performed close to or above the T_g of PS ($\sim$ 106 °C). Four drawing temperatures were used: 106 °C, 116 °C, 126 °C, and 136 °C. The bars were elongated uniaxially at a strain rate of $\dot{\epsilon}$ =0.02 s^{-1} and a draw ratio of λ =3. After drawing, the bars were immediately quenched to a temperature below T_g by using a freezing spray.

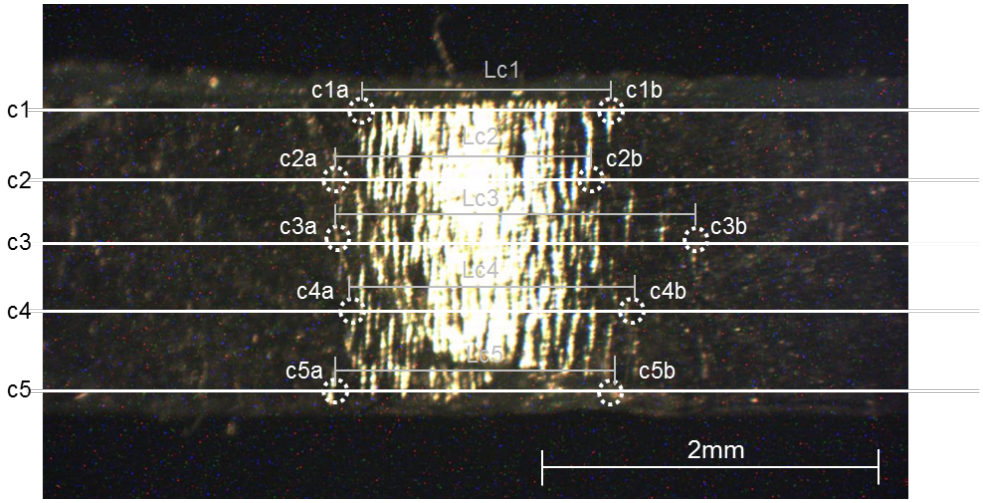


Figure 3.21: Micrograph of the craze measurements in a real specimen. Values for each measurement line (C1-C5) are shown, and will be used to obtain the average craze length, L_c, to be used in calculations.

3.6.2 Birefringence measurements

The birefringence in the oriented specimens was calculated by measuring the relative retardation, r , of the optic axes in the plane of the oriented bars when light is transmitted. This was accomplished by using an Olympus BX51 microscope fitted with polarizing optics and a thick Berek rotary compensator. In polarized light microscopy, two filters are placed in a path of light, one below the objective, known as polarizer, and one on top of the specimen, called the analyzer. The polarizer filters the light rays to allow only light waves in one orientation to pass through. A simple schematic of a polarizer microscope can be found in Figure 3.22

When the analyzer is perpendicular to the polarizer, all light rays are cancelled. Birefringent objects have the ability to rotate or modify the light rays, and therefore appear bright in a dark (cancelled) background. In this case, the oriented molecules in the stretched specimens cause the light to be refracted, and hence exhibit some birefringence.

Measurements were made by light transmission through the full thickness of each oriented PS bar at room temperature in a white light environment.

The optical birefringence, Δn was computed through equation 3.11,

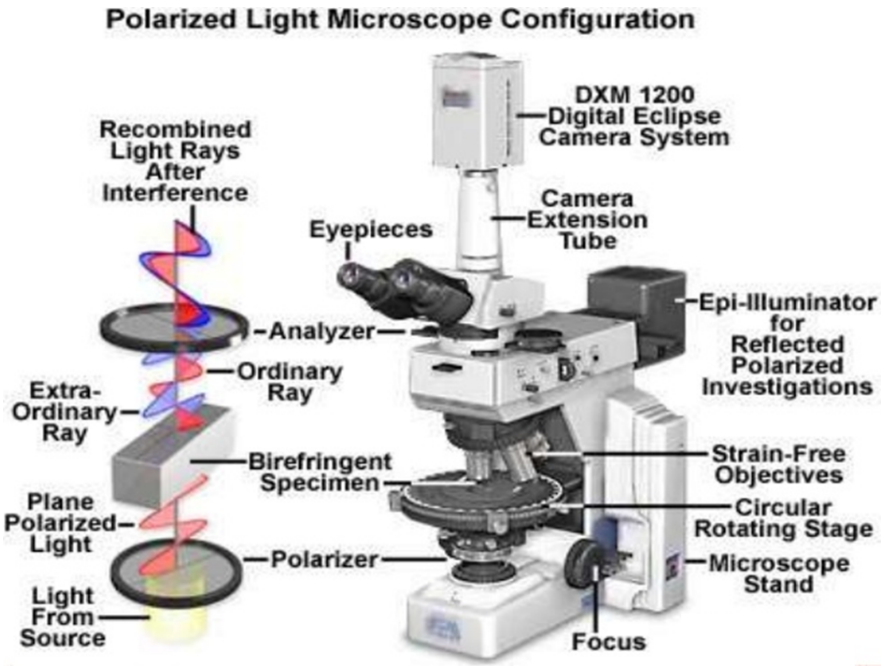


Figure 3.22: Illustration of a polarized microscope configuration from [25].

$$\Delta n = \frac{r}{d} \tag{3.11}$$

where d is the specimen thickness measured using a micrometer.

3.7 Rheology

Rheology studies the flow and deformation behaviour of melts. It has since recent years become the preferred method of linear and non-linear viscoelastic characterisation of polymer melts. Rheological tests are performed using a rotational rheometer, which is essentially a device that imposes and measures rotations and torques. Depending on the fixture or geometry used, it is possible to obtain specific information on the behaviour of polymers. The rheological tests in this study were performed using an Anton Paar MCR-302 rheometer in air atmosphere, with parallel plate, cone and plate and extensional fixtures. A more

detailed explanation of the configurations used is provided below.

3.7.1 Linear rheology

Linear rheology refers to the regime of behaviour in which polymers behave in a linear viscoelastic manner, i.e. stress is proportional to strain at any given time. Recently, steady-state oscillation has gained acceptance as the preferred method for linear viscoelastic characterisation. In oscillatory tests, the shear strain and stress varies sinusoidally. In this test, the polymer is usually constrained between a top and bottom plate, and is sheared through the sinusoidal movement of the top plate. The configuration for this test can be two flat parallel plates (pp), or a cone-and-plate (cp), as shown in Figure 3.23.

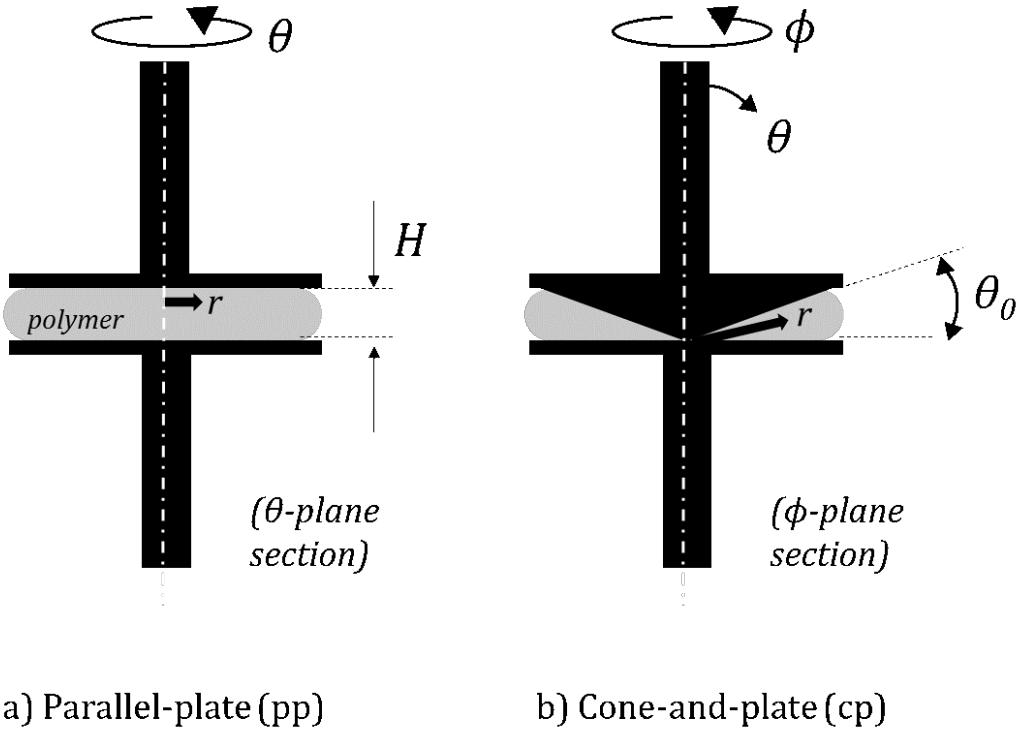


Figure 3.23: Parallel-plate and cone-and-plate geometries for rheological tests, from [26; 27].

In a cone and plate configuration, the relationships between shear stress, τ,

and shear strain, γ, depend on the radius R, and angle of the cone top plate θ. The shear stress, τ, and the strain rate, $\dot{\gamma}$ can be easily derived by correlation with the applied torque, Γ, and the angular velocity, Ω, as per equations 3.12 and 3.13.

$$\tau_{cp} = \frac{3\Gamma}{2\pi R^3} \tag{3.12}$$

$$\dot{\gamma_{cp}} = \frac{\Omega}{\theta} \tag{3.13}$$

Parallel-plate geometries are found to be more challenging when analysing the mathematical definition for a shear stress over the cross-section, A, of the material. Looking at a simple Newtonian case for shear flows, the shear strain, γ is defined by the displacement, x_0, at specific positions in z, represented by the height, h.

$$\gamma = \frac{x_0}{h} \tag{3.14}$$

Hence, the shear strain rate, $\dot{\gamma}$, simply becomes the differential change of γ over time,

$$\dot{\gamma} = \frac{d\gamma}{dt} = \frac{v_0}{h} \tag{3.15}$$

In a parallel-plate set up, the velocity profile of the contained polymer is in fact changing as a function of its position, z, with respect to the bottom plate, as it can be seen in Figure 3.24.

To calculate the shear-stress this needs to be determined by correlating the torque, Γ, to angular velocity, Ω. These terms will be affected by the radius R of the top and bottom plates, as well as the radial position of the polymer r, with respect to R. Taking this into account, the shear stress and shear rate equations for a parallel-plate configuration are given by,

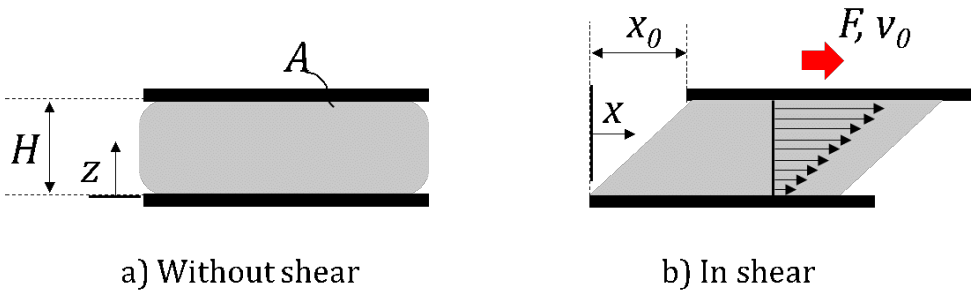


Figure 3.24: Velocity profile for a parallel plate configuration in shear.

$$\tau = \frac{2\Gamma}{\pi R^3}\left[\frac{3}{4} + \frac{d\ln(\Gamma/2\pi R^3)}{d\ln\dot{\gamma}_R}\right] \tag{3.16}$$

$$\dot{\gamma} = \frac{r\Omega}{H} \tag{3.17}$$

where H, is the gap size between the top and bottom plates.

A photograph of the experimental set up of the rheometer used in this study can be found in Figure 3.25.

3.7.2 Non-linear rheology

Non-linear viscoelasticity can be tested through transient tests. In these tests, the shear rate is kept constant and the polymer deviates from linearity in what is commonly represented as an overshoot. To evaluate the effect of frequency, the tests are done at a variety of strain rates (from $0.01\,s^{-1}$ to $10\,s^{-1}$).

3.7.3 Extensional rheology

A novel configuration for extensional tests is that proposed by Martin Sentmanat, the Sentmanat Extensional Rheometer, SER [28] . A miniature bar specimen is located between drums that counter-rotate at the same angular speed. The

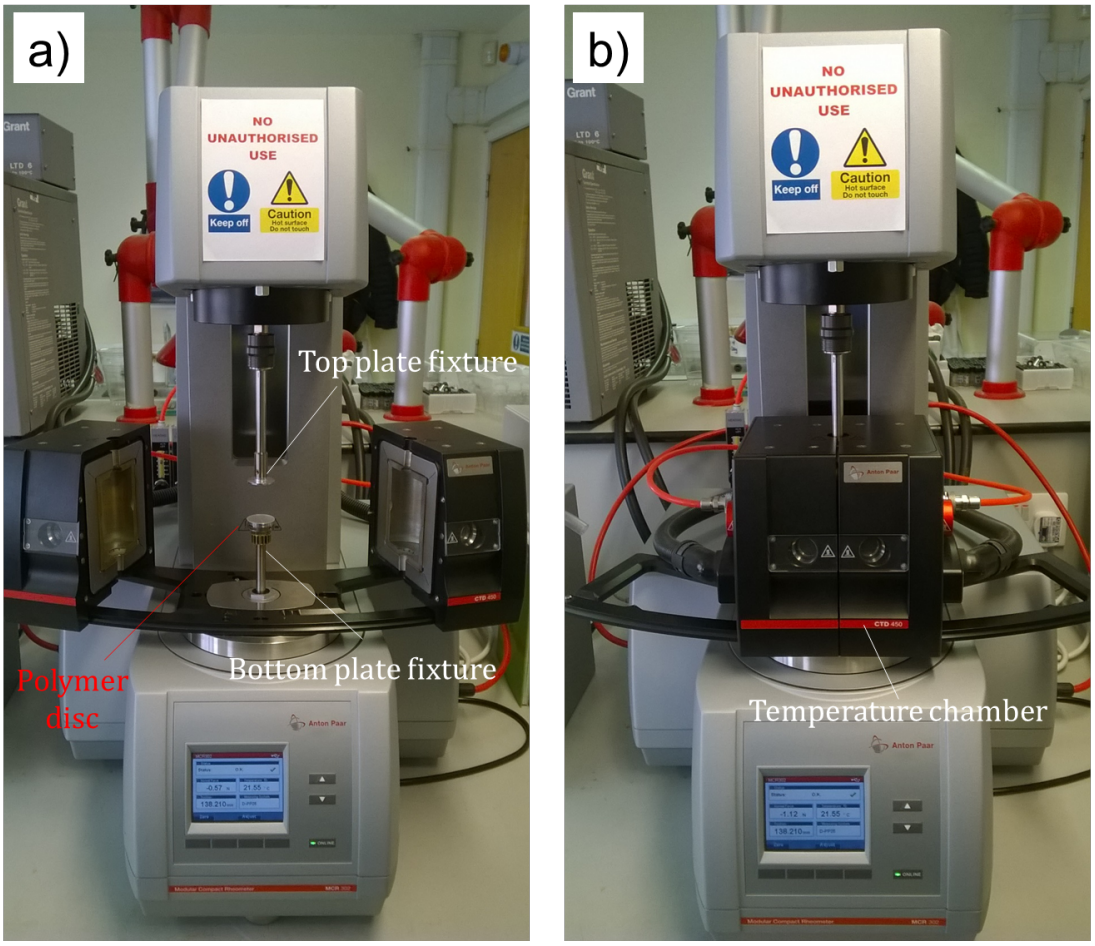


Figure 3.25: Experimental setup for oscillatory and transient shear rheology in an Anton Paar MCR-302 rheometer.

resistance of the drums is hindered by the stretching response of the sample, as this is elongated in an analogous way as a tensile test or fiber wind-up techniques would do. A schematic illustration of the SER system is shown in Figure 3.26.

A photograph of the experimental set up for extensional rheology used in this study can be found in Figure 3.27.

Extensional flow measurements are useful, because they are very sensitive to the molecular structure of the polymeric system. When the true rate of extension, also known as Hencky strain rate, is constant, the degree of molecular orientation is much higher than the stretching that occurs in flows in simple shear [28].

For a constant drive shaft rotation rate, Ω, the Hencky strain rate of the

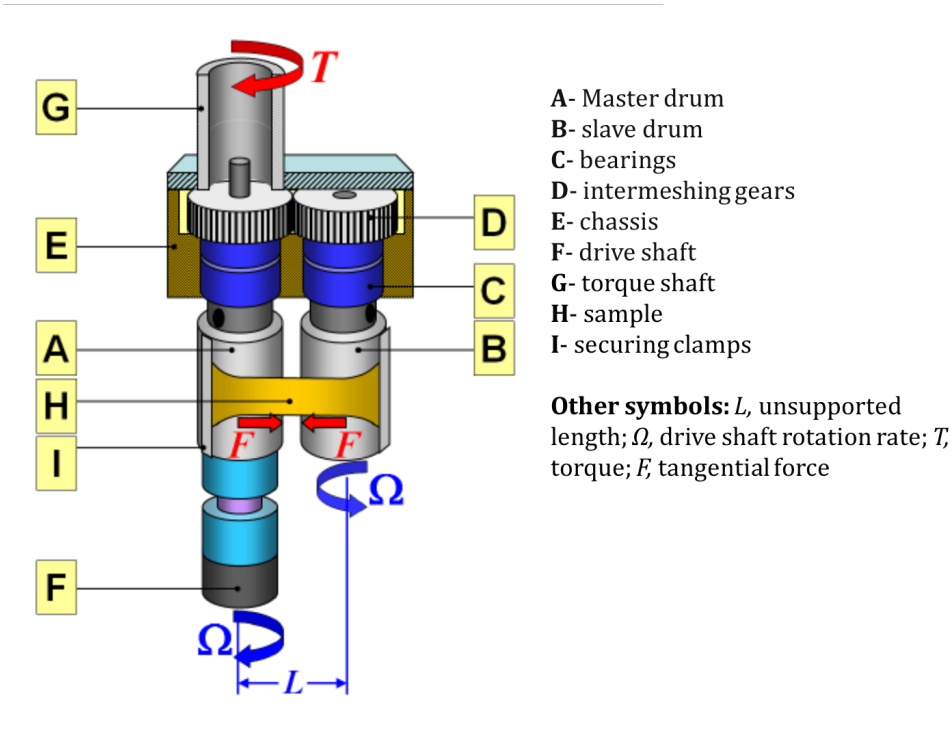


Figure 3.26: Configuration of a SER system from [27; 28].

specimen can be expressed as:

$$\dot{\epsilon}_H = \frac{2\Omega R}{L_0} \tag{3.18}$$

where R is the radius of the wind-up drums, and L_0 is the fixed sample length, which is equal to the centerline distance between the master and slave drum. The torque of is given by $\Gamma = 2FR$, with F being the stretch force. Since the cross-area will be changing as a results of the constant stretching of the specimen, the tensile stress growth function, $\sigma(t)$ is expressed as equation 3.19:

$$\sigma(t) = \frac{F(t)}{\dot{\epsilon}_H A(t)} \tag{3.19}$$

where $F(t)$ is the instanteneous extensional force at time t exerted by the sample as it resists stretch as determined from the measured Γ.

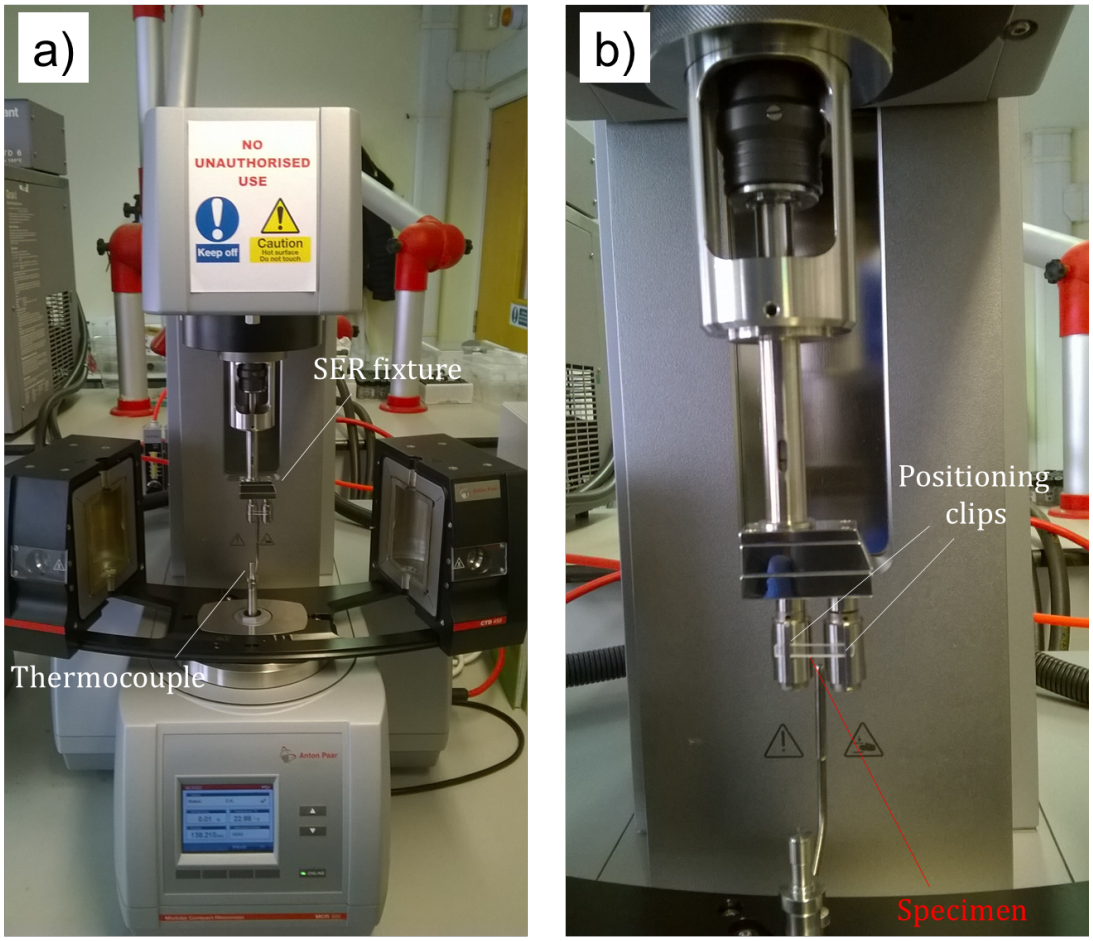


Figure 3.27: Experimental setup for extensional rheology of an Anton Paar MCR-302 rheometer.

3.7.4 Rheological Data Analysis

REPTATE, Rheology of Entangled Polymers: Toolkit for Analysis of Theory and Experiment , is a powerful and versatile rheological software developed by Alexei Likhtman and Jorge Ramirez to aid rheologists and scientists interpret rheological data [102]. REPTATE offers a readily available materials database and rheological theories library to help understand and analyse rheological experiments. It is particularly useful for users to manipulate dynamic measurements and present data in specific formats. REPTATE covers most rheological procedures, as it includes windows targeting LVE, NLVE rheology, as well as enabling the user to

upload other complementary data such as GPC molar mass distributions. One valuable tool REPTATE offers is the possibility of producing master curves at one chosen temperature using TTS. This allows to produce a single plot over a broad range of frequencies by shifting the data obtained at different temperatures to a common reference temperature. In this study the reference temperature is set at 170°C. The use of a reference temperature of 170°C was decided as an arbitrary value high above the glass transition temperature, and for which multiple data is available to enable direct comparison for theory validation. The master curves produced using REPTATE will be further discussed in section 6.3.

REPTATE is extremely helpful is in the determination of intrinsic material parameters. A "calibration procedure" is carried out in designated calibration samples, namely monodisperse materials. There has been some debate over how the accuracy of the master curves or model used may offer different values for the material parameters: M_e, G_e and τ_e [6]. Nevertheless, these parameters are required in order to fit existing rheological models, and the calibration procedure hereby mentioned has become customary in the analysis of LVE data. Details for the calibration procedure used in this study are also examined in section 6.3.

Chapter 4

Molar Mass Analysis

4.1 Prelude

In the preceding section, the experimental methods and representative examples for the characterisation of the polymeric materials studied were presented (e.g. SEC and DSC). This chapter aims at analysing in more detail how the interpretation of the data obtained using these techniques can provide fundamental understanding of the variations in the chemical and thermal properties of PS as a function of varying molar mass. Specific attention is given to the unintended consequences associated with polymer blending; the chosen approach was to recreate what is sought by end polymer processers where polymer mixing is performed to obtain a balance between solid (i.e. mechanical) and melt (i.e. flow) properties to comply with end product and manufacturing requirements.

Molar mass distributions and glass transition characteristics of the polymer systems presented in this study are interpreted using fundamental models. The differences seen between the models and experimental data are discussed in the frameworks of molar mass sensitivity, polydispersity, and processing side effects (e.g. thermal degradation or oligomeric evaporation), which exert a critical effect in the character of the resulting blend.

4.2 SEC data

ASTRA's raw data was processed using an in-house MatLab code following the procedure outlined in section 3.2. The calculated normalised weight fractions for the PS materials used in this study are presented in the subsequent sections.

In Figure 4.1, the $\overline{M}_n$ and $\overline{M}_w$ averages obtained from the ASTRA software by manual trimming, and those obtained using our MatLab code are compared. The fact that both these values lie on top of the diagonal signifies that there is a very small difference between the two data averaging methodologies. In order to analyse quantitatively the differences between both sets of data, we report the normalised difference, Δ, calculated through expression 4.1,

$$\Delta_n = \frac{|\overline{M}_{n1} - \overline{M}_{n2}|}{(\overline{M}_{n1} + \overline{M}_{n2})/2} \quad ; \quad \Delta_w = \frac{|\overline{M}_{w1} - \overline{M}_{w2}|}{(\overline{M}_{w1} + \overline{M}_{w2})/2} \tag{4.1}$$

where $\overline{M}_{n1}$ and $\overline{M}_{n2}$ refer to the number molar mass averages of the MatLab and ASTRA calculations, respectively. The same expression can be used to calculate the normalised difference for the weight average when substituting for $\overline{M}_{w1}$.and $\overline{M}_{w2}$, respectively. The normalised difference will be reported as a percentage value (%).

The averaged reported Δ_n was found to be ~6.77, and Δ_w was calculated at ~2.59. The low figures prove the resemblance between the two methods is quite high, and this validates that the MatLab technique hereby developed provides enough statistical confidence for the automation of the trimming molar mass limits in the polymer distributions obtained from SEC analysis.

4.2.1 SEC: Monodisperse and blends

Figure 4.2 presents the data for the normalised weight fractions of monodisperse materials BF, BG and BH (a), alongside their corresponding blends (b) as processed using our MatLab sequence. The corresponding numerical values are displayed for reference in Tables 4.1 and 4.2.

The MMDs of the monodisperse materials are representative of narrow dis-

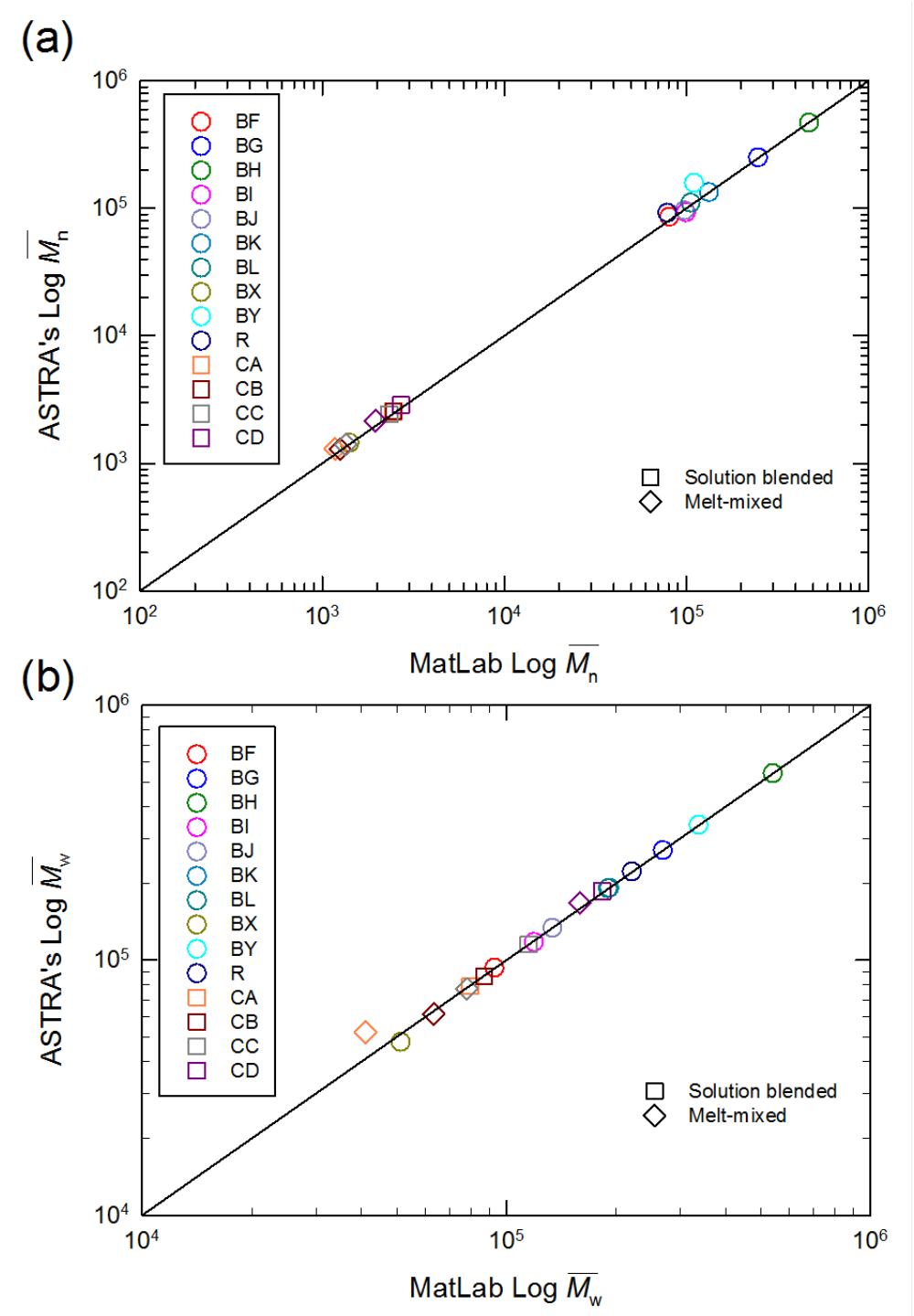


Figure 4.1: Data comparison for the (a) $\overline{M}_n$, and (b) $\overline{M}_w$ averages, as obtained from ASTRA and processed using MatLab. All materials have been colour coded. Polydisperse blends have been colour coded to refer to their blending ratio (e.g. molar mass), and distinguished by square symbols to refer to the blends obtained by solution blending, and diamonds to refer to the blends obtained through melt-mixing.

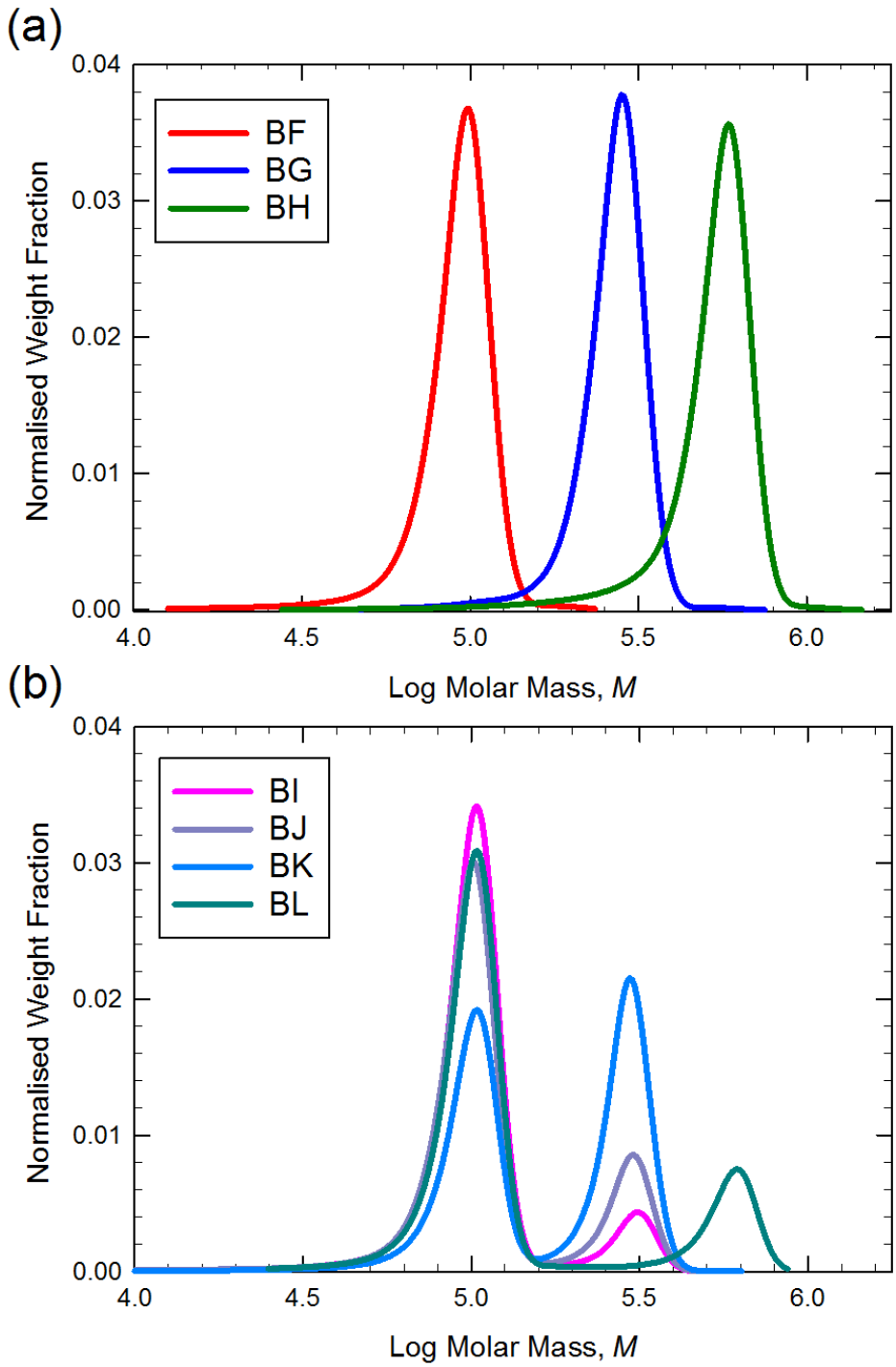


Figure 4.2: Molar mass distributions of (a) monodisperse materials, and (b) their corresponding blends obtained using MatLab.

Table 4.1: Molar mass details for monodisperse materials used in this study.

Code	System	Description	$\overline{M}_n$ [g/mol]	$\overline{M}_w$ [g/mol]	PDI
BF	Atatic Monodisperse	Low $\overline{M}_w$	86,113	93,378	1.084
BG		Medium $\overline{M}_w$	251,330	269,910	1.074
BH		High $\overline{M}_w$	469,960	540,270	1.150

Table 4.2: Molar mass details for bimodal blends of monodisperse PS materials used in this study.

Code	System	Blending composition	$\overline{M}_n$ [g/mol]	$\overline{M}_w$ [g/mol]	PDI
BI	Monodisperse blends	90%BF, 10%BG	93,201	117,830	1.26
BJ		80%BF, 10%BG	96,625	133,900	1.26
BK		50%BF, 50%BG	134,030	192,150	1.43
BL		80%BF, 20%BH	110,830	191,210	1.72

tributions and inherently low levels of polydispersity. From Figure 4.2 the clear increase in molecular weight as one shifts from material BF (further left) to material BH (further right) becomes evident. If Figure 4.2 (a) and (b) are analysed in conjunction, it is possible to see that the low and high peaks of the monodisperse blends distributions effectively lay in the position of the constituent materials, i.e. BF and BG for blends BI-BJ, and BF and BH for blend BL. As one would expect, the height of the peak is related to the wt% of the constituent material within the blending composition. The peaks for material BF are seen to decrease in height as more of the higher molar mass component is added, and consequently the peaks of the latter are seen to increase with reducing content of BF. These results are also reflected in Tables 4.1 and 4.2, where $\overline{M}_n$ and $\overline{M}_w$ correspondingly increase with higher content of BG and BH.

4.2.2 SEC: Polydisperse and blends

The SEC data for the polydisperse materials and their corresponding blends, was analysed in a similar fashion to the data of the monodisperse polymers and

blends. The MMDs results of the polydisperse materials are presented in Figure 4.3 (a) and (b) as processed using our purposed-built MatLab sequence. The data is also displayed in the form of Tables 4.3 and 4.4, where the information of molar mass averages, PDI and composition is summarised.

Table 4.3: Molar mass details for polydisperse materials used in this study.

Code	System	Description	$\overline{M}_n$ [g/mol]	$\overline{M}_w$ [g/mol]	PDI
R	Atactic Polydisperse	Dow Chemical PS680E	92,471	222,700	2.41
BX		Sigma Aldrich	1,452	47,799	32.91
BY		Sigma Aldrich	158,580	339,240	2.14

Table 4.4: Molar mass details for bimodal blends of polydisperse materials used in this study.

Code	System	Blending composition	$\overline{M}_n$ [g/mol]	$\overline{M}_w$ [g/mol]	PDI
CA_{sb}	*Solution blended (THF)*: Polydisperse blends	95%BX, 5%BY	2,537	79,189	31.21
CB_{sb}		90%BX, 10%BY	2,572	86,337	33.56
CC_{sb}		80%BX, 20%BY	2,429	115,410	47.51
CD_{sb}		50%BX, 50%BY	2,877	186,630	64.86
CA_{mm}	*Melt-mixed (extruder)*: Polydisperse blends	95%BX, 5%BY	1,302	52,187	40.07
CB_{mm}		90%BX, 10%BY	1,297	61,468	47.40
CC_{mm}		80%BX, 20%BY	1,407	77,247	54.91
CD_{mm}		50%BX, 50%BY	2,165	167,640	77.43

In Figure 4.3 (a), the data for polydisperse materials BX, BY and R already shows some fundamental differences compared to the monodisperse materials. To start with the breath of the distributions are broader, spanning over a wider range of molar mass. Although materials R and BY only show a single peak, it is possible to note that the extent of the lower molar mass tail spreads over a range of molecular weights. These observations are consistent with the $\overline{M}_n$ and $\overline{M}_w$ averages reported in Table 4.3 that are clearly susceptible to the lower and higher molar mass ends of the distribution, followed by a corresponding increase in the PDI. In the case of material BX the distribution appears to be bimodal,

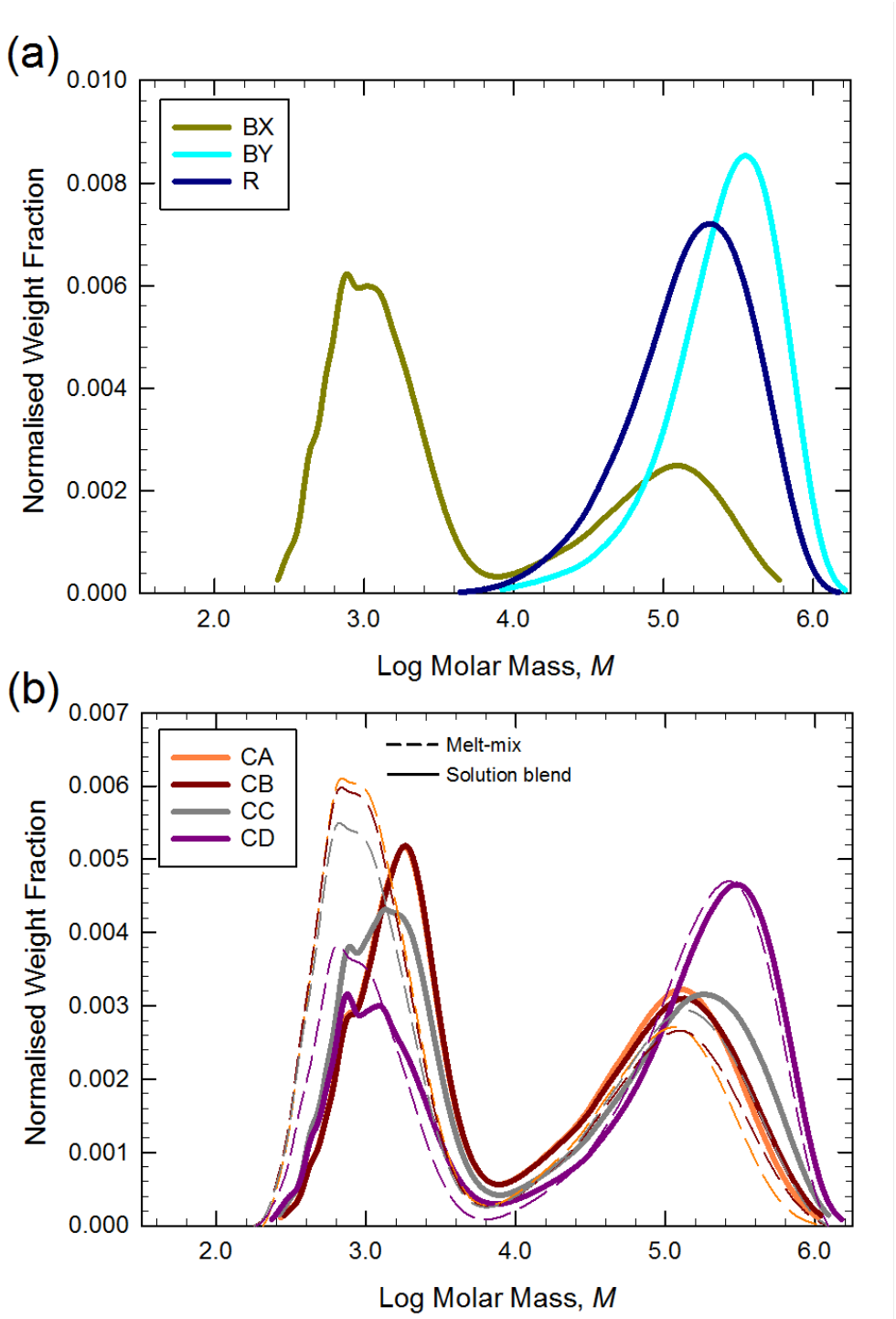


Figure 4.3: Molar mass distributions of (a) polydisperse materials and (b) their corresponding *mm*-blends and *sb*-blends obtained using MatLab.

with clear peaks at the lower and higher ends of the molar mass spectrum. This material was quoted to have a $\overline{M}_w = 35\,\text{kg/mol}$ by the manufacturer. Yet, as reported from our GPC data, the value seems to be closer to $\overline{M}_w = 48\,\text{kg/mol}$. The lower molar mass fractions of material BX are clearly reflected in the $\overline{M}_n$ of this material, as this approaches extremely low values, as far as 1.4 kg/mol. This yields extremely high levels of polydispersity in the range of PDI∼33.

The combination of the inherently bimodal polymer BX, with the high molar mass polydisperse system BY results in some very interesting blends. In all the blends -regardless of their mixing method- the presence of material BX is manifested in the fundamentally low values of $\overline{M}_n$, in the range of 1.3-2.9 kg/mol. As the wt% content of BY in the blend is increased, a corresponding rise in the PDI is perceived in all cases. One peculiarity that can be observed, is the presence of lower molar mass fractions in the *mm*-blends compared to the blends produced through solution blending. In Figure 4.3 (b), this appears as a noticeable shift to the left in the melt-mixed distributions over the solution blended ones. In the data in Table 4.4, this is revealed in the almost doubled values in $\overline{M}_n$. This is more pronounced for blends CA-CC, but blend CD appears to have molar mass averages in closer agreement between the two blending methods. It is important to note that although it would have been beneficial to measure any residual solvent in the solution blended samples using infrared spectroscopy, the evidence of the SEC along with carefully oven drying at constant mass suggest no solvent was found.

In Table 4.5, the data between the *sb*-blends and the *mm*-blends is compared as a function of the percentage difference of the $\overline{M}_n$, and $\overline{M}_w$ averages as calculated through expression 4.1.

Table 4.5: Δ% difference between solution blended and melt mixed polydisperse blends.

Code	Δ_n [%]	Δ_w [%]
CA	64.33	41.11
CB	65.94	33.65
CC	53.31	39.62
CD	22.20	10.72

A bigger difference is seen in $\overline{M}_n$, compared to $\overline{M}_w$ for all blends. This is a consequence of the lower mass fractions that are present in the melt-mixed blends that drop the average and increase the disagreement between the molar mass data between the two blending methods. As the content of material BY is increased, the differences in $\overline{M}_w$ between the two blending techniques appear to narrow. The height of the second peak increases as more of the weight percentage (wt%) of constituent material BY is added, as longer molecules are being added into the mixtures. In Figure 4.3 (b), it is possible to see that the peaks at the higher molar mass end for blends CD_{sb} and CD_{mm} almost overlap, a behaviour which is not observed in the rest of the blends. In the lower molecular weight samples (CA and CB), the amount of higher molecular weight fractions seems to be decreased in the *mm* specimens when compared to the samples obtained by *sb*. The position of the peaks, does however correspond to a clear shadowing of the higher molar mass tail of component BY. Additionally, if one is to closely analyse the distribution of material BX and compare it against those of the melt-mixed samples, it would appear as if polymer BX was missing some lower molar mass fractions compared to the distributions reported for the *mm*-blends.

It has been argued that the standard relations used in universal calibration of SEC methods (i.e. Mark-Houwink equation), between molecular weight and intrinsic viscosity tend to break down at low molecular weight [103]. The inaccuracy of this equation in the low molar mass range has been previously reported and confirmed with refractive index studies [104]. The main issue is that at low molecular weights, particularly for PS, some of the properties over which SEC is dependent (e.g. refractive index and intrinsic viscosities), do not remain constant. In supporting studies [103; 105], it was found that using the radius of gyration is a better measure of the elution behaviour than the hydrodynamic volume ($[\eta]M$) for analysing SEC, but room for improvement was still required for monitoring exclusion of relatively short molecules (~200-1000 g/mol). The equipment used in this study was calibrated using PS standards and the Mark-Houwink equation to determine universal viscosity and molecular weight relationships, yet these measurements were compared against absolute molecular weight data obtained from light scattering detectors, which gives confidence that the molar mass differences between the the $mm-$blends and material BX are real and consistent with the

SEC's detection boundaries. To explain the nature of these discrepancies, other contributing issues such as the effects of the blending processing method have to be more closely analysed (as will be done in the next section).

4.2.3 Molar mass simulations

The SEC data for the constituent materials (i.e. monodisperse and polydisperse) was used to perform blending simulations using our purposed-built MatLab code. The code offers the possibility of generating artificial molar mass distributions by combining the distributions of the component materials at specific weight blending ratios. The subscript $-th$, will be used to identify the molar mass averages associated with this theoretical ideal blend. Complementary to the calculation of $\overline{M}_n$ and $\overline{M}_w$ averages, it was decided to also procure the information for the molar mass averages of the low, $p1$, and high, $p2$ molar mass peaks found at the ends of the blends distributions. These averages are termed $\overline{M}_{n,p1}$ and $\overline{M}_{w,p1}$, for the low molar mass peak, and $\overline{M}_{n,p2}$ and $\overline{M}_{w,p2}$ to refer to the higher end. In the case of blend BL, a third notation $p3$, is used to refer to the peak that arises from the contribution of the higher molar mass component BH.

4.2.3.1 Monodisperse blends

Artificially generated MMDs of the monodisperse blends BI-BL were rendered by combining constituent materials BF, BG and BH in the weight blending ratios previously described (Table 4.2). To report the values for the individual peaks of the bimodal blend distributions in the experimental and simulated data, it was required to establish some trimming limits that laid at the valley (i.e. closer to the baseline) between the two peaks. This threshold molar mass value used to define the start and end points of the bimodal peaks is referred to as M_{valley}. As it has been established in the previous chapter (section 3.2.1), the arbitrary determination of the averaging trimming limits has an effect on the reported $\overline{M}_{n,p1}$, $\overline{M}_{w,p1}$, $\overline{M}_{n,p2}$, $\overline{M}_{w,p2}$ and $\overline{M}_{n,p3}$ and $\overline{M}_{w,p3}$. To evaluate the impact of defining M_{valley}, it was decided to report the differences between three specific values of M_{valley}, arbitrarily defined at $\log M = 5.15, 5.20, 5.25$, for blends BI-BK

and $\log M = 5.35, 5.40, 5.45$ for blend BL and identified with roman notation (I, II and III). These limits were used for the computation of $\overline{M}_{n,p1}$, $\overline{M}_{w,p1}$, $\overline{M}_{n,p2}$, $\overline{M}_{w,p2}$, $\overline{M}_{n,p3}$ and $\overline{M}_{w,p3}$ and are shown for reference in Figure 4.4.

The computed molar mass averages for the experimental and theoretical data are presented in Tables 4.6 and 4.7. Following the format established before, the differences between the experimental and theoretical calculated averages are tabulated, and are presented in Figure 4.5.

Table 4.6: Experimental and predicted, *th*, molar mass averages of monodisperse blends BI, BJ, BK, and constituents BF and BG.

Code	$\overline{M}_n$ [g/mol]	$\overline{M}_w$ [g/mol]	$\overline{M}_{n,p1}$ [g/mol]	$\overline{M}_{w,p1}$ [g/mol]	$\overline{M}_{n,p2}$ [g/mol]	$\overline{M}_{w,p2}$ [g/mol]
BF	86,113	93,378	-	-	-	-
BI	93,201	117,830	86,188	97,241	281,550	293,570
BI_{th}	92,192	111,030	85,914	92,902	260,490	271,270
BJ	96,625	133,900	83,077	95,005	279,930	289,850
BJ_{th}	99,169	128,680	85,992	93,027	263,810	273,870
BK	134,030	192,150	88,782	97,721	279,450	288,450
BK_{th}	128,300	181,640	86,399	93,677	265,950	275,520
BG	251,330	269,910	-	-	-	-

Table 4.7: Experimental and predicted, *th*, molar mass averages of monodisperse blend BL, and constituents BF and BH.

Code	$\overline{M}_n$ [g/mol]	$\overline{M}_w$ [g/mol]	$\overline{M}_{n,p1}$ [g/mol]	$\overline{M}_{w,p1}$ [g/mol]	$\overline{M}_{n,p3}$ [g/mol]	$\overline{M}_{w,p3}$ [g/mol]
BF	86,113	93,378	-	-	-	-
BL	110,830	191,210	86,545	98,460	549,750	578,330
BL_{th}	102,950	182,760	86,433	94,102	529,820	556,520
BH	469,960	540,270	-	-	-	-

As can be seen, the differences between the experimentally measured and the predicted molar mass averages are extremely small (in the order of 0.13% to 7.9%).

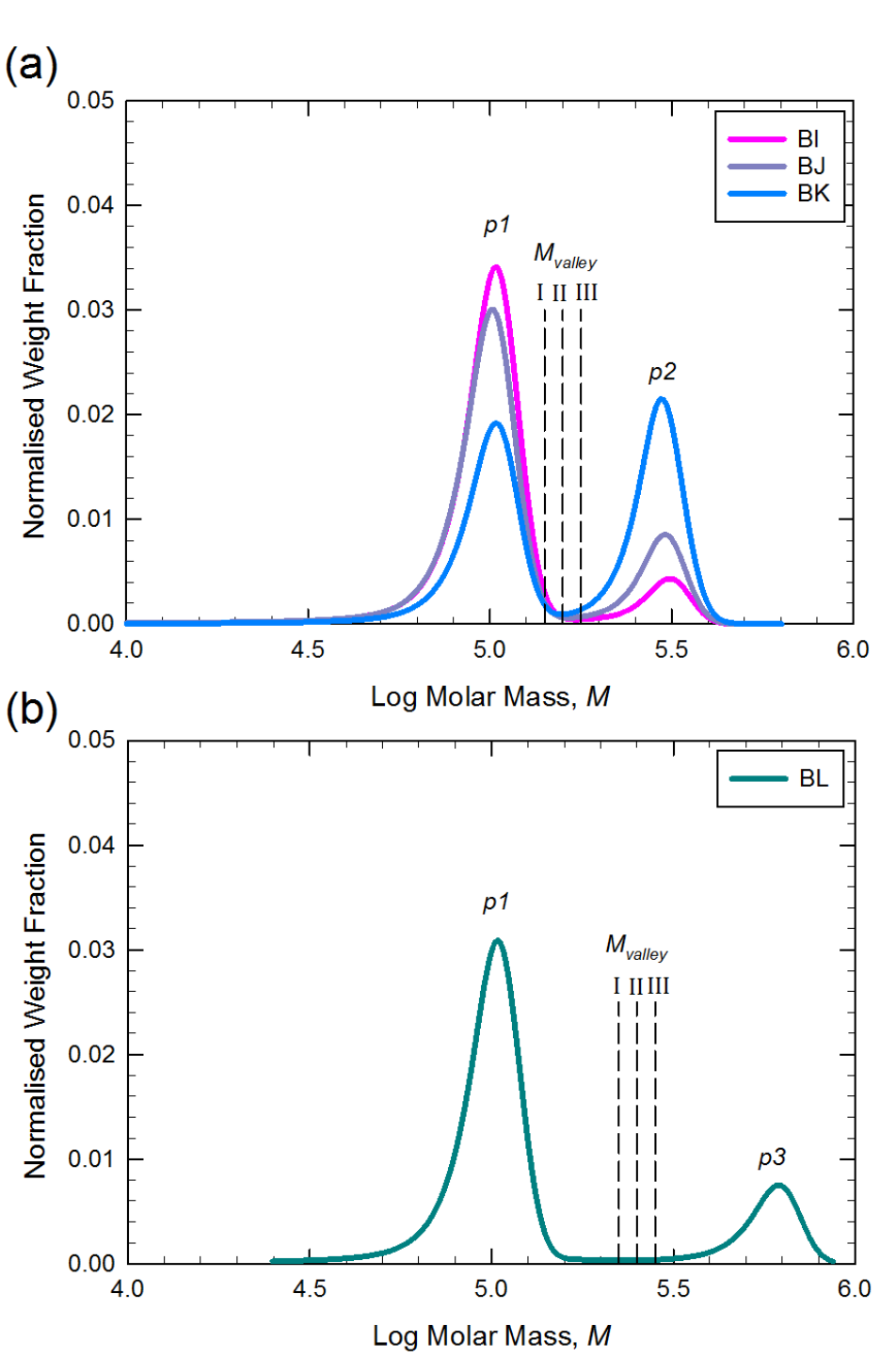


Figure 4.4: Trimming limits I, II , III for the computation of $\overline{M}_{n,p1}$, $\overline{M}_{w,p1}$, $\overline{M}_{n,p2}$, $\overline{M}_{w,p2}$, $\overline{M}_{n,p3}$, and $\overline{M}_{w,p3}$ in the bimodal monodisperse blends BI, BJ, BK, and BL.

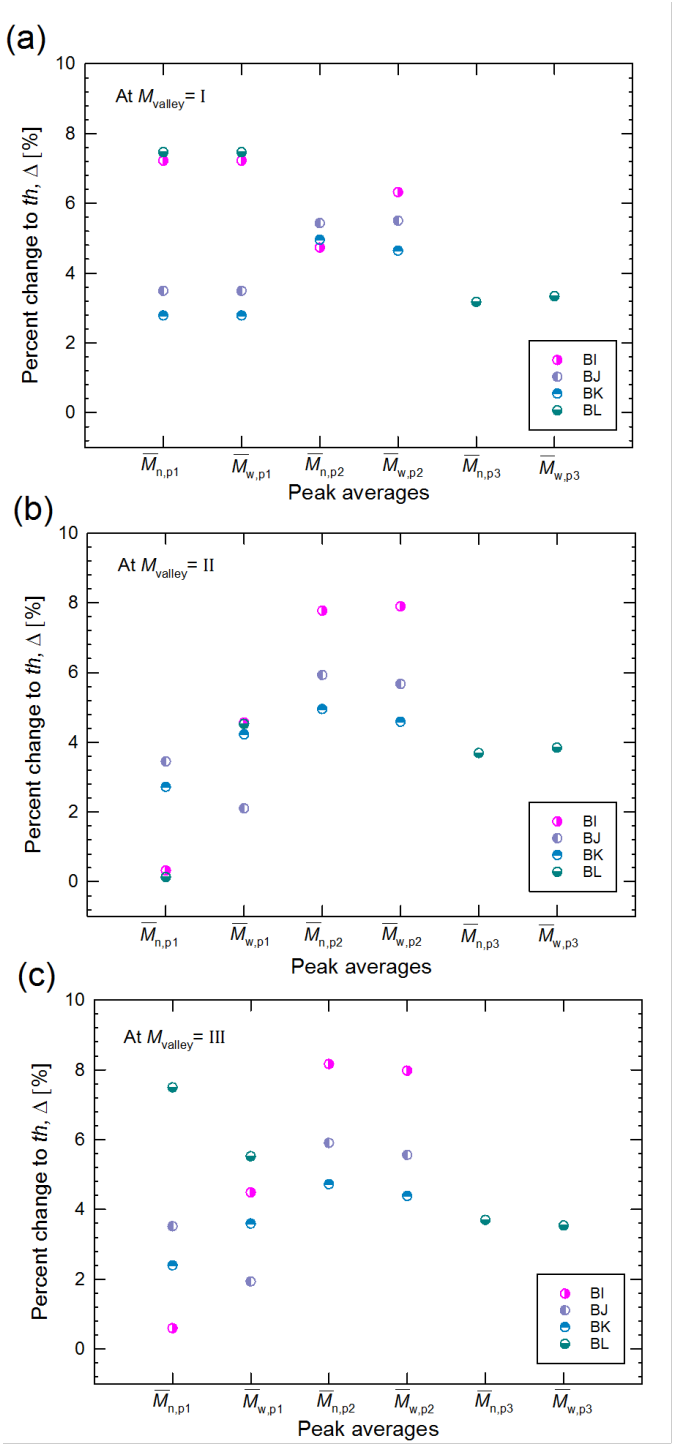


Figure 4.5: $\Delta\%$ between the simulated blends (-*th*) and the experimental data when defining M_{peak} at (a) $\log M = 5.15$ / $\log M = 5.35$, (b) $\log M = 5.20$ / $\log M = 5.40$, and (c) $\log M = 5.25$ / $\log M = 5.45$.

In all, an overall good agreement is observed between the averages calculated in the SEC experimental distributions and those obtained by artificial simulation. The slightly higher values of the experimental blends compared to theory could be explained by some losses during the solution blending process. One additional observation is the very close values obtained for $\overline{M}_{n,p}$ and $\overline{M}_{w,p}$, which is a result of low polydispersity in these blends. It can be concluded that the blending of these monodisperse blends (obtained by solution blending [96]), is very effective at producting what is expected by an ideal blending of the monodisperse material constituents.

4.2.3.2 Polydisperse blends

When determining the 'ideal' blending distributions using the data for the polydisperse blends, the results are very different. To begin with, the SEC data of the polydisperse blends confirmed the presence of smaller molar mass fractions in the melt-mixed samples that appeared to be absent in the solution-blended materials. This contribution is also reflected in the reported lower $\overline{M}_n$ and $\overline{M}_w$ values in Table 4.4. In addition, the analysis of the peak molar mass averages in the polydisperse blends is seen to be susceptible to the definition of M_{valley}. $\overline{M}_{n,p}$ and $\overline{M}_{w,p}$ averages are seen to increase or decrease as a function of the trimming limits (i.e. the value of M_{valley}); and due to the high levels of polydispersity in these materials, even small contributions of a representative sample of molar mass fractions (i.e. low or high molecular weights) can lead to enhanced differences in the averaging process. This susceptibility of trimming limits in the manipulation of SEC data is a recognised and ongoing debate [97], as it can easily bias and affect the quality of chromatographic analyses.

Following the procedure used in the monodisperse materials, three arbitrary values of M_{valley} were defined to quantify the differences between the experimental data and the simulated prediction. The trimming points for the definition of M_{valley} values I, II and III, were set at $\log M = 3.8, 3.9, 4$, as shown in Figure 4.6.

It is possible to note that a wide molar mass range is considered for analysis in the melt-mixed specimens compared to the solution blended samples as the distributions of the *mm*-blends shift slightly to the left. Since $\overline{M}_n$ is susceptible

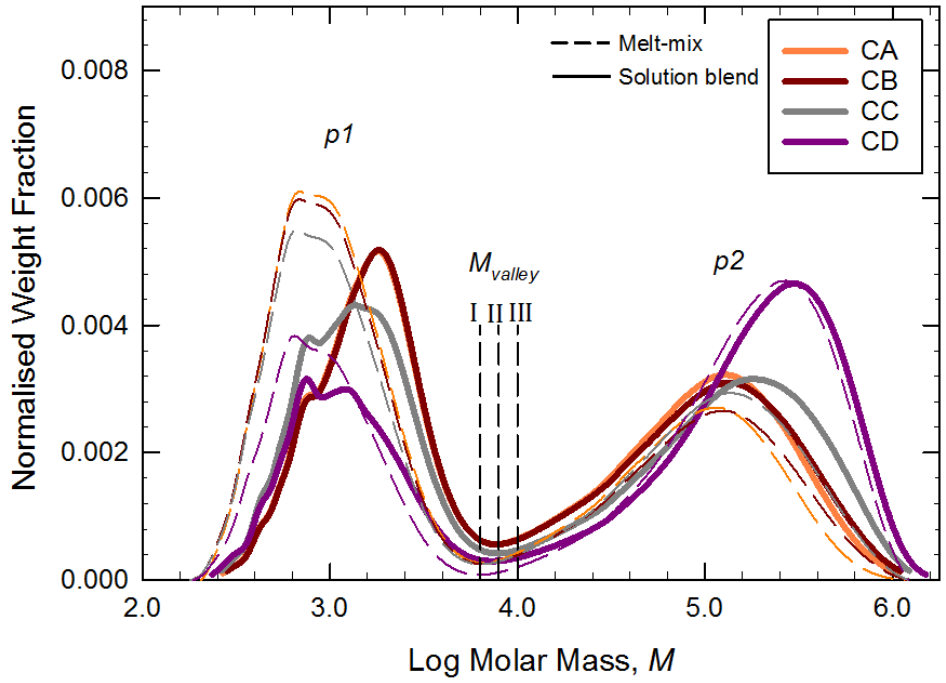


Figure 4.6: Trimming limits I, II, III for the computation of $\overline{M}_{n,p1}$, $\overline{M}_{w,p1}$, $\overline{M}_{n,p2}$ and $\overline{M}_{w,p2}$ in the bimodal polydisperse blends CA-CD.

to the number of fractions, rather than their weight, the $\overline{M}_n$ averages calculated for the *mm*-blends will yield lower values compared to those of the *sb*-specimens. In recognition of this issue, the value of M_{valley} was fixed at the valley at which all the *sb*- and *mm*-curves could meet, $\sim \log M = 3.8$, as presented in Figure 4.6.

The molar mass averages calculated for the blends and the artificially generated distributions are presented in Table 4.8. The corresponding differences between the experimental and theoretical averages for the melt-mixed and solution-blended materials are presented in Figure 4.7 (a)-(f).

When looking at the theoretical molar mass average data in Table 4.8, this is seen to exceed the averages $\overline{M}_n$ and $\overline{M}_w$, reported for the melt-mixed blends, while underestimating those of the solution blended samples. For the solution processed blends, $\overline{M}_n$ and $\overline{M}_w$ do appear to replicate more closely the theoretical values as the wt% of material BY is increased. The molar mass averages for

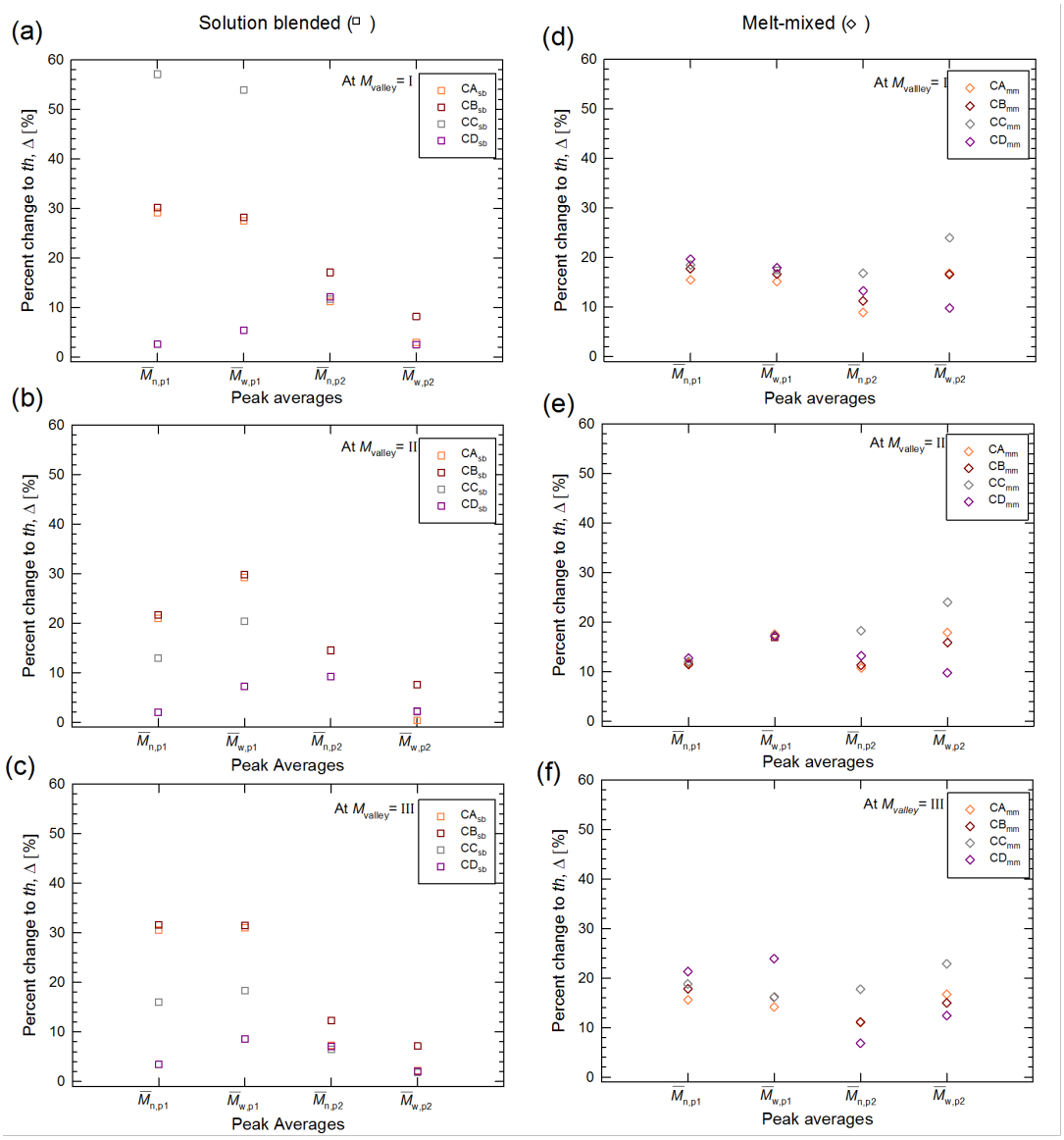


Figure 4.7: $\Delta\%$ between the simulated blends (-*th*) and the experimental data when defining M_{peak} at (a)/(d) $\log M = 3.8$, (b)/(e) $\log M = 3.9$, (c)/(f) $\log M = 4.0$, for the solution blended (squares) and melt-mixed materials (diamonds), respectively.

Table 4.8: Molar mass averages of *sb*, *mm*, and *th* (predicted) MMDs of polydisperse blends and constituents BX and BY.

Code	$\overline{M}_n$ [g/mol]	$\overline{M}_w$ [g/mol]	$\overline{M}_{n,p1}$ [g/mol]	$\overline{M}_{w,p1}$ [g/mol]	$\overline{M}_{n,p2}$ [g/mol]	$\overline{M}_{w,p2}$ [g/mol]
BX	1,452	47,799	932	1,387	50,463	128,520
CA_{mm}	1,302	52,187	798	1,191	50,676	130,840
CA_{sb}	2,537	79,189	1,251	1,829	49,542	150,430
CA_{th}	1,529	62,304	933	1,387	55,413	154,990
CB_{mm}	1,297	61,468	780	1,173	53,794	150,360
CB_{sb}	2,572	86,337	1,264	1,842	50,761	163,700
CB_{th}	1,613	76,878	933	1,387	60,229	177,630
CC_{mm}	1,407	77,247	775	1,164	59,167	168,240
CC_{sb}	2,429	115,410	1,677	2,409	62,305	208,840
CC_{th}	1,812	106,030	933	1,387	70,047	214,130
CD_{mm}	2,165	167,640	766	1,158	88,476	256,420
CD_{sb}	2,877	186,630	957	1,464	89,547	275,810
CD_{th}	2,880	193,480	933	1,387	101,070	282,870
BY	158,580	339,240	-	-	-	-

the individual peaks are more difficult to analyse, as these are susceptible to the definition of a trimming threshold value, M_{valley}, as discussed earlier. In any case, one clear trend found in Table 4.8 is the inherently higher $\overline{M}_{w,p}$ values reported for the *sb*-blends. This is a clear confirmation of the presence of higher molar mass fractions that are either absent or reduced in number in the blends obtained by melt mixing. To support the discussion of the differences found in the molar mass averages between the two blending methods, an additional Table 4.9 reports on the Δ between the melt-mixed and the solution blended molar mass data.

From Table 4.9 it is possible to see that $\overline{M}_{n,p1}$ is reported to be 22%-44% higher in the solution blended samples, while $\overline{M}_{n,p2}$ is 2%-6% lower when compared to the melt-mixed blends. These results clearly evidence the effect of choosing a fixed M_{valley} value that can discriminate the quantity of lower molar mass fractions that are present in either one of the analysed peaks in a bimodal molar mass distribution. As a result, the MMDs section containing the largest amount

Table 4.9: Δ difference in the peak molar mass averages between the melt-mixed and solution blended materials at $M_{valley} = I$.

Code	$\Delta\overline{M}_{n,p1}$ [%]	$\Delta\overline{M}_{w,p1}$ [%]	$\Delta\overline{M}_{n,p2}$ [%]	$\Delta\overline{M}_{w,p2}$ [%]
CA	44.17	42.25	-2.26	13.93
CB	47.31	44.39	-5.80	8.49
CC	73.62	69.71	5.17	21.53
CD	22.20	23.12	1.20	7.29

of lower molar mass species will produce a lower $\overline{M}_n$, where the averaging is susceptible to the presence of smaller molecules. It can be seen, though that for blend CD, where the molar mass distributions of both blending methods appear to be closer in shape, the reported averages are more in agreement (Δ =1.2% and 7.3%, for $\overline{M}_{n,p2}$ and $\overline{M}_{w,p2}$, respectively).

The observed over and under estimation of the molar mass averages in the *mm* and *sb* blends, can be explained by consideration of the side effects that can originate from different polymer blending methods.

Melt-mixing is perhaps the most accessible and commercially-viable approach used in large industrial polymer production, as this can be easily performed during the hopper feeding of polymer pellets in injection or extrusion processes. All that is required is a mere scaling calculation of the weighted fractions (wt%) of the constituents materials for the desired polymer formulation. In melt-mixing, the main risk for the indirect modification of the polymer properties is degradation. Some polymers are known to degrade when subjected to continuous thermal cycles, thus breaking molecules and lowering the molecular weight of the system [106]. Extensive work has been done in characterising the thermal degradation of polystyrene [107; 108; 109]. In their study of thermal degradation of anionic polystyrene, Costa *et al.* [110] looked at the degradation mechanism of PS originated by the reaction of chain ends. By use of a thermobalance coupled to a gas chromatograph they identified the degradation products of monodisperse PS. Their study concluded that at an early degradation stage, the concentration of unsaturated chain ends increases in proportion to the amount of vaporised toluene. As the degradation proceeds, these unsaturated chain ends downgrade by scission

and further evaporation into dimeric, trimeric, fragments. Although the authors showed that, at the initial degradation stages the evolution of toluene is independent of molecular weight, lower molar mass polymers have a larger number of chain ends, which could speed up the degradation process further since these are prone to become unsaturated chain sites. It is worth highlighting that the quoted sensitivity of the equipment was of 0%-1%, and apparently no traces of monomers which could be present in the polymers could be detected when degrading PS below 250 °C. This is an interesting remark, since Costa *et al.*'s smaller PS sample had a quoted $\overline{M}_n = 4000\,\mathrm{g/mol}$ compared to the $\overline{M}_{n,p1} = 766\,\mathrm{g/mol}$ seen in some of our *mm*-blends. The importance of this observation is that previous degradation studies in PS have mainly focused in the analysis of monodisperse samples with molecules in the order of ∼1000 g/mol. Nevertheless relative comparison studies in highly polydisperse with some amount of molar mass fractions in the range of 100 g/mol are fundamentally non-existent. Hence the observed degradation of such small molecules in our polydisperse blends at times as short as 15min for 200 °C could be a result of accelerated unsaturated chain end formation. In this study a potential measure to reduce such degradation would be to modify the mixing process, either by reducing the speed of the rotating screws, along with using a lower temperature and shorter mixing times.

Solution blending is a technique preferentially used when different particle sizes of the constituent materials can lead to segregation. This method involves diluting the two polymer systems in a solvent to get them to blend well in order to make a homogeneous product. Although more time consuming, solution blending tends to be the preferred choice for testing new experimental formulations, particularly for partially miscible and immiscible materials (e.g. food molecules). In solution-blending the danger relies in the possible evaporation of oligomers and extremely short molecules during the filtration and precipitation stages, thus losing the low molecular weight tail of the polymer solution. Huang *et al.* [111] recognised this issue during the preparation of PS blends diluted in oligomers for their study on the extensional properties of concentrated solutions. In their study, the oligomers $\overline{M}_w = 1.9\,\mathrm{kg/mol}$, and the systems were representative of binary blends of monodisperse materials. In our studied materials, the situation is significantly more complex as the oligomers found in the blends can

be as small as 175 g/mol, as reported for the smaller fractions measured through GPC. In addition, the systems are seen as highly polydisperse (BXs PDI∼33), thus the risk of oligomer evaporation becomes highly likely.

The varying chemical and thermal properties associated with polymer blending have been identified before, and polymer scientists recognise the risks associated with polymer blending practice. Although a large number of studies have been devoted to the analysis in the immiscibility of blends of two different polymers [112; 113; 114], similar reviews for systems of blends of the same polymer with varying architecture or molar mass have remained elusive. The results provided by the SEC analysis conducted here were able to highlight the differences between the MMDs of the *mm*-blends and *sb*-blends; particularly at the lower molar mass end. These findings are of significant relevance to standard mixing practice, as they report on the consequences that can indirectly modify the character of a blend. Furthermore, because experimental studies of similar nature often involve blends of monodisperse materials, the real impact of polydispersity may not be fully accounted for, as is exposed in this study.

4.3 DSC data

As has been reported in section 3.3, variations of molar mass are reflected by a corresponding change in T_g. The overall premise is that as $\overline{M}_n$ decreases, T_g drops in a linear relationship with $1/\overline{M}_n$. In this section, the differences in T_g for the studied materials are analysed as a function of their measured DSC data. The reported data was extracted by taking the mid-point T_g value at the deflection slope. Three specimens were tested per material using the methodology described in section 3.3.

4.3.1 Monodisperse and blends

Representative heat flow versus temperature profiles for the monodisperse materials and their corresponding blends are presented in Figure 4.8 (a) and (b). The averaged results have been compiled in Table 4.10.

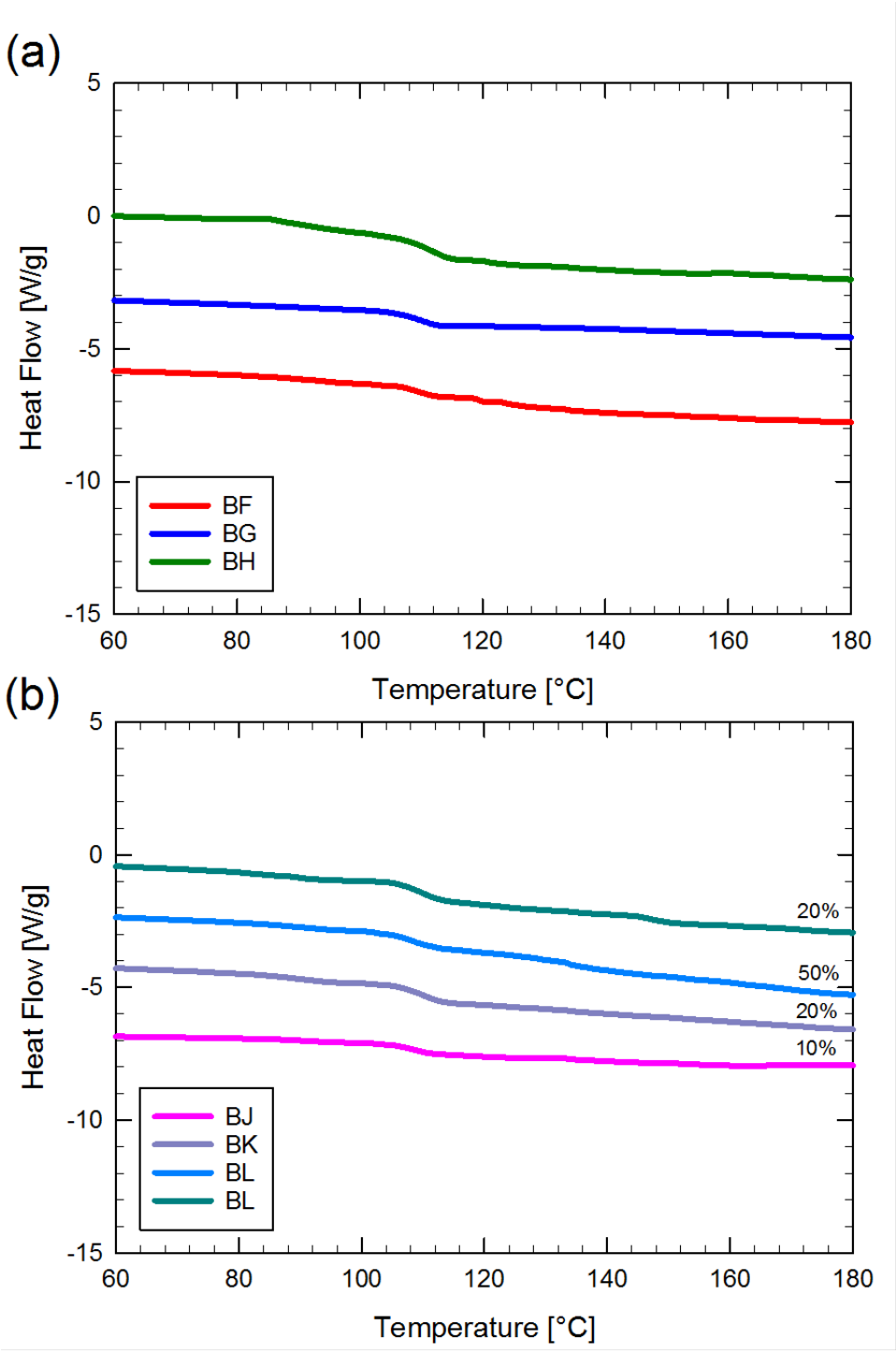


Figure 4.8: DSC results for (a) monodisperse materials and (b) their corresponding blends.

Table 4.10: DSC results for the monodisperse materials used in this study; mean value along with the standard error for three measurements is reported.

Code	Average T_g [°C]
BF	109.2±0.75
BG	110.4±1.05
BH	112.1±1.25
BI	108.9±0.92
BJ	109.3±0.97
BK	109.4±1.46
BL	110.9±1.26

The monodisperse materials (BF, BG and BH), show little variation in their reported T_g values, with only a difference of ±3 °C. T_g is seen to increase slightly as one shifts from the lower molar mass material (i.e. BF) to the higher molecular weight system (i.e. BH). When looking at the T_g data of the monodisperse blends in Table 4.10, it appears these follow this same trend, and as the wt% of the higher molar mass component is increased a corresponding rise in the reported T_g is observed. It is worth highlighting that in sufficiently entangled systems of similar sizes, the differences in T_g are expected to be very small. Peter *et al.* [115] state that in polymer systems with a mixture of different chain lengths, if these are seen to have a similar size ratio, the effect of changing T_g is small (e.g. the disparity in sizes, is low, $\delta = 0.8$). The effect of increasing a relative small fraction of concentrated shorter molecules is reflected only as changes in the relaxation times, favouring the glass transition of the pure, longer chains system. Yet, in the case of large size disparity, where the mixture is polarised into short and long molecules of roughly same weight fractions ($\delta \leq 0.65$), the shorter chains are seen to inhibit glass formation and a plasticising effect is found, thus depicting a decreased T_g. Other studies have documented similar increases in T_g when increasing the molar mass of homopolymer blends [116], in compliance with our reported observations.

4.3.2 Polydisperse and blends

The DSC temperature profiles for the polydisperse materials and their corresponding blends are presented in Figure 4.9 (a) and (b), and Table 4.11.

Table 4.11: DSC results for the polydisperse materials used in this study; mean value along with the standard error for three measurements is reported.

Code	Average T_g [°C]
R	108±0.62
BX	70.7±0.32
BY	109.3±3.12
CA_{mm}	66.4±1.84
CA_{sb}	83.7±0.52
CB_{mm}	68.1±3.30
CB_{sb}	83.9±2.40
CC_{mm}	68.5±2.30
CC_{sb}	85.5±6.21
CD_{mm}	87.2±1.33
CD_{sb}	91.7±8.69

The results for the monodisperse materials (BF-BH), monodisperse blends (BI-BL) and polydisperse systems (R,BY) were in close agreement to the reported T_g parameter for linear PS ∼106 °C [21]. Nevertheless, this was not observed for polydisperse material BX and polydisperse blends CA-CD, where the average value was between ∼60 °C and ∼90 °C. In [115], Peter *et al.* showed that T_g decreases linearly with increasing solvent concentration at least up to a 25% as covered by their experimental work. Stukalin *et al.* [117], studied the depression of T_g in polymer melts diluted by low molar mass species. They argued that the plasticising effect of shorter chains is reflected in corresponding reductions in T_g and a "softening" of the polymer matrix in the glass state. Their study involved the simulation of T_g shifts of PS diluted by flexible short oligomers (up to 20% mass of diluent), using a combination of the Adam-Gibbs entropy theory. They reported that the depression in T_g of the polymer mixture relative to the undiluted polymer is found to decrease as the size of the diluent or plasticiser agent increases, and to saturate as the size of the diluent becomes large enough.

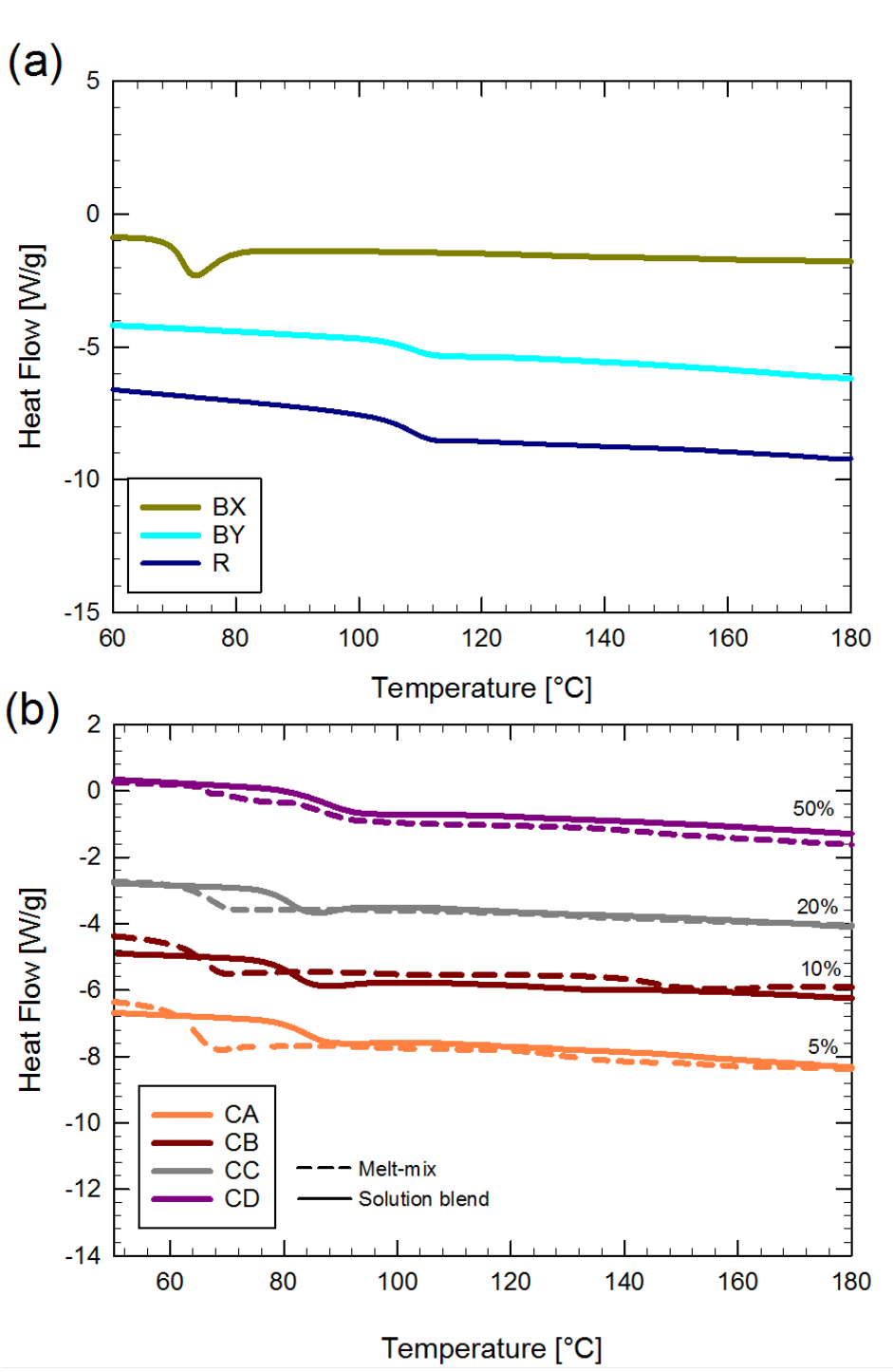


Figure 4.9: DSC results for (a) polydisperse materials and (b) their corresponding blends.

Thus, small oligomeric species (monomers) exert the most pronounced depression of T_g. The behaviour reported by Stukalin seems to be in good agreement with the observed T_g changes in our *mm* and *sb* blends, particularly in the melt-mixed samples where, as the amount of lower molar mass fractions decreases with an increased content of material BY, the T_g is seen to rise correspondingly.

Similarly, one would expect to see a change in T_g as a higher molar mass component is added in the blend, but the DSC plot is virtually the same across the polydisperse *sb*-blends CA-CC. This could be due to two reasons: a) some solvent residue, or b) tiny weight fractions, i.e. oligomers, in the distribution may be evaporated along with the solvent, hence modifying the composition of the blends. The latter, could also explain why the three blends share a similar behaviour, as they are all lacking the fundamental lower molar mass tail that could more precisely define their differences in blending compositions.

4.3.3 Tg simulations

The repercussions of the choice of blending method are also reflected in the DSC results. The data reported in Table 4.11 is supportive of the observations that the T_g in the *mm*-blends is lower than the *sb*-blends, and of material BX. The T_g difference in blending method is found to be ∼20 °C. This trend is true except for material CD, where the T_g in both samples is virtually the same. Following the SEC evidence, as the percentage of lower mass fractions (i.e. shorter molecules) is higher in the melt-mixed samples, it is not surprising to encounter a corresponding drop in T_g compared to the solution-blended materials.

Changes in the glass transition temperature of miscible blends, T_{gb}, can be modelled using empirical equations describing the molar mass dependence of T_g. Two models that have been suggested are the early model proposed by Wood [118], equation 4.2,

$$T_{gb} = w_1 T_{g1} + w_2 T_{g2} \tag{4.2}$$

And the more widely accepted Fox[119] equation 4.3.

$$\frac{1}{T_{gb}} = \frac{w_1}{T_{g1}} + \frac{w_2}{T_{g2}} \tag{4.3}$$

where T_{g1} and T_{g2} are the glass transition temperatures of the constituent materials, blended at weight fractions w_1 and w_2, and T_{gb}, is the glass transition temperature of the blend.

By using these relationships, it is possible to estimate corresponding apparent weight fractions, w_1' and w_2' in the blends. This approach is particularly useful in the present study, as it enables theoretical calculations for the expected changes in T_g as a result of blending. Following the methodology proposed by Kim and Burns [120], w_1' for Wood's equation can be defined by,

$$w_1' = \frac{T_{gb} - T_{g2}}{T_{g1} - T_{g2}} \tag{4.4}$$

While equation 4.5 is applicable to Fox's model,

$$w_1' = \frac{T_{g1}(T_{gb} - T_{g2})}{T_{gb}(T_{g1} - T_{g2})} \tag{4.5}$$

The calculation of the apparent weight fractions following Wood and Fox models are compared in Table 4.12 for the monodisperse blends, and Table 4.13 for the polydisperse blends. The theoretical value, th, was calculated by assuming equations 4.2, and 4.3 for the calculation of T_g.

The w fractions calculated for monodisperse blends BI and BJ appear to be in closer agreement to the prediction, nevertheless the gap between the predicted T_g and that experimentally measured appears to broaden with an increase in molar mass of the blend. Particularly in blend BL, it appears that the 20% weight contribution of component BH is sufficient to rise the T_g almost by two degrees compared to that of the dominant base material BF. It is worth highlighting that in monodisperse materials with such close temperature differences variations within 1 °C-2 °C appear almost unnoticeable in the DSC spectra (as per figure 4.8).

The w' calculations reported for the polydisperse blends follow a remarkable resemblance to the trend of the SEC and DSC results. When fitting the blends'

Table 4.12: Comparison of w_1' and w_2' as a function of T_g for the monodisperse blends using Wood and Fox equations.

Code	Wood		Fox	
	w_1'	w_2'	w_1'	w_2'
BI	0.917	0.083	0.916	0.084
BI_{th}	0.9	0.1	0.9	0.1
BJ	0.917	0.083	0.916	0.084
BJ_{th}	0.8	0.2	0.8	0.2
BK	0.833	0.167	0.832	0.168
BK_{th}	0.5	0.5	0.5	0.5
BL	0.414	0.586	0.407	0.593
BL_{th}	0.8	0.2	0.8	0.2

Table 4.13: Comparison of w_1' and w_2' as a function of T_g for the polydisperse blends using Wood and Fox equations.

Code	Wood		Fox	
	w_1'	w_2'	w_1'	w_2'
CA_{mm}	1.108	-0.108	1.175	-0.175
CA_{sb}	0.640	0.360	0.538	0.462
CA_{th}	0.95	0.05	0.95	0.05
CB_{mm}	1.062	-0.062	1.098	-0.098
CB_{sb}	0.634	0.366	0.532	0.468
CB_{th}	0.90	0.10	0.90	0.10
CC_{mm}	1.051	-0.051	1.081	-0.081
CC_{sb}	0.591	0.409	0.486	0.514
CC_{th}	0.80	0.20	0.80	0.20
CD_{mm}	0.545	0.455	0.440	0.560
CD_{sb}	0.423	0.577	0.325	0.675
CD_{th}	0.50	0.50	0.50	0.50

experimentally measured T_g values into the Wood and Fox's models, the latter appear to overpredict the amount of material BX that is present in the melt-mixed samples, while underpredicting the weight fraction of this in the $sb-$blends.

Since the T_g of the constituent materials (BX and BY) were seen to be in excess

of the T_g values obtained for the *mm* samples, not surprisingly, the apparent weight fractions calculated for blends CA-CC overestimate the amount of material BX, while yielding negative values for the contribution of material BY. Because Wood's and Fox's models are sensitive to the T_g of the constituent materials, one way to obtain better predictive accuracy will be to pass material BX through the extruder and then measure its T_g. The expectation is that because material BX is composed of many unentangled fractions (such as its subsequent melt-mixing blends), these will degrade, and hence the T_g measured using DSC will yield a lower value, more in compliance to those experimentally reported for the melt-mixed blends.

In the case of CD, the amount of material BY seems to exert a similar dominant contribution in the *mm* and *sb* blends evidenced by an agreement among the mixing techniques, and between these and the theory prediction. This also reflects an interesting trend, which suggests that not only does the molar mass of the constituent materials have an effect over the properties of the blend, but a wt% content limit of the higher molar mass component appears to exist, over which the behaviour of the blend is shifted to that of w_2. This transitioning behaviour in T_g and molecular weight appears to be repeatable, and has been extensively reported by various authors. In their fragility study, Santangelo and Roland [121], characterised monodisperse PS systems of varying molar mass (590 g/mol-929,000 g/mol) using DSC. Their results, when compared in the form of T_g vs. $\overline{M}_n$ plots (using the Kanig-Ueberreiter equation [122], equivalent to that of Fox and Flory [4]) showed that T_g increased linearly with increasing molecular weight up to a $\overline{M}_n$ value where it plateaus. This transitioning value was estimated to be M_e. When comparing the behaviour of PDMS to that of PS the authors attributed the differences on T_g to the flexibility of their respective chain species. Their argument is that in PDMS the ether linkage in the backbone confers nearly free rotation, evidenced in a corresponding low T_g. The configurational freedom conferred by chain ends has a small effect, and thus T_g is independent of molecular weight down to very low $\overline{M}_w$ values. In PS, on the contrary, the benzene ring act as a bulky side group that enhances intermolecular cooperativity, resulting in a relatively high T_g and one that is more molecular-weight dependent. The T_g of the polydisperse blends analysed in this study is observed to change in a

molecular-weight dependent manner, in agreement to Santangelo *et al*'s. observation [121].

More recently, other studies have tried to correlate the impact of miscibility in the recorded glass transition broadening of blends of two different polymer systems. Lau *et al.* [116] investigated the impact of concentration in the recorded T_g phase separation for blends of polystyrene and poly(α-methylstyrene) of varying molar mass. They evidenced that the broadening of T_g is both a result of concentration and solubility. When looking at the composition dependence of T_g through the use of various different equations derived for copolymer systems (including those of Wood and Flory), Lau concluded these were unable to fully describe the observed experimental calorimetry response. Chung and Kornfield [123] followed up on the idea that in miscible blends changes in component dynamics are manifested by anomalously broad glass transitions and complex viscoelastic properties. The authors used a combination of polyisoprene (PI) and poly-vinylethylene (PVE) blends to study the composition-dependency of the glass transition temperature, $T_g(\phi)$. Through the use of two-dimensional nuclear magnetic resonance (2D NMR), the authors concluded that as the content of the higher temperature component (high-T_g), PVE increased, the difference between the motion dynamics of the two blend species increased. Therefore the macroscopic T_g value of the blend becomes a result of the individual T_gs of the constituent materials and their inherent compositional dependences from each other.

Lodge and McLeish [29] (followed later by Lipson and Milner [124]) have extended these ideas of chain connectivity and self-composition experienced by the constituent materials' T_g within a blend to develop mathematical models for quantifying the impact of these effects in the glass transition of the resulting polymer blend. Their premise stands on the grounds of local dynamics as they argue that, depending on their surrounding environment, chains can experience different temperature dependencies. In general they discuss the fact that within a polymer solution the lower T_g component in the blend will be closer to the dynamics experienced by it in its pure melt, whereas the higher T_g component is likely to display a lower value, closer to the T_g of the blend average. This local heterogeneity is often referred to as "concentration fluctuations", which defines local regions spontaneously rich in component A or B [29]. This problem

of temperature and composition dependence in polymer blends goes far beyond the reported changes in T_g, and is even deemed responsible for the span of the relaxation spectra in the viscoelastic properties of polymer blends. This subsequently leads to the ultimate failure of the time-temperature superposition in some blends with large differences in their components' T_gs, as will be further discussed in section 6.4.2.

Lodge and McLeish propose that to evaluate the temperature dependence of two consituent materials within a blend, one must acknowledge the behaviour of the monomeric friction factor ζ for each component as this is expected to control the relaxation behaviour of the polymer. The authors define the length scale of ζ to be determined by the Kuhn length, l_K. The conformational relaxation of a Kuhn length is influenced by the concentration of monomers within a volume, $V \sim (l_K)^3$. The second assumption is that in a determined volume V centred on a monomer of polymer type A, there will be on average an excess of A monomers relative to the bulk concentration. Hence, due to chain connectivity, a monomer of polymer A will experience the interaction of a certain number of other A monomers in the vicinity [29]. Consequently a polymer A experiences on average an effective local concentration ϕ_{eff} defined by equation,

$$\phi_{eff} = \phi_s + (1 - \phi_s)\phi \tag{4.6}$$

where ϕ_s is the "self-concentration" determined from the volume occupied by a Kuhn length's worth of monomers, given by,

$$\phi_s = \frac{C_\infty M_0}{k\rho N_A V} \tag{4.7}$$

where C_∞ is the characteristic ratio, M_0 refers to the repeat unit molar mass, k is the number of backbone bonds per repeat unit, N_A is Avogadro's number, and ρ is density.

Lodge and McLeish cited the ϕ_s of PS to be 0.27 [29]. Although the model was initially envisioned for polymer blends of chemically different polymer systems with varying T_gs, due to the significant molar mass differences between materials BX and BY, these can be classified as two systems with inherently distinctive

relaxation timescales. The model is applied to our systems to verify whether the concepts of chain connectivity and self-concentration are capable of modelling the temperature dependence of the blends of two polymer with the same chemical structure, but significantly varying molar masses. Consequently, $\phi_s = 0.27$ will be used for both material BX and BY. The effective temperature of each component is calculated by assuming $T_g^{eff}(\phi) = T_g(\phi) \mid_{\phi=\phi_{eff}}$, as proposed by Lodge and McLeish, although the effective T_g is determined from the macroscopic $T_g(\phi)$, this is evaluated at ϕ_{eff} rathen than ϕ. To calculate T_g for a particular blend concentration one can simply follow Flory's expression (equation 4.3). A case study of this methodology for the blends of materials BX and BY is provided in Table 4.14.

Table 4.14: T_g^{eff} for materials BX and BY as a function of concentration, ϕ_{eff}.

ϕBX	ϕBY	ϕ_{eff}BX	ϕ_{eff}BY	T_g^{eff}BX	T_g^{eff}BY	T_g^{eff}blend
0	1	0.27	1	95.46	109.25	109.25
0.1	0.9	0.34	0.93	92.26	105.08	103.64
0.2	0.8	0.41	0.85	89.27	101.21	98.57
0.3	0.7	0.49	0.78	86.46	97.62	93.98
0.4	0.6	0.56	0.71	83.83	94.28	89.80
0.5	0.5	0.63	0.63	81.35	91.15	85.97
0.6	0.4	0.71	0.56	79.01	88.23	82.46
0.7	0.3	0.78	0.49	76.81	85.49	79.22
0.8	0.2	0.85	0.41	74.72	82.91	76.23
0.9	0.1	0.93	0.34	72.74	80.49	73.45
1	0	1	0.27	70.87	78.20	70.87

The data from Table 4.14 has been plotted along with the T_g data points obtained for the melt-mixed and solution blended samples in Figure 4.10.

The data for the solution blended samples is found to be lying above the T_g^{eff} prediction for material BY, while the data of the melt-mixed blends is located below the tracer calculated for material BX. This complies with the previous over and under predictions calculated using w in Wood and Flory's equations. Lodge's model demonstrates qualitatively that the temperature dependence of polymer blends is ruled by chain connectivity and self-concentration experienced by the constituent materials. This simple model, also highlights that the theoretical

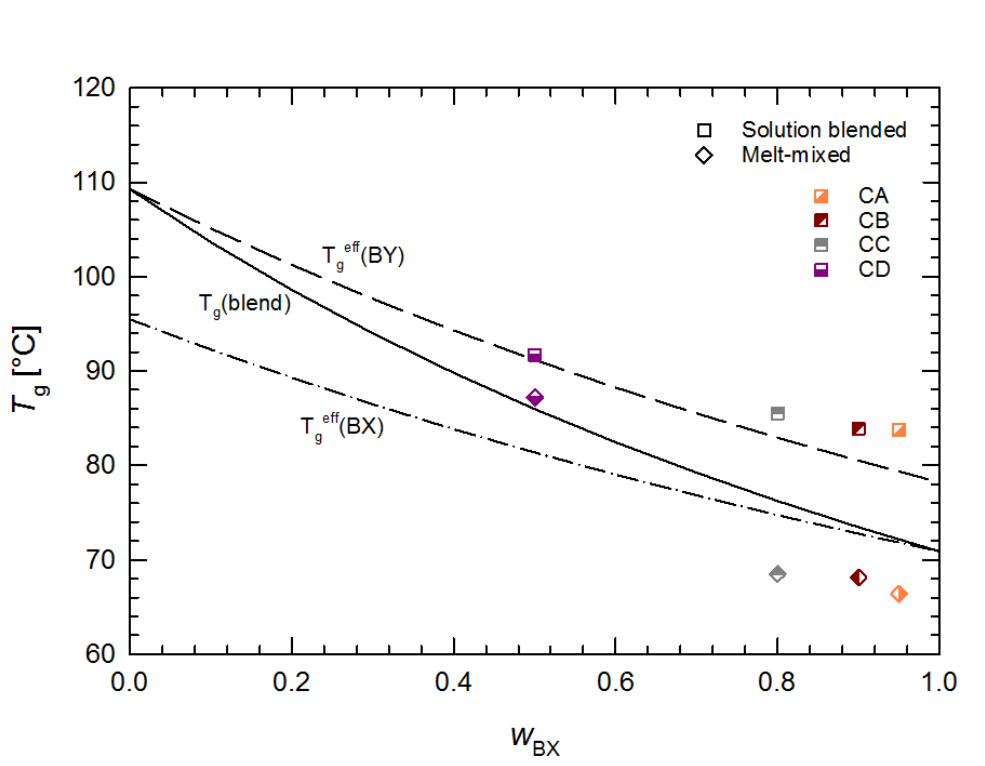


Figure 4.10: Effective glass transition temperatures for BX/BY blends using the Lodge and McLeish T_g^{eff} model [29]. Solution blends are shown in squares, while melt-mixed materials are shown as diamonds.

temperature dependency of the studied BX/BY blends is certainly in discrepancy with the experimental data of the melt-mixed and solution blended materials. For the studied set of materials, the analysis using Lodge and McLeish's model shows the over and under estimation also observed from the 'ideal' blending approached used to analyse the SEC data. Both models agree in that the composition of the obtained polydisperse blends deviate from the 'ideal' mixture. The validity of Lodge and McLeish approach, is that it interconnects the concept of T_g, with other dynamic characteristics, such as packing length, and chain connectivity that are seen have an impact in the rheological response of such materials. Furthermore, the model serves to explain that the deviation from such molar mass characteristics will have corresponding offsets in temperature dependence expected from mixing rules equations. Although the applicability of such mixing equations has been questioned [116; 124], the relevance of their contribution in

providing first hand quantitative insight to the complexity of chain relaxation dynamics in polymer blends has been demonstrated here.

4.4 Conclusions

The SEC and DSC data showed evidence of clear differences between blends produced with the same composition (and weight ratios), but different blending methods. Available mixing models for the analysis of molar mass distributions and calorimetry data were applied to produce simulations for comparison and validation of the experimental data. The models seemed to accurately describe the SEC and DSC behaviour of the monodisperse blends, with only minor deviations observed (<10%) from the theoretical prediction. Nevertheless, when applied to polydisperse blends a clear over and under estimation of the experimental data was observed for the melt-mixed and solution blended samples, respectively. These differences were attributed to the side-effects associated with the blending procedure of choice. It was determined that melt-mixing introduces the risk of polymer thermal degradation. This degradation process is seen to be accelerated by the presence of unsaturated chain ends that downgrade by chain scission into dimeric, trimeric fragments. In the case of the polydisperse blends analysed in this study, it seems that the broad lower molar mass tail of constituent material BX degraded during the mixing process, thus producing blends with an increased content of lower molar mass fractions. The blends produced by solution blending were seen to be prone to oligomer evaporation during the filtration and precipitation stages. This was reflected in a significant loss of the lower molar mass tail in the MMD of the analysed blends, congruent with higher reported molar mass averages and T_gs than their melt-mixed counterparts.

Although the models cited here have been extensively applied and validated in monodisperse materials and partially miscible copolymer blends, it would appear that little information is available for homopolymer blends of highly polydisperse systems of vastly different molar masses. The results of this study elucidate on the complexity of extrapolating these models when faced with blending side effects (e.g. thermal degradation or oligomeric evaporation), and provide a clear

picture for polymer manufacturers of how polymer blending procedures could inadvertently modify the SEC and T_g character of a resulting blend.

Chapter 5

Crazing Analysis

5.1 Prelude

In the preceding section, the breath in MMDs and the changes in T_g as a result of blending and polydispersity were discussed. This chapter aims at analysing how the molar mass and molar mass distribution are manifested in the craze initiation process in polystyrene. It is known that crazing proceeds failure in this material, and understanding how this process develops will undoubtedly serve polymer scientists fine tune the in-service endurance and performance for this type of glassy polymer. In this chapter, the use of a former piecewise linear model [20] that captures the influence of molecular weight in craze initiation for monodisperse materials is explored and discussed against novel experimental data obtained through isochronal three point creep bending tests. Where the model seems to fail, new theories of polymer physics will be used to lengthen the constitutive equations in order to make these suitable to predict the behaviour of more complex polydisperse systems. To enable data comparison a correction method was applied to account for observed differences in the radii of the testing rigs used by De Focatiis and those manufactured as part of this research. The correction procedure is detailed in Appendix B.

5.2 Crazing: monodisperse blends

To aid the reader in the interpretation of the results exposed in this chapter a summary for the $\overline{M}_n$ and $\overline{M}_w$ data obtained from SEC in chapter 4 is presented in Table 5.1. Full details for such materials can be referred to in pages 109 and 110.

Table 5.1: Molar mass details for bimodal blends of polydisperse materials used in this study.

Code	System	$\overline{M}_n$ [g/mol]	$\overline{M}_w$ [g/mol]
BF	Monodisperse-Low $\overline{M}_w$	86,113	93,378
BG	Monodisperse-Medium $\overline{M}_w$	251,330	269,910
BH	Monodisperse-High $\overline{M}_w$	469,960	540,270
BI	90% BF, 10% BG	93,201	117,830
BJ	80% BF, 20% BG	96,625	133,900
BK	50% BF, 50% BG	134,030	192,150
BL	80% BF, 20% BH	110,830	191,210
R	Polydisperse-Dow Chemical $\overline{M}_w$ 216 kDa	92,471	222,700
BX	Polydisperse-Sigma Aldrich $\overline{M}_w$ 35 kDa	1,452	47,799
BY	Polydisperse-Sigma Aldrich $\overline{M}_w$ 350 kDa	158,580	339,240
CA_{sb}	Solution blend: 95% BX, 5% BY	2,537	79,189
CB_{sb}	Solution blend: 90% BX, 10% BY	2,572	86,337
CC_{sb}	Solution blend: 80% BX, 20% BY	2,429	115,410
CD_{sb}	Solution blend: 50% BX, 50% BY	2,877	186,630
CA_{mm}	Melt-mix: 95% BX, 5% BY	1,302	52,187
CB_{mm}	Melt-mix: 90% BX, 10% BY	1,297	61,468
CC_{mm}	Melt-mix: 80% BX, 20% BY	1,407	77,247
CD_{mm}	Melt-mix: 50% BX, 50% BY	2,165	167,640

For the purpose this research, all the quoted errors in the experimental measurements refer to the standard error, σ_M. The formula for the standard error is provided in equation 5.1.

$$\sigma_M = \frac{S}{\sqrt{n}} \tag{5.1}$$

where S is the standard deviation (defined in chapter 3, equation 3.5), and n refers to the number of tests. Unlike the standard deviation, which measures the variability among a data set from the mean, the standard error provides a probabilistic measure of how far the sample mean of the data is likely to be from the true population mean. The standard error, then becomes a measure of the precision of the sample mean versus the true mean of the population. As the size of the sample data grows larger, the standard error is seen to decrease, in contrast to the standard deviation, which is highly susceptible to the dispersion of the data.

The monodisperse materials, along with their bimodal blends were tested in isochronal three point creep using the procedure outlined in section 3.5.2 at a range of different creep times: 10 s, 60 s, 300 s and 1800 s. The results of these tests are presented in Table 5.2.

Table 5.2: CIS of monodisperse materials, and their corresponding blends as a function of creep times.

Material	Creep time / No. of Tests							
	10 s [MPa]	No. Tests	60 s [MPa]	No. Tests	300 s [MPa]	No. Tests	1800 s [MPa]	No. Tests
BF	-	-	-	-	16.03±0.10	2	-	-
BG	28.63±1.37	3	23.05±1.01	3	22.16±1.32	11	18.0±1.37	2
BH	25.14±4.75	3	22.74±2.43	3	23.56±1.08	9	18.45±2.61	2
BI	-	-	17.50±1.0	2	17.57±0.51	7	-	-
BJ	27.29±0.63	2	25.04±0.63	2	21.98±1.67	8	-	-
BK	24.83±0.16	2	22.64± 0.60	2	20.44±1.19	10	-	-
BL	29.28±1.30	2	25.16±1.03	3	23.09±1.87	10	-	-

The results in Table 5.2 confirm a series of important phenomena related to crazing. First of all, as the creep time increases, the CIS decreases, which in accordance to Kramer [15], Donald [17] and De Focatiis [24]; as more time passes the material is able to form crazes at a reduced stress. The second observation to draw from this data, is the fact that there are only limited of representative

measurements for materials BF and BI. The reason for this was that it proved very difficult to promote the formation of crazes in these materials particularly since longer times resulted in fracture of the specimen. De Focatiis [20] reported similar difficulties in monodisperse materials with $\overline{M}_w = 68,000\,\mathrm{g/mol}$, stating that the reason for this failure has to do with the limited ability of the polymer to entangle itself. Following the remarks noted by Yang [37], polymers with $M < 2M_e$ are unable to sustain stable craze growth, and stability of the craze growth is seen to increase with molar mass. It is important to note that although the reported value for material BF was only based on two quantitatively measured specimens, the total number of tested specimens was 15. Unfortunately, it was very difficult to grow crazes in this material, and either no crazes were formed or the specimen failed before it could be inspected. Hence, the reported two measurements are representative of the threshold value of the applied stress at which all the other specimens were tested, and as a result provide enough qualitative evidence of was observed experimentally.

Even though blend BI only has 10% by weight of material BG, it is already seen to behave differently to its dominant constituent material BF, and it was indeed possible to obtain a crazing stress for the blend at 60 s, which was impossible with monodisperse material BF. The interest in this behaviour is that the combination of a highly entangled material (BG), with a moderately entangled one (BF) could exert some effect in the crazing behaviour of the blend even only when minor quantities are added. The third and final comment is seen in the reported value of CIS for the higher $\overline{M}_w$ blend, BL. It appears that BL yields a higher CIS value compared to any of the other blends and to its own constituent monodisperse material BH. If one was to follow the idea that higher molecular weight materials are able to dissipate loads better due to their associated capacity of achieving more entanglements, then surely the CIS of this material will be expected to be lower than blend BJ or BK. Nevertheless, this is not the trend observed in our results, where the CIS value is actually higher, particularly at shorter creep times. One thing to note though, is the greater scattering in the data of the higher molar mass materials (BL and BH) compared to the other systems, where perhaps the average trend, could simply be a consequence of the amount of limited data points.

To confirm the agreement between the time dependence observed in the monodisperse materials tested here and the data published in [20], the rate of change of crazing stress obtained by calculating the difference in the crazing stress over time, was plotted was plotted against molar mass. The data published by De Focatiis, and that for samples BG and BH are shown in conjunction with the disentanglement prediction and scission regression limits in Figure 5.1.

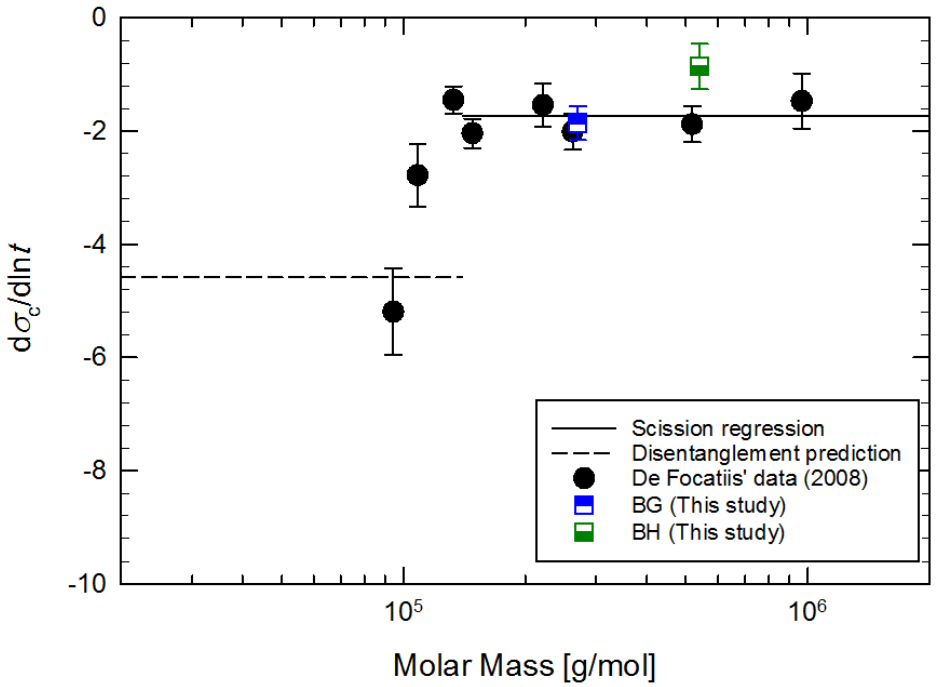


Figure 5.1: Rate of change of craze initiation stress with log time as a function of molar mass for materials BG and BH and for literature data from ref [20].

The results of Figure 5.1 effectively confirm that the data for materials BG and BH accurately lies in the region of chain length associated with chain scission crazing.

Due to the reported time-dependence in the formation of crazes, it was decided to focus our results solely in the creep time at $t = 300\,\mathrm{s}$, as it seems to be a sufficiently long time to allow for craze formation and be measured accurately, but short enough to be stable for all our experimental samples without causing failure. The 300 s crazing given data for monodisperse materials and their associated

blends is reported in Figures 5.2 for the combination of BF-BG materials, and 5.3 for the combination of BF-BH, as a function the fraction of higher molar mass component.

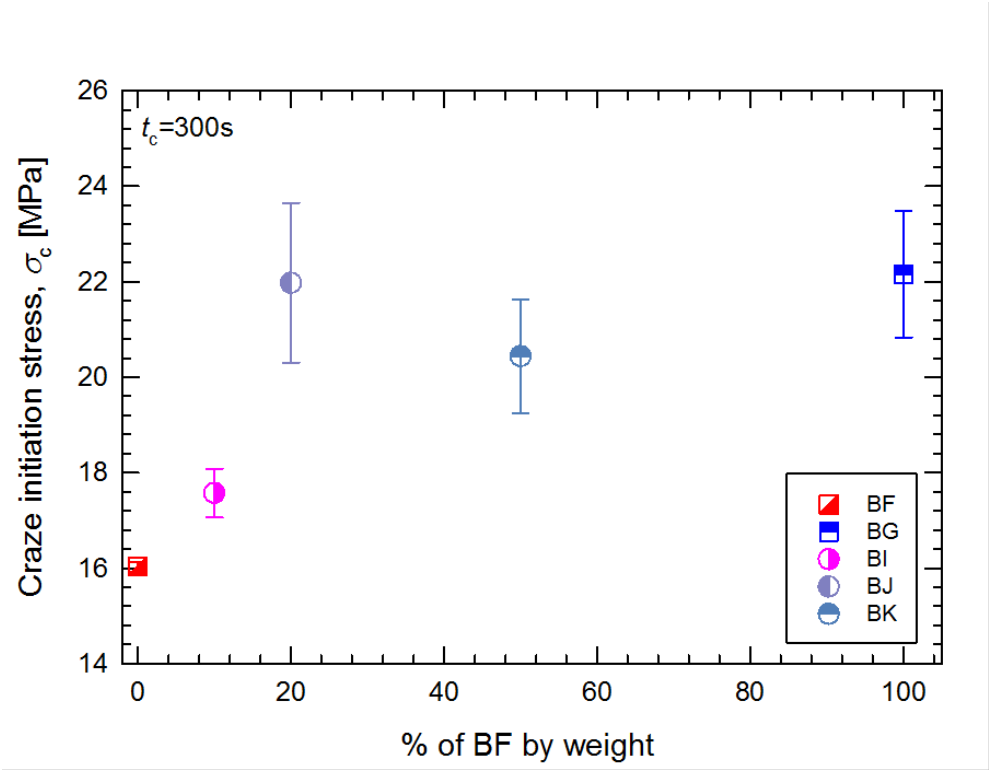


Figure 5.2: CIS of monodisperse materials BF and BG, and their corresponding blends as a function of % BG by weight.

The results in Figures 5.2 and 5.3 clearly reveal that as soon as even as little as 10% of the higher molar mass component is added into the lower molar mass monodisperse matrix, a noticeable increase in CIS is recorded. In systems of polymer blends, it has been reported that the composition and molecular weight of the constituent materials have a severe impact on the toughness properties of the blend. In ABS, the molecular weight and composition of the styrene-acrylonitrile (SAN) matrix is crucial in achieving mechanical endurance. It is known that if the SAN matrix is less than $2M_e$, no significant toughening takes place with rubber addition, as crazing is suppressed and the material becomes brittle [125].

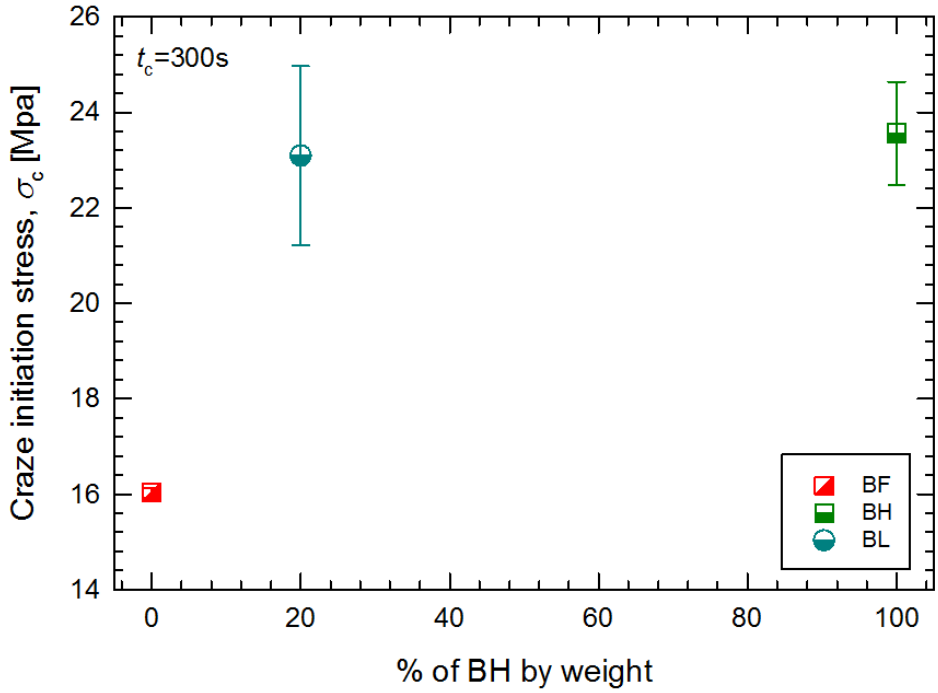


Figure 5.3: CIS of monodisperse materials BF and BH, and their corresponding blend as a function of % BH by weight.

Craze formation also was noted to become more stable with the addition of a higher molar mass material. Particularly in material BI compared to BF, a network of a couple of crazes was observed under the microscope, while in material BF craze formation was indeed very difficult to achieve with only a single craze being recorded in at least two measurements. The evident rise in CIS of the blends is attributed to the addition of a higher molar mass component. As the blend represents a mixture of different chain-lengths, and molar masses, the entanglement network is modified altering the crazing dynamics in relation to the larger molar mass species. Prior studies [126] have shown similar increases in tensile strength for a range of polystyrene acrylonitrile (PSAN) with increasing molar mass, and more recently the improvement from brittle-to-ductile transition of PS as a function of molar mass and blending [127]. Also apparent is that as the CIS in the blends increases, it reaches the value obtained in the pure higher molar

mass component with just a small fraction of this component. The interesting thing to note in this last argument, is to identify where exactly the blend reaches saturation. In other words, what is the exact formulation at which one can achieve the best properties of both constituent materials (i.e. good flow/melt properties, with sufficient endurance, and high CIS values)?

5.3 Blending model for CIS

From basic polymer theory [40], the molar mass distribution of a polymer can be treated as the addition of several weight fractions. If the macroscopic behavior of the polymer is considered to be the cumulative result of these fractions, it is then possible to generalize the fraction of a specific molar mass, M, through a molar mass fraction parameter, $\phi(M)$

$$\phi_\theta(M) = \frac{n(M)M^{\theta-1}}{\sum\limits_M n(M)M^{(\theta-1)}} \tag{5.2}$$

where $n(M)$ is the number of moles of species M, and θ refers to a power law molar mass parameter. In this context, $\theta = 1$ gives the number fraction and $\theta = 2$ gives the weight fraction. In such a view, this same principle can be extended to the calculation of specific molar mass averages. By considering a specific θ-fraction, a generalized expression for the θ-average can be computed using equation 5.3

$$\overline{M}_\theta = \frac{\sum\limits_M n(M)M^\theta}{\sum\limits_M n(M)M^{(\theta-1)}} = \sum_M \phi_\theta(M)M \tag{5.3}$$

where $\theta = 1$ and $\theta = 2$ give the well known $\overline{M}_n$ number-average molar mass and the weight-average molar mass $\overline{M}_w$, respectively.

Now that we have established some fundamental expressions that serve to

quantify the molar mass fractions that are found within a polymer distribution, it is required to attribute these with specific values that can describe their associated input in the CIS. By making use of the θ-parameter, and the recognition of De Focatiis' step-limiting crazing dynamics, it is possible to postulate a simple model for craze initiation. If one considers that each molar mass fraction within a blend, namely $\phi(M)$, contributes to the overall craze initiation stress, this contribution can be determined based on the experimental value of a measured $\sigma_c(M)$ at its monodisperse length scale. Following this assumption, the total crazing stress can therefore be predicted using equation 5.4

$$\sigma_{c,\theta} = \sum_{M} \phi_\theta(M)\sigma_c(M) \tag{5.4}$$

where ϕ_θ represents the associated fraction scaled to the θ-power, of constituent materials BF, BG and BH, and $\sigma_c(M)$ is simply their experimentally measured value. In this sense, the weight-predicted CIS of blend BI is found through: $\sigma_{c,\theta=2} = (0.9(BF) * 16.4MPa) + (0.1(BG) * 20.2MPa)$. The true value of equation 5.4 relies on the fact that the θ-parameter proposed in this study allows to gradually quantify the effect that higher molar mass species within the polymer distribution exert on the craze initiation stress. This is achieved by plausibly capturing specific molar mass moments within the distribution.

Similar studies have attempted at establishing a correlation between polymer physical properties and molecular weight averages. In their analysis of tensile properties in polystyrene Bersted and Anderson [46] gave a successful attempt at predicting the variability in tensile strength between the molar mass distributions of both monodisperse and polydisperse polystyrene systems. Their study was able to present accurate mechanical predictions for both sets of experimental data through the introduction of a failure property parameter, M_T. The main difference between our proposed expression and that suggested by Bersted and Anderson is that the θ-parameter represents a numerical constant that can be associated with all the molar mass fractions that constitute a polymer distribution. In Bersted and Anderson's study, the M_T parameter was pragmatically calculated

using the number average, which again, is restrictive by its sensibility to the lower molecular weight fractions of the distribution. In [128] Donald provided a similar study for a series of varying molecular weight blends of PS/PPO; she aimed at quantifying the changes in the craze extension ratio λ, as a function of the increase in the entanglement length, l_e and M_e due to blending. Donald's strategy was to use the rule of mixtures as a first approximation to associate the changes in the entanglement network as a function of the higher molar mass component (PPO, wt%, χ). Although the study did elucidated some important pheonmena that will be further discussed in the upcoming sections, the clear limitation of this model is in its lack of ability to be extrapolated to full MMDs, where λ is no longer a function of the additive contribution of two components, but a full spectrum of distinguishable molar mass fractions.

To test the validity of our proposed model, we first apply equation 5.4 to our bimodal monodisperse blends. The chosen methodology consisted in identifying the θ value that could give the best prediction for all blends (BI, BJ, BK, BL), and then multiply the corresponding ϕ_θ by its corresponding σ_c value in the monodisperse scale. To identify the value of θ, an optimisation was carried out on all the experimental data by minimising the root-mean-square (rms) error between our calculated (i.e. predicted) value of CIS and that obtained experimentally. Figure 5.4 presents the rms error as a function of θ.

As can be seen, the minimum error was found at $\theta = 3.78$. This θ value was applied to equation 5.4 to calculate our predicted values for $\sigma_{c,\theta}$. For comparison, values of $\theta = 1$ and $\theta = 2$ were also applied to the data. The results for these predictions are shown in Figure 5.5. The data has been plotted with the corresponding experimental error bars and error bars from the propagation of errors in the prediction. The latter are not readily visible, since the propagation of initial errors in the order or 0.50-4 MPa gets minimised when taking the rms error.

It is apparent that $\theta = 1$ (Figure 5.5(a)) and $\theta = 2$ (Figure 5.5(b)) considerably underpredict the experimentally measured craze initiation stresses of the blends (by 7%-26% and 5%-21%, respectively). A third plot showing the predicted CIS values for $\theta = 3.78$ is presented in 5.5(c), where the agreement between both sets of data is in the error order of 1%-7%.

It is impossible not to recall Deanin's study [2] on the elongation of PVC

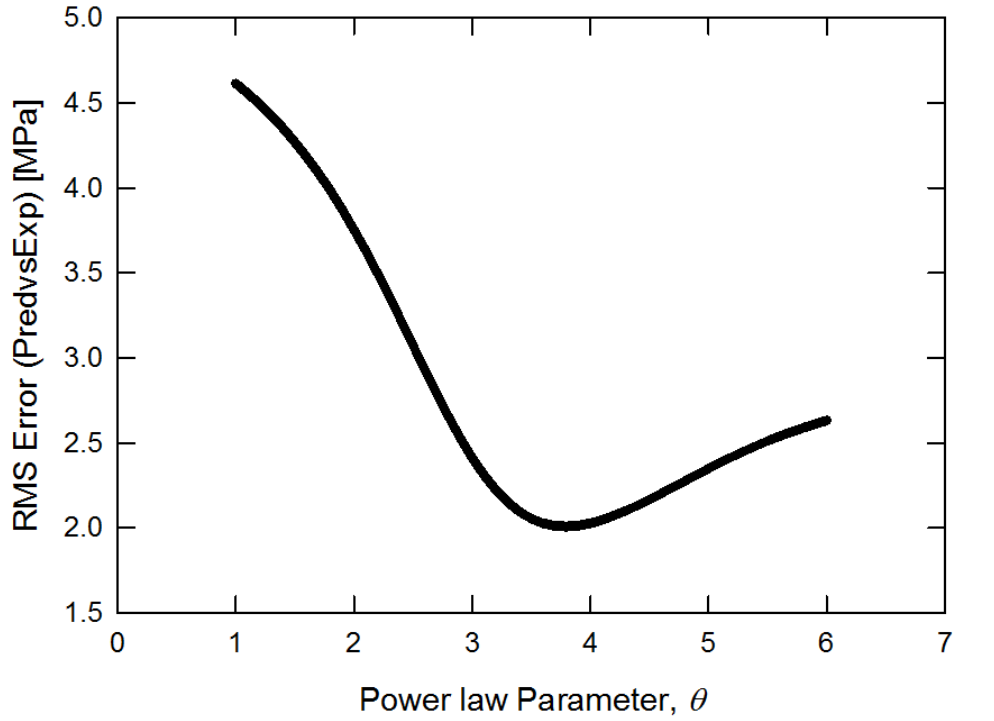


Figure 5.4: Calculation of the rms between the predicted CIS, and the experimental CIS, as a function of parameter θ. Lowest error margin found at $\theta = 3.78$.

when looking at these results. In Deanin's study, the correlation of ultimate elongation molar mass averages improved as these were increased to a higher moment of the distribution (i.e. $\overline{M}_z$). Our Figure 5.5 shows a similar behaviour where crazing in our bimodal blends also appears to be heavily weighted with respect to the higher molar mass fractions as the rms becomes smaller with an increase in θ. Furthermore, these results confirm that the use of a θ-power law, is able to capture the transitioning crazing response that can be expected when shifting from one molar mass to another. To have a more visual representation of how the crazing behaviour appears to be more heavily dominated by a higher molar mass, or moment in the distribution, the $\overline{M}_z$ and $\overline{M}_{\theta=3.78}$ averages have been plotted in the SEC distributions of the monodisperse blends in Figure 5.6.

Even though the applicability of the θ-parameter in the bimodal blends showed a good degree of correlation between experimental and predicted data, the fit

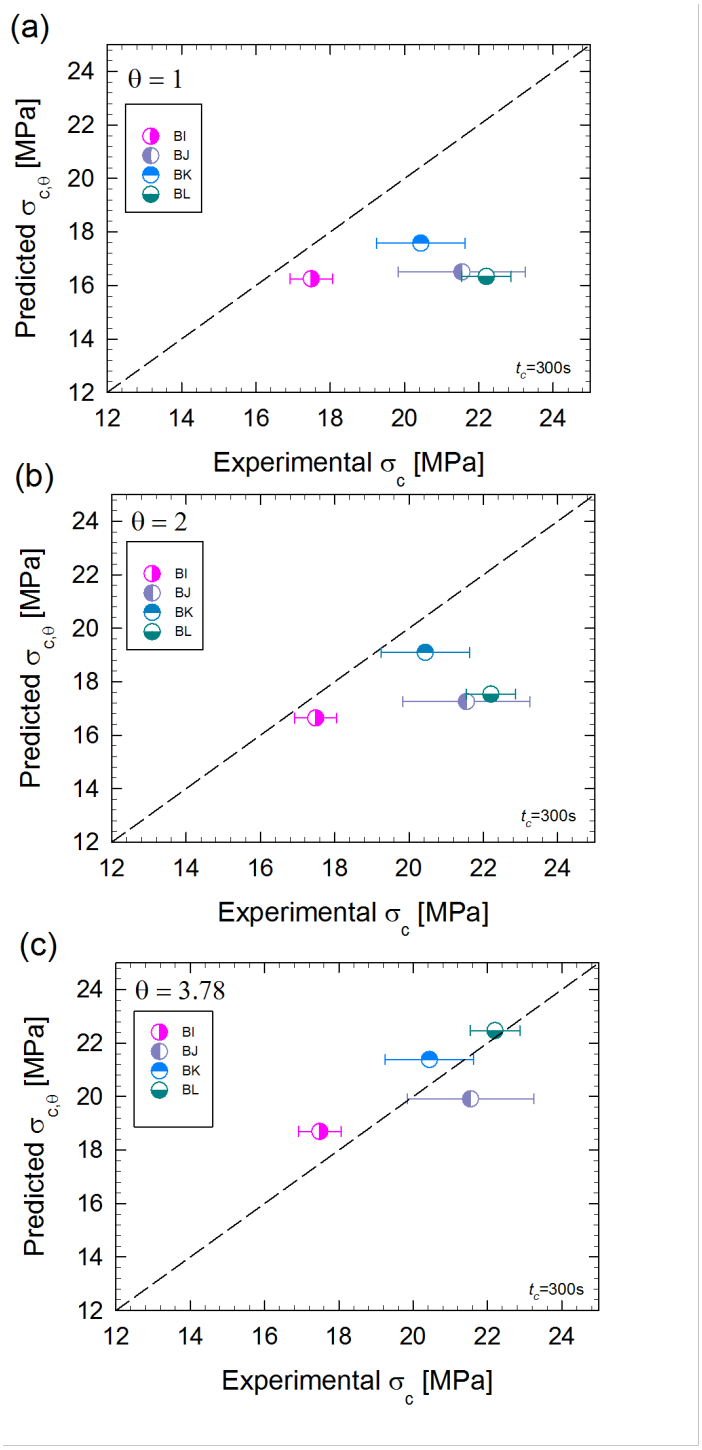


Figure 5.5: Predictions for the calculated CIS when solving for θ are presented against the experimental data, at (a) $\theta = 1$, (b) $\theta = 2$, and (c) best rms fit at $\theta = 3.78$.

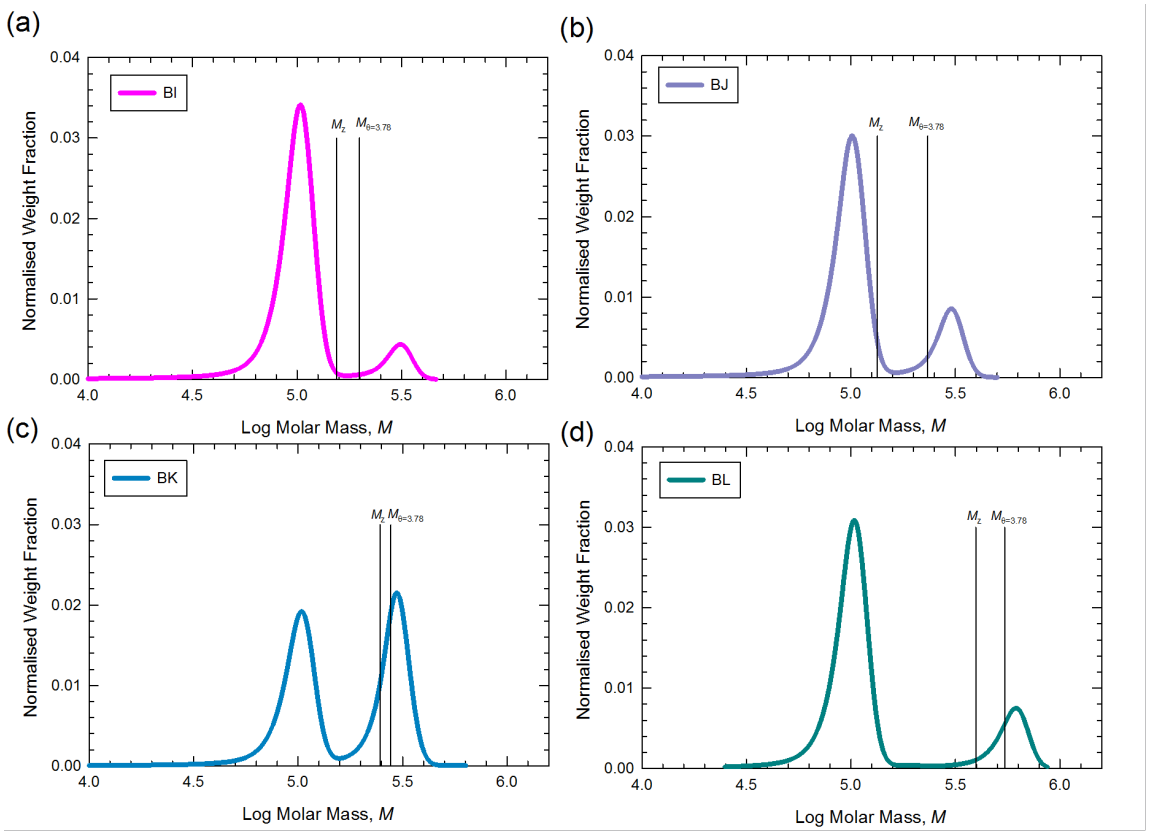


Figure 5.6: $\overline{M}_z$ and $\overline{M}_{\theta=3.78}$ averages plotted in reference to their location within the GPC distributions of monodisperse blends: (a)BI, (b)BJ, (c)BK and (d)BL.

was obtained through mere substitution of blending ratios, and not taking into account the full extent of the molar mass fractions that constitute the whole distributions of the monodisperse component materials. Due to the narrow polydispersity of the latter, it is expected that such a simple model will yield positive results with acceptable levels of accuracy (1%-7% error). Nevertheless, one of the limitations of this approach is the inability to produce error bounds for the value of the power law exponent theta, θ. In order to address this it was decided to perform a more statistical error analysis, using the Monte Carlo method.

5.4 Monte Carlo simulation

Monte Carlo (MC) methods are used to determine the propagation of uncertainties, and to understand what is the relationship between the uncertainty in a prediction with respect to variations in its defining parameters.

In this particular study, it is useful to consider how the scatter in the experimental data obtained in the monodisperse materials and blends could affect the statistical determination of the value of θ. To address this, the Monte Carlo method uses individual probability distributions of random numbers for each of the individual experimental variables. By doing so, it is possible to determine the probability distribution of a specific parameter defined by the combinations randomly chosen from the "known" uncertainty distributions of the individual data inputs [129].

To pursue the applicability of this method, a MatLab code was written in which a large number ($n = 1000$) of normally distributed values for the input experimental variables (e.g. materials BF-BL) were considered. The distributions were computer-generated by using the given values for the mean and standard deviation of the materials. The end result is a distribution array of length n for each one of the analysed monodisperse materials and blends. These randomly produced distributions, consistent with the experimental measurements of crazing stress, were fitted to the crazing model of equation 5.4 to determine a probability distribution of θ. In Figure 5.7 the calculated MC probability distribution of θ is plotted against the probability density function (pdf) , and the cumulative density function (cdf) to establish confidence intervals (CI) for the determination of errors.

The 'ideal' shape for the experimental data will be to follow the pdf distribution (dashed black line in figure 5.7). Yet, because of the wide scattering in the data (particularly a higher crazing stress value for BJ compared to BK), it is possible to note that at ∼0.9 the data starts deviating from the linearity of the pdf distribution. Due to this deviation in the data with respect to the probabilistic fitting lines occurring at ∼95% confidence interval; it was best to determine the propagation of uncertainty and delimiting of error bounds at a confidence interval of 90% ([1.75,17.34]). Thus, θ was determined at 2.59, which is the limit

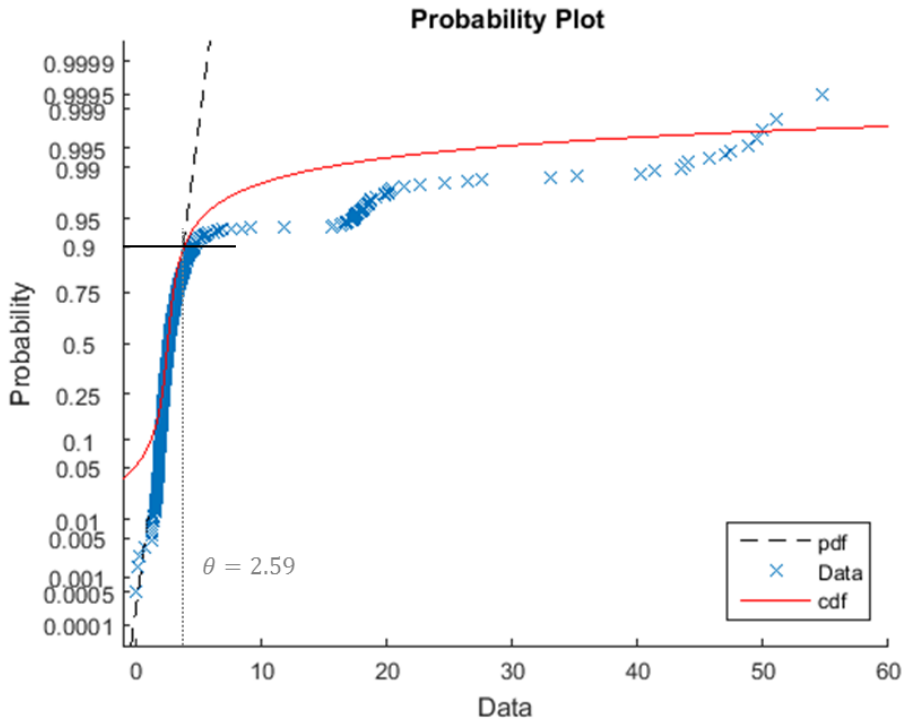


Figure 5.7: Probability plot of the MC analysis of θ. The calculated MC probability function for θ is shown against the pdf and cdf to establish a confidence interval at 90%.

at which the data is still within the pdf linearity at CI=90% ([1.75,17.34]). The attained limits will be used when representing the predictive uncertainty of applying θ =2.59 in the simulations for the calculation of σ_c using equation 5.4. The use of a statistical-error approach in the determination of θ allows defining predictive error bars. The results of applying the new θ value of 2.59, along with the 90% confidence limits at 1.75 and 17.34 is presented in Figure 5.8.

Although the new MC calculated $\theta = 2.59$ differs from the $\theta = 3.78$ obtained using a much more simplistic rms fitting approach, the predictive error bars do apn the experimentally measured values, whilst still securing the predictive ability of the applied $\theta = 2.59$ at a range of 2-16% reported accuracy with respect to the observed experimental values.

Since the MC method represents a more refined approach to the uncertainty in using predictive parameters, such as θ, the remaining analysis of the polydisperse

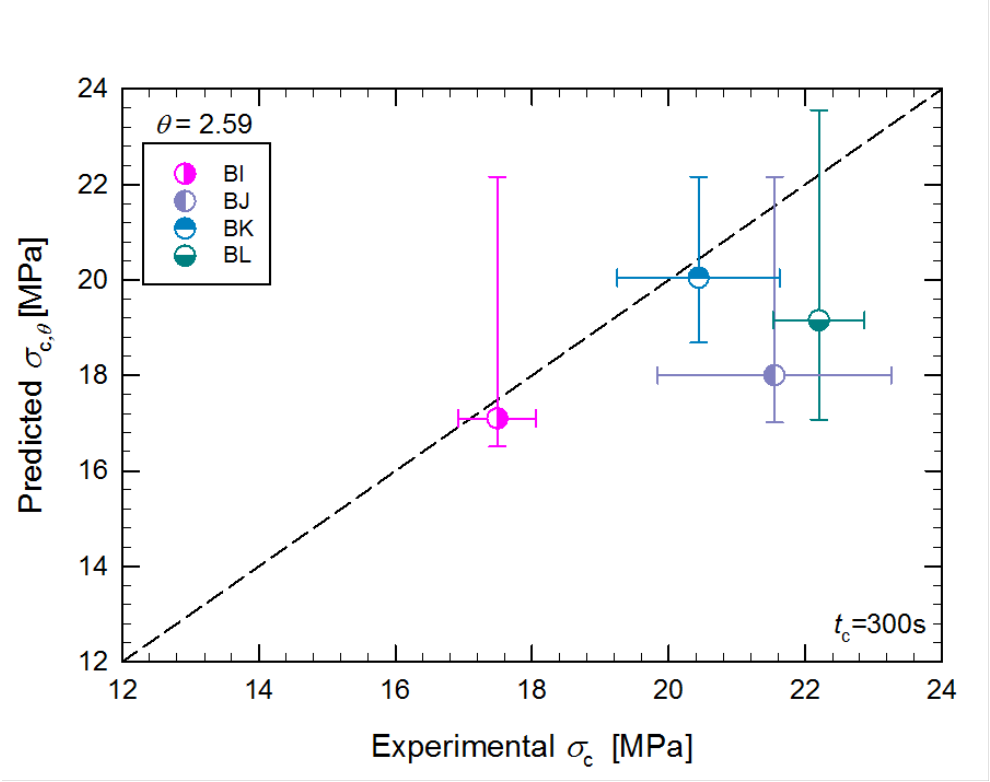


Figure 5.8: Predictions for the calculated CIS when solving for θ =2.59 and a 90% CI [1.75,17.34], represented by vertical error bars.

materials will be conducted using the proposed MC θ =2.59 (90% CI [1.75,17.34]). Other considerations need to be put in place if one were to extend this model for polydisperse systems, as the CIS value is observed to vary in accordance to the contribution of multiple molar mass fractions observed within the distribution. In the next sections, we will show how this issue is addressed.

5.5 CIS model in polydisperse materials

The obvious approach in trying to predict the CIS of our polydisperse materials will be to employ the θ-value found from the Monte Carlo simulation to input this into equation 5.4 for the calculation of σ_c. Nevertheless, the complication when trying to assess the predictions for polydisperse polymers is one cannot afford to ignore their polydispersity. In this sense, equation 5.4 could not work by mere

generalisation of molar mass fractions, as it was done with the bimodal blends, in turn polydisperse materials require a more quantitative account of the fractions comprising their distributions. For this matter, it is required to associate specific M fractions with corresponding CIS values. To achieve this, we use the 3-stepwise liner model for monodisperse materials proposed by De Focatiis [20], in which we can associate a given molar mass to a specific analogous value of σ_c.

Two advantages are seen in using this model: first, the experimental technique is virtually the same, hence theory compatibility directly applies. Secondly, compared to other models (e.g. Kramer and Berger [14]) De Focatiis identified clear molar mass limits in monodisperse PS systems that can be transferred to our data for model validation purposes. Furthermore, contrary to other studies [86] that analyse the shifting from britte-to-ductile transition of semi-crystalline materials categorised by their test temperature and strain rate, De Focatiis' model enables to analyse inherently different crazing data of glassy polymers obtained at differing temperatures, environments and strain rates by calculation of σ_c using an equation that considers chain motion through τ_R, and chemical kinetics through the Eyring equation [20]. What is even more remarkable about De Focatiis model, is that clear transitioning molar mass limits have been replicated in exogenous data [91]. Although some discussion has been ongoing over the feasibility of chain scission actually occurring at those crazing stress values [130], it has been reported that there is a correlation between the strain energy release rate for crack opening, G_{lc}, the entanglement network density, Σ_e, and the force needed to break one molecular chain, f_s. Brown was able to report $f_s = 1.4 \times 10^{-9}$N in PMMA by assuming $G_{lc} \propto (\Sigma_e f_s)^2$, showing good agreement with the chain breaking force 3×10^{-9}N estimated by Kausch and $2.5 - 12 \times 16^{-9}$N by Odell and Keller [86]. Since free surface is an inherent element of crazes, and free surface is in itself a type of void structure it is possible to find some validity in this argument. Once a craze reaches a specific strain energy the stress borne by the fibrils' network may concentrate into an individual segment of the craze causing this to fail by scission. Whether this mechanism is entirely dependent on chain rupture or whether it represents a combination of disentanglement failure or slip-link contribution, remains elusive as these sort of chain micro-dynamics are nearly impossible to be measured experimentally, and can only be modelled

based on polymer physics. Plummer [90] supports this idea of craze stability via the entanglement density by highlighting that crazing is crucially dependent on the extent to which forces can be transmitted between individual chains through their associated molecular interlocking.

We take the disentanglement and chain scission thresholds previously presented in Figure 7 in appendix B to provide a clearer picture of the molar mass limits at which the crazing dynamics are seen to change, and enter the corresponding regimes of: I) dilution, II) disentanglement and III) chain scission, as the polymer is seen to increase in molar mass. Furthermore, the new limits highlighted in Figure 5.9, also depict clear molar mass values at which these mechanisms are observed to occur, namely M_c (referred to as M_{crit} in De Focatiis' study) and M_∞.

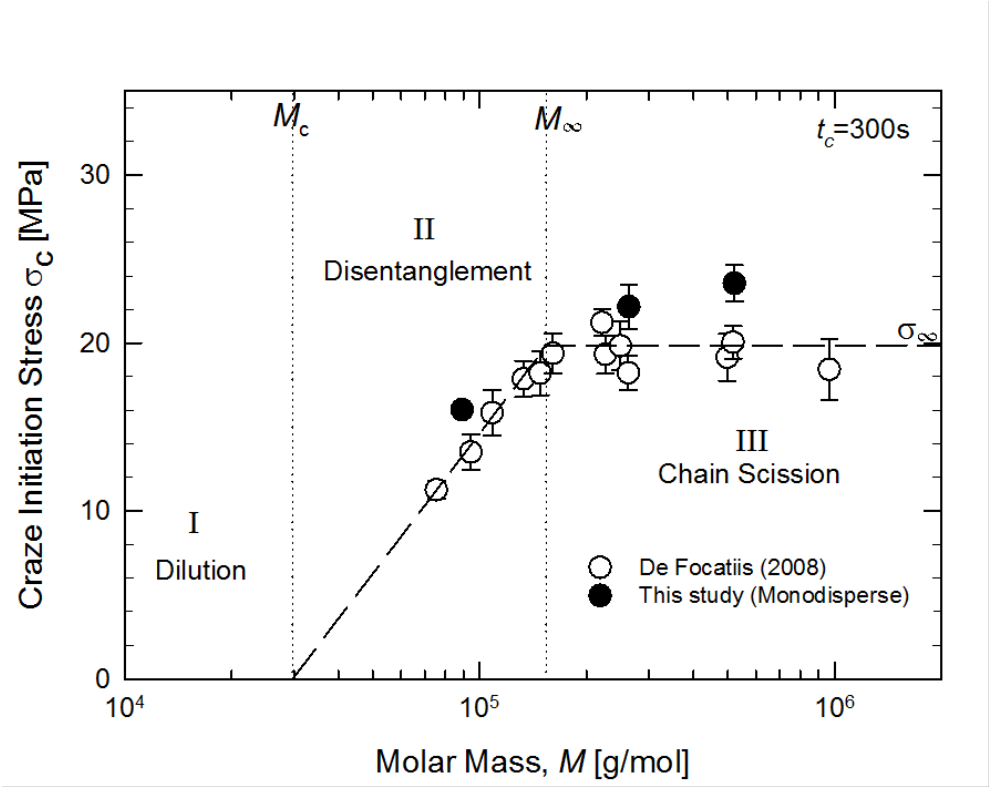


Figure 5.9: 3-linear step model for CIS for monodisperse materials as proposed by [20].

In polydisperse distributions, molar mass fractions can span across all three

crazing regimes. Hence, the contribution of $\phi_\theta(M)$ must be based on a corresponding crazing mechanism, and equal $\sigma_c(M)$. This relationship is presented through,

$$\sigma_c(M) = \begin{cases} 0\,, & M < M_c \\ \sigma_\infty \times \dfrac{(M - M_c)}{M_\infty - M_c}\,, & M_c < M < M_\infty \\ \sigma_\infty\,, & M > M_\infty \end{cases} \tag{5.5}$$

where $\sigma_\infty = 19.85$ MPa defines the chain scission crazing stress limit value at $M_\infty = 154\,\text{kDa}$; while $M_c = 31.8\,\text{kDa}$ represents the critical molar mass limit at which the network becomes entangled and crazing by disentanglement occurs.

With the aid of a systematic logarithmic sequence produced in Matlab, it was possible to run simultaneous calculations of using equation 5.4: $\sigma_{c,\theta} = \sum_M \phi_\theta(M)\sigma_c(M)$, where the crazing stress of a specific molar mass is defined by expression 5.5, and the corresponding fraction, $\phi_\theta(M)$ is defined through the θ-parameter as stated in equation 5.2.

The three core polydisperse materials used in this study, namely R, BX and BY, were analysed to perform the model validation. In Figure 5.10, the distributions of these polymers have been plotted along De Focatiis' 3-linear segment model to highlight the differences in their distributions, and the molar mass contributions to the CIS.

It is worth noting that while the distributions for materials R and BY lie primarily in the disentanglement and chain scission regimes, material BX shows a distinct bimodal distribution that spans across all three regimes, with a significant fraction lying in the dilution region.

A calculation was performed to obtain $\sigma_{c,\theta}$ in the polydisperse distributions of materials R, BX and BY using a Matlab code, with θ=2.59 along with its corresponding statistical errors. Is worth reminding the reader that it proved impossible to form stable crazes in material BX, as specimen preparation was exceptionally challenging due to its extreme brittleness, alongside with multiple specimens fracturing upon testing. Nevertheless, one specimen was capable to

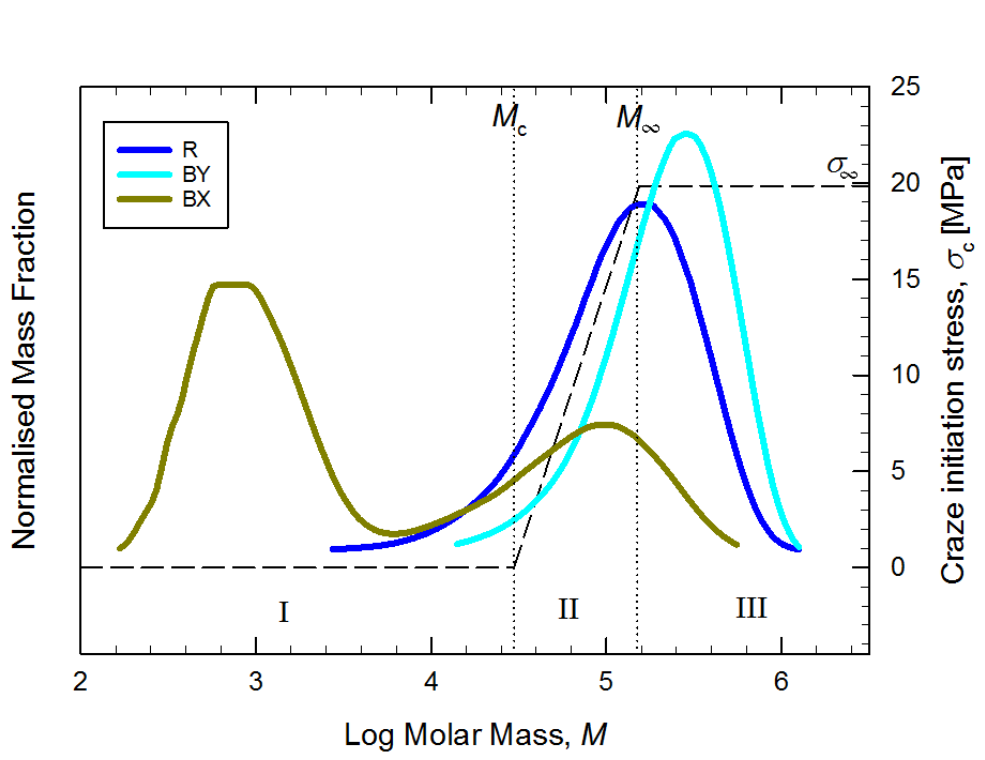


Figure 5.10: 3-linear step model [20] for CIS alongside MMDs of polydisperse materials.

sustain loading at a recorded 2.4 MPa for the observed 300 s, but broke before optical inspection of crazes could be carried. The relevance of this measurement is that it provides an upperbound on the crazing stress that can be used as a reference for comparison against the obtained predictions. The predicted values for the polydisperse materials are presented in 5.11 against their experimental data.

Figure 5.11, shows that the predicted CIS values for polydisperse materials R and BY are underpredicted by 21% and 18% respectively. This discrepancy suggests that the crazing stress may be more strongly affected by the higher molar mass fractions that accounted by the $\theta = 2.59$ model. It is interesting to note that this behaviour supports the observation previously made by De Focatiis [24] that the craze initiation stress for polydisperse material R seemed to be in closer agreement with the values observed in a monodisperse material with similar weight average, rather than with the same number average. The

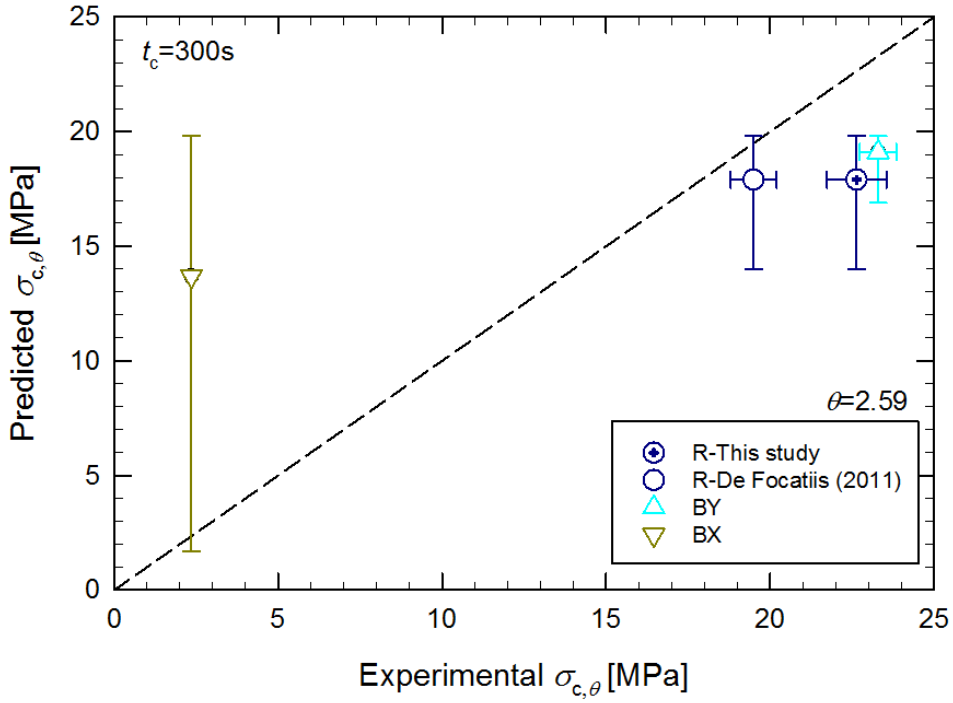


Figure 5.11: Experimental vs predictions of CIS at θ=2.59 90% CI [1.75,17.34] for polydisperse materials R,BX and BY.

CIS predicted for material BX was ∼13.7 MPa, a value six times higher than the recorded applied maximum stress to which the material was subjected before breaking. Even though only one experimental measurement of 2.35 MPa was able to be recorded, approximately 4 samples of material BX were produced and subjected to 3-point bending. Nevertheless, all other three samples were seen to fail prematurely due to the inherent brittleness of this material. The validity of such a recorded measurement, is that it provides a qualitative value for the very low endurance (∼2MPa) that such material has to undergo applied stresses, and that was verified by the complexity and premature failure observed whilst preparing, loading and testing the miniature specimens.

The inaccuracy of the prediction and hence, very wide error bars seen for material BX may be connected with the bimodal shape observed in this poly-

mer's the molar mass distribution, where the contributions to $\sigma_{c,\theta}$ span across the dilution, disentanglement and chain scission regimes. The predicted value was calculated by accounting only the contributions of the molar mass fractions that lay within the disentanglement and chain scission boundaries, as has been replicated by various authors in the referred literature [15; 18; 20; 128]. This assumes that the molar mass fraction that lies in the dilution regime contributes nothing to the crazing stress and that it does not adversely affect the contribution to craze resistance of the other regions. Yet, experimentally the crazing response of material BX is much poorer than might be expected, and this could be due to the large unentangled fraction, and its effect on the entangled chains. Deblieck [86] states that the stress crack growth (SCG) of a material is best measured by assessing the effective entanglement density, or the amount of load bearing chains per unit surface. In [131], Fetters *et al.* proposed a scaling relationship to estimate the entanglement density for polyolefins. Deblieck's observation is that for an entanglement to be truly effective (i.e. load bearing on the time scale of the experiment) it is required that $\overline{M}_n \geq \zeta M_e$, where ζ is the monomeric friction coefficient. Hence, in the modification of the model that follows we will look to properly account for the dilution effect in the entanglement network involved in the crazing process of highly polydisperse blends.

5.6 Hybrid CIS-DTD model

The inability to capture the behaviour of a wide bimodal polydisperse material using the present model suggests that other considerations need to be put in place. Since crazing is a mechanism that initiates as the result of chains stretching, and subsequent flow between entanglements, it is useful to have look at how this event occurs in a rheological timescale. It is well known that some relationships between the strain hardening modulus G_p, and the entanglement network (i.e. M_e) have been attempted in the past [132]. For our crazing model, it is useful to employ Marrucci's ideas of dynamic tube dilation [77], to explain the observed brittleness of material BX. DTD is the idea that constraint release mechanisms in molecules or entanglements are modified by the dilating character of the tube

diameter at reduced polymer concentration. The main effect of this is seen in the tube diameter expanding as the polymer concentration is reduced. This reduction also affects the overall dynamics of the long chains, and the number of entanglements decreases as the molar mass between two entanglements, M_e, becomes larger with reduced polymer concentration. Several rheological studies [133; 134; 135] have been able to predict the viscoelastic response of polybutadiene and polyisoprene blends and solutions by making use of the DTD and fine-tuning the value of the dynamic dilution exponent, α (as discussed in section 2.5.1). In equation 2.13 Shahid presents an expression to account for the decrease in moduli observed as a function of diluting a series of monodisperse PS with their oligomers. We take Shahid's original equation to define the effective molar mass between entanglements M_e' as:

$$M_e' = \frac{M_{e,0}}{c} \tag{5.6}$$

where $M_{e,0}$ is the initial value of M_e; and assuming α and $\phi(t)$ are set to one. Here, the concentration, c, can be interpreted as the polymer concentration of sufficiently long and entangled chains as to contribute to the calculation of $\sigma_{c,\theta}$. Therefore, c can be computed as:

$$c = \sum_{M_e}^{\infty} w(M) \tag{5.7}$$

where the subscript $w(M)$ defines the normalised weight fraction of molar mass M. Referring to the definition of number of entanglements in a fully entangled melt (∞), Z is,

$$Z = \frac{M}{M_{e,0}} \tag{5.8}$$

Then if M_e is assumed to change into M_e' as a result of DTD, one could expect Z to decrease into a new Z' value, termed the effective number of entanglements, given by

$$Z' = \frac{M}{M_e'} = \frac{cM}{M_{e,0}} \tag{5.9}$$

This implies that as the system becomes more diluted by chains of $M < M_e$, the concentration of long chains, c, decreases, as does Z', with a corresponding increase in M_e'. The implications of this effect are that as the number of entanglements is decreased, so is the entanglement density, which is known to exert control in the crazing dynamics, particularly in the disentanglement regime. This would suggest that when a craze experiences the DTD effect, the probability of a chain to be entangled by its ends and undergoing fibril stretching is reduced, consequently a polymer chain that was just above the minimum requirement to sustain chain entanglement (i.e. $Z = 2$), is now unable to do so. This idea shares similarities with some observations made by previous authors. In his model for crazing [18], Plummer recognises that M_c (the molecular weight associated with a craze crossing), will decrease as the amount of scission increases, thus increasing the number of chain ends per unit volume. Donald [128] also hinted at this issue in her study of PS and PPO blends, where she noted that the thermal degradation of PPO could lead to a greater apparent M_e by reducing the number of effective entanglements. She also recognised that the extreme weakness of the studied blends was a result of the high stress that was concentrated in the small number of load bearing PPO chains, compared to the large diluting fraction of PS chains (unentangled chains).

Returning to our data, the practicality of this argument is that if we associate the idea of DTD with the De Focatiis 3-linear step crazing model it is possible to relate σ_c to Z rather than M. Because DTD theory is based upon the entanglement concept, and this can be quantified using Z the proposed model can be interpreted in terms of the effective number of entanglements, Z'. As a result, the piecewise linear model can now expressed as equation 5.10,

$$\sigma_c(Z') = \begin{cases} 0\,, & Z' < Z'_c \\ \sigma_\infty \times \dfrac{(Z' - Z'_c)}{Z'_\infty - Z'_c}\,, & Z'_c < Z' < Z'_\infty \\ \sigma_\infty\,, & Z' > Z'_\infty \end{cases} \tag{5.10}$$

with $Z'_c = cM_c/M_e$ and $Z'_\infty = cM_\infty/M_e$. Hence the crazing stress of a given component of the distribution shifts to a lower molar mass equivalent, depending on the magnitude of c. The new predictions of crazing stress corrected for dilution can therefore be calculated using expression 5.11.

$$\sigma_{c,\theta} = \sum_{Z'} \phi_\theta(Z')\sigma_c(Z') \tag{5.11}$$

The outcome of incorporating such DTD effect will be manifested as a horizontal shift to the left of the polymer distribution. Taking BX as our reference material, we re-plot Figure 5.10, substituting for Z in the horizontal axis. The values for Z and Z' were calculated through 5.8 and 5.9, respectively.

The outcome of this is that although the stress limits of De Focatiis crazing model remain the same, the contributions to crazing that arise from the polymer chains are effectively diluted by the DTD effect.

The effect of applying this correction is to change the prediction of crazing stress for material BX from 13.7 [1.7, 19,8] MPa to 4.7 [0.6, 6.8] MPa, much closer to the experimentally recorded value of 2.4 MPa, and within the 90% CI.

In Table 5.3, we present the $\sigma_{c,\theta}$ data calculated for the materials analysed so far: monodisperse systems, along with their bimodal blends, and the polydisperse materials. These calculations were obtained by applying equation 5.4 -i.e. without the effect of DTD-, and equation 5.11 -i.e. considering the effect of DTD-, where the value of $\phi_\theta(M)$ was taken directly from the GPC distributions of our test materials. A value of $\theta = 2.59$ with 90% confidence intervals, and $M_e = 15900\,\mathrm{g/mol}$ (obtained from rheological data on the monodisperse materials as outlined in section 6.3) were used throughout the calculations.

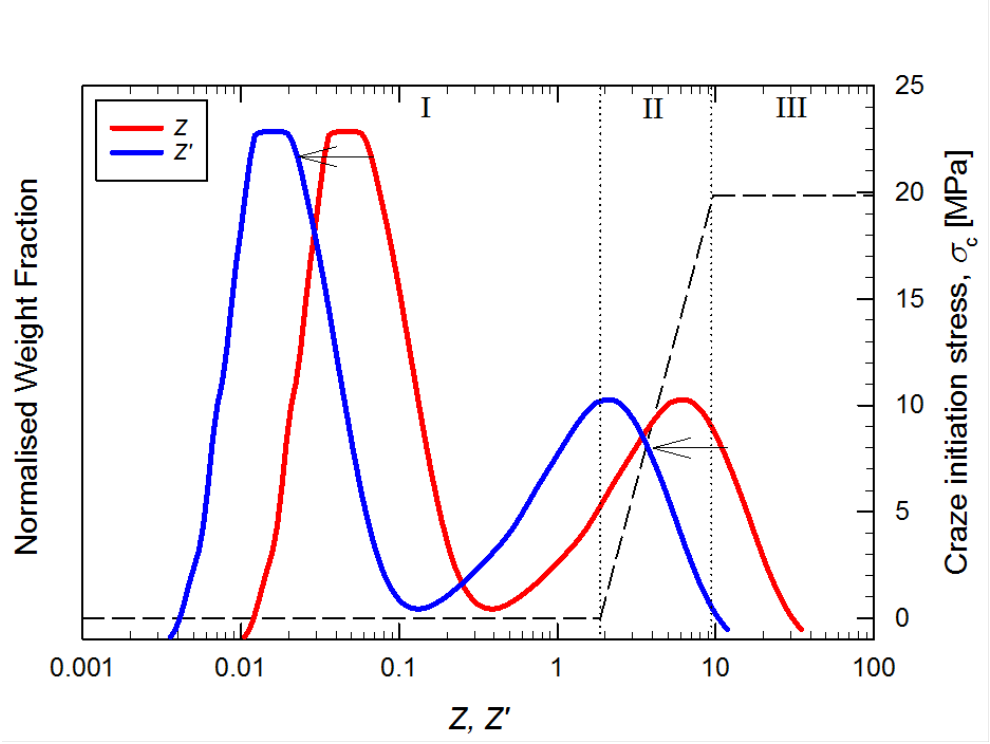


Figure 5.12: SEC distribution of material BX as a function of Z; along with the 3-linear step crazing limits.

Table 5.3: Results for $\sigma_{c,\theta}$ without and with (w/) DTD (at $\theta = 2.59$ with a 90% confidence interval of [1.75, 17.34], $M_e = 15900\,\mathrm{g/mol}$).

Code	Exp.σ_c [MPa]	Pred.$\sigma_{c,\theta}$ without DTD [MPa]	Pred.$\sigma_{c,\theta}$ with DTD [MPa]	c	M_e'	Z	Z'
BF	16.03±0.1	13.62 [13.11, 14.73]	14.66 [13.70, 17.96]	0.99	15926	5.87	5.86
BG	22.16±1.3	19.77 [19.67, 19.84]	19.77 [19.67, 19.84]	1.00	15900	16.97	16.97
BH	23.56±1.1	19.81 [19.72, 19.84]	19.81 [19.72, 19.84]	1.00	15900	33.98	33.98
BI	17.57±0.51	14.68 [13.72, 17.99]	14.66 [13.70, 17.96]	0.99	15988	7.41	7.37
BJ	22±1.67	15.58 [14.34, 18.81]	15.56 [14.32, 18.78]	0.99	15999	8.42	8.37
BK	20.44±1.19	17.62 [16.27, 19.54]	17.61 [16.25, 19.52]	0.99	15930	12.08	12.06
BL	23.09±1.87	16.18 [14.31, 19.65]	16.16 [14.29, 19.62]	1.00	15900	12.02	12.02
R	22.64±0.91	17.90 [14.01, 19.85]	17.59 [13.76, 19.50]	0.98	16185	14.01	13.76
BX	2.35	13.74 [1.66, 19.85]	4.69 [0.57, 6.77]	0.34	46627	3	1.02
BY	21.23±1.82	19.13 [16.90, 19.85]	19.00 [16.80, 19.72]	0.99	16004	21.33	21.19

By looking at Table 5.3, it can be seen that the DTD is more effective in predicting the behaviour of polydisperse system BX, which represents the material

with the highest amount of unentagled fractions. The model shows virtually no change when applied to all the other polymeric systems, as their concentration levels of highly entangled chains are close to unit, and even polydisperse materials R and BY have high concentrations of entangled chains (c =0.98-0.99). This more detailed interpretation of the effects of the different length scales within a blend on crazing is not only physically more realistic, but also able to produce more accurate predictions of crazing stress in all the materials analysed. The main contribution of the CIS-DTD model, as seen in Table 5.3, is that although it offers a relatively minor improvement in polymeric systems were $c \sim 1$, it provides a more realistic and quantitatively accurate prediction for materials with high levels of polydispersity, as is the case of material BX. What this suggests is that the application of such a model does become necessary when MMDs are fundamentally bimodal (e.g. polarised) and containing a number of unentangled fractions. It is worth emphasizing that the applicability of such a model has real industrial value, since a lot of processes often include the addition of plasticisers or low molar mass polymers to facilitate the melting and subsequent processing of polymer mixtures.

A feature of the proposed model is its use of the polymer's molar mass distribution to compute σ_c, and that the θ-parameter has some theoretical relevance to concepts of chain dynamics, unlike other models proposed by other authors [18; 46; 128]. In light of these findings, the CIS model with the inclusion of the DTD effect will be put to test in more complex systems, such as in the case of polydisperse blends.

5.6.1 Hybrid CIS-DTD model: polydisperse blends

The inclusion of a DTD effect into the 3-linear step crazing model, termed the hybrid CIS-DTD model, showed little improvement in predicting the CIS of systems with inherently low polydispersity levels and sufficiently entangled molar mass fractions (e.g. monodisperse materials and their bimodal blends). Nevertheless, it led to an improved accuracy in predicting the response of complex polydisperse polymers, such as BX, a highly bimodal system. The obvious next stage in the validation of this model is to test it against more challenging sce-

narios, e.g. our bimodal polydisperse blends of materials BX and BY. CIS in the polydisperse blends was measured at a loading time of 300 s. Due to the difficulty in loading and extreme brittleness during specimen preparation, it was only possible to obtain a single measurement for the *mm*-samples of materials CA and CB. The difficulties in growing stable crazes in systems where $\overline{M}_w < M_{crit}$ have been reported [128], and according to Yang [37] there is an inability to grow crazes below $\sim \overline{M}_w = 40,000$ g/mol. Interestingly enough, our samples represent highly complex test subjects, as all of the polydisperse blends studied here show a $\overline{M}_w$ above the 40,000 g/mol limit, but their $\overline{M}_n$ values are as low as 1300 g/mol. Loading of these specimens had to be carried with particular care, with tiny loads being applied to the centre of the specimens leading to maximum stresses of as little as 3 MPa to avoid fracture in the sample. The optical analysis of the miniature specimens also required special measures; due to the tiny appearance of crazes, the specimens were inspected before testing, and once the test finished after they were carefully dried, to ensure the crazes were real, and not just some remaining DEG adhering to the surface of the specimen. Representative micrographs of this analysis for materials CB_{sb}, CC_{sb}, and CD_{sb} are presented in Figure 5.13.

The crazing pattern seen in the optical micrographs was found to be very similar between the *sb* and the *mm* blends. The results for the experimentally recorded σ_c are presented in Figure 5.14.

As per the bimodal monodisperse blends, it is possible to observe the same transitioning increase in σ_c as more BY component is added. Another very interesting remark is the fact that the CIS values reported for the *sb*-samples are systematically higher than those seen for the *mm*-samples, up to an accountable difference of ~2 MPa to 7 MPa, as per material CD. One additional feature is the apparent linear increase in the values of the blends with a higher addition of component BY. As previously observed by De Focatiis [20], polymer materials are seen to follow a linear relationship between σ_c and $\log M$ when found in the disentanglement regime. The $\overline{M}_w$ for most of the polydisperse blends reported here lies between 79 kDa and 186 kDa, which suggests that with the exception of material CD_sb, the blends do in fact follow a disentanglement dominated crazing process that will be evidenced by the linear relationship observed in the data.

The experimental CIS results, along with the calculated CIS predictions using

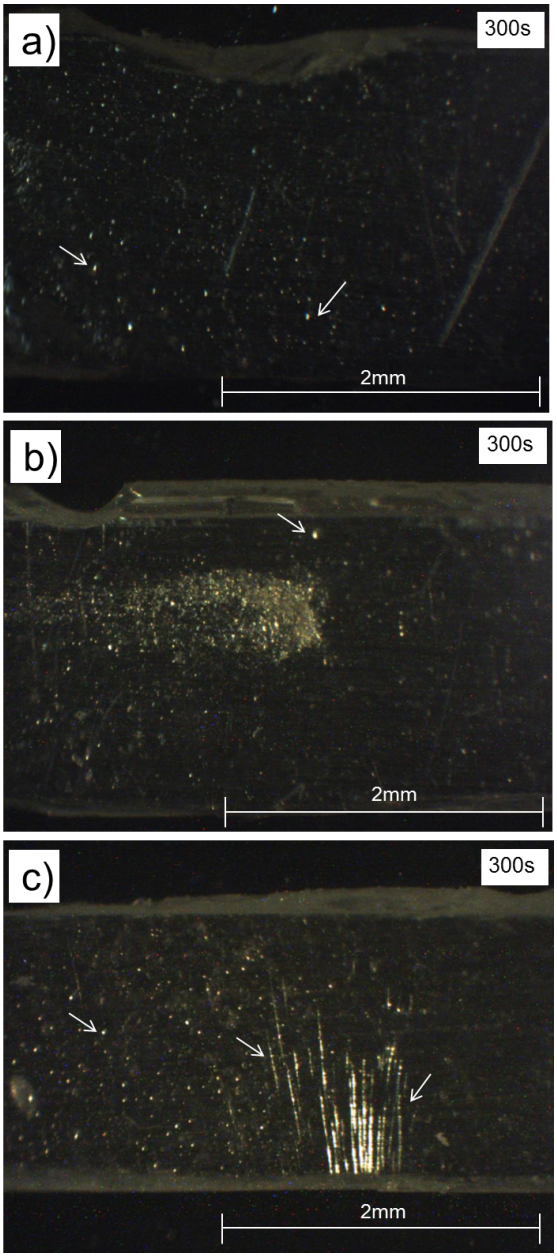


Figure 5.13: Micrographs of polydisperse blends (a) CB_{sb}, (b) CC_{sb} and (c) CD_{sb} at 300s. Crazes are pointed with arrows.

the value of θ=2.59 and a 90% CI for the polydisperse blends are presented in Table 5.4, following the format used before in Table 5.3.

CIS predictions for the polydisperse blends present a remarkable closer agree-

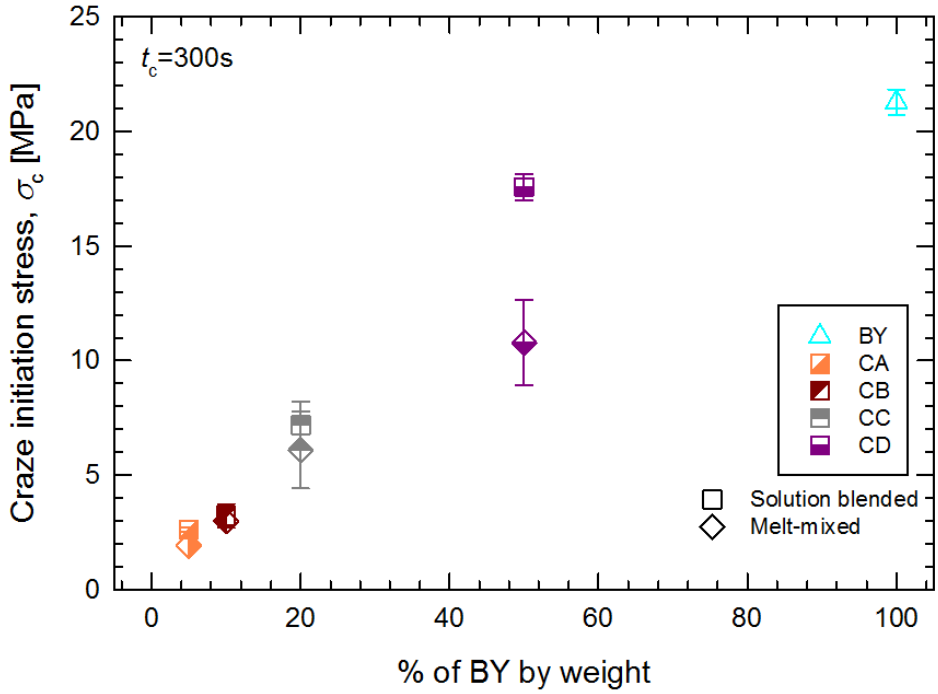


Figure 5.14: CIS of polydisperse bimodal blends of materials BX and BY, as a function of %BY by weight

Table 5.4: Results for $\sigma_{c,\theta}$ with (w/) and without DTD (at $\theta = 2.59$ with a 90% confidence interval of [1.75, 17.34], $M_e = 15900$).

Code	Exp.σ_c [MPa]	Pred.$\sigma_{c,\theta}$ without DTD [MPa]	Pred.$\sigma_{c,\theta}$ with DTD [MPa]	c	M'_e	Z	Z'
CA_{sb}	2.61±0.09	14.89 [2.87, 19.85]	7.18 [1.38, 9.56]	0.48	33002	4.98	2.40
CA_{mm}	1.92	13.96 [1.74, 19.85]	5.14 [0.64, 7.32]	0.37	43122	3.29	1.21
CB_{sb}	3.21±0.51	15.24 [2.92, 19.85]	7.37 [1.41, 9.60]	0.48	32875	5.43	2.62
CB_{mm}	2.98	14.75 [1.87, 19.85]	5.63 [0.72, 7.58]	0.38	41656	3.93	1.50
CC_{sb}	7.18±1.02	16.47 [3.23, 19.85]	8.30 [1.63, 10.00]	0.50	31559	7.04	3.55
CC_{mm}	6.09±1.68	15.50 [2.30, 19.85]	6.70 [0.99, 8.59]	0.43	36725	4.91	2.12
CD_{sb}	17.57±0.56	18.00 [5.33, 19.85]	11.77 [3.49, 12.98]	0.65	24318	11.73	7.67
CD_{mm}	10.77±1.86	17.81 [4.71, 19.85]	11.18 [2.96, 12.46]	0.63	25325	10.10	6.34

ment to the experiments, but only when including DTD. Contrary to Table 5.3, an increase of σ_c can be observed as a direct result of an increasing c. Similarly, the effect of the dilating tube is evidenced in the increasing M'_e and correspond-

ing decrease in Z'. What is also noticeable is that the CIS reported for the solution-blended samples is higher than those seen for the melt-mixed specimens. This result is clearly linked to the MMD of the materials reported in section 3.2, where the blends produced through a melt-mixing method showed wider distributions that extend further into the low molecular mass tail of the chromatographic spectrum.

Figures 5.15 and 5.16 take the data in Table 5.4 and present it in the form of experimental vs. predicted graphs, where the diagonal represents a perfect agreement. The accuracy of the predictions for the melt-mixed samples is reported is as high as ∼96% for some of the systems analysed; similarly, accuracy levels of up to 84% were observed for the solution-blend data. The slight underprediction seen in the model replicates the pattern reported for all the other polymer systems, but it is evident that the DTD inclusion to the model helps to quantitatively capture the contribution of unentangled fractions better than before where they were assumed to contribute nothing into the CIS calculations. When analysing both Figure 5.15 and 5.16 in conjuction, it is possible to observe that the prediction error bars (e.g. vertical lines) differ at the bottom end, where the prediction boundaries offered for the blends produced using melt-mixing offer a lower bound which is representative of the lower molar mass that comes as a result of thermal degradation in such materials.

In his micro-indentation study of crazes, van Melick [136] also reported increases of 25% and 30% in the critical craze-nucleation stress when PPO is added into a PS matrix. He states that the role of the network density on the process of craze nucleation is critical, but he acknowledges the importance of other parameters such as molecular mobility. The hybrid CIS-DTD model proposes a new method for describing the challenges of craze nucleation as a function of changes in molecular distributions. A 'negative' dilution effect arises from the decrease in the number of entanglements due to the drop in concentration of highly entangled chains, as a result of entanglement tubes widening from an increased fraction of short (unentangled) chains within the distribution. Plummer [18; 90] recognised a similar effect in his predictive study of disentanglement and crazing of PS and PES, where he states that the inaccuracy of the model may be related to an additional molecular weight dependence of a plasticising effect

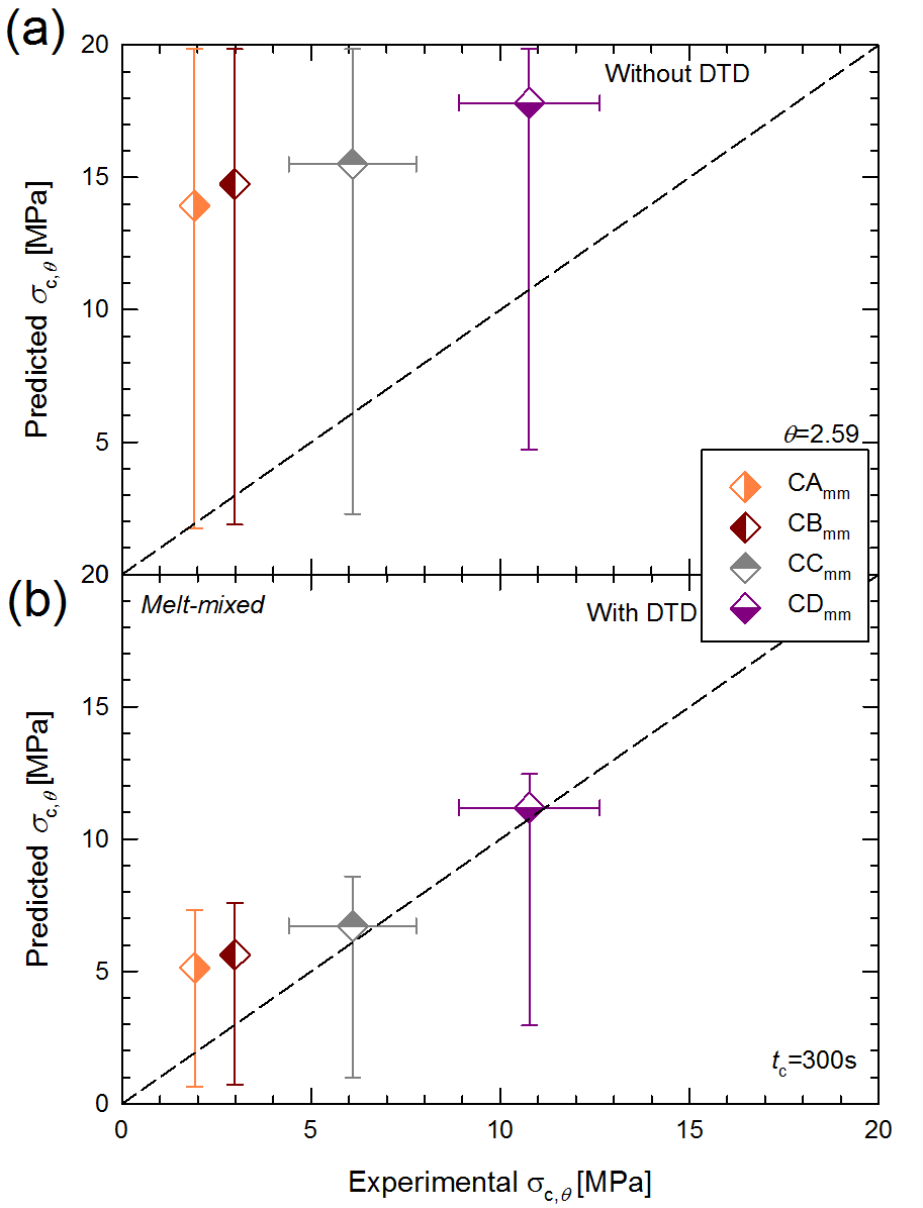


Figure 5.15: Experimental vs. prediction of CIS in the melt-mixed materials at θ =2.59 90% CI [1.75, 17.34] (a) without and (b) with the inclusion of the DTD effect.

due to the low molecular weight tail in the distribution. Although the DTD has mostly been applied to flow dynamics, there is consistent evidence to support

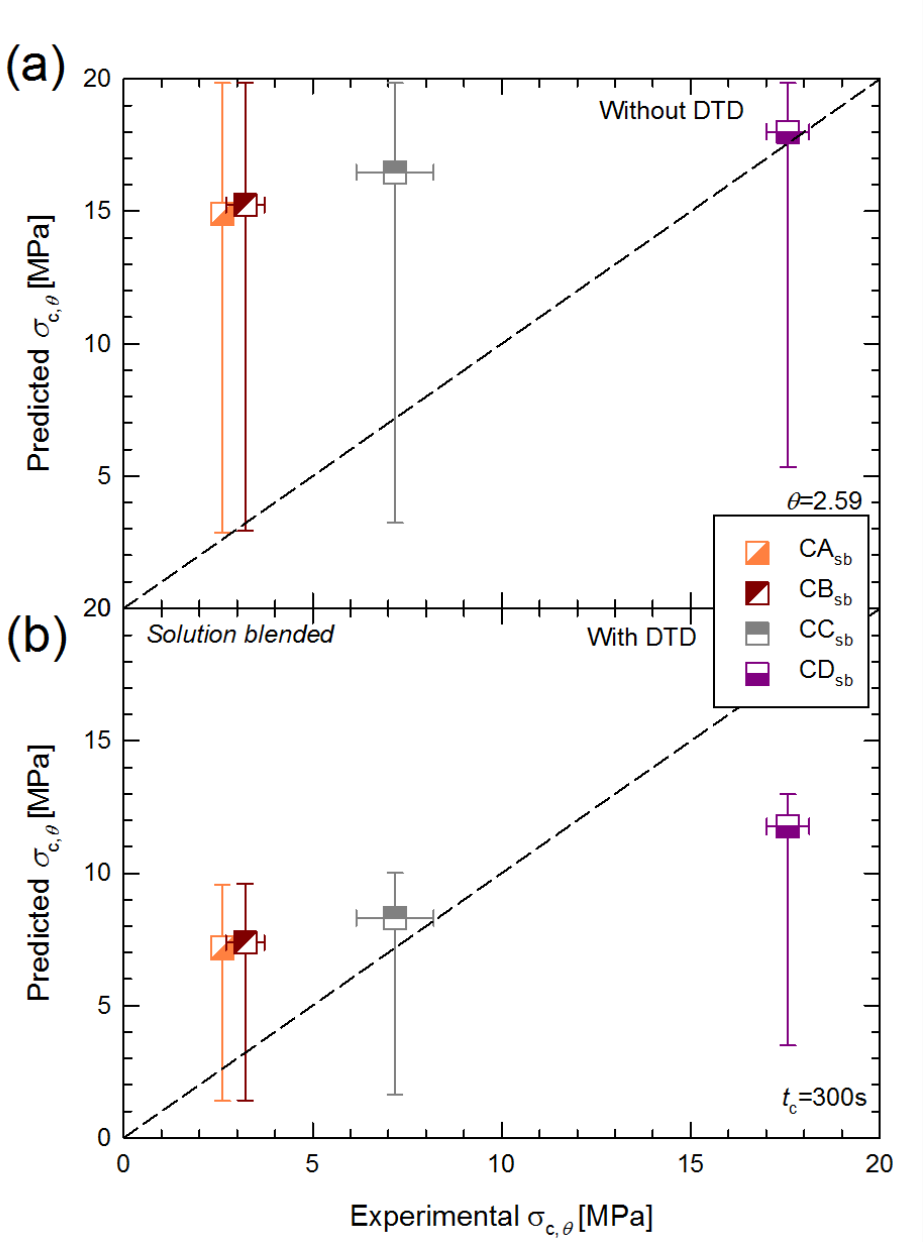


Figure 5.16: Experimental vs. prediction of CIS in the solution blended materials at θ =2.59 90% CI [1.75, 17.34] (a) without and (b) with the inclusion of the DTD effect.

the modelling of solid-state properties based on melt physics. In [132], Haward analysed the strain hardening of polyethyelene, emphasising on how pragmatic

calculations of the strain modulus G_p, could be attained through its association with M_e via equation 2.8. Haward recognises that the analogy between the theory proposed by rubber elasticity and large strain processes in thermoplastics can only be extrapolated to the latter by recognising the concept of the entanglement network (which acts as the rubber crosslinks). Haward validated the association between G_p and the rheological rubber plateau modulus, G_0^N, by assuming the former is obtained by a purely rubbery elastic response. His approach confirmed similarities in the order of magnitude, and in some cases equalities between both parameters [86; 137; 138]. Along these lines, Kramer[139] carried a study for the relationship between the fracture toughness parameter, G_{IC}, and the craze criterion for craze stability in low molecular weight materials. The predictions correlated the extension ratio of the fibril, and the root mean square end-to-end distance of the PS molecule to predict that G_{IC} decreases as $\overline{M}_w^{1/2}$.

5.7 Birefringence and crazing

5.7.1 Birefringence and orientation

As has been suggested before in section 2.7.5, orientation can influence the character and formation of crazes. Hence, understanding how anisotropy has an effect on the loading capability, and hence stress dissipation that arises from craze formation in glassy polymers becomes relevant, as most manufacturing processes (i.e. injection, extrusion) imprint an often unintended degree of orientation into the drawn polymer. Drawn specimens of monodisperse materials and their monodisperse blends were produced following the procedure described in section 3.6.1. The miniature crazing specimens were cut from the elongated bars, and examined for birefringence (section 3.6.2) prior to immersion in DEG for subsequent crazing experiments. The measured averaged birefringence is reported as a function of specimen drawing temperature in Tables 5.5 and 5.6. All specimens studied were drawn at a fixed stretch of $\lambda = 3$.

The reported results show that birefringence increases as the drawing temperature approaches the glass transition temperature ($\sim$106 °C) and the associated

Table 5.5: Birefringence measurements of drawn monodisperse materials.

Code	Drawing Temperature [°C]	Birefringence [-Δn]	No. Tests
BF	106.77	0.0169±0.002	4
	117.45	0.0058±0.0002	4
	127.07	0.0014±0.00005	4
	137.07	0.0002±0.00002	2
BG	106.81	0.0225±0.002	3
	116.39	0.0088±0.009	4
	126.6	0.0048±0.0003	4
	136.62	0.0025±0.00009	4
BH	106.78	0.0198±0.005	2
	116.31	0.0085±0.0005	5
	127.09	0.0053±0.0002	5
	136.5	0.0047±0.0003	5

timescales for the observed chain lengths become insufficient to achieve relaxation. To facilitate analysis, the birefringence data is plotted as a function molar mass in Figure 5.17.

These molar mass plots also depict more graphically why materials BG and BH present higher birefringence values (in the region of 16%-23%, and 28%-91% increase, respectively) when compared to the rest of the observed samples. It coincides with the fact that these materials have the higher $\overline{M}_w$ averages at 269 kDa and 540 kDa, respectively. The initial origins in the study of birefringence were examined through the phenomenon of photoelasticity [140; 141]. The orientation of polymer molecules could be studied by the applied mechanical stress and polarization of light passed through the specimen in what is commonly known as the stress-optical coefficient. The stress-optical coefficient explains the onset and increase of birefringence in proportion to the stress that develops during drawing.

As polymer dynamics has grown further in the understanding of viscoelasticity through tube models and relaxation times, to better interpret the aforementioned data, it will be convenient to apply the concept of Weissenberg number, Wi. This number is associated with the various relaxation times of the polymer, and is defined as the product of the rate of deformation experienced by the polymer, $\dot{\epsilon}$

Table 5.6: Birefringence measurements of drawn monodisperse blends.

Code	Drawing Temperature [°C]	Birefringence [-Δn]	No. Tests
BI	106.52	0.0140±0.001	4
	117.28	0.0048±0.00008	5
	126.96	0.0011±0.00006	4
	136.63	0.0002±0.00002	4
BJ	106.81	0.0150±0.002	4
	117.21	0.0070±0.0003	4
	127.17	0.0011±0.0001	4
	137.22	0.0002±0.0003	4
BK	106.9	0.0150±0.0009	5
	117.27	0.0051±0.0007	4
	127.47	0.0019±0.0007	5
	136.54	0.0007±0.0008	4
BL	106.29	0.0130±0.002	4
	116.82	0.0052±0.0002	5
	127.28	0.0016±0.0003	4
	136.93	0.0005±0.0001	4

, and the characteristic relaxation time, τ. Depending on the timescale analysed the latter could simply be substituted by τ_e, τ_R or τ_d, to give the corresponding Wi_e, Wi_R and Wi_d. The choice of using a distinctive timescale comes from the fact that polymers are known to be defined by a spectrum of multiple relaxation times, which govern the material's nonlinearity and elasticity at different length scales [142].

The usefulness of the Weissenberg number is that it serves to define the degree of anisotropy or orientation generated by the deformation experienced by the polymer system. Thus, it becomes an effective measure to describe polymer flows with a constant stretch history, such as in the case of "frozen-in" birefringence. Following the study of Luap and coworkers [143], it is recommended to refer to the Wi_R time, derived from the longest Rouse time defined by equation 2.9, as this governs the stretch relaxation of polymer chains.

To apply the aforementioned concepts, the birefringence data of the monodis-

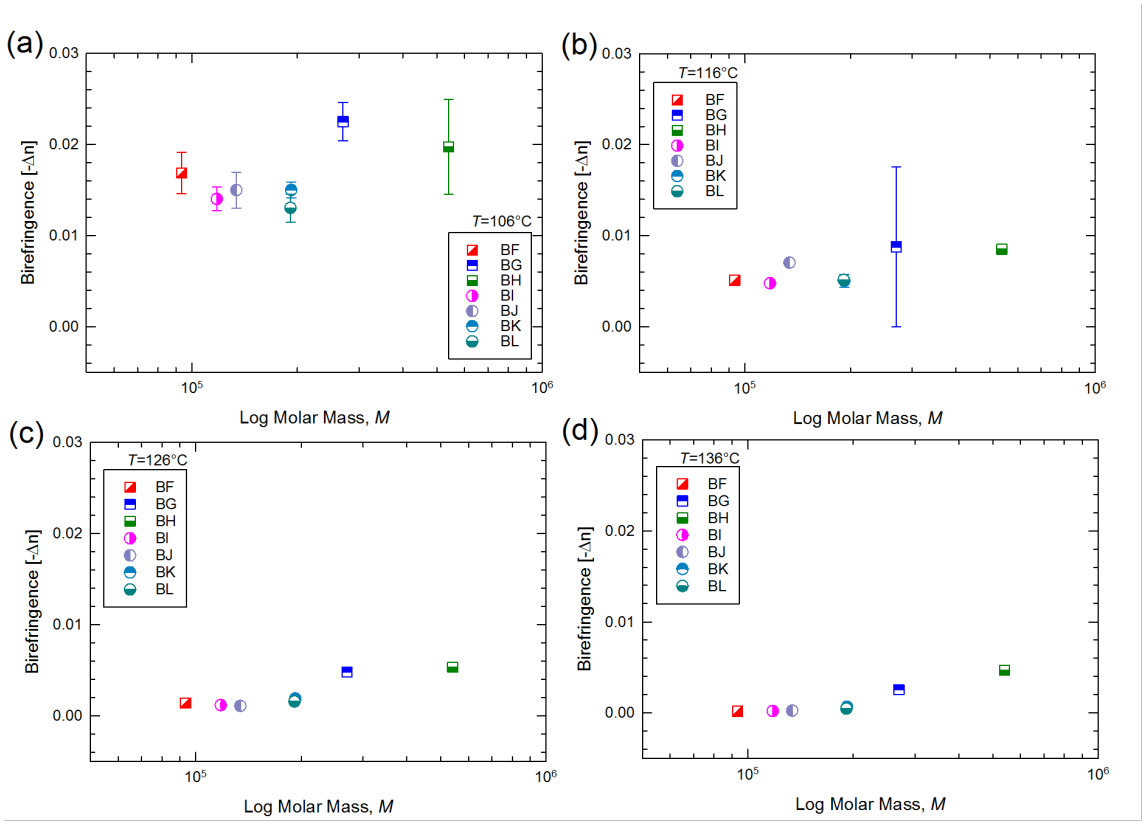


Figure 5.17: -Δn as a function of molar mass, M, and drawing temperature: (a) 106°C, (b) 116°C, (c) 126°C, and (d) 136°C.

perse materials and blends is plotted as a function of drawing temperature in Figures 5.18 and 5.19. The temperatures at which Wi_R=1 for all materials have been calculated and plotted for reference. In [12], De Focatiis reported the Wi_R of polymers AF ($\overline{M}_w$=262 kDa) and AG ($\overline{M}_w$=518 kDa), to be found at 154 °C and 174 °C, respectively, which is in close agreement to the temperatures calculated for Wi_R^{BG} and Wi_R^{BH}. Our materials share a close similarity in their reported $\overline{M}_w$ averages to De Focatiis' data.

From Figures 5.18 and 5.19 two trends can be clearly identified: the first is the already reported decrease in birefringence as drawing temperature is increased. This change can be traced back to the reported Rouse relaxation time of the material, which becomes effective at temperatures above 140 °C as per the quoted Wi_R points. A Weissenberg number greater than unity implies that re-

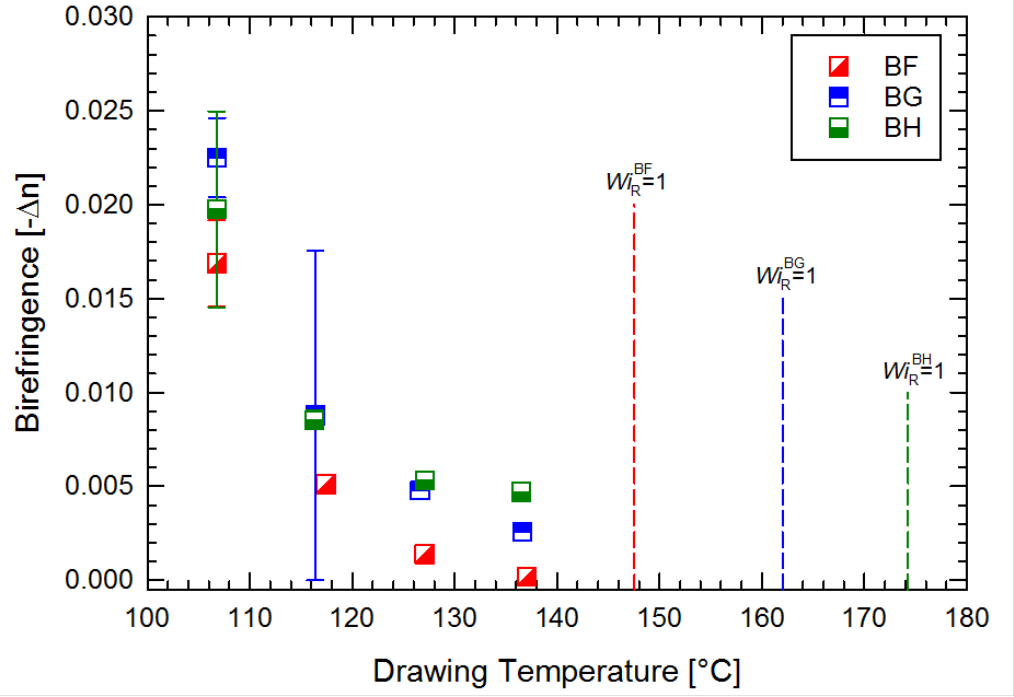


Figure 5.18: Measurements of the birefringence vs. drawing temperature for monodisperse materials BF, BG and BH. Also illustrated are the temperatures at which Weissenberg numbers are equal to unity.

laxation does not occur during stretching on the length scale associate with the corresponding relaxation time [12]. This means, that as the drawing temperature shifts towards a glassy state, Wi increases and thus the material is unable to relax the deformation and chain stretch is frozen in. Secondly, the molar mass, or chain length, dependence associated with longer relaxation times can be identified in the higher birefringence values noted for materials BG and BH when compared to lower molar mass sample BF. In the blends this is even more evident as it is seen that blends BK and BL show very similar Wi numbers, arising from the similarities in their reported $\overline{M}_w$ averages. Now that the orientation of the samples has been characterised in terms of birefringence, it is possible to associate this with craze initiation, as will be explained in the next section.

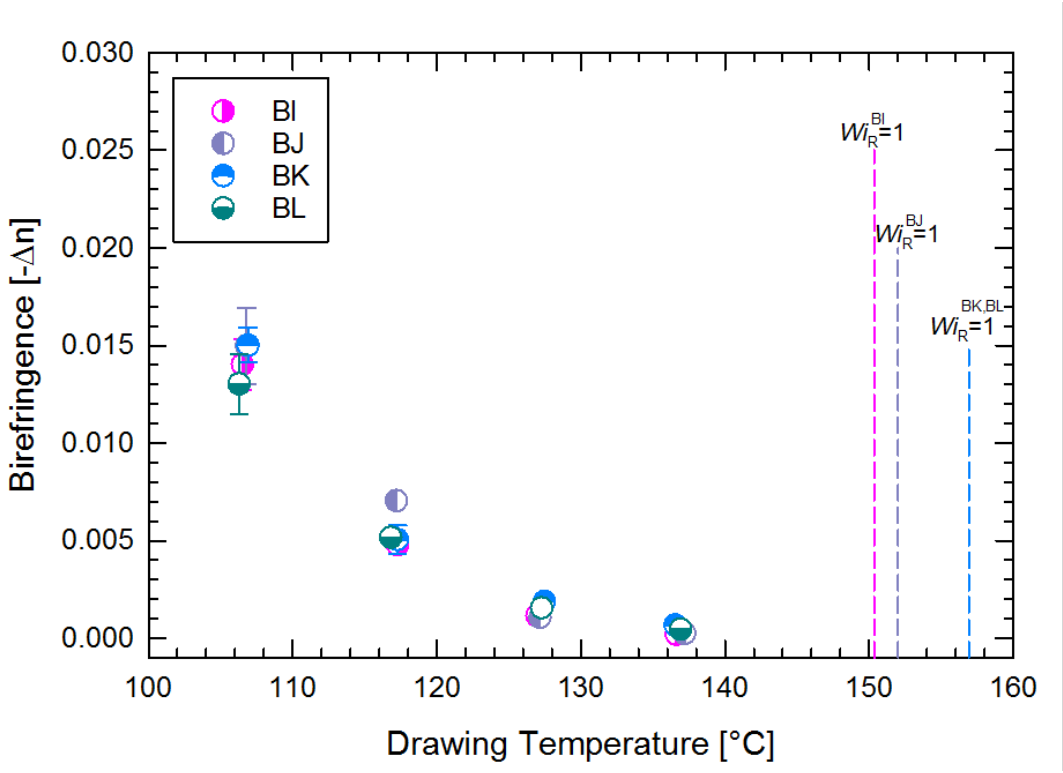


Figure 5.19: Measurements of the birefringence vs. drawing temperature for monodisperse blends BI, BJ BK and BL. Also illustrated are the temperatures at which Weissenberg numbers are equal to unity.

5.7.2 Crazes in oriented specimens

The pattern of oriented crazes has been analysed before by Farrar and Kramer in their study of thin films of PS [144]. TEM analyses showed that the microstructure of crazes was dependent on orientation. The crazes formed in parallel to the orientation direction were many and short. Samples strained perpendicular to the orientation axis were seen to produce a reduced number of longer and wider crazes. From TEM micrographs, Farrar confirmed the existence of a midrib region in the parallel samples that appeared to be absent in the perpendicular specimens. He concluded that the absence of this midrib in the perpendicular crazes reduced the effective strain hardening mechanism, thus preventing the craze from thickening and dissipating the applied load. Quantitative measurements of the volume

fractions of fibrils, v_f, using microdensitometry supported this statement, as the v_f for the perpendicular crazes $\simeq$0.05 was considerably lower than those reported in isotropic (v_f $\simeq$0.25) and parallel (v_f $\simeq$0.45) specimens. This suggests that the load bearing capacity of crazes grown perpendicularly to the orientation axis is reduced compared to those formed in parallel. This argument is consistent with experimental evidence, where the tensile strength of polymer materials is seen to increase when the load is applied in parallel to the drawing direction [145; 146].

In this study, crazes were only formed parallel to the orientation direction. The crazes in bars oriented at temperatures closer to the polymer's T_g (i.e. $\simeq$ 106°) proved challenging to form, in agreement with De Focatiis [21]. The pattern of the crazes was that of a blurry and not well-defined character, almost as fine dots creating an opaque region within the transparent specimen when viewed under the microscope. As the drawing temperature was increased, the crazing pattern became more similar to the long-streaked and well-defined crazes seen in isotropic specimens. In figure 5.20, the evolution of the crazing pattern for blend BI is presented for reference in a series of micrographs. Crazes can be seen to become more defined as the drawing temperature is increased.

In Figures 5.21 and 5.22, the measured crazing stress at $t_c = 300\,\mathrm{s}$ is reported against drawing temperature.

The plots show a remarkable increase of crazing stress as the amount of frozen-in orientation is increased, regardless of the polymer molar mass characteristics. This means that at low drawing temperatures the relaxation of the polymer does not occur on the associated observation length scale. Hence, at these temperatures the polymer relaxation on a sub-entanglement length is repressed, causing a rise in the crazing stress, and eventually suppressing it [21]. At higher drawing temperatures, the relaxation time of the polymer becomes more significant within the observation time frame, and as a result the crazing stress drops, almost reaching the level of isotropic samples. These results correlate with what is observed in the micrographs, since at low drawing temperatures it was really difficult to observe any well defined crazes, as per the suppression mechanism described by De Focatiis [21]. One noticeable remark is the inherently lower σ_c value observed for material BH at 106°C compared to its counterparts BF and BG. The reason for this discrepancy may come from the fact that the miniature specimens used

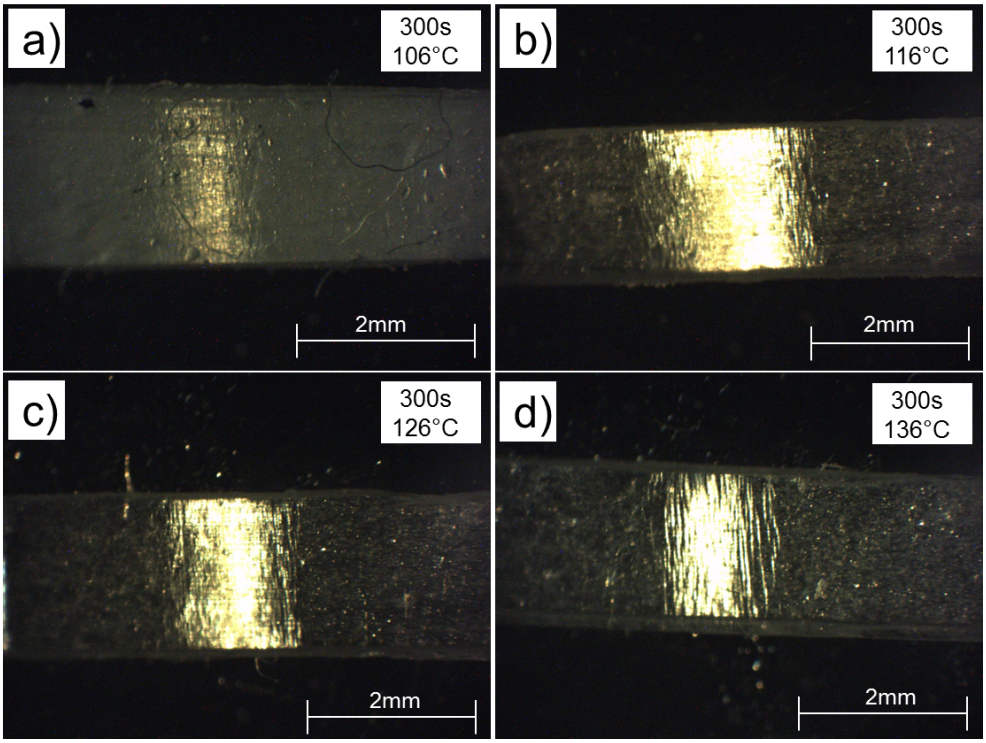


Figure 5.20: Micrographs of crazing pattern of oriented monodisperse blend BI at different drawing temperatures: (a) 106 °C, (b) 116 °C, (c) 126 °C, and (d) 136 °C.

for crazing tests, were taken at the gripping ends of the oriented samples, and hence may have experienced some additional relaxation that could have dropped the orientation and hence crazing stress of the samples.

Following the format used in [21], the σ_c values for the oriented specimens are presented in Figures 5.23 and 5.24 in plots of comparative $\sigma_c - \sigma_{c,iso}$ vs -Δn. The graphs illustrate the average increase in crazing stress for each test condition relative to the mean for isotropic specimens, plotted versus the average birefringence measured on the actual miniature beam crazing specimens. A limit for linearity of the stress-optical rule for PS was selected at 1.6 MPa [143], corresponding to a birefringence of -0.0072. The linear regression data published in[21] is shown in the data as solid lines, while Δn=-0.0072 is delimited with a dashed line.

Analysing these graphs, it can be observed that at low levels of birefringence ($\leq$-0.0072), the monodisperse materials and their bimodal blends appear to follow

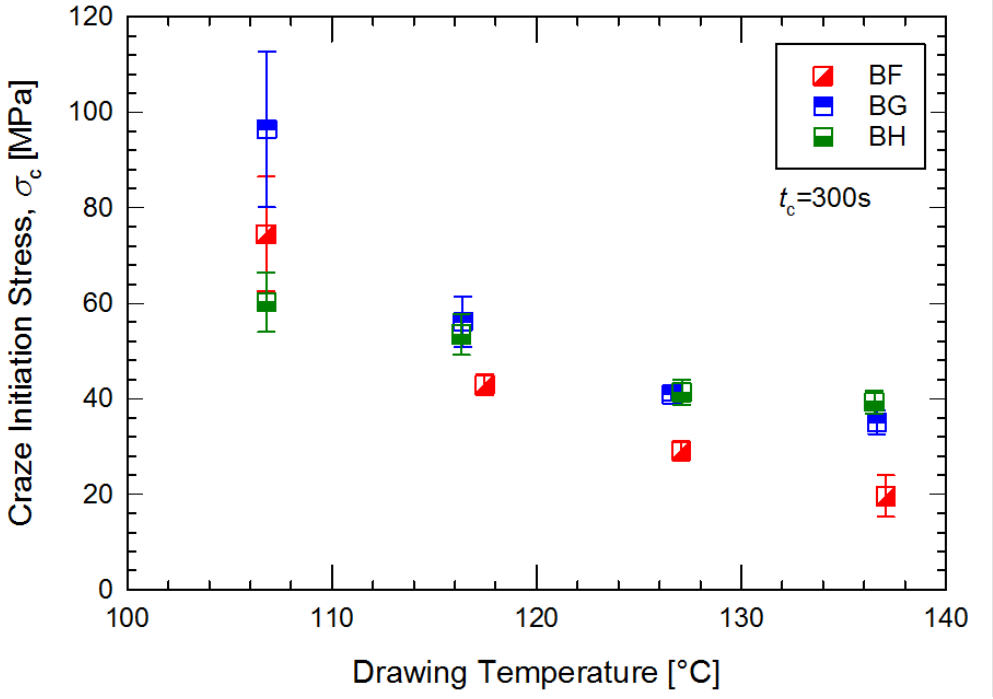


Figure 5.21: Measurements of the crazing stress vs. drawing temperature for monodisperse materials BF, BG and BH.

the linearity of the stress-optical rule suggested in [21]. Furthermore it shows that the crazing stress is influenced by the degree of orientation independently of the molar mass of the materials. At higher birefringence values ($\geq$-0.0072), the materials stop following the linearity of the stress-optical rule and the scattering of the data preludes a more conclusive determination.

The similarity between the crazing behaviour in oriented materials of varying molar mass studied here, and the study performed by De Focatiis in monodisperse samples confirms that in oriented specimens molecular stretch is primarily what controls the increase in crazing stress. σ_c is found to rise with increasing orientation, and it relaxes back to the value of isotropic specimens on a timescale associated with the longest Rouse time of the polymer. The data reported here has not yet been published, and could provide an excellent platform for the further exploration of the theory of crazing in oriented polymers applied to PS blends of

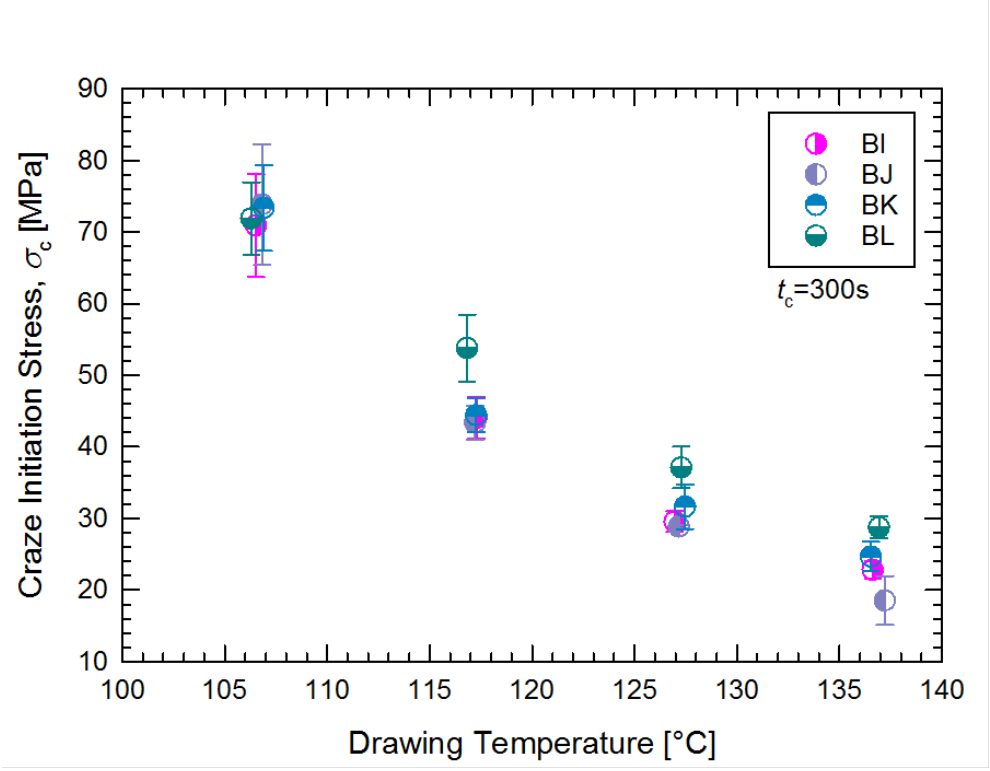


Figure 5.22: Measurements of the crazing stress vs. drawing temperature for monodisperse blends BI-BL.

any given molar mass.

5.8 Conclusions

This chapter has studied craze formation in a series of PS systems, ranging from low polydispersity levels to highly complex polydisperse blends. A θ-parameter inspired by polymer theory of molar mass distributions, was included into De Focatiis' piecewise linear model [20], and applied to the molar mass distributions for the prediction of CIS in monodisperse systems. Good agreement (70%-90% accuracy) was achieved when predicting CIS values for the monodisperse systems, monodisperse bimodal blends and mildly polydisperse materials, but the model failed to capture the behaviour of highly polydisperse bimodal blends. To capture

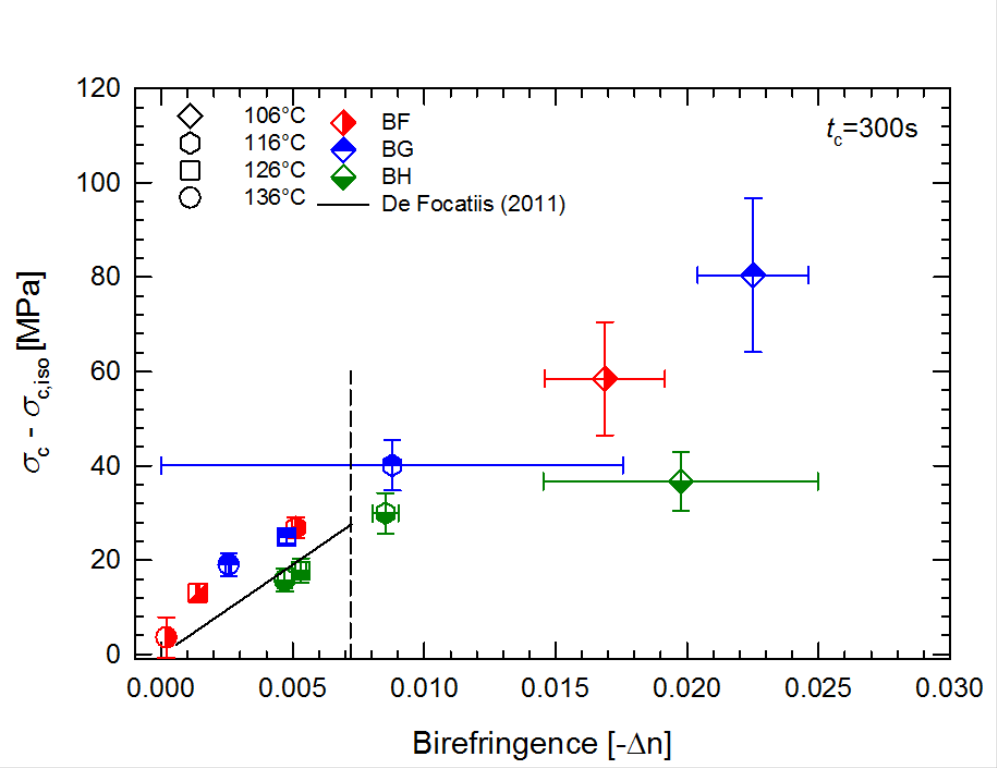


Figure 5.23: Measurements of the increase in crazing stress relative to that of isotropic specimens in monodisperse systems BF, BG and BH, plotted versus the birefringence, $-\Delta n$, measured directly on the crazing test specimens. Dashed line represents the limit for linearity of the stress-optical rule, while solid line represents De Focatiis [21] birefringence linear prediction for monodisperse materials.

this behaviour an additional DTD effect was incorporated into the theory, leading to a remarkable improvement of up to 50% accuracy in predicting σ_c for these systems. DTD assumes that the saturation of the system by short chains (too short to entangle), causes the concentration of long chains to drop, thus decreasing Z into an effective Z', and hence reducing the ability of the entanglement network to sustain stable craze formation.

Additionally, crazing was studied in bimodal monodisperse blends as a function of frozen-in orientation. The theory of crazing in oriented polymers of Maestrini and Kramer [94] was applied following De Focatiis and Buckley's [21] study in monodisperse PS. The results confirm that in drawn blend specimens,

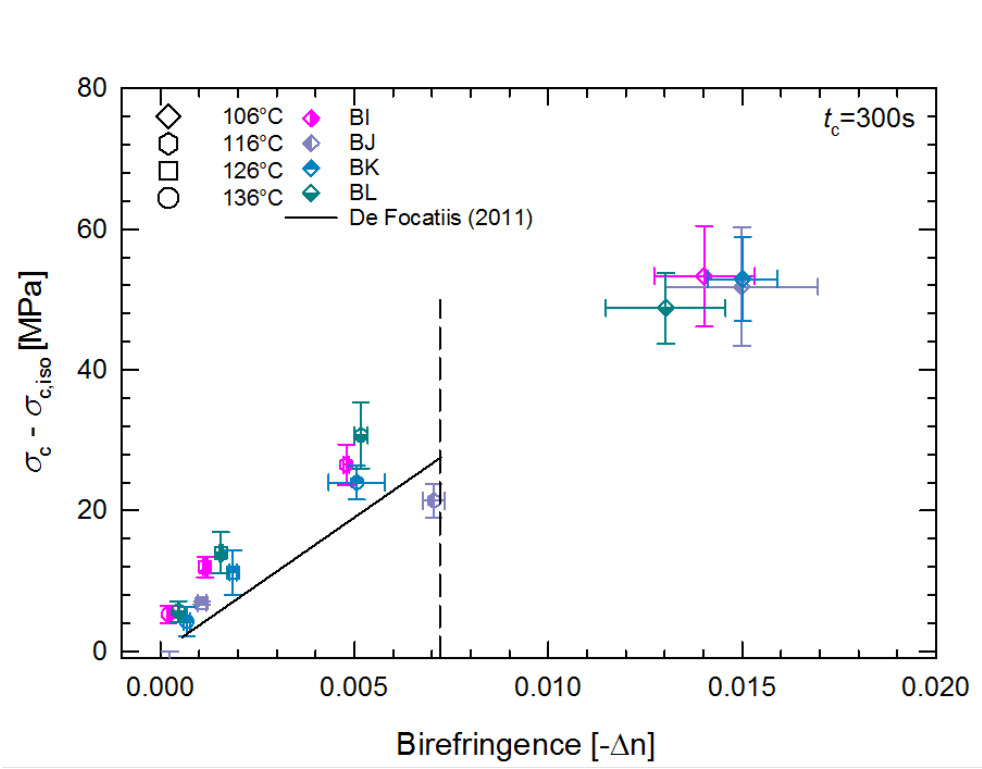


Figure 5.24: Measurements of the increase in crazing stress relative to that of isotropic specimens in bimodal blends of monodisperse systems BI, BJ, BK and BL, plotted versus the birefringence, $-\Delta n$, measured directly on the crazing test specimens. Dashed line represents the limit for linearity of the stress-optical rule, while solid line represents De Focatiis [21] birefringence linear prediction for monodisperse materials.

orientation controls the rise in crazing stress over molar mass, at least at birefringence levels where the linearity between the stress-optical rule applies.

This work has presented novel values for the σ_c of PS bimodal monodisperse and highly polydisperse blends. The extreme complexity of growing crazes in samples with a high % of unentangled fractions proved challenging, particularly due to the inherently extreme brittleness of the specimens, with some corresponding adaptations having to be put in place; still, small crazes in the form of concentrated spots could be detected by optical microscopy. The relevance of the obtained results, is that they allowed for the further development of an

existing crazing model ([24]) to include other effects such as active dilution of the entanglement network by the lower molar mass tail of the distribution, which before was only assumed to have no contribution. This effect is now captured by the enhanced model, and is consistent with other crazing mechanisms that have been previously described by other authors [15; 17; 18; 89; 90; 91; 128], but never tested before in systems with such high levels of polydispersity.

The study of crazing and birefringence in oriented bimodal blends of varying molar mass has provided novel data for the extension of the research initiated by De Focatiis [21] which suggested to use birefringence as a predicting parameter, to be used in conjunction with constitutive models [12] when looking at predicting the crazing stress of PS systems, regardless of their molar mass and process history characteristics.

Chapter 6

Rheological Analysis

6.1 Prelude

The SEC and DSC characterisation of the studied materials was reported in chapter 4 on page 105. SEC analysis enabled characterisation of the variations in the molar mass distributions and molar mass averages of the monodisperse, polydisperse and blends systems. DSC showed that, in materials with a higher content of unentangled fractions, considerable decreases in T_g were reported. Using a model by Lodge and McLeish [29], it was possible to see that the influence of the interactions between short and long molecules cannot be simply quantified by mere weight of blending fractions, and often dilution effects should be accounted for when examining the effective relaxation behaviour of binary and polydisperse blends. In chapter 5 on page 139, the model of De Focatiis [20] for the determination of the craze initiation stress was refined through the inclusion of a DTD effect derived from polymer melt physics. By consideration of this mechanism, the CIS of highly polydisperse PS blends could be better simulated. Whilst it has been experimentally feasible to make use of rheological concepts to model the solid-state of mechanically observed phenomenon, it is known that some aspects of non-linearity can be better characterised through the shearing of polymers in their molten state. Hence, the purpose of this chapter is to make use of the

latest rheological theories to explain the phenomenologically observed responses of the studied materials when tested under oscillatory shear, steady shear and elongational shear.

6.2 Validation of LVE configuration

Rheological tests were performed in oscillatory shear, transient shear and extensional modes as described in section 3.7. The rheological tests in this study were performed using an Anton Paar MCR-302 rheometer in air atmosphere. The size of the plates matches the size of our press-moulded discs, hence additional discs were produced for rheology following the method described in section 3.4. The results of these tests are presented below.

Linear rheological measurements were collected through steady-shear oscillation tests using a 25 mm parallel plate geometry with a 0.5 mm gap size in air atmosphere. Frequency sweep tests were carried at an angular frequency, ω, between ω =0.1 s^{-1}-100 s^{-1}, and a temperature profile of T =120 °C-200 °C.

The initial test consisted of a small assessment using material R to verify the accuracy of the equipment and data acquisition of the Anton Paar rheometer. The idea was to compare the obtained data with the data reported previously by De Focatiis [10], using a cone and plate configuration. Therefore, two tests were performed: the first one using a 25 mm parallel plate configuration, and the second test using a cone and plate set up with a cone of 0.3 ° and 25 mm diameter. The data obtained at each temperature was then shifted using time-temperature superposition in REPTATE (as explained in section 3.7.4), to provide a single master curve for each polymer at a reference temperature of 170 °C. The results for these experiments are presented in Figure 6.1.The data has been presented colour coded, with blank symbols for the storage modulus(G'), and centre-dotted symbol refers for the loss modulus, G" . The data published by De Focatiis has been included for reference.

From these results it is possible to observe that the data is not influenced by the rheological configuration of choice (either parallel plates or cone and plate). Similarly, a good agreement and superposition in the plots is observed, showing

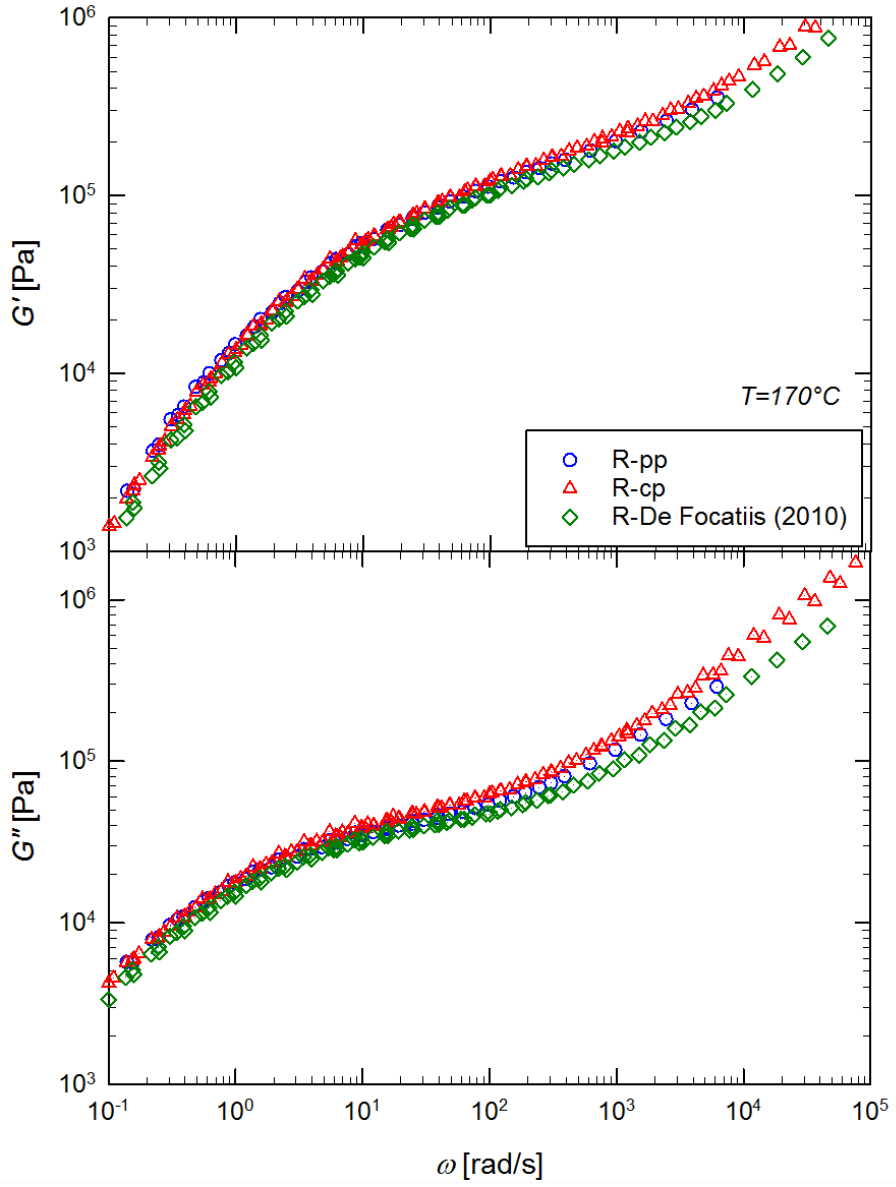


Figure 6.1: G' and G" moduli at 170∘C using TTS, for polymer R: using parallel plate (pp), using cone and plate (cp) and reported by De Focatiis[10].

good repeatability in the material response as measured by our equipment, as well as in comparison to the results obtained by De Focatiis. The remaining materials were all characterised using only the parallel plate configuration for the

outstanding oscillatory trials.

6.3 LVE monodisperse material parameters

As it has been previoulsy stated, the first step in the analysis of rheological data is to establish intrinsic material parameters, M_e, G_e and τ_e. In order to define these, we used the oscillatory data obtained from testing our linear monodisperse PS melts (BF, BG and BH); the data was then uploaded into the optimizer REPTATE and the microscopic theory of linear polymer melts of Likhtman and McLeish [80], L-M, was applied. Material parameters M_e, G_e, and τ_e were calculated by treating them as variables to yield the best fit of the L-M theory for monodisperse materials. This "calibration" approach is common and has been used by various authors [6; 7; 9; 10]. The values of the parameters obtained are as follows: $M_e = 15.9\,\text{kDa}$, $G_e = 253.6\,\text{kPa}$ and $\tau_e = 0.0014\,\text{s}$. Figure 6.2 presents a $G', G"$ vs. Frequency mastercurve plot of the fit of the L-M prediction (lines) and data (symbols).

As it can be seen the data and theory fit nicely together in graph 6.2. The accuracy at the higher end (higher frequencies) tends to drop, since the model breaks when entering the glassy regime. The error between the data and the theory reported by REPTATE is based on an error minimisation method using a downhill simplex algorithm for data fitting. What this means is that the data is analysed as a function over constrained variables (e.g. theory parameters), and the resemblance between the calculation and the data are compared and averaged to provide a mean error value. Values closer to zero represent high similarity between the data and the theory, whilst interger numbers represent considerable deviations. The error reported between our experimental data for materials BF, BG and BH and the LVE response predicted by the L-M theory is in the region of 0.01. Details of the error for each individual material are presented in Table 6.1.

In table 6.2 we compare our obtained parameters against those identified for polystyrene in recent literature [6].

The parameters agreeably lie within the limits of current published data, and

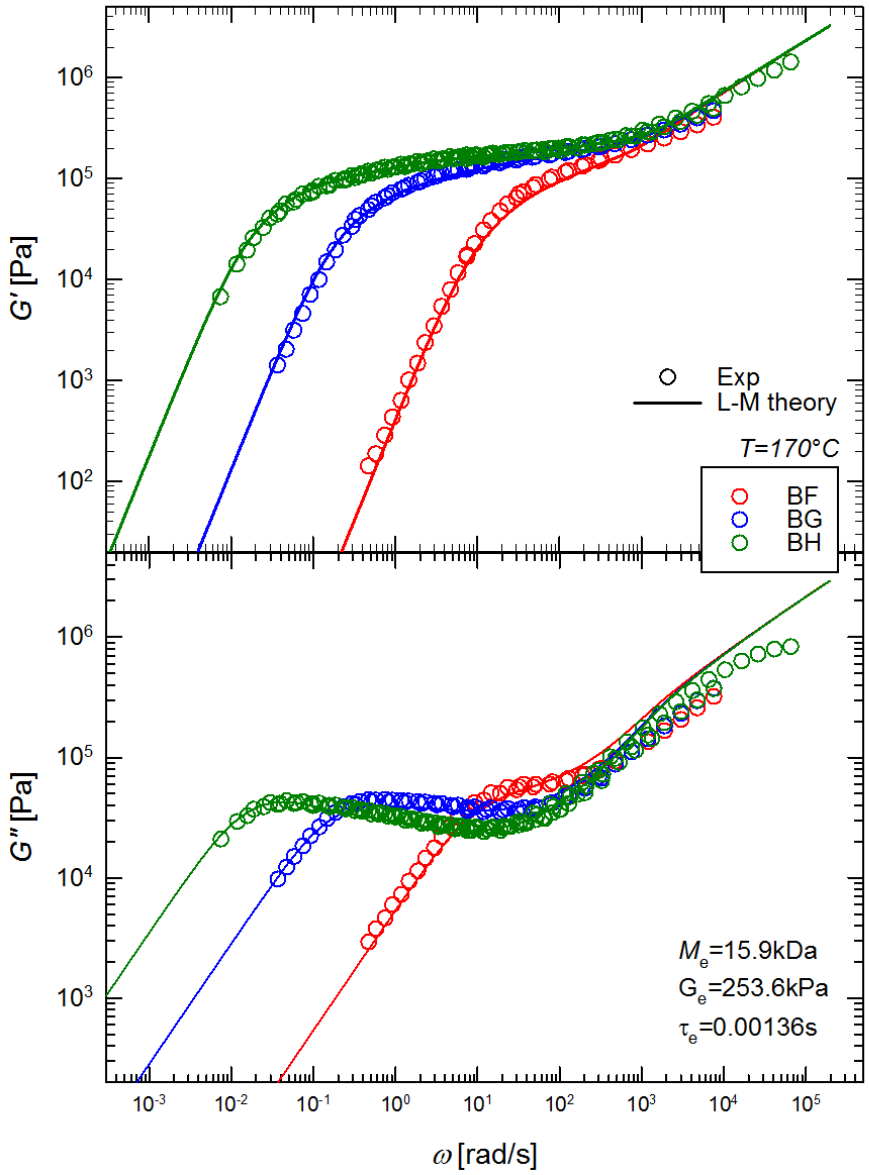


Figure 6.2: Master curve plots for monodisperse materials BF, BG and BH (symbols), plotted against REPTATE simulations using the L-M theory (lines), and obtained fitting parameters M_e, G_e, τ_e.

hence will be used as the material parameters of choice for further simulations made in this study.

Table 6.1: Prediction error between L-M theory and monodisperse materials BF, BG and BH.

Material	L-M theory error
BF	0.012
BG	0.004
BH	0.002

Table 6.2: Material parameters for PS, adapted from[6].

Publication	M_e [g/mol]	G_e [MPa]	τ_e [s]	Temperature [°C]
Likhtman [7]	14470	0.275	0.00092	169.5
VanRuymbeke [76]	18500	0.25	0.0008	170
Park-Larson [147]	14400	0.25	0.0033	167
VanRuymbeke [148]	16000	0.2625	0.0008	169.5
Pattamaprom [149]	16625	0.25	0.002	169.5
This study	15900	0.25	0.0014	170

Basic interpretation of linear and non-linear data requires easy access to fundamental material values, linear parameters and calculated parameters. Following the format suggested in [9], the data for the studied monodisperse PS systems is presented for references in Table 6.3. The reptation time, τ_d was computed using REPTATE.

Table 6.3: Parameters for the studied monodisperse materials. Material parameters are as obtained from SEC analysis, linear parameters are obtained from linear oscillatory shear, and calculated parameters are computed from the other parameters.

Material values				Linear parameters			Calculated parameters		
Code	$\overline{M}_w$ [kg/mol]	c	PDI	G_e [MPa]	τ_e [s]	M_e [g/mol]	Z	τ_R [s]	τ_d [s]
BF	93.4	1	1.08				5.87	0.05	0.17
BG	269.9	1	1.07	0.253	0.0014	15900	16.97	0.39	7.70
BH	540.3	1	1.15				33.98	1.56	85.08

6.4 PS materials LVE master curves

Once the material parameters have been defined, the next step is to produce the master curves for the oscillatory data of the systems analysed in this study. The results are detailed in the upcoming subsections.

6.4.1 Monodisperse blends

The first set of data was that of the bimodal monodisperse blends; the data is presented in Figures 6.3 and 6.4. These plots show nicely how as the higher molar mass component is added, the blend starts to shift slightly to the left, as per the increase in the relaxation times previously noted by [6]. It is also possible to see how the plateau region is extended, a signature of the entanglements, and longer chains. Finally, a set of "shoulders" can be observed in the lower frequency region, resulting from the combined contribution of longer and shorter chains, this, as discussed in the literature 2.5.1, can yield to lower compliance values resulting from a broadening of the distribution of relaxation times. In his comparative study of monodisperse binary blends, Watanabe [70] notes that the position of the shoulders depends little on the long chains, but the height does increases with the addition % of long chains, replicating the results observed in this study.

6.4.2 Polydisperse and blends

The analysis of the polydisperse blends data was somehow less straight forward. Due to the great difference in T_g between the higher constituent material BY and the matrix polymer BX, it deemed necessary to find a more appropriate processing method to ensure a better comparison of their viscoelastic responses and respective blends. Shahid [8] has previously reported a method [150] to work under the iso-T_g condition. This procedure ensures the data is at a constant distance from the reference temperature, T_{ref} by considering the differences between this and the polymers' T_g. Hence, the data for the master curves are created by obeying the condition T_{ref}-T_g=constant. Although Shahid was able to shift the data using this method to ensure a good overlap of the viscoelastic response in

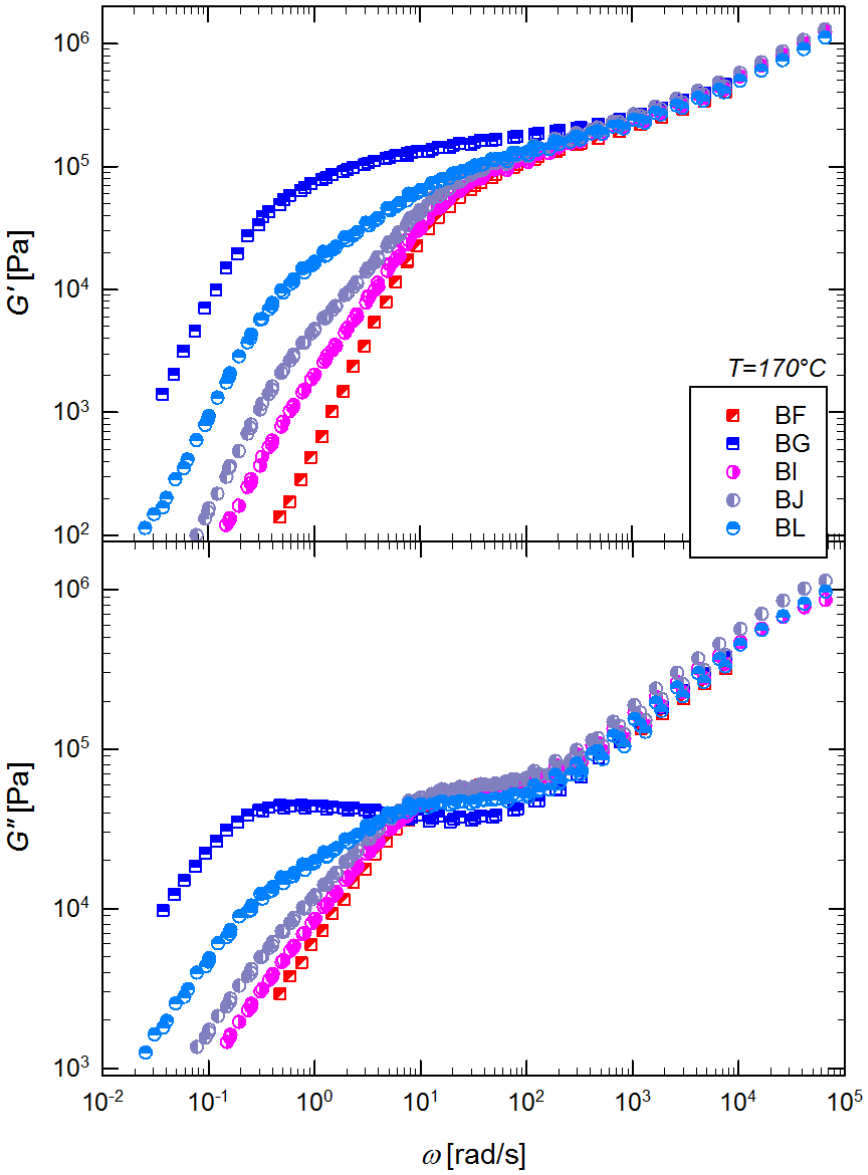


Figure 6.3: Master curves of monodisperse materials BF and BG, and their corresponding blends.

the high frequency region for his diluted blends; the method proved to be less successful for our data as the differences in T_g found between our materials are in the order of 22 °C-45 °C compared to Shahid's range of 2 °C-12 °C. It was found

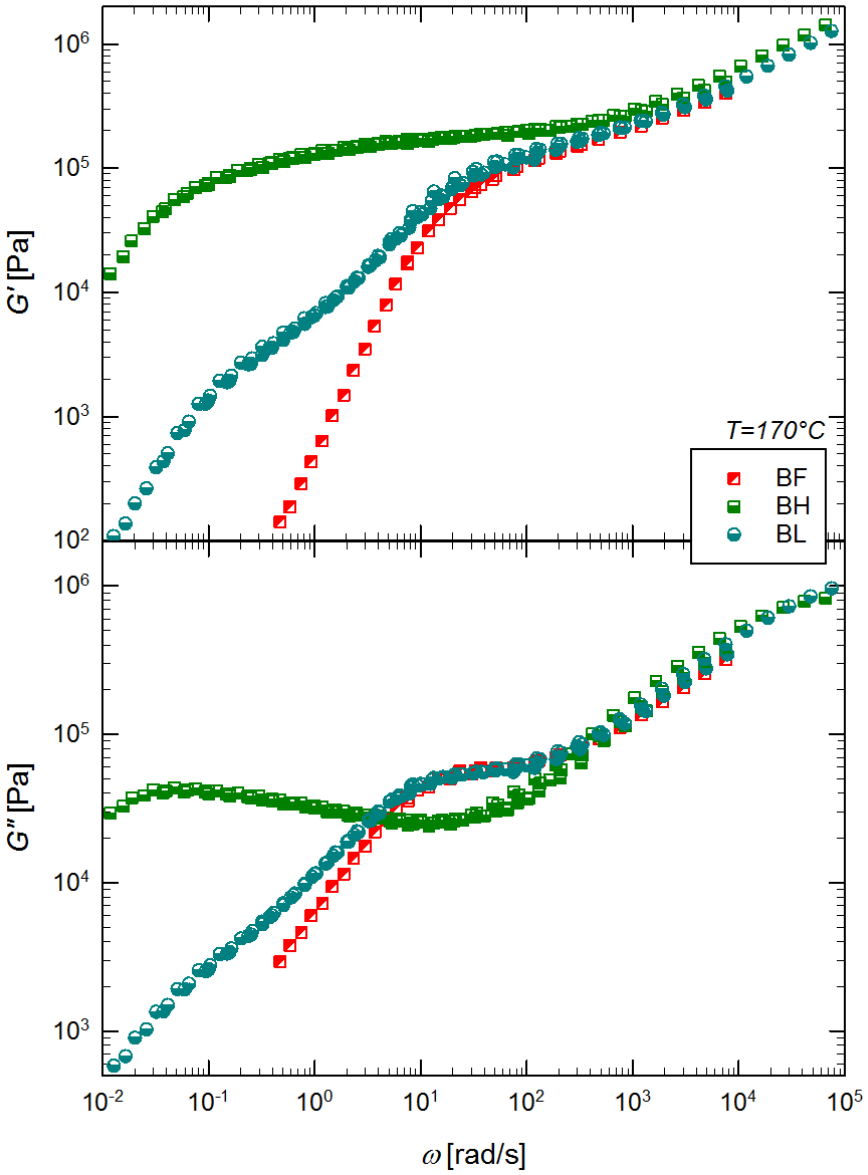


Figure 6.4: Master curves of monodisperse materials BF and BH, and their corresponding blend.

that such great deviations between T_g were too large to produce suitable shifting parameters that could work for all of our polydisperse materials.

In view of these challenges, an alternative method was selected. We applied

the approach proposed by REPTATE [102], which states that when shifting the LVE data of very short chains it is important to consider the dependence of T_g with the molecular weight of the sample. This change is roughly related to the amount of free ends (i.e. $\overline{M}_n$). To enable this consideration in TTS, the following phenomenological expression is used:

$$T_g = T_g^{\infty} - \frac{CT_g}{\overline{M}_n} \tag{6.1}$$

This leads to a modified equation for the horizontal shift from 2.4 to equation 6.2.

$$\log_{10} a_T = \frac{-C_1(T - T_0 + \frac{CT_g}{\overline{M}_n})}{T + C_2 + \frac{CT_g}{\overline{M}_n}} \tag{6.2}$$

It has been stated that the dependence of free ends in T_g, is described by a $1/\overline{M}_n$ relationship[3; 4; 5]. This follows the argument that at lower T_g the amount of free ends is increased, and hence the molecules are more mobile due to higher amounts of specific volume. Through this relationship, it is possible to retrieve CT_g from T_g vs $1/\overline{M}_n$ plots, as the value of slope k. In Figure 6.5 we use the DSC data in section 3.3, to obtain CT_g.

Linear regression on the data yielded a value of CT_g =58.348. This value was input into REPTATE to obtain the best TTS fit for the polydisperse and blends materials master curves with the use of expression 6.2. The data for the polydisperse materials and the blends obtained by solution blending is presented in Figure 6.6, while the data for the polydisperse blends produced through melt-mixing is shown in Figure 6.7. This sort of correction method due to differences in the glass transition temperature arising from variations in molar mass is not uncommon, and in fact other authors have reported corrections of the sort when dealing with the characterisation of diluted monodisperse PS systems [151].

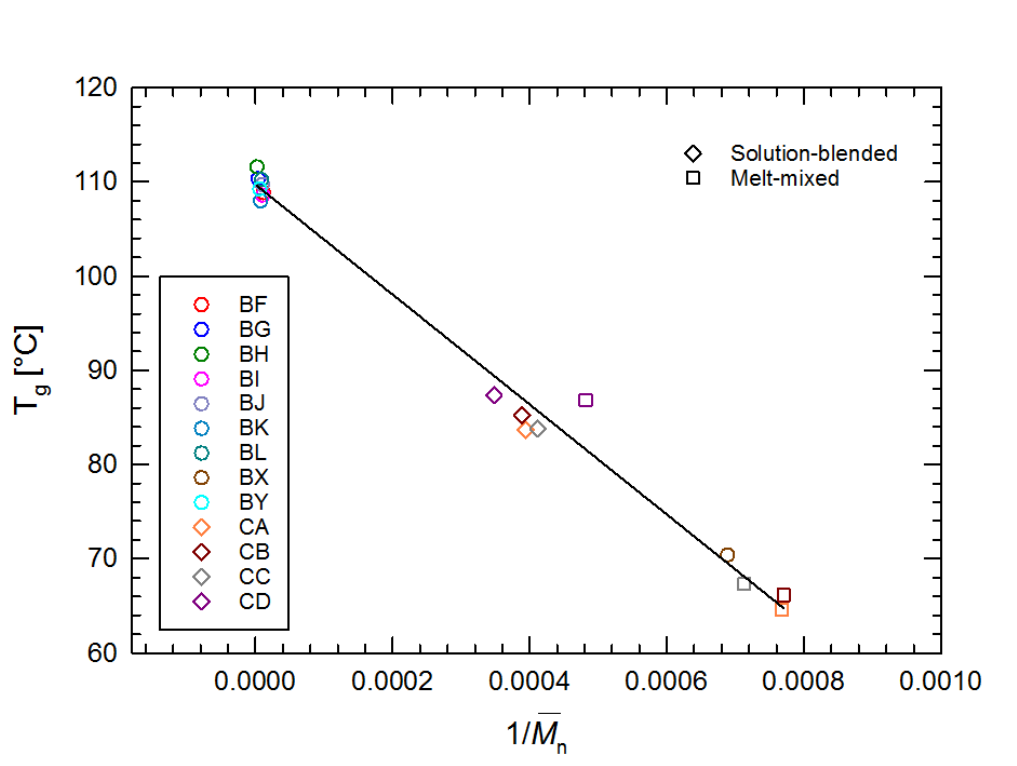


Figure 6.5: T_g dependence on $1/\overline{M}_n$.

From Figures 6.6, and 6.7 it is possible to see that the G_e plateau and transitioning slopes for $G' = 2$ and $G" = 1$, are less pronounced than those seen in monodisperse materials, which is characteristic of polydisperse distributions. This is associated with the wider breath of the polymer distribution, where the relaxation times are greatly spanned towards a much larger range. In the graph, this effect is perceived in the longer extent of the G_e plateau, with a more curved shape rather than the almost perfect horizontal line observed in the monodisperse materials. This is correspondingly observed in the less pronounced transitions into the terminal zone (lower frequencies). Although G_e is considered a material parameter, one can still identify a slight drop in the plateau as this goes to lower molar mass values. This effect is even more noticeable in the melt-mixed data, where there is a significant difference between material CD and the rest of the blends. An additional observation is the shape of the response of material BX,

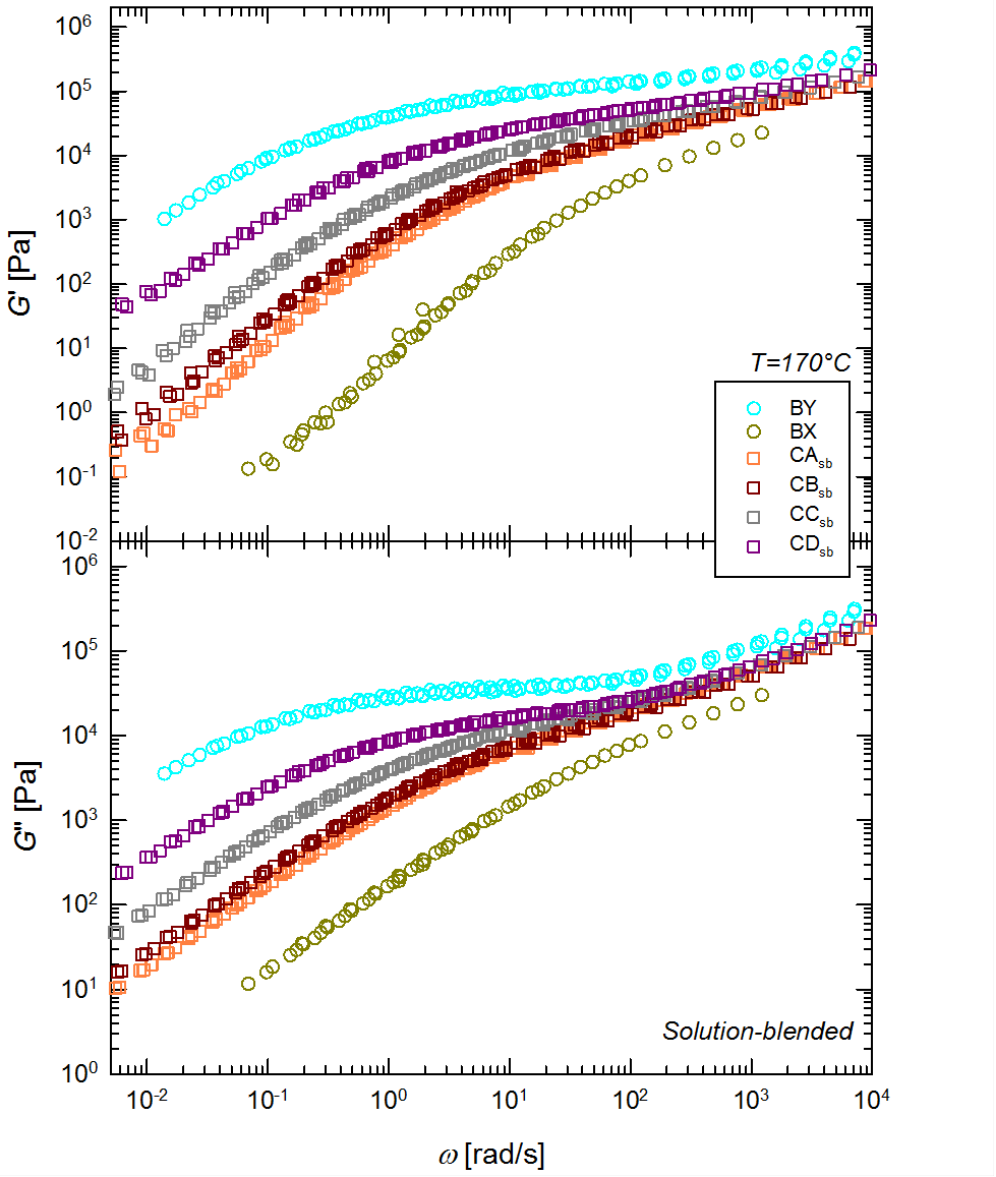


Figure 6.6: Master curves of polydisperse materials BX and BY, and their corresponding blends obtained by solution blending.

characteristic of unentangled chains [6].

The raw data presented here will be analysed with the corresponding LVE theories in the upcoming section.

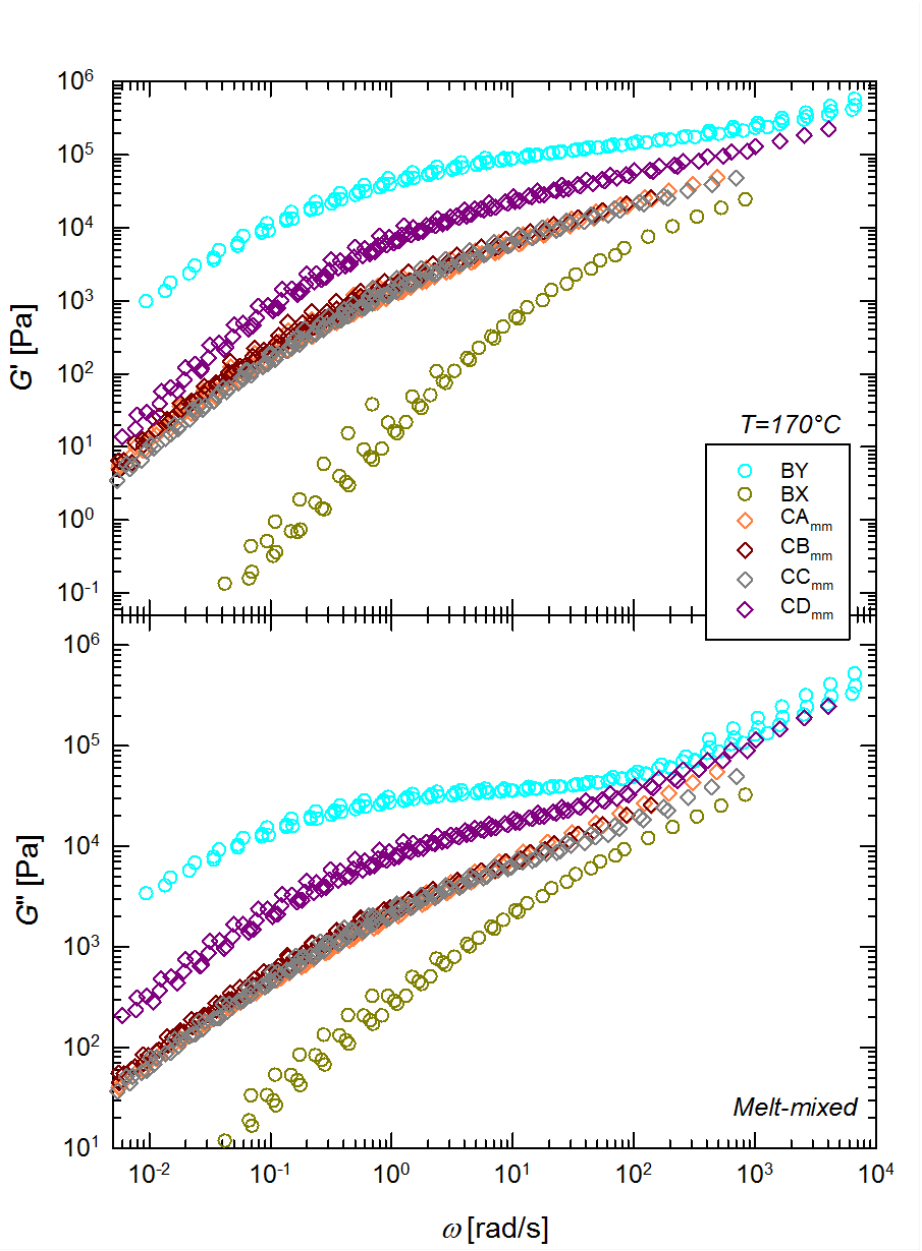


Figure 6.7: Master curves of polydisperse materials BX and BY, and their corresponding blends obtained through melt mixing.

6.5 REPTATE LVE simulations

In section 2.5.1, current LVE models to predict the viscoelastic responses of polymer melts were discussed. One of the benefits of REPTATE is that it encompasses a rheological library of latest theories to fit specific experimental data. The advantage is that through the use of REPTATE these models can be assessed by comparing the reported error between experimental data and the chosen rheological model. In these sections the latest LVE models for binary blends and polydisperse materials are applied to our polydisperse systems, as well as to monodisperse and polydisperse blends to evaluate their predictive accuracy. The whole purpose of this analysis is to identify where the theories fail, and where there is some agreement between them on the treatment of multiple relaxation times derived from the multiplicity of chain lengths.

6.5.1 Polydisperse materials: pDR theory

The first theory we made use of is the polydisperse double reptation theory, pDR, first proposed by des Cloizeaux [152] and Tsenoglou [75]. REPTATE's treatment of this model incorporates CLF, CR and longitudinal stress relaxation along the tube through the application of the L-M theory [7]. CR is treated by assuming double reptation ($\alpha = 1$), by fitting parameters M_e, G_e, τ_e and M_0, where M_0 refers to the molecular weight of a Rouse monomer. One extremely useful feature of REPTATE is that when applying the LVE pDR theory, it is possible to extract the MWD data directly from a GPC file. Taking des Cloizeaux approach, the relaxation in the pDR model can be defined by considering that the stress points between two molecules of different sizes, a short chain $-_S$, and a long one $-_L$, will disappear if one of these two chain relaxes. The relaxation is thus a product of the additive contribution of the unrelaxed fractions of the initial tube at time, (t). In its simplest form, the generalised expression for the pDR theory is given by equation 6.3 [6; 39; 152; 153].

$$G(t) = G_N^0 \left[\sum_M \phi_M (F_M(t))^{1/2} \right]^{\alpha} \tag{6.3}$$

where the term $F_M(t)$ represents the unrelaxed fraction measured on the scale of monodisperse polymer species M (i.e. μ_M), including the double reptation effect.

The theory is known for its suitability to predict the behaviour of polydisperse systems, and hence it was applied to materials R, BX and BY. In this study parameters M_e, G_e, τ_e are extracted from the value obtained for the monodisperse materials, while variables M_0 and α are fitted by the model. The MMD data was input into REPTATE by uploading the materials' corresponding GPC files. Comparative G'-G" plots between experimental data and theory predictions are presented in Figure 6.8, the error values between experimental and theory are shown for reference in Table 6.4.

Table 6.4: Prediction error between pDR theory and polydisperse materials.

Material	pDR theory error
R	0.024
BX	2.378
BY	0.013

The double reptation model seems to work well for the data of materials R and BY with error estimates below 0.025. Because this model is based in the assumption that an entanglement between two chains relaxes as one of the chain diffuses away, it works best when the relaxation times in the polymer are not too different [6]. This is why it appears to fail when trying to account for the behaviour of material BX, as this represents a very polarised distribution with a high degree of unentangled fractions considerably below the critical molecular weight for an entanglement ($M_c = 2M_e$). Further extensions based on the double reptation model include Carrot's [153] where the premise is to consider various relaxation processes occurring simultaneously (a.diffusion of the chain, b.diffusion between entanglements, and c.local motions, i.e. high-frequency relaxation processes), and assume an additive contribution based on a mixing rule. In this mixing rule the kernel, or surviving fraction of original tube segments at time (t), is described by a function of relaxation times representative of a distribution of monodisperse species, M (e.g. $F(t, M)$). Most recently, Leonardi [154], improved Carrot model by recognising the effect of tube renewal, which means that in a

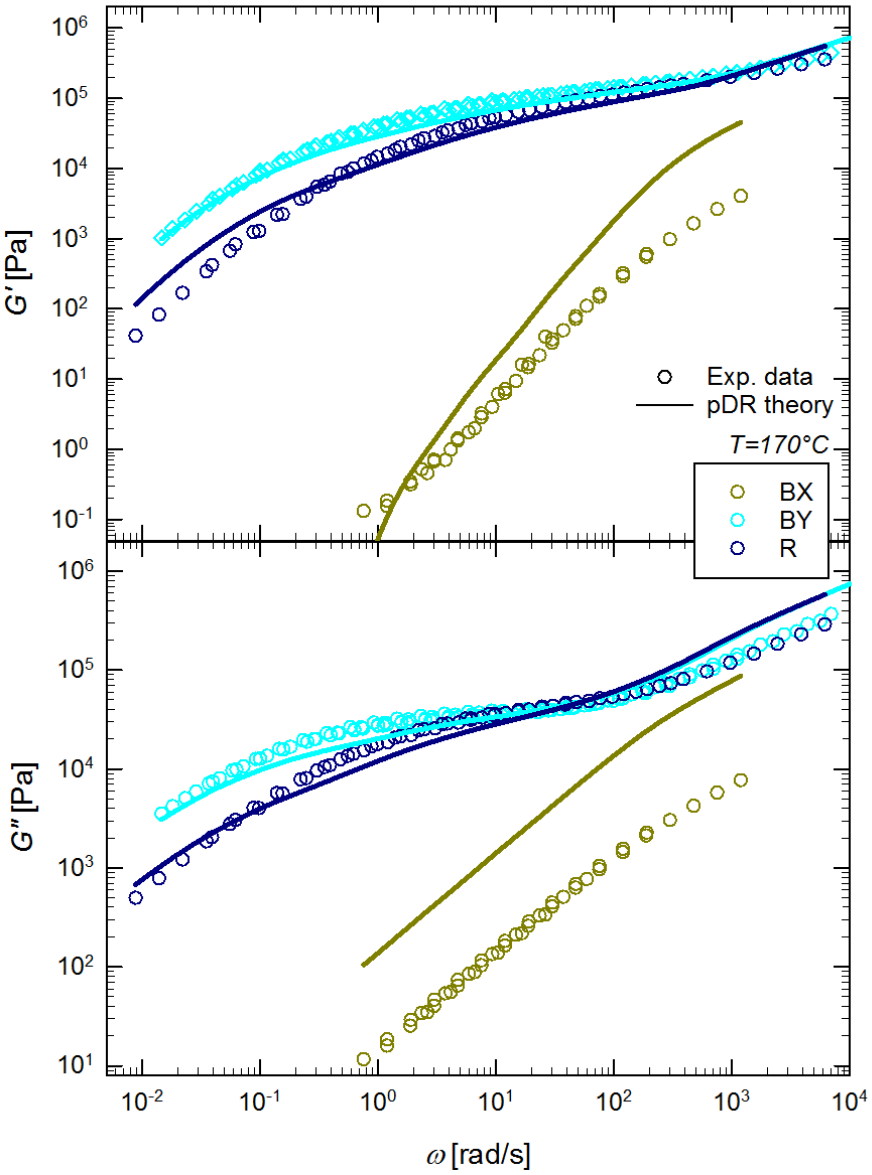


Figure 6.8: Master curve plots for polydisperse materials R, BX and BY (symbols), plotted against REPTATE simulations using the pDR theory (lines).

polydisperse environment the chain does not stay in a fixed tube, the tube itself is time dependent, and may change or disappear as the surrounding chains that define it start to diffuse. The data reported in this study for polydisperse PS sug-

gests that the predictive accuracy of the pDR theory including the effect of tube renewal seems to only really improve the terminal relaxation time of polydisperse systems with PDIs of >3. Nevertheless, for well-entangled samples with smaller polydispersity ($\sim$ 2), tube renewal effects were negligible. Materials R and BY are representative of the latter, which means that the prediction obtained from REPTATE is indicative of this state of the theory, and hence approximates to the best quality of simulation that can be achieved. For material BX, it would appear as if the current rheological theories provided by REPTATE are still not capable of decoupling the effects associated with such high levels of polarised polydispersity (in fact material BX is a bimodal highly polydisperse polymer). Leonardi's model went as far as to account for reasonable predictions in a PS material with a PDI=3.4. The calculated level of polydispersity in material BX is PDI=32.9, certainly far from the estimations tested by Leonardi. In the next sections, the accuracy of the pDR model is compared against Rubinstein and Colby's model for binary mixtures in the rheological data of our monodisperse and polydisperse blends. Here, the contributions and limitations of both theories are highlighted in further detail.

6.5.2 Blends: R-C and pDR theories

6.5.2.1 Monodisperse blends

In the case of binary monodisperse blends the theory developed by Rubinstein-Colby, R-C [74; 155] offers some solid ground to determine their rheological properties. REPTATE handles this theory by defining parameters based on the molar mass information of the blend; namely the $\overline{M}_w$ of the its constituents ($\overline{M}_{w1}$ and $\overline{M}_{w2}$), as well as their blending ratio by mass, ϕ (which refers to the wt% of $\overline{M}_{w1}$). The R-C theory considers that the stress relaxation in a binary blend can be defined by the relaxation functions of two distinctively defined weight components, ϕ_S, i.e. volume fraction of short chains, and ϕ_L, i.e. volume fraction of long chains. This is described in equation 6.4 [155].

$$G(t) = G_N^0 \Big[\phi_S \mu_R(t, N_S) + \phi_L \mu_R(t, N_L)\Big] \tag{6.4}$$

where μ_R represents the unrelaxed fraction of short and long chains (i.e. the fraction of polymer that has not escaped from the initial tube at time (t)), and N refers to the number of chain segments.

When talking about polydispersity and mixing, it is worth recognising that mixtures are characterised through the use of mixing rules. Two such mixing rules are the "linear mixing rule" [64] and the "quadratic mixing rule" [39; 156]. The main differences between these two is that the former considers simple reptation, while the latter makes use of the double reptation and entanglements concepts. In these rules, G_N^0 is mainly defined by the kernel $F(t, M)$, which describes the relaxation behaviour of a molecular weight fraction with a molecular weight M. Additional parameters such as $\beta = 1 + \alpha$ are used to characterise the nature of the mixing. Overall, the main differences between the original mixing rules and more recently defined models [76; 152; 157; 158] is the treatment given to the kernel function. Although these models have reached a very high level of maturity, extensive research and academic collaborative work [134; 159] is still being carried out, to try to explain the variations of the exponential mixing parameters (e.g. α).

Below we analyse the data for our monodisperse and polydisperse blends using REPTATE's pDR and R-C theories, and emphasize on the traits that are captured by each of them. The data is compared against the other more recent models cited in the literature to try to identify any advances in rheological theories that may not be included in REPTATE's library. The experimental data and REPTATE predictions for monodisperse blends of systems BF/BG and BF/BH are presented in Figures 6.9 and 6.10, respectively. The error values between the experimental data and the theories used are compared in Table 6.5.

The tabulated errors in Table 6.5 present two interesting phenonmenon: it appears as if the R-C theory is more suitable in the prediction of blends BI and BJ, where PDI is ∼1.2-1.3. The pDR on the other hand, appears to yield a lower error margin for blends BK and BL, which have higher PDIs. When having

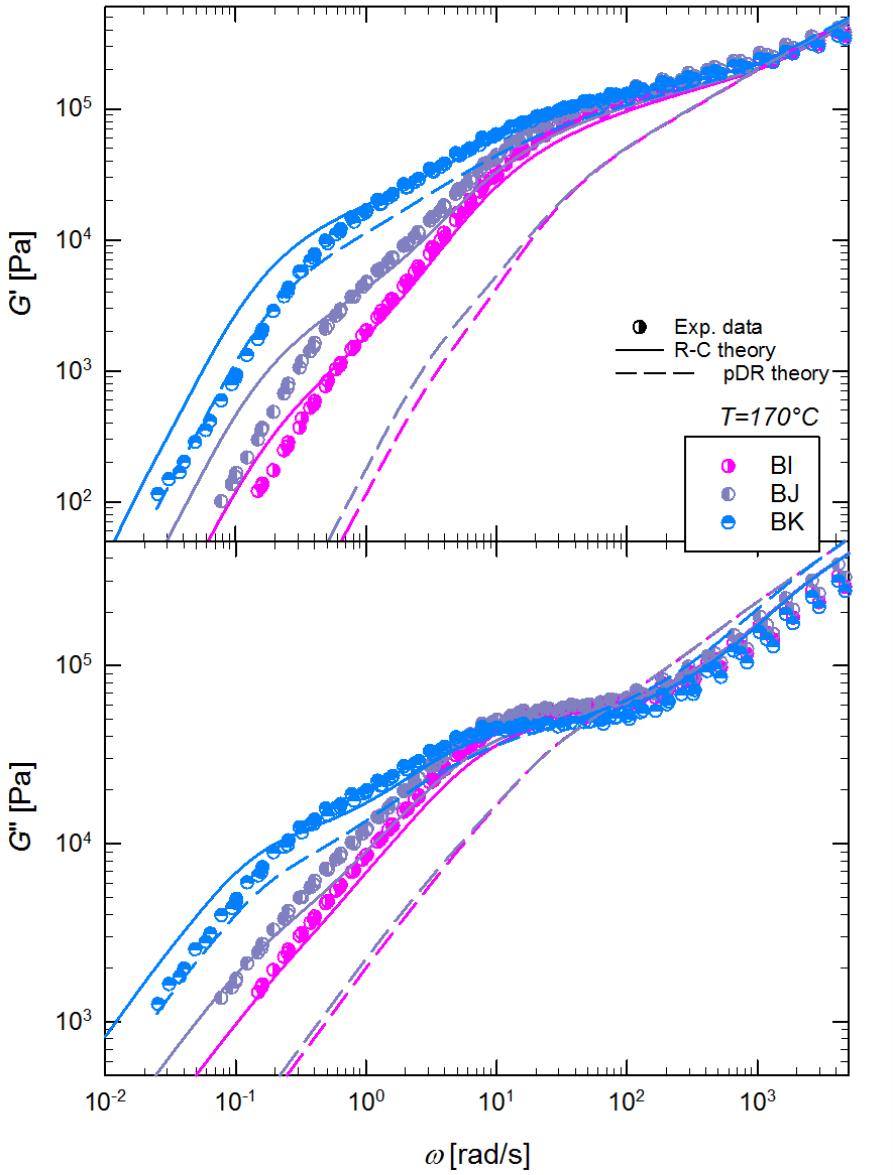


Figure 6.9: Master curve plots for monodisperse blends BI, BJ and BK (symbols), plotted against REPTATE simulations using the R-C (lines) and pDR (dashed) theories.

a closer analysis at the R-C predictions in our monodisperse blends, the theory shows a good agreement at capturing the behaviour of the blends at higher

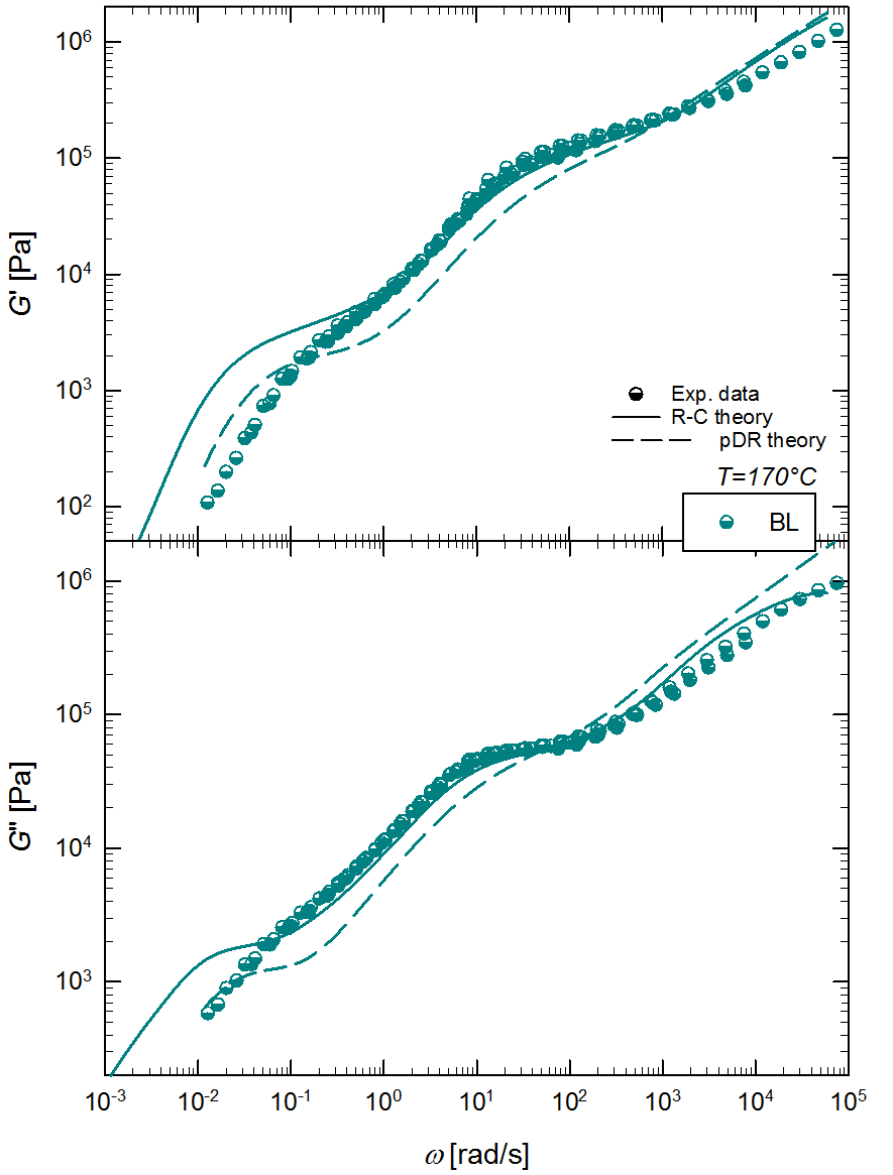


Figure 6.10: Master curve plots for monodisperse blend BL (symbols), plotted against REPTATE simulations using the R-C (lines) and pDR (dashed) theories.

frequencies, where the relaxation of component BF clearly dominates the dynamic behaviour at shorter times. The theory seems to struggle at the terminal region, where the contribution of the higher molar mass tail becomes more domi-

Table 6.5: Prediction error between R-C and pDR theories to experimental data of monodisperse blends.

Material	R-C theory error	pDR theory error
BI	0.029	0.503
BJ	0.037	0.698
BK	0.039	0.019
BL	0.099	0.058

nant. It is interesting to compare these findings with the polydispersity study of Leonardi [154] where he examines the models of Mead [160], Maier [161] against his own. His results for the dynamic moduli of PS blends showed that Mead's model overestimated the relaxation time, while Maier underestimated the moduli at the terminal zone. Leonardi's model seemed to reduce these problems with the inclusion of tube renewal. A similar level of accuracy was later reported by Carrot [158], who builds upon the idea of a polydisperse model than includes CLF and DTD. Our predictions for the R-C theory seem to follow a similar trend to Mead's model, where the relaxation of the longer chains is overestimated. In here, it would appear as if the prediction was highly differentiated by assuming only two contributions: the relaxation time of the short chains τ_S and long chains τ_L, without really considering the intermediate relaxation processes that arise from the short-long entanglements or the distribution of intermediate chain-lengths. Since blends BI and BJ have small fractions of the higher molar mass component ($\phi_L \leq 0.2$ wt%), it seems most of the response predicted by the R-C theory is influenced by the relaxation behaviour of constituent BF. At the terminal region though, the R-C simulation gives a sharper kink at the set of the relaxation contribution of material BG, compared to the smooth transitioning response that is actually experienced by the blends. In this end, the pDR seems to be more successful, at least in the case of blends BK and BL. Here, the relaxation of the materials seems to follow a more uniform distribution that spans from times corresponding to BF to those reached by the BG/BH components. Watanabe [68; 69; 70] studied extensively the effect of relaxation in binary monodisperse PS blends as a function of varying blending percentages of the higher molar mass component. His observations confirmed that there is a definitive shifting relax-

ation behaviour conditioned to whether the volume fraction of long chains ϕ_L was above or below a critical value ϕ_c. He established the following arguments:

- At $\phi_L \leq \phi_c$: the relaxation of short chains takes place first, but entanglements of short-long chains prevailed at long times, followed by entanglements of two long chains exhibiting the behaviour of a diluted solution (long chains dissolved in short chains).
- At $\phi_L \geq \phi_c$: the relaxation of short-long entanglements appear at intermediate times followed by the relaxation of entanglements between long chains at sufficiently long times, characteristic of concentrated solutions of long-long chains.

These arguments clearly describe the transitioning stages that have been reported for our monodisperse blends. BI and BJ are better categorised as dilute solutions ($\phi_L \leq \phi_c$), while BK and BL are examples of concentrated long chains at the terminal region. It is important to recognise that in our materials even the short chains are seen as entangled chains, they simply depict a shorter relaxation time compared to the longer molecules of the higher M component. This effectively have some implications as to the degree of dilution that is actually experienced by the system.

Nowadays, the observations made by Watanabe have been further explained using the concepts of CR, CLF, and DTD. As mentioned earlier in sections 2.5.1, and 5.6, the DTD theory serves to account for the effect that comes from an accelerated motion of short chains which consequently speeds up long chain relaxation by means of a diluted tube. This affects mainly the relaxation time of the long component in binary blends with widely separated molecular weights. Depending on the degree of entangling of the short chains, a partial or full dilation effect can be accounted for [135; 162]. What this means, is that when short chains are below the entanglement requirement (e.g. $\leq 2M_e$ for PS) they act as a solvent and hence full DTD is assumed. Yet for short chains that are entangled ($\geq 2M_e$), partial DTD occurs, and the relaxation of the long chains includes a delay representative of an internal equilibration time of long-long segments. Van Ruymbeke [135] terms this an CR-activated fluctuation (CR-CLF),

which describes the tension re-equilibration process undergone by the long chains inside a tube that dilates to the rhythm set by the release/re-formation of the short-long entanglements that define the tube constraints. The application of a refined version of these theories has more recently been tested by Shahid [8] in diluted PS systems. In the next section (6.5.2.2), we aim at comparing the R-C and pDR simulations performed in our polydisperse blends.

6.5.2.2 Polydisperse blends

REPTATE's pDR and R-C theories were applied to the LVE data of our polydisperse blends, the results of the solution blended and melt mixed samples are presented in Figures 6.11 and 6.12. The accompanying error data is displayed in Table 6.6.

Table 6.6: Prediction error between R-C and pDR theories to experimental data of polydisperse blends.

Material	R-C theory error	pDR theory error
CA_{sb}	0.577	0.081
CA_{mm}	0.637	0.409
CB_{sb}	0.389	0.089
CB_{mm}	1.029	0.224
CC_{sb}	0.549	0.040
CC_{mm}	1.892	0.259
CD_{sb}	0.477	0.047
CD_{mm}	1.129	0.042

There is a quantifiable improved accuracy in the simulations using the pDR theory over the R-C model in all the polydisperse blends, regardless of the blending procedure used. These results are as expected, since the relaxation of the R-C is very polarised as accounted by the $\overline{M}_{w1}$ and $\overline{M}_{w2}$ contributions of the constituent materials; and this does not really considers a wider distribution of relaxation times associated with a range of $\phi(M)$. Hence, this shows that the R-C theory deems inadequate at capturing such a high level of segmented polydispersity. In the pDR theory, as observed for the monodisperse blends, the simulation provides a smoother curve compared to the R-C theory. This has been attributed

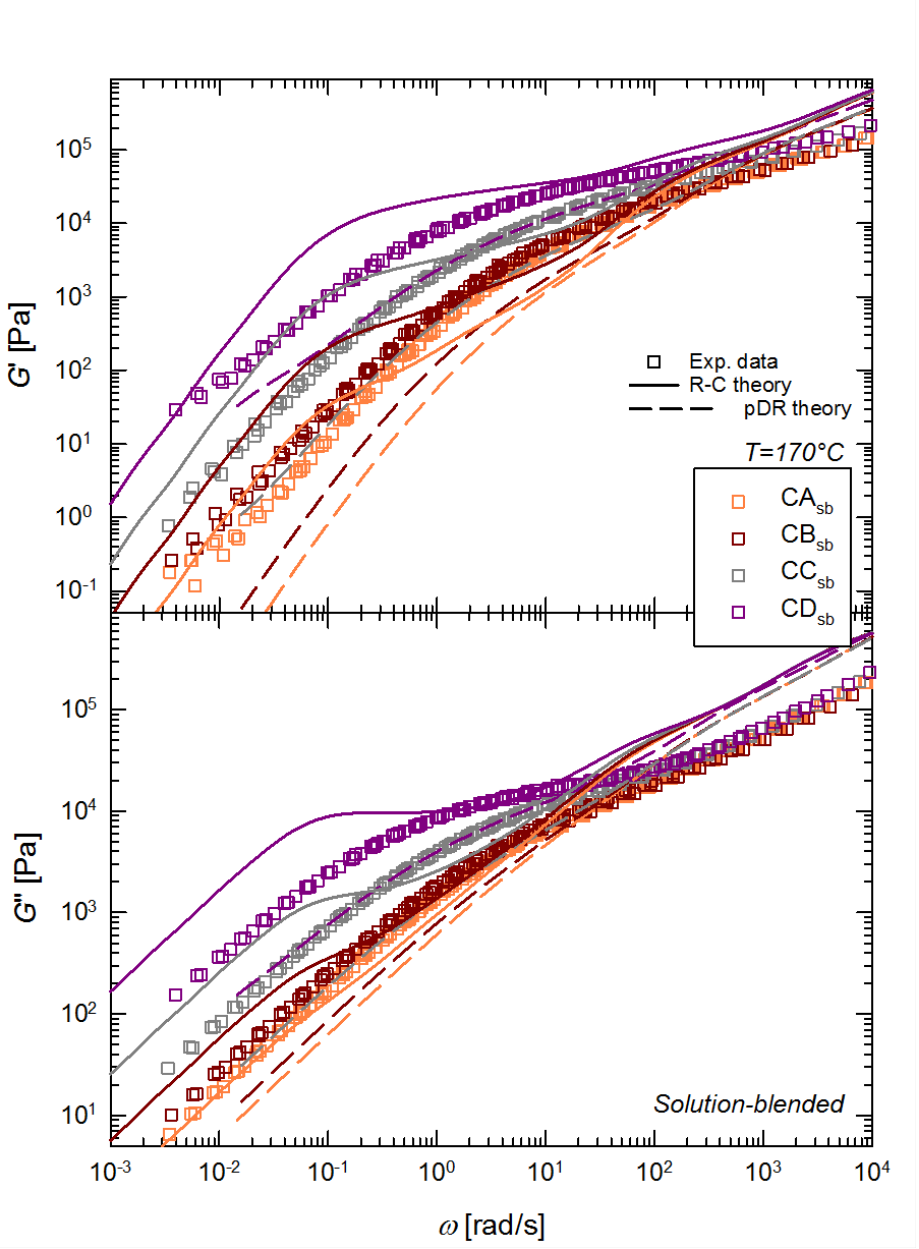


Figure 6.11: Master curve plots for solution blended polydisperse blends (symbols), plotted against REPTATE simulations using the R-C (lines) and pDR (dashed) theories.

to the effect of polydispersity as noted by [6; 163], where the scaling of $G' \sim \omega^2$ and G" $\sim \omega$ is no longer obeyed. An additional observation is the clear exis-

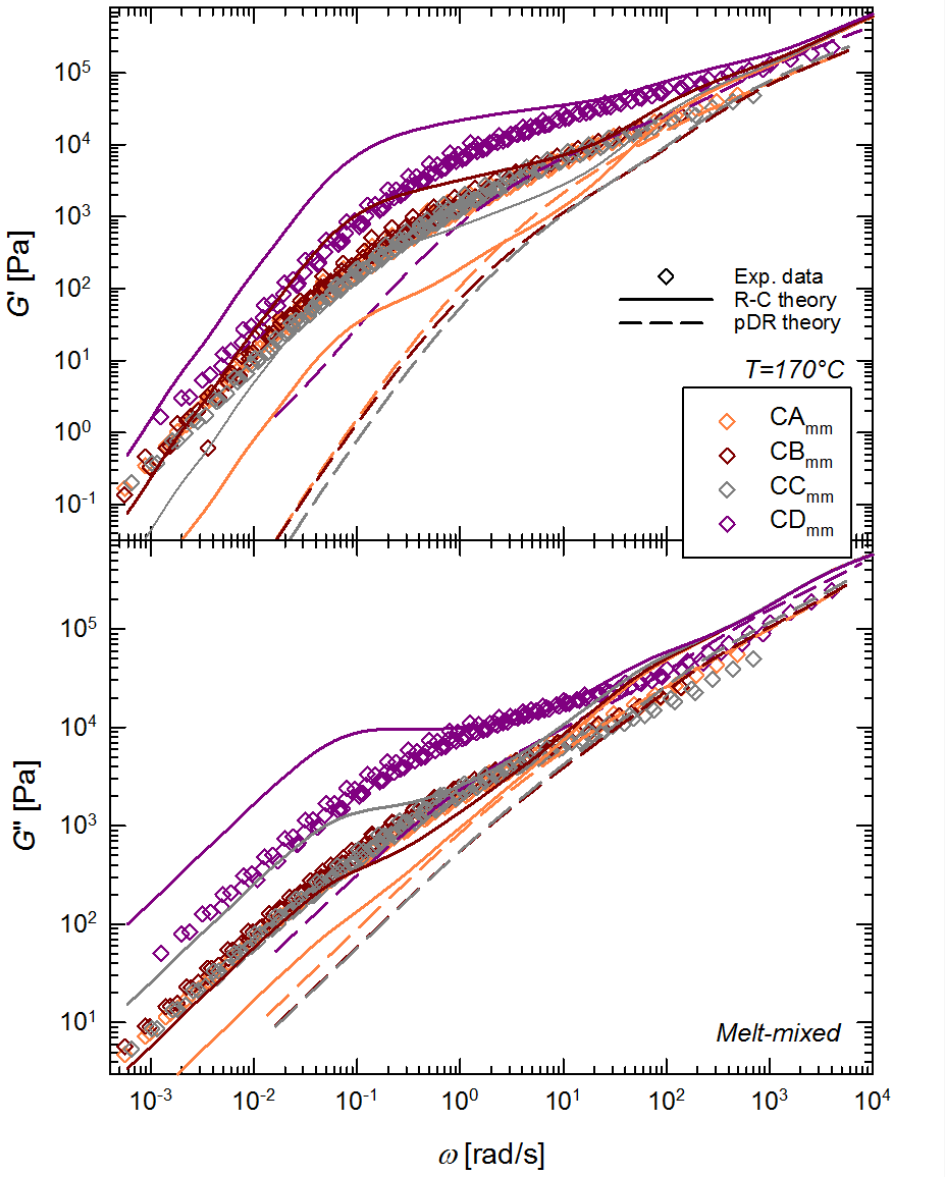


Figure 6.12: Master curve plots for melt-mixed polydisperse blends (symbols), plotted against REPTATE simulations using the R-C (lines) and pDR (dashed) theories.

tence of a "kink" or "double-plateau" identified in the predicted R-C response, as this represent the transitional relaxation behaviour from $\overline{M}_{w1}$ to $\overline{M}_{w2}$. This

lack of identifiable transitional relaxation plateaus is a distinctive feature that differentiates the shape in the curves of binary monodisperse blends, compared to binary blends of polydisperse constituents. At intermediate frequencies, it is possible to see the appearance of a plateau modulus as the addition of component BY is increased. Van Ruymbeke [6] describes the plateau modulus to be the "signature of entanglements"; due to the large unentangled fractions that conform the polydisperse blends hereby presented, the evidence of a plateau can only be seen to become more noticeable as the addition of the higher molar mass component is increased. In [158], Carrot notes that the relaxation times for the shorter chain species in systems of multiple chain lengths are unchanged whatever the composition, but the relaxation time of the long chains is significantly shortened especially when the amount of short chains is increased. Auhl and coauthors [164] examined the effect of blending an unentangled polyisoprene (PI), $\overline{M}_w = 2.4\,\mathrm{kg/mol}$, with a higher molar mass component, $\overline{M}_w = 1131\,\mathrm{kg/mol}$, and the shape of the oscillatory data reported for the unentangled sample is in agreement with the absence of a plateau observed in the shape of our constituent material BX. Also, in their studies of rheological properties of carefully synthesized narrow distributions for a range of polystyrenes, Onogi *et al.* [165] present G' data that resembles the transition of unentangled systems ($\overline{M}_w = 8.9\,\mathrm{kg/mol}$) to highly entangled polymers ($\overline{M}_w = 581\,\mathrm{kg/mol}$) in agreement with our reported data. Finally, at the high frequency region the behaviour of all blends is observed to be similar; this indicates that the effect of polydispersity is attenuated due to the dominance of Rouse process in this region, as suggested in [163].

The quality of the prediction for the available theories to be used in the treatment of polydisperse systems applied in our polydisperse blends do not seem to reach the low error margins reported for all the other polymers described in the precedent sections. The most interesting remark about the presented sets of data is the fact that such unentangled systems may lie outside the boundaries established for the treatment of most of these models. In fact, in the cited Carrot's study [158] for modelling the LVE of a polydisperse PS, the kernel function to treat polydispersity is assumed to be derived from defined M_e and M_c values, where c is the polymer concentration in a polymer solution. If this were to be the case, a considerable amount of fractions that rule the behaviour of these blends

will be lying below the M_e limit, and therefore omitted when simulating the flow behaviour.

The LVE data of the materials studied here has hinted at differences between the treatment in the current available models to tackle molar mass contributions and the effect of polydispersity in rheological theories. In the upcoming section 6.6, NLVE behaviour will be analysed with the treatment of transient and extensional data.

6.6 Non-linear Viscoelasticity

Rheological measurements were performed in transient mode at a single temperature of T =170 °C, and different strain rates, $\dot{\gamma}$, ranging from $\dot{\gamma}$=0.003 s^{-1}-10 s^{-1}.

Extensional rheology was performed with a Sentmanat fixture of a double barrel rotating system at a single temperature of T =170 °C. The materials were drawn at different shear rates, ranging from 0.01 s^{-1} to 10 s^{-1}. Strips of 20 mm x 3 mm x 3 mm of heated press discs were cut with the laser in preparation for the test. The chamber was set at 170 °C, and the strip of polymer was placed in the distance between the barrels and held in place with the aid of mechanical inserts that trapped the sample against the hot surface of the cylinders. The specimen was left to rest inside the chamber for a period of 60 s before starting the shear sequence.

To facilitate a preliminary discussion, the results of both transient and extensional measurements are presented in a single graph following the convention of recently published literature [9; 10]. This representation allows to have a visual overlook of the stress-softening and stress-hardening processes that come with the corresponding relaxation and orientation mechanisms experienced by polymers during steady shear (i.e. transient shear tests) and uniaxial elongation (e.g. extensional tests), respectively. The data presented in these graphs shows the Linear Viscoelastic Envelope, LVE, as a thick black line. Following the theory of linear viscoelasticity the linear envelope can be calculated through the following expression using REPTATE[102]:

$$G_{linear}(t) = AdjustG_0 * \sum_{i=0}^{N_{modes}} G_i * \tau_i \left(1 - exp\left(-\frac{t}{\tau_i}\right)\right) \tag{6.5}$$

where G_i and τ_i refer to the modulus and relaxation time corresponding to individual Maxwell modes fitted on the LVE mastercurves data. In this study 10 Maxwell modes were used to fit each one of the analysed materials. $AdjustG_0$ is a parameter introduced by REPTATE for fitting experimental non-linear rheological data. The Maxwell modes were obtained using a specific module in REPTATE. In Figure 6.13, we present the Maxwell modes' predictions as obtained when fitting the nodes to the LVE mastercurve of material BH, to illustrate the applied procedure.

The transient and extensional experimental data have been split into sections, by classifying the materials in accordance to their level of polydispersity, following the format used in chapter 4 on page 105 and chapter 5 on page 139.

6.6.1 Monodisperse materials

The transient and extensional data of materials BF, BG and BH is presented in Figures 6.14 to 6.16.

The first thing to highlight in the reported plots is the disagreement of our extensional data with regards to the LVE envelope by approximation of a Trouton ratio of 3, as per the established theory [27; 166]. In fact, this is true for all the extensional data for our analysed materials. Although the authors acknowledge that the quality of these results may preclude a conclusive analysis of the data, it feels valuable to report this as it introduces new opportunities for widening and refining the research initiated here. The rather odd extensional response documented here is attributed to difficulties in the adjustment of the SER fixture in the rheometer. Unfortunately, due to experimental time-constraints and a delay in the inspection of the adjustable feature by the service provider, it was impossible to re-run the tests.

Categorically, the extensional behaviour of monodisperse materials has been

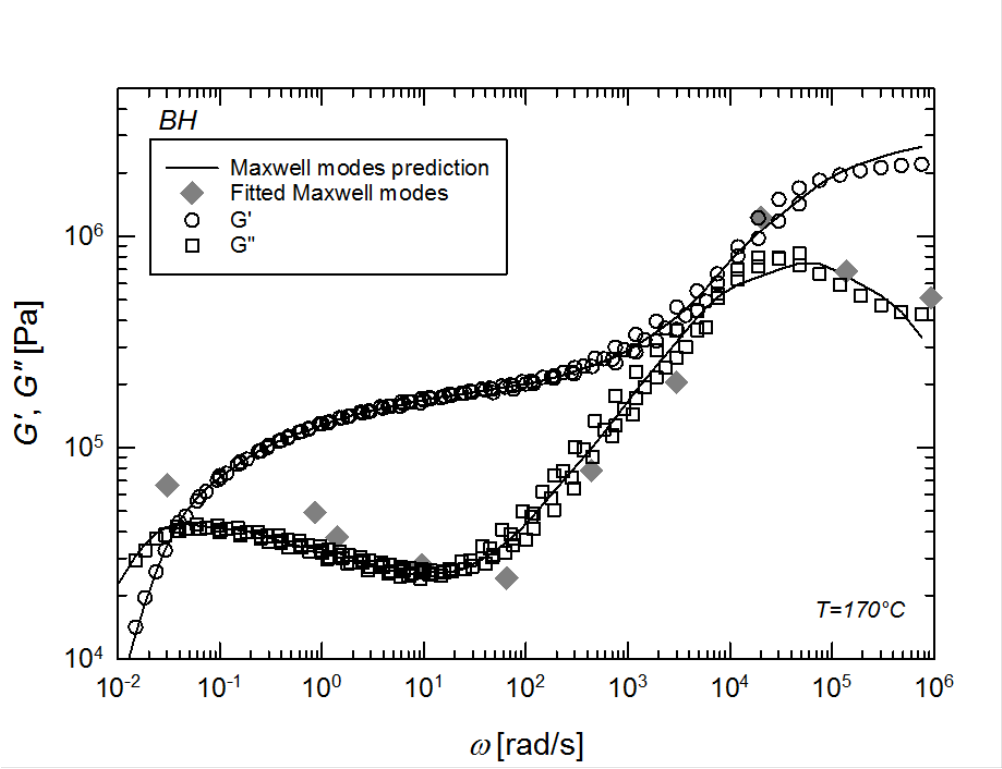


Figure 6.13: Ten Maxwell modes (filled diamonds) are fitted to the mastercurve of material BH at 170 °C. The obtained predictions are shown with continuous black lines, while the experimental data is presented with blank symbols.

reported to follow the linear viscoelastic envelope at low strain rates, while at high strain rates it transitions to a nonlinear behaviour [167]. The data suggests that this behaviour is observed in the extensional response of materials BG and BH. Even if the extensional data is seen to be shifted above the determined linear envelope, and the exposed equipment difficulties may prelude a more conclusive statement, a qualitative analysis of the obtained data will be carried, and this will aim at being interpreted under the fundamentals of how chain alignment and stretching occur in non-linear rheology.

In the analysis of transient data of monodisperse materials, the expected behaviour as previously documented by other authors [168], is the following: at small strain rates ($\dot{\gamma}\tau_d$ <1) the response is linear, in agreement with the de Gennes reptation model [62; 169]; at slightly larger strain rates ($\dot{\gamma}\tau_d$ >1), the

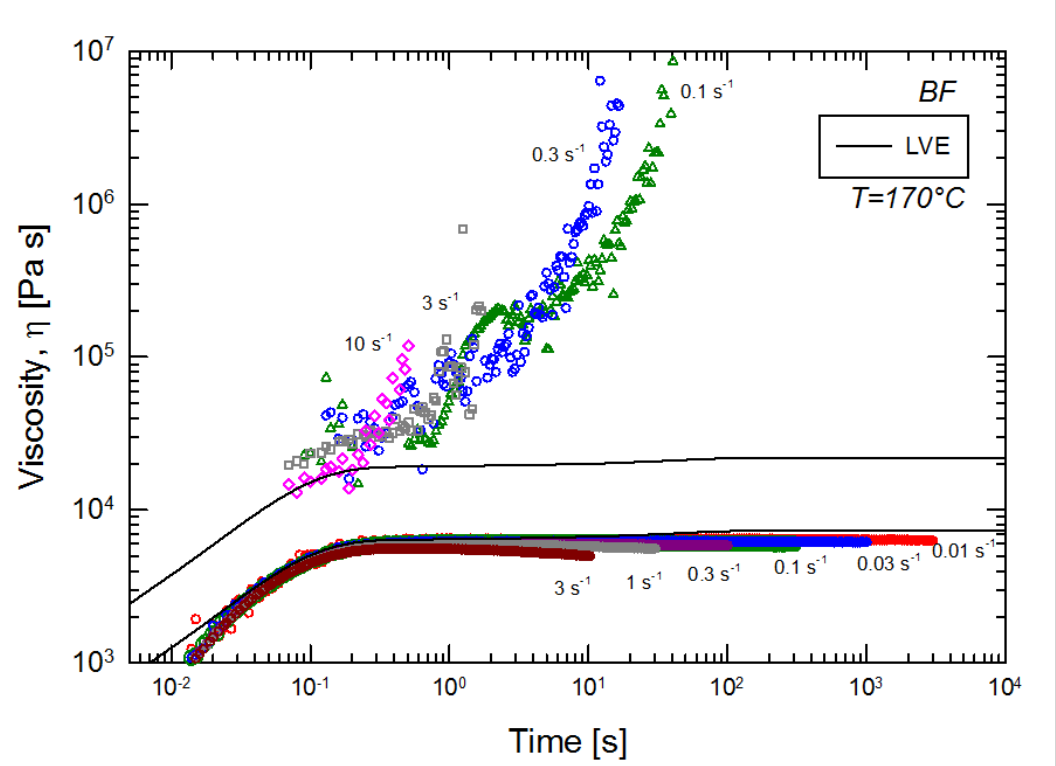


Figure 6.14: Extensional and transient shear viscosity for material BF. The linear envelope is presented as a continuous black line. The applied shear rate is indicated alongside corresponding data.

behaviour follows the constitutive equation of Doi and Edwards [63]. Yet, at even higher strain rates, where the Doi theory seems to fail, the mechanisms of chain stretch, CR, and convective constraint release, CCR, have been introduced to improve the description of transient rheological experimental data (chronologically by Pearson [168], Mead [170] and Likhtman-Graham [9; 79]). Chain stretch occurs as the chains are seen to elongate when flows are faster than the reciprocal Rouse time τ_R [171]. CCR describes the process by which a chain end passes through a particular region of the polymer network releasing the contribution to the entanglement constraints on its surrounding molecules. Constraint release events are seen to increase in proportion with the strain rate providing an orientational relaxation mechanism, counteracting the aligning effect of shear flow and reducing the predicted stress maximum [172].

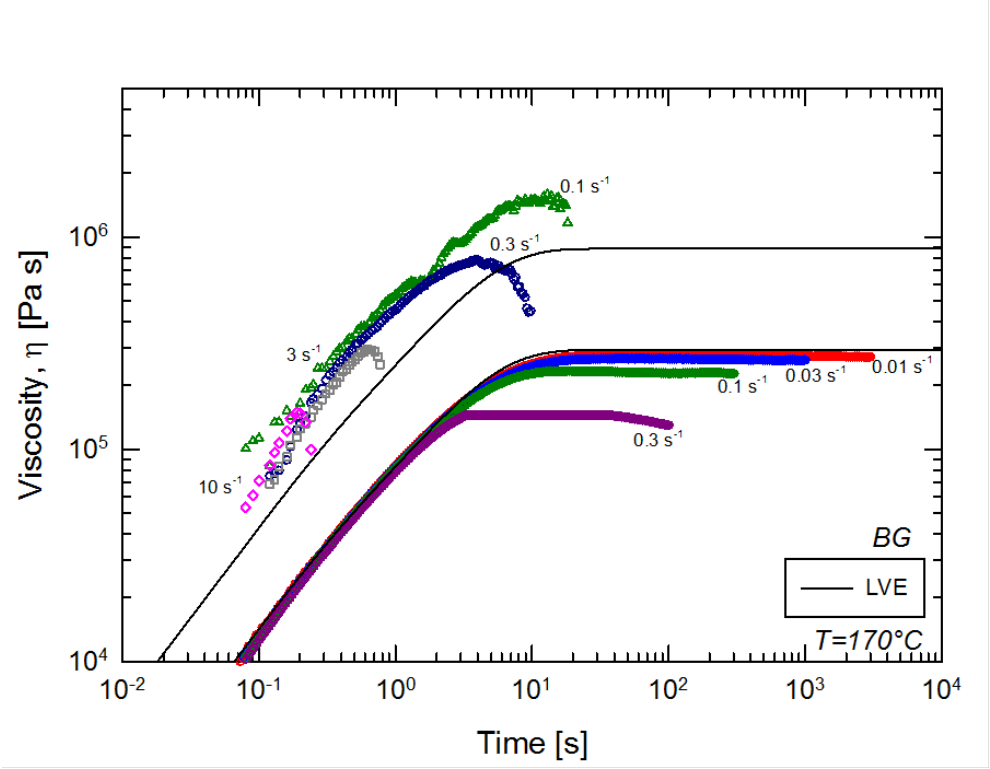


Figure 6.15: Extensional and transient shear viscosity for material BG. The linear envelope is presented as a continuous black line. The applied shear rate is indicated alongside corresponding data.

The shear rheology of material BF appears to be in the linear response. This is expected as the reptation time of the material is calculated at 0.17 s, which means that the shear rates are slower than the reciprocal τ_d. The same sort of behaviour will be expected in extension, which suggests that the apparent strain hardening that is observed is a result of the aforementioned experimental difficulties, and the data is not conclusive.

For material BG and BH, in Figures 6.15 and 6.16 respectively, it appears that the materials to deviate from linearity at higher strain rates, particularly material BH where this effect is evident even at a rate of $3\,s^{-1}$, as the resistance to stretching rises with increasing molar mass. The shear rheology of material BG shows shear thinning at rates above $0.1\,s^{-1}$, consistent with a reptation time in the order of 10 s, not far from the reported 7.7 s for this material. In the exten-

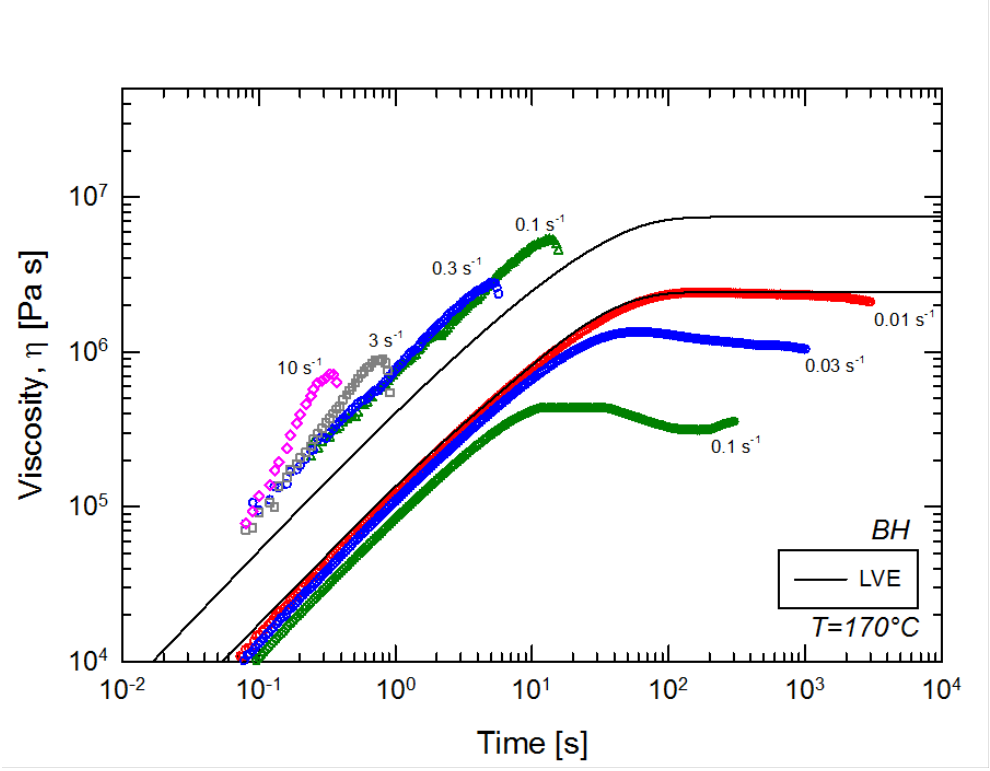


Figure 6.16: Extensional and transient shear viscosity for material BH. The linear envelope is presented as a continuous black line. The applied shear rate is indicated alongside corresponding data.

sional data, the applied flow rates show no transient overshoot, which suggests weak alignment and no-chain stretching, again consistent with the timescale of the observed reptation and Rouse times. For material BH, the apparent shear thinning that occurs at a rate of $0.01\,\mathrm{s}^{-1}$ is expected to occur for a reptation time of about 100 s, in proximity to the observed 85 s for this material. At $0.1\,\mathrm{s}^{-1}$, the appearance of a weak overshoot suggest alignment but not stretching which occurs at the observed τ_R and τ_d timescales. The extensional data in Figure 6.16 suggests that at fast shear rates (3 and $10\,\mathrm{s}^{-1}$), the material depicts strain hardening consistent with its Rouse time. In rates of 0.1 and $0.3\,\mathrm{s}^{-1}$, these are greater than $1/\tau_d$, but smaller than $1/\tau_R$, hence it is expected the chains will orient, but not stretch characteristic of the shear thinning effect. Another plausible explanation is the onset of extension thinning as a result of samples breaking [173],

which was the case for these samples.

In all three materials studied here, as the strain rates become higher, it is possible to observe the deviations from linearity and relaxation mechanisms reported in the cited literature. Similarly, as the monodisperse materials increase in molar mass (transition from BF to BH), the effect of relaxation becomes more noticeable at smaller strain rates, i.e. non linearity starts to appear even at $0.01\,s^{-1}$ in material BH compared to material BG.

6.6.2 Polydisperse materials

Unfortunately due to the inherent high brittleness of material BX it was impossible to prepare specimens of good enough quality for extensional testing. Hence the data provided here for this material is solely for transient experiments. The transient and extensional data of materials BX and BY is presented in Figures 6.17 and 6.18.

With the recognition of the noise and limited information that can be extracted from the extensional data of material BY, it is possible to see strain-hardening particularly at higher strain rates ($3\,s^{-1}$ and $10\,s^{-1}$). In their study of the effect of polydispersity in the extensional behaviour of entangled polymers, Ye *et al.* [163] compare the shear extensional behaviour of a 18-monodisperse-components polystyrene blend against the rheological behaviour of a monodisperse PS material with a similar reported $\overline{M}_w$. The results show that the polydisperse blend, reported higher extensional viscosity values, at two different applied strain rates ($1\,s^{-1}$ and $0.1\,s^{-1}$). The observation is that the onset of extension hardening in the polydisperse blend is a result of the high molecular weight components, where different polymer chains contribute at different time scales. By comparing the data reported for material BH ($\overline{M}_w = 540\,kg/mol$) against that for material BY ($\overline{M}_w = 339\,kg/mol$), a similar observation can be made. Despite the fact that BH has a higher $\overline{M}_w$ than BY, the extensional viscosity of the latter is seen to increase as much as a factor of 5 at the same applied strain rate (e.g. $0.1\,s^{-1}$).

The transient data for materials BX and BY show some distinct differences. The most notable observation is the lack of a strain-softening behaviour in spec-

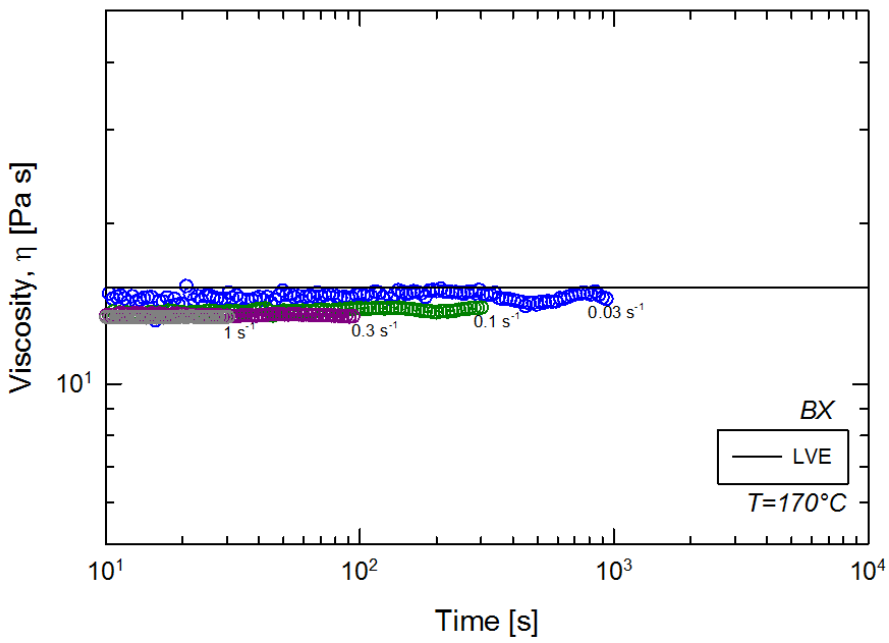


Figure 6.17: Transient shear viscosity for material BX. The linear envelope is presented as a continuous black line. The applied shear rate is indicated alongside corresponding data.

imen BX, regardless of the increase in the applied strain rate. It is important to recognise that the tube model and its derived theories rely on the capacity of polymer molecules to entangle and disentangle through motion within their tubes to explain the observed experimental mechanisms of stretching, orientation and relaxation experienced by the polymer network under applied stimuli. The inherently low viscosity values (in the order of 10^1) of material BX keep fairly constant at different strain rates suggesting that the chain stretch and convective constraint release mechanisms that serve to characterise the stress-overshoots and consequent shear thinning of the steady shear response, are not present in the experimental behaviour of this material. Particularly in the ROLIEPOLY model of Likhtman and Graham [79], and later refined GLaMM model [9], one of the universal parameters used in the prediction of transient and extensional

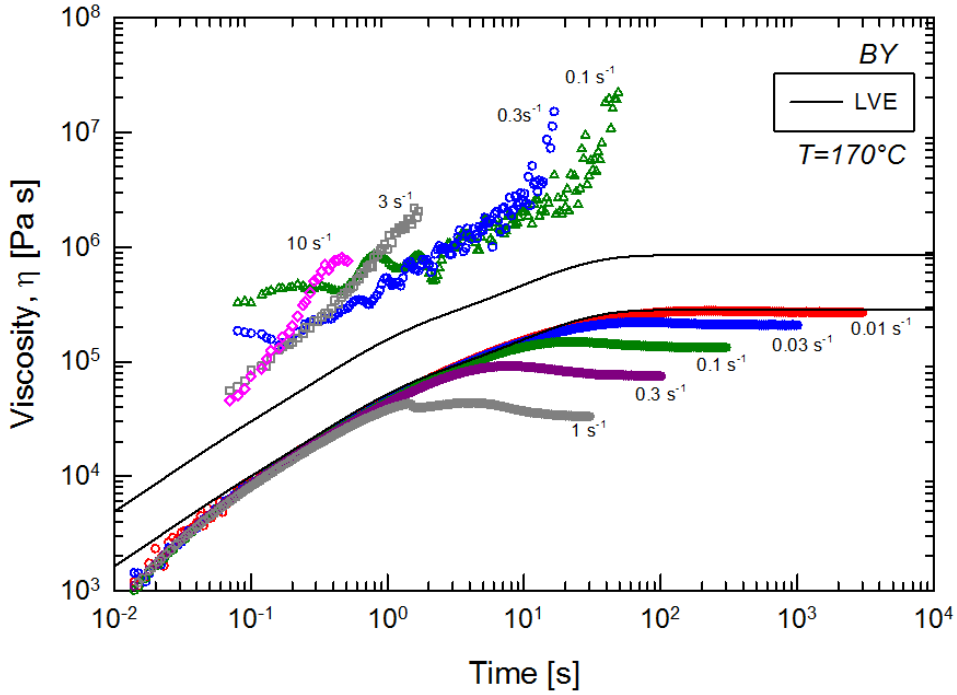


Figure 6.18: Extensional and transient shear viscosity for material BY. The linear envelope is presented as a continuous black line. The applied shear rate is indicated alongside corresponding data.

data is M_e, which lies above 65 wt% of the molar mass unentangled fractions that constitute the molar mass distribution of polydisperse material BX. Although in reality one can argue that this polymer is inherently brittle to produce any sort of end-product, it must be acknowledged that this is a readily available commercial material, and most likely it is used as a blending polymer for fine-tuning manufacturing processes. The relevance of the data hereby reported, is to provide a picture into how such a complex, bimodal polydisperse distribution with a high content of unentangled fractions exerts a dominant effect in the rheological behaviour of this polymeric system, and it shows how the relaxation of the majority of the unentangled short chains overshadow the presence of the remaining long chains (∼35 wt%). In fact, the high degree of unentangled fractions, act as a dilutant on the longer chains, rendering the material unable to depict

the characteristics of an entangled system as described by the latest rheological theories.

In contrast, the response of material BY, follows the very characteristic steady shear response that has been previously modelled for linear PS melts; where as the response deviates from linearity the chain stretch mechanism produces the stress-overshoots, followed by a CCR and CLF mechanisms that cause the characteristic shear thinning. Most recently, other authors [174; 175] have used organic molecules (e.g. DNA) to suggest that the shear thinning seen in the steady flow behaviour of polyethelyene and polystyrene melts, respectively, can be further improved by considering a tumbling effect. Their findings are supported by non equilibrium molecular dynamic simulations, NEMD, and suggest that as the molecules tumble at high strain rates, the stretch experienced by the molecule is reduced through the tumbling function $\phi(t)$. The authors believe that considering a tumbling effect improves the quality of the simulation for non-linear steady flows, as it works in conjunction with the CCR contribution.

6.6.3 Monodisperse blends

The transient and extensional data of monodisperse blends BI-BL is presented in Figures 6.19 to 6.22.

As acknowledged, the noise in the extensional data of the blends hinders definitive arguments. Yet, relying on the information that can be drawn from the presented plots the following observations can be made: a) strain hardening is observed in all blends at all strain rates, regardless of their molar mass and blending ratios; b) as the strain rate is increased, a more accentuated and earlier deviation is observed from the LVE envelope; and finally, c) even though prior studies [164] have predicted that stretch relaxation times can be enhanced upon blending, the noise in the data prevents from making this type of definitive conclusions.

In recent years, the focus of polymer physics has shifted to explain the differences observed in the non-linear behaviour between polymers melts (e.g. narrowly distributed, monodisperse systems), and polymer solutions (e.g. polymer melts that are diluted using unentangled systems, i.e. oligomers). Particular interest

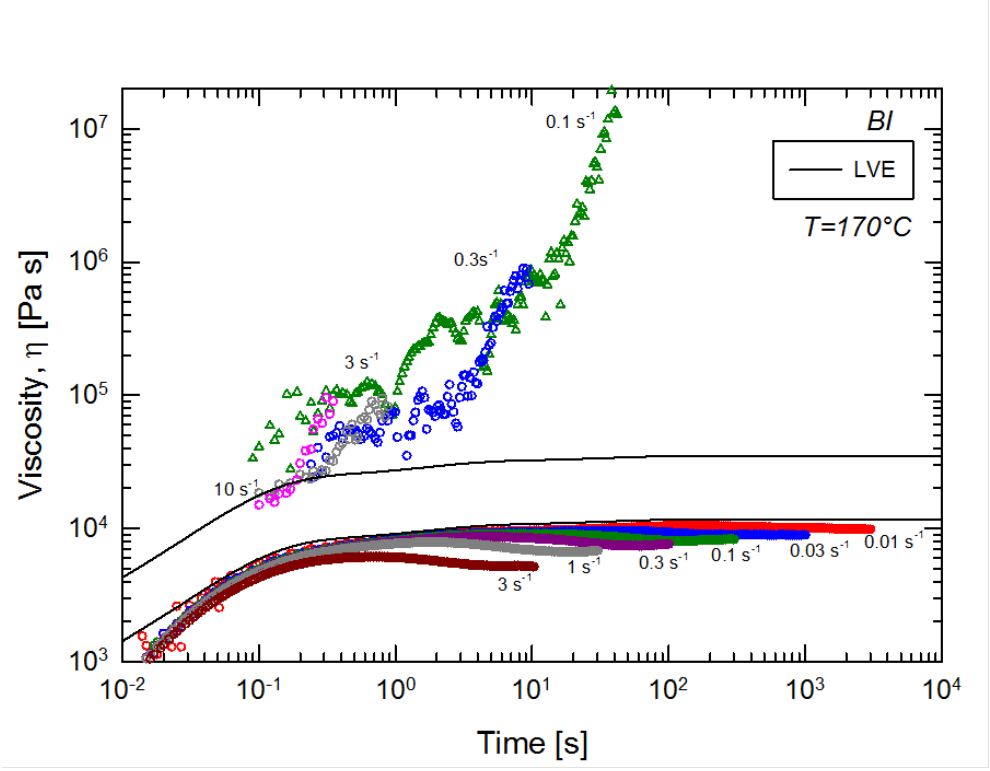


Figure 6.19: Extensional and transient shear viscosity for material BI. The linear envelope is presented as a continuous black line. The applied shear rate is indicated alongside corresponding data.

has arisen in determining why when subjected to uniaxial elongations, polymer melts behave differently than their solutions even when having the same number of entanglements. In this area, the work of Huang and co-workers [111; 151; 176; 177] has provided a bulk of experimental data to evidence and interpret these differences. The authors take the premise that if two polymer systems share the same number of entanglements, Z, their rheological responses are expected to show a similar trend. To validate this argument they have produced a series of "diluted" systems by combining narrowly dispersed PS materials, 285 kg/mol and 545 kg/mol (i.e. monodisperse samples, such as per this research), with their oligomers (e.g. 972 g/mol to 4290 g/mol) to produce solutions synthesised using a similar solution blending method as the one followed in this study. Their results showed that in the linear viscoelastic response, the mastercurves of both the melts

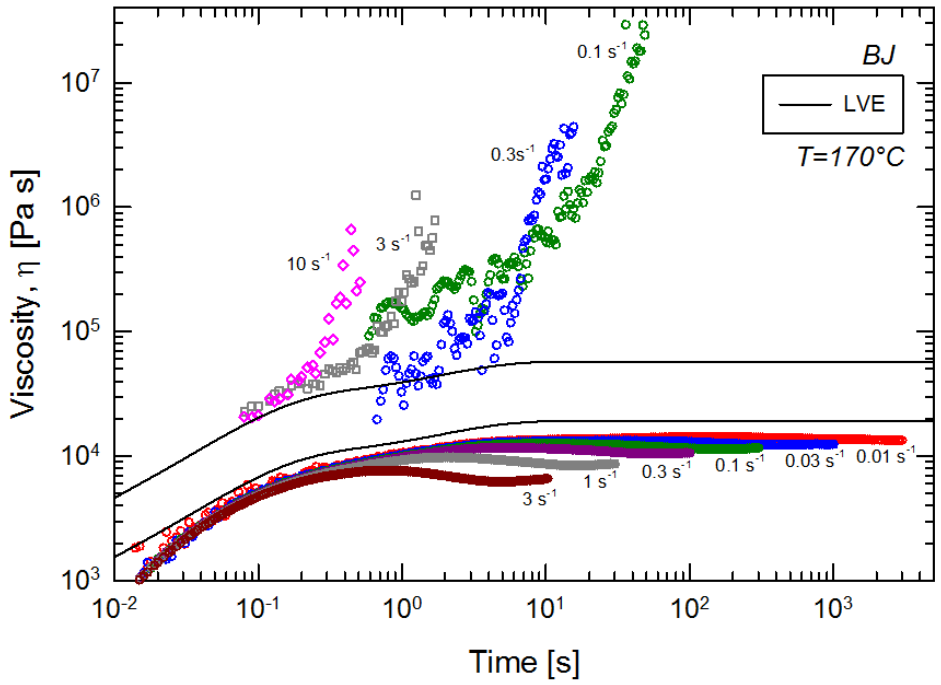


Figure 6.20: Extensional and transient shear viscosity for material BJ. The linear envelope is presented as a continuous black line. The applied shear rate is indicated alongside corresponding data.

and solutions overlap nicely, confirming the good applicability and universality of the tube theory. In the non-linear response characterised by the extensional viscosity the authors found that at low strain rates, both melts and solutions behave linearly following the LVE envelope, but at higher strain rates a recognisable increase in the strain hardening of the solutions was identified. The authors attribute this to two effects: 1) an increase in the strain hardening with the number of Kuhn steps per entanglement (N_e); and 2) the sensibility of finite extensibility, λ_{max} to the effect of dilution, as in principle, a polymer chain can be stretched more in a diluted environment than a concentrated one.

If the data for the studied monodisperse blends was to be analysed in a similar format to that followed by Huang *et al.*, it would be convenient to compare the responses of monodisperse material BG ($Z = 16.97$), with blends BK ($Z = 12.08$)

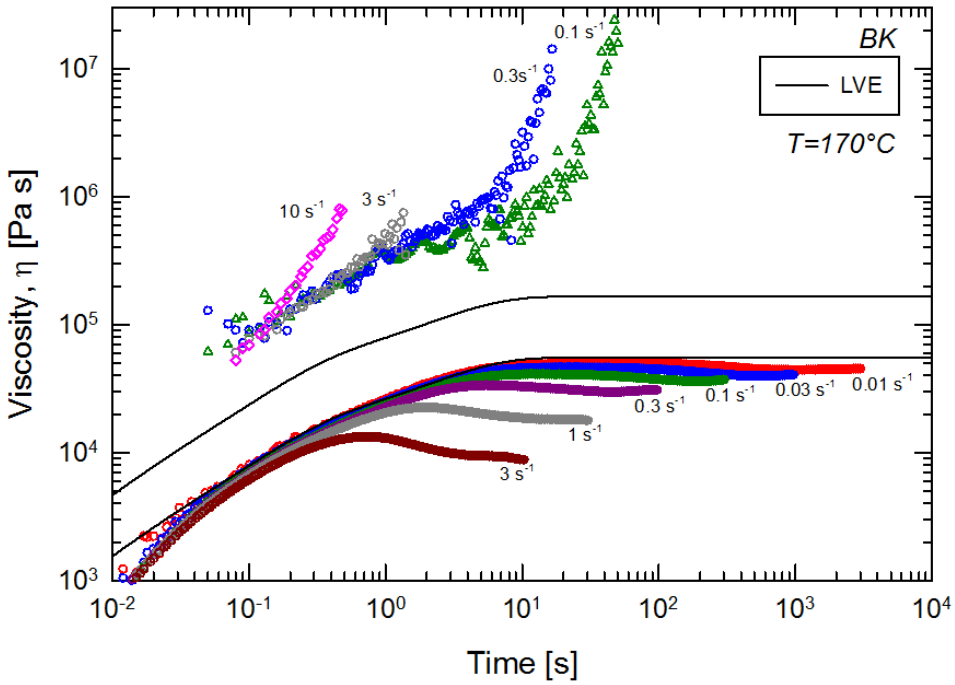


Figure 6.21: Extensional and transient shear viscosity for material BK. The linear envelope is presented as a continuous black line. The applied shear rate is indicated alongside corresponding data.

and BL ($Z = 12.02$). From Figures 6.15, 6.21 and 6.22, a noticeable increase in the extensional viscosity is reported for the blends compared to the monodisperse material at the same strain rate. Similarly, when comparing the strain hardening response of blend BK against that of blend BL, is possible to note the pattern observed by Huang *et al.*, where the strain hardening effect was seen to be more pronounced in the blend with a lower oligomer concentration. In agreement to the reported behaviour of blends BK (50 wt%), and BL (20 wt%), where the latter depicts slightly higher values of extensional viscosity at the same times and strain rates, possibly a contribution of the longer chains of component BH, in addition to the quoted finite extensibility effects.

One observable feature of the transient data in the plots of the reported monodisperse blends is the shape of the linear envelope. In comparison to the

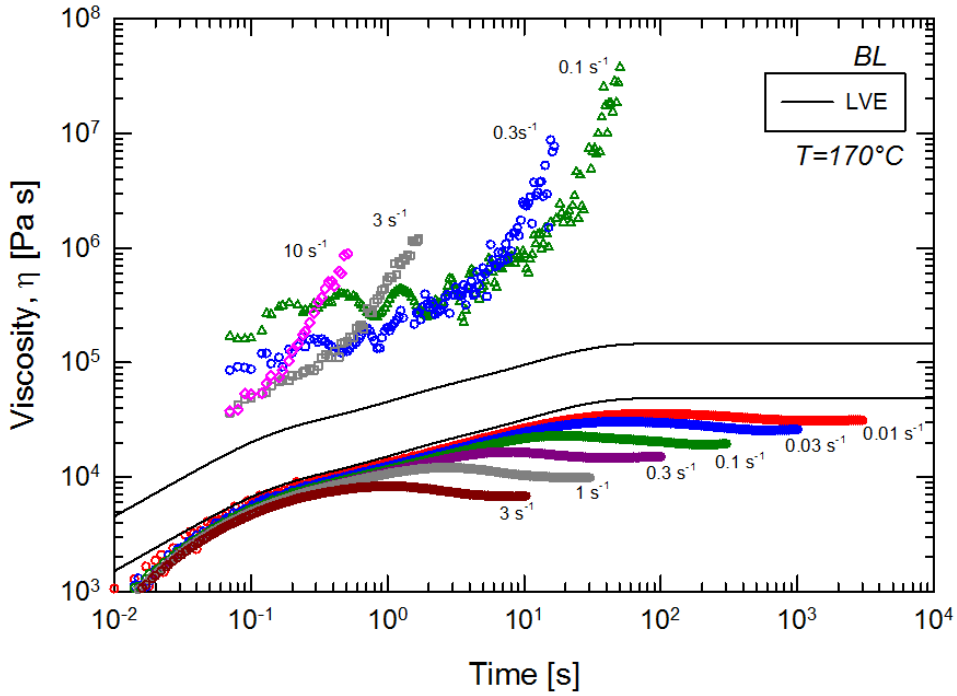


Figure 6.22: Extensional and transient shear viscosity for material BL. The linear envelope is presented as a continuous black line. The applied shear rate is indicated alongside corresponding data.

smooth linear and then transitioning plateau of the monodisperse materials, the envelope of the blends is seen to have two smooth, yet identifiable transitioning peaks. These are an evidence of the contributions in the relaxation scale of short and long molecules of the constituent components. To facilitate the analysis, figures 6.23 and 6.24 have been created, where the transient data of the constituent materials is presented in conjunction with that of their resulting blends at specific strain rates ($0.1\,s^{-1}$-$0.3\,s^{1}$).

These figures provide a better insight as to the transitioning behaviour and blending effects, namely: increasing molar mass and polydispersity. In both graphs, as expected, the viscosity is seen to increase with the addition of higher molar mass component. Yet, when the effect of the applied strain rate is taken into consideration it is possible to see that all blends present an earlier onset of

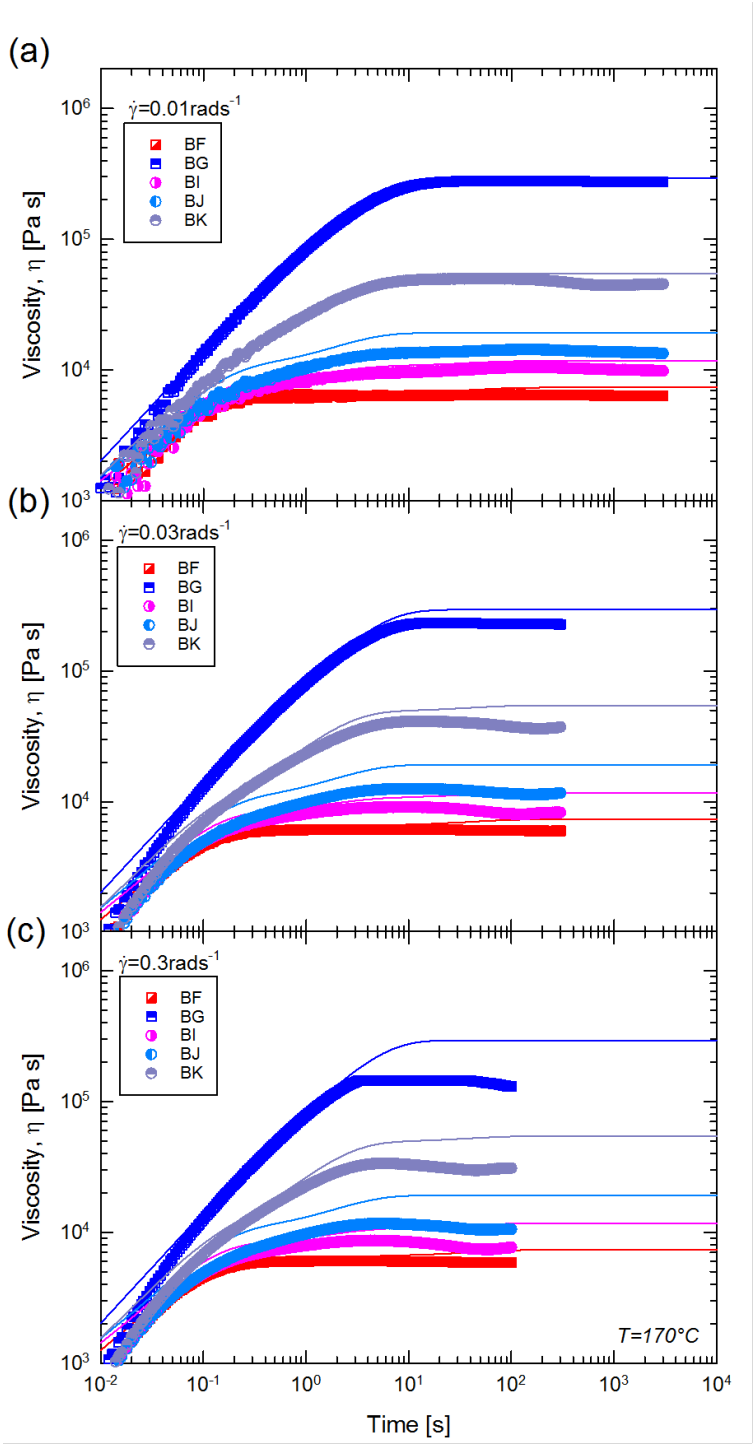


Figure 6.23: Comparative transient data at 170 °C for blends of materials BF and BG at varying strain rates: (a) $0.01\,s^{-1}$; (b) $0.03\,s^{-1}$; and (c) $0.3\,s^{-1}$. Linear envelopes are shown as continuous lines, while data is presented as symbols.

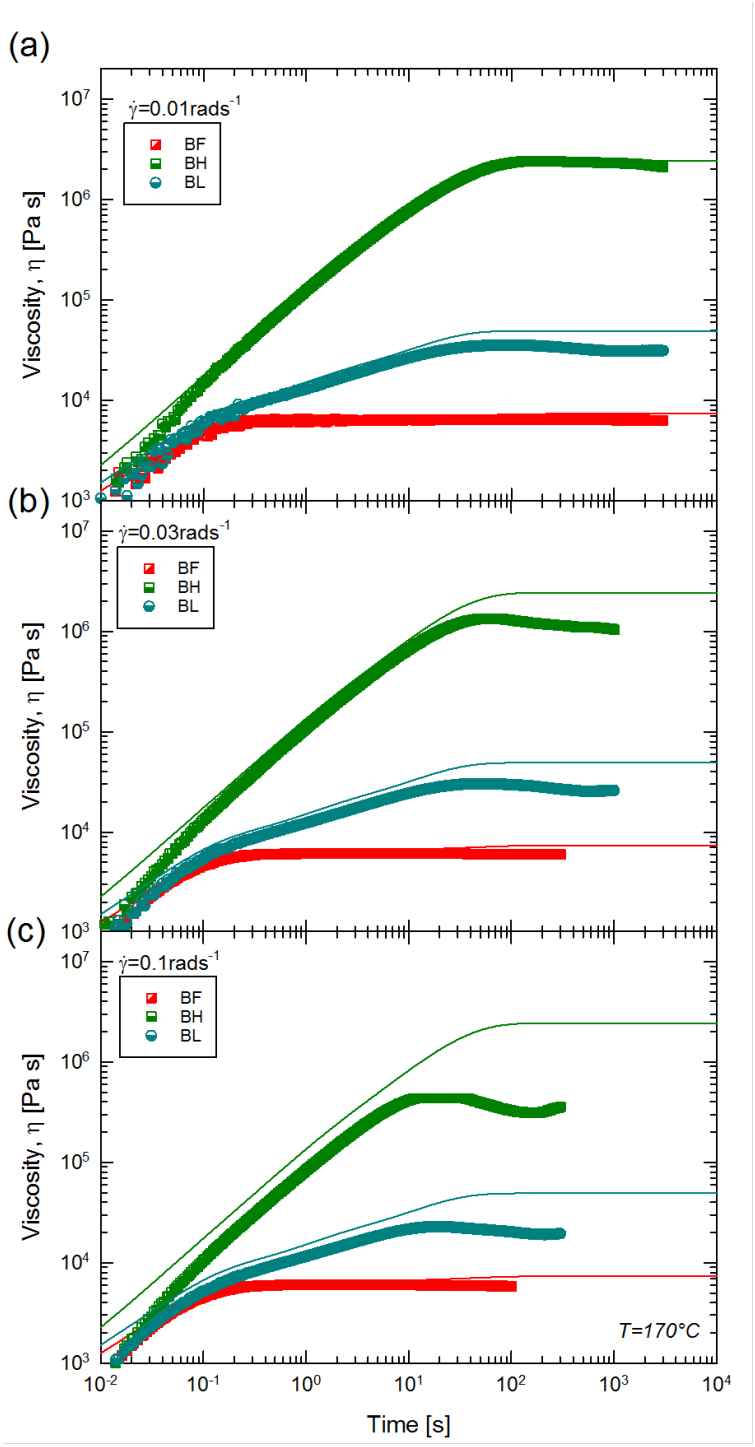


Figure 6.24: Comparative transient data at 170 °C for the blend of materials BF and BH at varying strain rates: (a) $0.01\,s^{-1}$; (b) $0.03\,s^{-1}$; and (c) $0.1\,s^{-1}$. Linear envelopes are shown as continuous lines, while data is presented as symbols.

non linearity, even at the lowest examined strain rate of $0.01\,s^{-1}$. The attributable mechanisms behind this (i.e. chain stretch and CCR) were discussed earlier in the transient data of the monodisperse materials in section 6.6.1. Yet, in this section, the differences of how these mechanisms are experienced within the entangled networks of monodisperse specimens and monodisperse binary blends, can be explained by understanding the relaxation threshold limits at which they are triggered. Read [172] suggests that in chain stretch, when the melt experiences deformation two main features define the onset of this mechanism: a) the first is the orientation of the tube; and b) the second is the point at which the chains become stretched based on the length scales associated around the tube diameter. For binary blends two timescales are triggered within the deformation process, one for the short molecules, i.e. S, and another one for the longer chains, i.e. L. Both these molecules will orient at different timescales, and will mutually influence the onset of the CCR mechanism as the increase in chain ends, resulting from a dominant majority of short chains within the matrix, speeds the relaxation time of the long molecules. This description serves to explain the appearance of an earlier and broader non-linear behaviour in the stress-undershoots of the reported experimental transient data. In the next section, it is compared how this transitioning behaviour is experienced in polydisperse blends where relaxation is an spectrum of an increasing contribution of short to long interacting molecules.

6.6.4 Polydisperse blends

The transient and extensional data of polydisperse blends CA-CD is presented in Figures 6.25-6.28. Bear in mind the data of both solution blended and melt-mixed samples has been concentrated into one single graph with the use of captions.

As it has been mentioned in the exploration of current rheological trends for interpreting extensional data (i.e. section 6.6.3); a system can be considered diluted when the component added into an entangled polymer network is uncapable of producing entanglements. Viovy *et al.*[178] confirm that the tube only dilates when the constraints are below the entanglement molecular weight, M_e, following DTD theory.

In accordance to the format used for the bimodal monodisperse blends, the

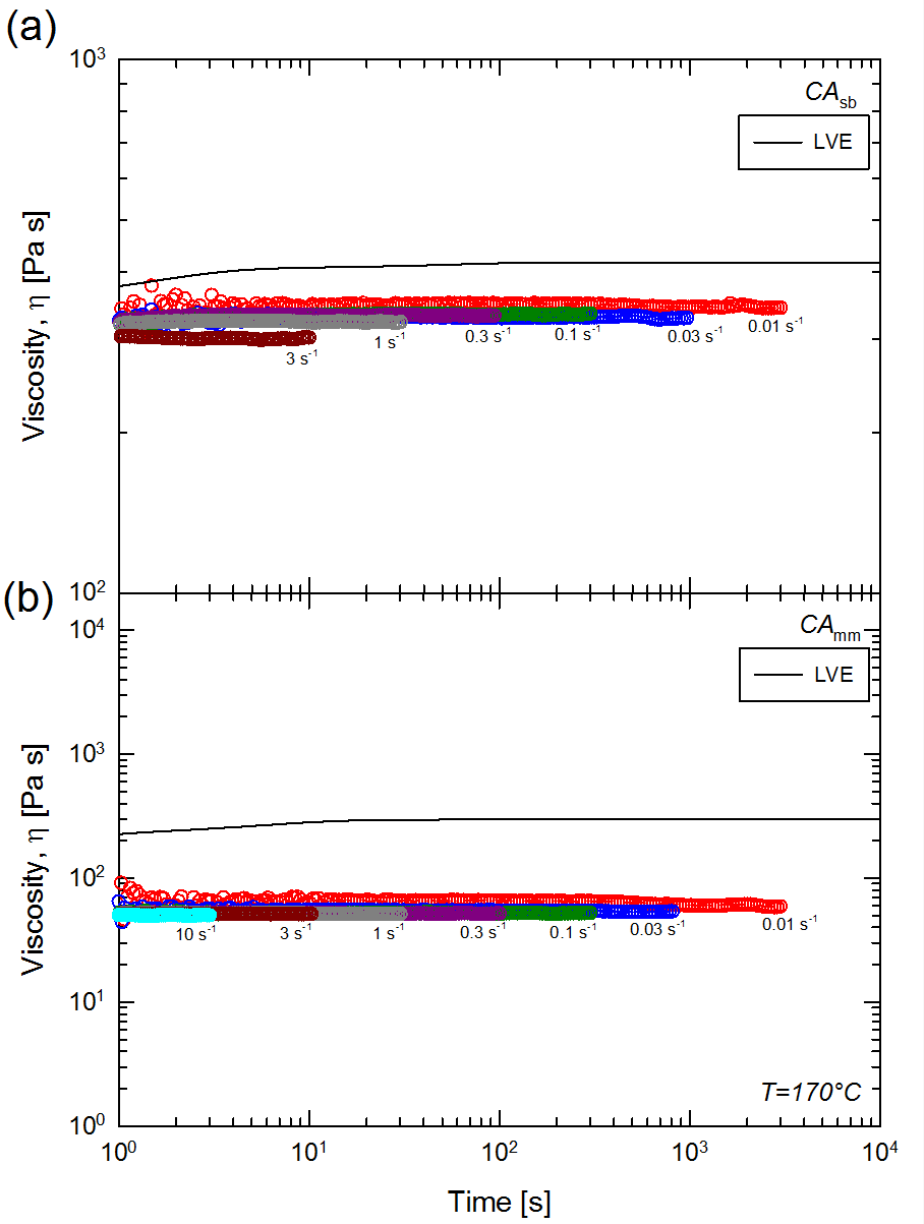


Figure 6.25: Transient shear viscosity for material CA; plots of: (a) solution blended and (b) melt-mixed samples have been identified with the corresponding subscripts ($-_{sb}$ and $-_{mm}$). The linear envelope is presented as a continuous black line. The applied shear rate is indicated alongside corresponding data.

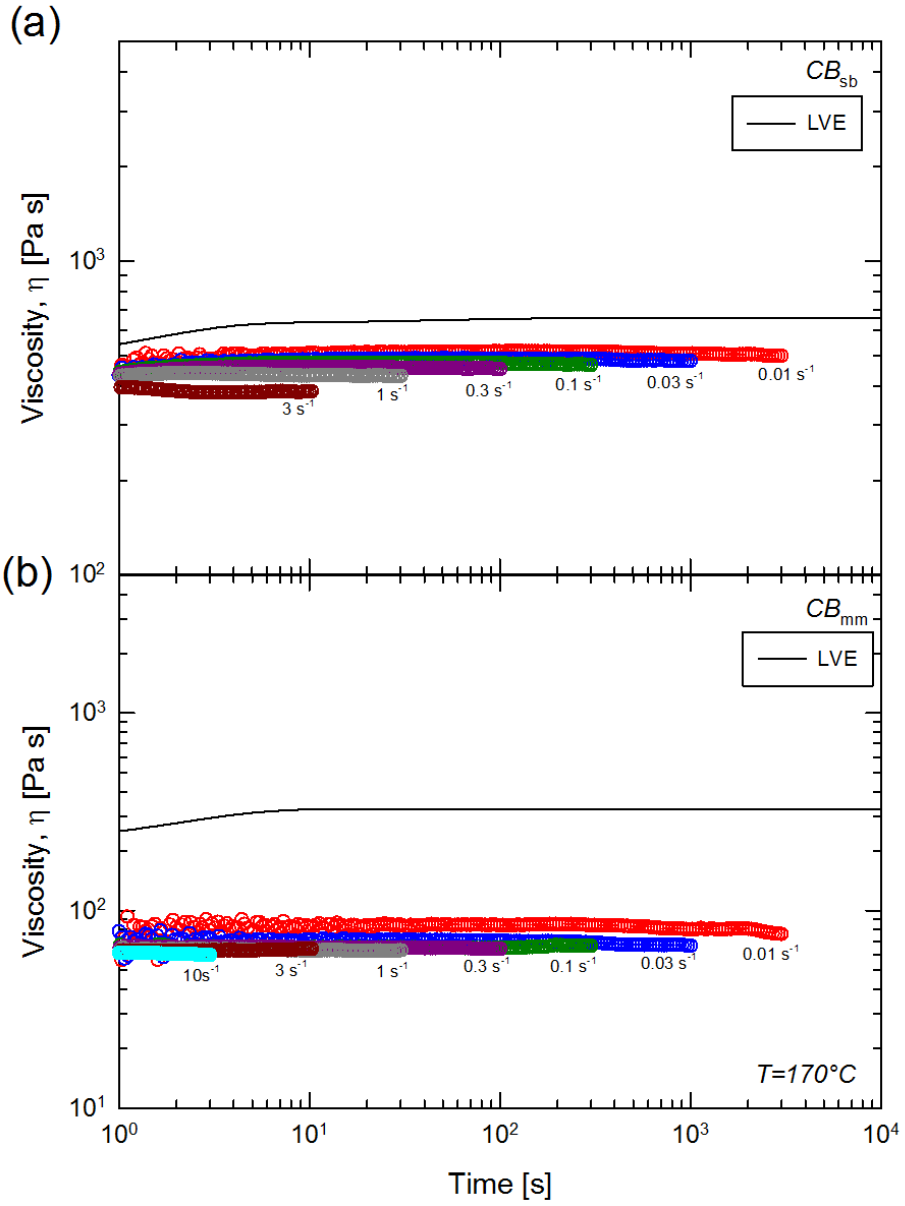


Figure 6.26: Transient shear viscosity for material CB; plots of: (a) solution blended and (b) melt-mixed samples have been identified with the corresponding subscripts ($-_{sb}$ and $-_{mm}$). The linear envelope is presented as a continuous black line. The applied shear rate is indicated alongside corresponding data.

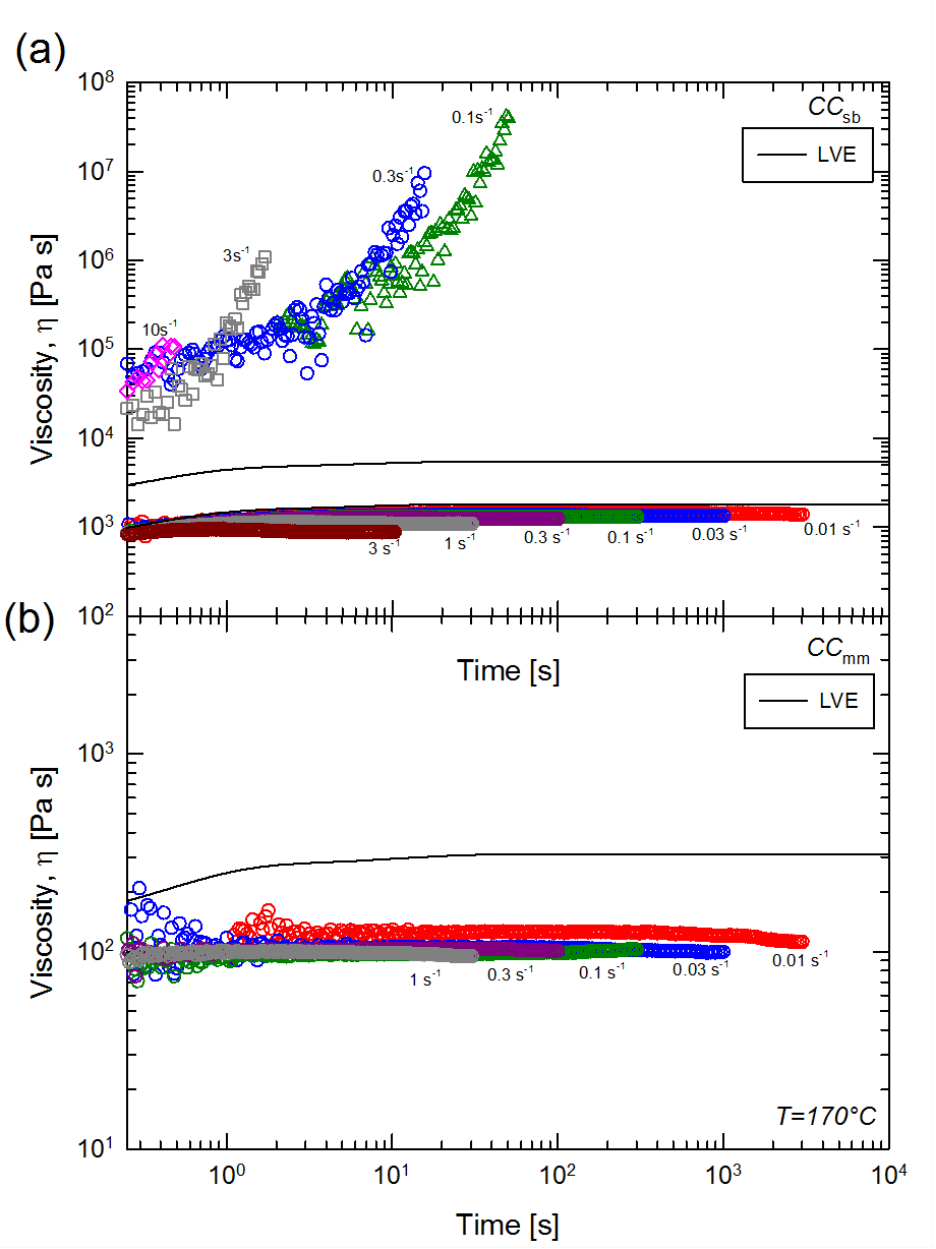


Figure 6.27: Extensional and transient shear viscosity for material CC; plots of: (a) solution blended and (b) melt-mixed samples have been identified with the corresponding subscripts ($-_{sb}$ and $-_{mm}$). The linear envelope is presented as a continuous black line. The applied shear rate is indicated alongside corresponding data.

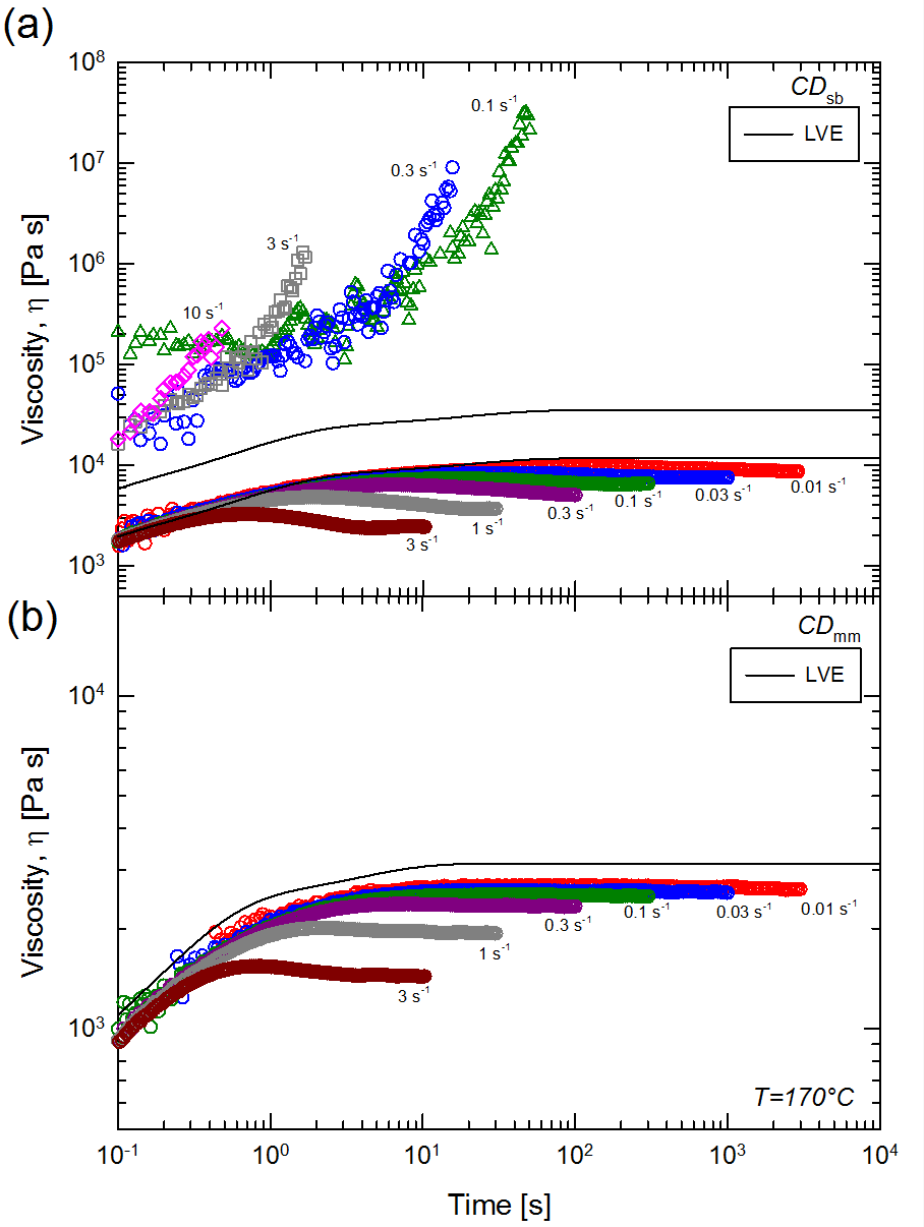


Figure 6.28: Extensional and transient shear viscosity for material CD; plots of: (a) solution blended and (b) melt-mixed samples have been identified with the corresponding subscripts ($-_{sb}$ and $-_{mm}$). The linear envelope is presented as a continuous black line. The applied shear rate is indicated alongside corresponding data.

transient data of the studied polydisperse blends is plotted in figures 6.29 and 6.30 transitioning from increasing content of BY at three specific strain rates ($0.03\,s^{-1}$-$1\,s^{-1}$).

One feature which was omitted by the settings in the time axis of the individual graphs for the studied polydisperse blends (6.25-6.28) is the apparent noise at very low frequencies that is similarly found in material BX. This effect is further decreased as the systems become capable of imposing some resistance to flow which manifests faster at higher strain rates. Figure 6.30 shows that in agreement with the higher amount of lower molar mass fractions found in the SEC distributions of the samples obtained through melt-mixing, these blends depict a closer behaviour to the large scattering observed at lower frequencies for material BX. The rather "flat" response observed for the blends CA-CC (regardless of the blending procedure used) evidences the high fraction of unentangled chains that compose the system; and it follows on the observation made for material BX, where the polymer network is uncapable of manifesting the entangling mechanisms that give rise to the characteristic stress overshoot followed by shear thinning present in the data of the monodisperse materials, monodisperse blends and polydisperse material BY. This observation keeps valid regardless of the fact that an increase in viscosity is measured as the addition of the higher molar mass component is incremented. Interestingly enough, as soon as the blending ratio reaches a 50 wt% contribution of the BY component, the described features for the onset of chain stretch and CCR become fully noticeable, particularly in the blend obtained through a solution blending procedure.

To the authors knowledge, although this behaviour has been previously studied in diluted systems of monodisperse PS materials (refer to section 6.6.3), there are currently no published data that consider a dilution effect coupled with an increase in polydispersity. Hence, the data provided in this section should promote an interesting platform for the testing, widening and enhancement of rheological physical models.

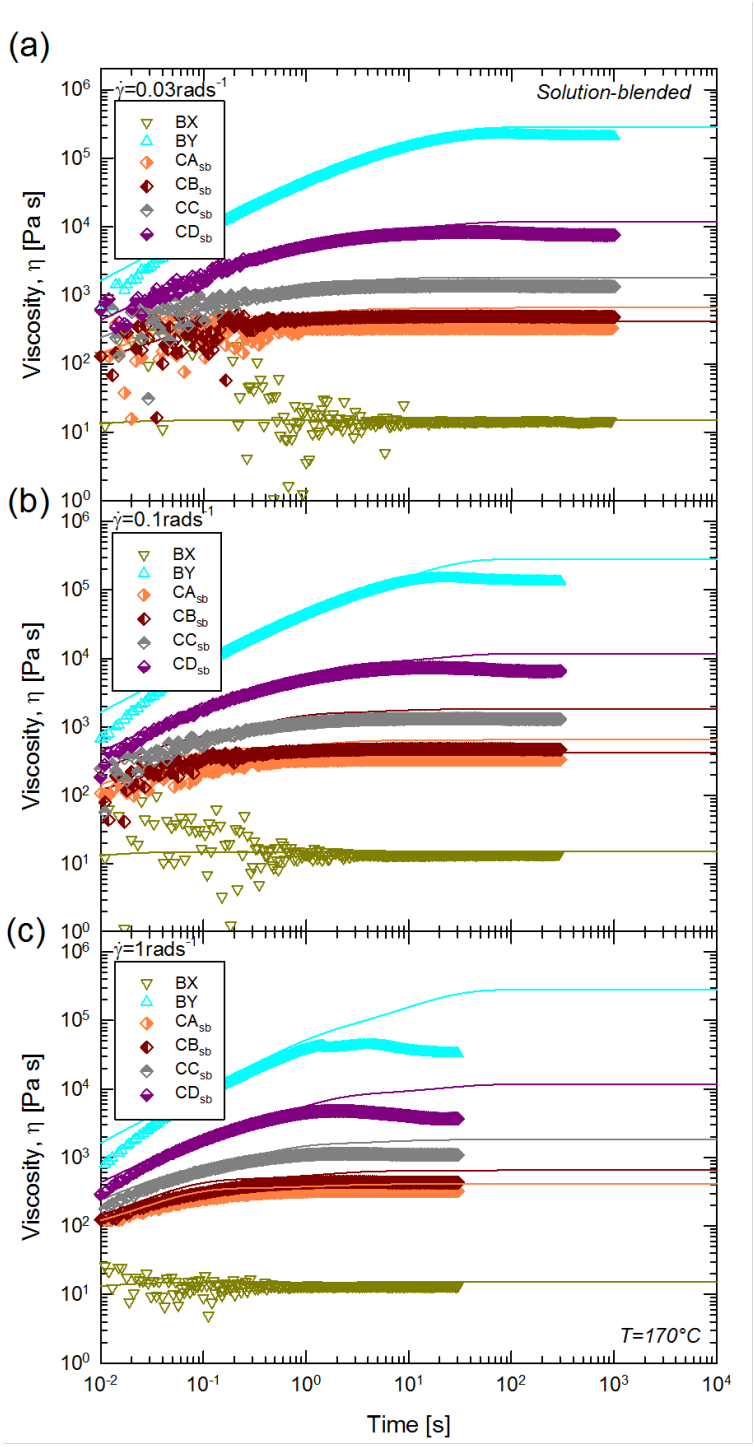


Figure 6.29: Comparative transient data at 170 °C for the solution blends of materials BX and BY at varying strain rates: (a) $0.03\,s^{-1}$; (b) $0.1\,s^{-1}$; and (c) $1\,s^{-1}$. Linear envelopes are shown as continuous lines, while data is presented as symbols.

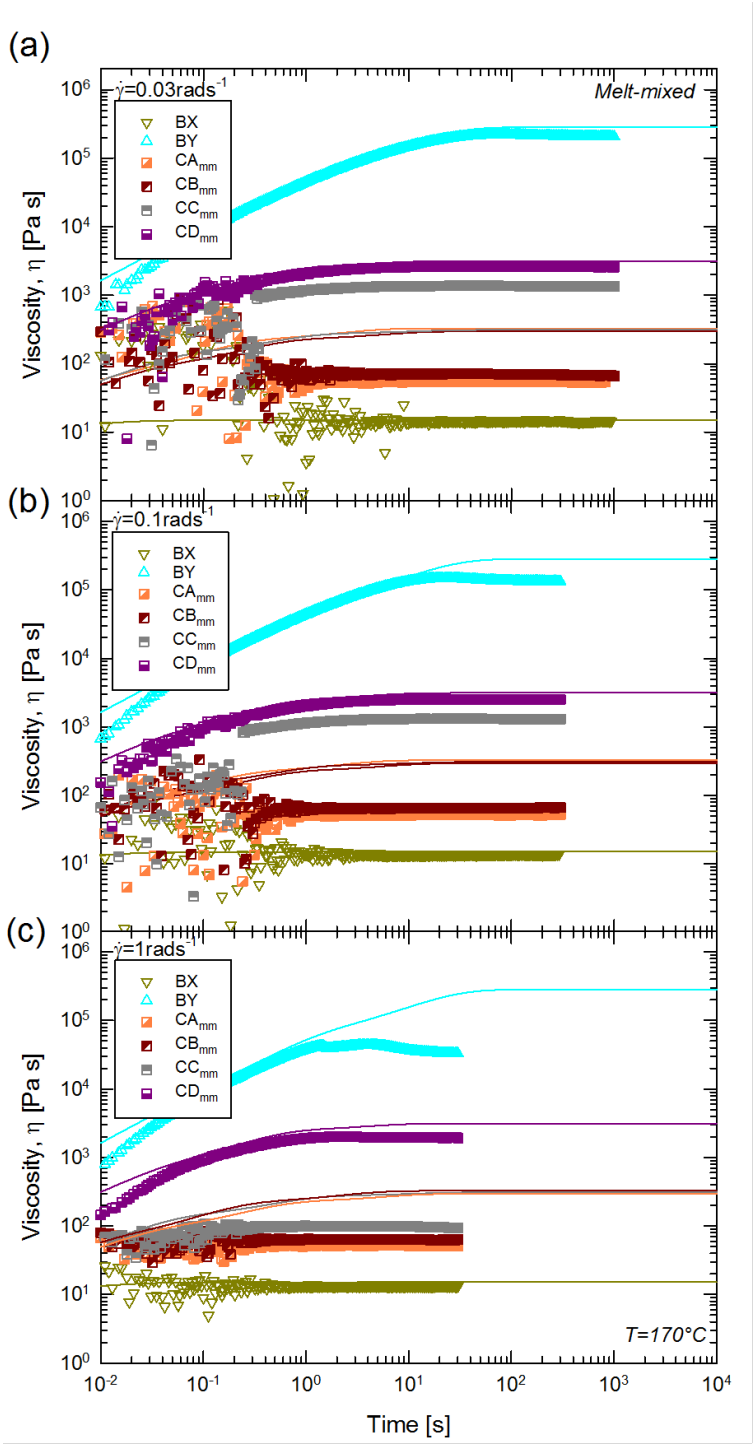


Figure 6.30: Comparative transient data at 170 °C for the melt-mixed blends of materials BX and BY at varying strain rates: (a) $0.03\,s^{-1}$; (b) $0.1\,s^{-1}$; and (c) $1\,s^{-1}$. Linear envelopes are shown as continuous lines, while data is presented as symbols.

6.7 Conclusions

Latest rheological models and theories have been used to interpret the experimental findings obtained through: oscillatory, transient and extensional tests.

LVE data of the studied materials was analysed by fitting of rheological models available in the REPTATE software toolkit. LVE materials parameters were obtained by fitting the L-M theory to the mastercurves of monodisperse materials BF-BH to define: M_e, G_e and τ_e. These parameters were input to obtain the mastercurves of the remaining materials. The mastercurves of the polydisperse materials BX and BY, as well as the monodisperse and polydisperse blends were examined by best-fitting the available rheological LVE theories: Rubinstein and Colby, R-C, for binary blends, and the polydispersity double-reptation theory, pDR, for highly polydisperse systems. As expected the R-C theory was found to be better suited to describe the LVE behaviour of the monodisperse blends, whilst the pDR theory showed a closer fit to the behaviour of the analysed polydisperse materials. Nevertheless, both theories deemed ineffective at fully capturing the experimental observations of the highly polydisperse blends (BX, and blends CA-CD). Effectively, the treatment in itself for processing the mastercurve of these systems included a horizontal shift factor correction in the data to consider the free end effect of T_g of the shorter molecules (e.g. lower molar mass fractions). In all, the transitioning of the data from monodisperse materials up to highly polydisperse blends with vast fractions of unentangled chains was able to reflect on the previously documented characteristics of polydispersity and the onset of entanglements, such as the deviations of the G' and G" slopes at the terminal region, and the identification of a steady, or double-stepped plateau as the systems increase the content of higher molar mass fractions.

To study the non-linear viscoelasticity of the analysed materials, the results of transient and extensional tests were treated phenomenologically by comparing the reported data with recently published literature [111; 151; 166; 167; 175; 176]. Experimental constraints and mechanical complications with the SER fixture used for the extensional tests hindered the quality of the reported results, and thus the observations included in this treaty will benefit from subsequent re-runs to confirm the veracity of these arguments. The overall observed trend in the

extensional response of the studied materials was that as the elongation strain rate was increased, earlier deviations from the linear envelope were detected; manifested through the characteristic stress overshoots, i.e. strain hardening behaviour. At the same strain rate, higher viscosity values were reported for the blends compared to monodisperse materials. This phenomenon was attributed to an increase in the effective stretch relaxation of the long chains as these are diluted by short chains [179].

Transient tests confirmed stress peaks followed by a shear thinning behaviour in compliance to what has been reported elsewhere [9; 79; 164]. The quality of these responses was seen to vary with respect to molar mass and strain rate. For a higher molar mass, deviations from linearity were seen to appear at lower strain rates. Similarly, at systems with higher $\overline{M}_w$ values, corresponding increases in the reported η were documented. In highly untentangled systems (BX, CA-CC), evidence of the chain stretch or CCR mechanisms could not be clearly identified. This outcome challenges the entangling dynamics that build the predictive success of current rheological models, and provide novel experimental data that could serve to provide some scientific grounds to the complexity of modelling diluted polymer systems with high levels of inherent polydispersity.

Chapter 7

Conclusions

7.1 Prelude

The subject of this thesis was to provide novel experimental evidence upon the manifestations and consequences of molar mass and molar mass distribution in the solid-state, i.e. crazing and birefringence, and melt-state, i.e. rheological behaviour, of glassy polymers using PS as a case study. The influence of blending inherently polydisperse commercial polymers of high molar mass, with materials with high degrees of unentangled fractions has led the focus of this work. Physical polymer theories, mainly constituted upon the concept of entanglements have been scrutinised to interpret the experimental data.

In this chapter, a summary of the most relevant contributions of this work is provided, under the following structure: first, the key findings outlined in each of the individual chapters presented in the main body of this thesis is provided in section 7.2. This is followed by a summary on the outcomes of this research in section 7.3. The chapter concludes with brief account of the recommendations for future work in section 7.4.

7.2 Key findings

The main findings of this work as described in the main body of this thesis are as follows:

7.2.1 Molar Mass Analysis

- An accountable larger fraction of lower molar mass species seen in the polydisperse blends produced using a melt-mixing approach, determined that this process introduces the risk of polymer thermal degradation that is accelerated at chain ends.
- SEC evidence also concluded that the polydisperse blends synthesised using a solution-blending procedure contained a lower than expected amount of low molar mass species, ocurring as a result of oligomer evaporation during the filtration and precipitation stages.
- Theoretical simulation of an 'ideal' blend at the studied weight ratios, corroborated that the obtained melt-mixing and solution-blending samples were over and under predicted, respectively.
- Further calorimetric evidence proved that in the case of the melt-mixed blends T_g was 4 °C below the T_g measured for the lower molar mass component BX. Similarly, in the solution-blending samples, T_g was seen to be above that of BX in all cases.
- Is worth noticing that the models explored for blending and T_g simulations had a much improved predictive accuracy in blends of monodisperse materials, where polydispersity remains low (PDI<2).

7.2.2 Crazing Analysis

- An isochronal three point creep bending technique for miniature specimens was used to produce novel craze initiation stress data of extremely brittle polydisperse blends.
- The CIS was seen to increase as a function of adding a wt% of a higher molar mass component, in both: monodisperse and polydisperse bimodal blends. Even as little as 10wt% addition, would increase the CIS by an order of 1.5 MPa, substantially improving the ability to undergo craze formation.

- Following the evidence of the SEC and DSC data, the CIS of the solution-blending samples was found to be higher (in the order of 2 to 7 MPa), compared to the blends obtained through a melt-mixing process.
- A piecewise linear model for the determination of molar mass limits in craze initiation stress was modified to account for a DTD effect that describes the dilution of the tube as a result of the unentangled fractions in the molar mass distribution, which decrease the ability of longer chains to sustain crazing, thus reducing CIS.
- The experimental data of the polydisperse blends was used to validate the new termed hybrid CIS-DTD model, positively accounting for a much improved predictive capability of CIS in highly polydisperse systems (70%-90% accuracy), whilst rendering equally suitable for the prediction of CIS in monodisperse materials of moderate dispersity levels.
- The effect of orientation was studied in monodisperse materials and their corresponding blends by measuring birefringence in drawn specimens, combined with isochronal three point creep tests. The results confirmed that it is orientation that controls the rise in crazing stress over molar mass, at least at the linear limits of the stress-optical rule.

7.2.3 Rheological Analysis

- In the analysis of LVE data, the theory of bimodal blends of Rubinstein and Colby was seen to yield a better simulation for the bimodal monodisperse blends, whereas the double-reptation theory was better suited to model broad polydisperse blends.
- In the treatment of the oscillatory shear data of the polydisperse blends, it was necessary to use a modified shift factor for the WLF for very short chains that considers the dependence of T_g described by a $1/\overline{M}_n$ relationship.
- Experimental complications arising from the extensional fixture precluded more conclusive arguments on the data. Yet, a qualitative analysis of the

tests was able to expose evidence of strain hardening in higher molar mass materials (e.g. BH and BY) at high strain rates (i.e. $3\,s^{-1}$ and $10\,s^{-1}$) characteristic of chain stretching occurring in the materials at the observed relaxation time.

- The effect of polydispersity in the extensional data was manifested as increased extensional viscosity values (i.e. a factor of 5) for a polydisperse material compared to a monodisperse material of similar $\overline{M}_w$. This comes as a result of high molecular weight components in the distribution contributing to the strain hardening process at different time scales.

- The rheological behaviour in transient shear of the monodisperse and polydisperse blends showed a progressively increasing shear thinning effect as the addition of the higher molar mass component was increased. This was seen to induce stretching effects on the molecules as the strain rates become faster than the observed relaxation timescale.

- The transient shear of the polydisperse blends was dominated by a linear response of the contribution of constituent material BX. Nevertheless, weak shear-thinning was observed, consistent with the contribution of the long molecules from material BY stretching, but being screened by the matrix of short chains from BX.

7.3 Summary

The polystyrene systems investigated in this thesis have come from a variety of sources covering both: a) analysis of highly monodisperse materials that are mainly used experimentally for theory validation, and b) readily available commercial polymers with various levels of polydispersity. The differences in the molar mass and molar mass distributions of all these systems offer a very wide spectrum of mechanical, and rheological properties that have served to characterise PS as a commodity polymer suitable for a broad range of applications (from kitchenware to IT equipment). Although PS is a material that has been studied for decades, the methodology of research appears to have tackled specific aspects

of polymer dynamics at any one time. Building a network of fundamental polymer physical concepts that have been progressively validated using experimental evidence as novel instrumentation and characterisation techniques become available. Perhaps one of the less conclusive topics on this stream of research has been the goal to parameterise molar mass and molar mass distribution characteristics into the core constitutive equations for polymer theories. The availability of securing a portofolio of 18 inherently different molar mass PS systems has provided this study with the resources to explore these theories, and where possible improve them based on novel experimental data. In addition, the actual blending and synthesis of some the blends was conducted in close similarity to the methods followed by polymer processers and manufacturers in an attempt to evaluate if such processes are seen to have any bilateral effects in the molar mass characteristics of the obtained systems.

Because the materials used came from different sources, it was necessary to obtain the information on their molar mass and molar mass distributions through chromatographic and calorimetry analyses, as detailed in chapters 3 and 4. The latter highlighted the differences in the composition of the molar mass distributions, whilst enabling the calculation of relevant molar mass information (i.e. $\overline{M}_n$, $\overline{M}_w$, PDI) for all the studied materials. One of the outstanding findings in this aspect, was the recognition of quantifiable differences in the molar mass averages and distributions observed in polydisperse blends produced with the same blending ratios, but different synthesising procedures. A lower molar mass tail of an increased amount of unentangled fractions was found in the blends produced through melt-mixing using an extruder. Whilst, the opposite was observed with blends produced through solution mixing in THF, and precipitation in methanol. The differences observed in the chromatographic results were supported by calorimetric data, that showed a reduced T_g (of -4 °C) in the melt-mixed samples when compared to their dominant polymer base constituent (BX). On the contrary, the solution blended samples were seen to be in excess of $\sim$13 °C when compared to their main polymer matrix. The mechanism behind the lower mass tail of the melt-mixed was found to be polymer degradation. Thermal inputs over a prolonged time are seen to accelerate polymer degradation as the presence of unsaturated chain ends downgrade by chain scission into oligomers. Conversely,

oligomer evaporation during the filtration and precipitation stages was determined as the cause for the solution blended samples to lose the weight fractions characteristic of the lower end of their molar mass distribution.

Chapter 5 analysed the craze initiation process of the studied materials, through the application of an isochronal three point creep bending technique developed for bulk miniature specimens. A piecewise linear model exclusively developed for monodisperse systems was used to initially analyse the CIS of the monodisperse materials and their blends. As expected, an increase of as litte as 10 wt% of the higher molar mass component in the blends was seen to rise the value of the experimentally measured CIS by ∼1.5 MPa. A constitutive equation for the determination of $\phi_\theta(M)$, namely the molar mass fraction parameter as a function of θ, the latter defined as the power law molar mass parameter, was derived from fundamental equations for the calculation of molar mass averages. The main contribution of θ is that it provides a numerical constant that can be associated with all the molar mass fractions that constitute a polymer distribution. $\phi_\theta(M)$ was implemented into an expression for σ_c to derive a constitutive equation capable of quantifying the contributions into the craze initiation stress of individual weight fractions from the experimentally obtained molar mass distributions (equation 5.4). To identify the most suitable value of θ two methods were explored: a root-mean-square error fitting on the data, and a Monte Carlo simulation. Since the latter offers probability certainty, a 90% CI at $\theta = 2.59$ was determined to run the calculations. These results showed that although the piecewise linear model was accurate at determining the CIS of the monodisperse materials and polydisperse systems with moderate polydispersity levels (PDI$\leq$ 3), this deemed ineffective at predicting the experimentally measured σ_c of the highly unentangled polydisperse materials BX, and blends CA-CD. To improve the model, the ideas of dynamic tube dilution, DTD, were integrated into the expression for σ_c. DTD suggests that as the tube dilutes, the molar mass between two entanglements becomes larger, thus decreasing the number of entanglements from Z to Z', the effective number of entanglements. By considering this effect, it was possible to modify the original equation of σ_c (equation 5.4) into a new expression based on Z' (equation 5.11). The effect of such a principle is that the shorter chains in the polymer molar mass distribution that lie in the unentangled/dilution regime

of the piecewise linear model are now assumed to modify the polymer dynamics of the longer chains, resulting in a "negative" contribution to CIS, where before these chains were assumed to have no effect. When introducing this correction in the model, the predictive accuracy of σ_c for the polydisperse systems was reported to be as high as $\sim$ 96% in the melt-mixed blends, and $\sim$ 84% in the solution blended samples. The improved model is now capable of more accurately predicting the crazing stress of highly polydisperse systems, whilst retaining its predictive capability for monodisperse materials.

A study of orientation and crazing stress was conducted in drawn specimens of the monodisperse materials and their blends. The degree of orientation was characterise through birefringence measurements. It was observed that as the drawing temperature of the materials was closer to the glass transition temperature the reported birefringence was three times higher. This increase in birefringence is expected, since as the drawing temperature shifts towards a glassy state the polymer is unable to relax the deformation and the chain stretch is frozen in. At the same drawing temperature, the birefringence was observed to be higher for the higher molar mass materials BG (at 116 °C, $\Delta n = 0.0088$) and BH (at 116 °C, $\Delta n = 0.0085$) compared to BF (at 116 °, $\Delta n = 0.0058$). The analysis of $\sigma_c - \sigma_{c,iso}$ against birefringence, showed that for both: monodisperse materials and blends, orientation is the dominant factor in the increase in crazing stress over molar mass, with the samples following the linearity of the stress-optical rule up to a birefringence limit of $\sim$-0.0072.

In chapter 6 current rheological theories and models were explored with the aid of the REPTATE toolkit. Oscillatory shear, transient shear and extensional tests were performed with a rheometer in air environment and a range of temperature and strain rates. To analyse the obtained data, the first step was to determine the linear parameters from the mastercurves of the oscillatory tests of the monodisperse materials. $M_e = 15900\,\mathrm{g/mol}$, $G_e = 0.253\,\mathrm{MPa}$ and $\tau_e = 0.0014\,\mathrm{s}$ were determined by fitting the L-M theory into the mastercurves obtained at 170 °C. These linear parameters were used to process the mastercurves for the rest of the other analysed polymer systems. As the materials were increased in molar mass, the features of polydispersity and entanglements became more evident. In the case of the monodisperse blends, a set of "shoulders" was seen to arise at

the lower frequency region which results from the combination of contributions between the longer and shorter chains of the constituent materials. Similarly, as the polymer molar mass is increased, it is possible to see that the plateau region extends, which has been describe as the "signature of entanglements". In the case of material BX and polydisperse blends CA-CB, the onset of a plateau was greatly suppressed due to a very large amount of unentangled fractions. The mastercurves of the oscillatory data were input into REPTATE to carry an optimisation based on the library of available theories for linear viscoelasticity. The R-C theory for binary blends was found to be better suited to describe the behaviour of the monodisperse blends, whilst the double reptation polydispersity theory was more effective at predicting the behaviour of polydisperse materials R and BY. Nevertheless, both theories deemed ineffective at simulating the behaviour of material BX and blends CA-CD. The R-C theory seemed to account for a very marked two-step (namely materials BX and BY) contribution in the rheological behaviour of the blends, ignoring the transitional relaxation plateau that is a distinctive feature of polydisperse materials. On the other hand, although the pDR theory does account for this transitioning feature, the obtained simulation failed to be accurate.

Transient shear showed that when the timescales of the tests were seen to be slower than the relaxation time, the materials showed a linear response. As the molar mass of the materials was increased, corresponding shear thinning, and occasional overshoots became more pronounced. These features are characteristic of the chain stretching and convective chain release mechanisms described in polymer theories of non-linear viscoelasticity. In the blends, these mechanisms become progressively more evident as the reported viscosity was seen to increase with the increased addition of a higher molar mass component. Due to complications with the SER fixture, the quality of the extensional data precluded to provide quantitative conclusions. Nevertheless, some relevant manifestations of molar mass and molar distribution could be detected. At the same strain rate, the monodisperse blends were seen to have a higher viscosity than their constituent monodisperse components. This phenomena is a result of the effective stretch relaxation of the long chains being increased due to the diluting effect of the surrounding short chains.

7.4 Concluding remarks and further work

This work has introduced an improved piecewise linear model to predict the craze initiation stress in monodisperse and polydisperse PS systems. It would be useful to refine this model further by testing it against experimental data of systems with varying molecular architectures (e.g. branched systems, rather than just linear), or alternative chemistries of glassy polymers. Further adjustments to the model accounting for these aspects could expand its applicability.

Although the results confirmed, quite encouraging, that orientation poses a more significant controlling role in the determination of crazing stress than does molar mass for oriented specimens, further measurements of more complex polydisperse blends are required to cover the whole spectrum. The authors recommend the further application of this theory in oriented samples of materials such as system BX, or blends CA-CD. Nevertheless, some complications in the preparation of these samples are to be expected since their inherent brittleness may pose significant challenges in traditional methods of tensile elongation.

Unfortunately, complications with the SER fixture of the extensional tests excluded a more conclusive quantification of the obtained data. Still, some relevant questions arose from the interpretation of the results: is the strain hardening observed on the monodisperse blends real? If so, it would appear that both components exhibit this behaviour, which suggests that the effect of chain stretching increases upon blending as initially suggested in [164]. Further testing is required to verify the validity of this observation. Also, there seems to be virtually no difference in the rheological response of blends CC and CD, despite the latter having a 30wt% increase in the content of BY. This result is rather surprising, and re-run of the tests in these materials could dissipate whether the observed behaviour is real or an experimental artifact.

Appendix A: Crazing rigs

As part of this research it was decided to manufacture new sets of crazing rigs to be able to test multiple specimens at a given time. Figure 1 shows the technical CAD drawings that were provided to the University of Nottingham workshop for manufacturing. The finished devices are shown in figures 2 and 3.

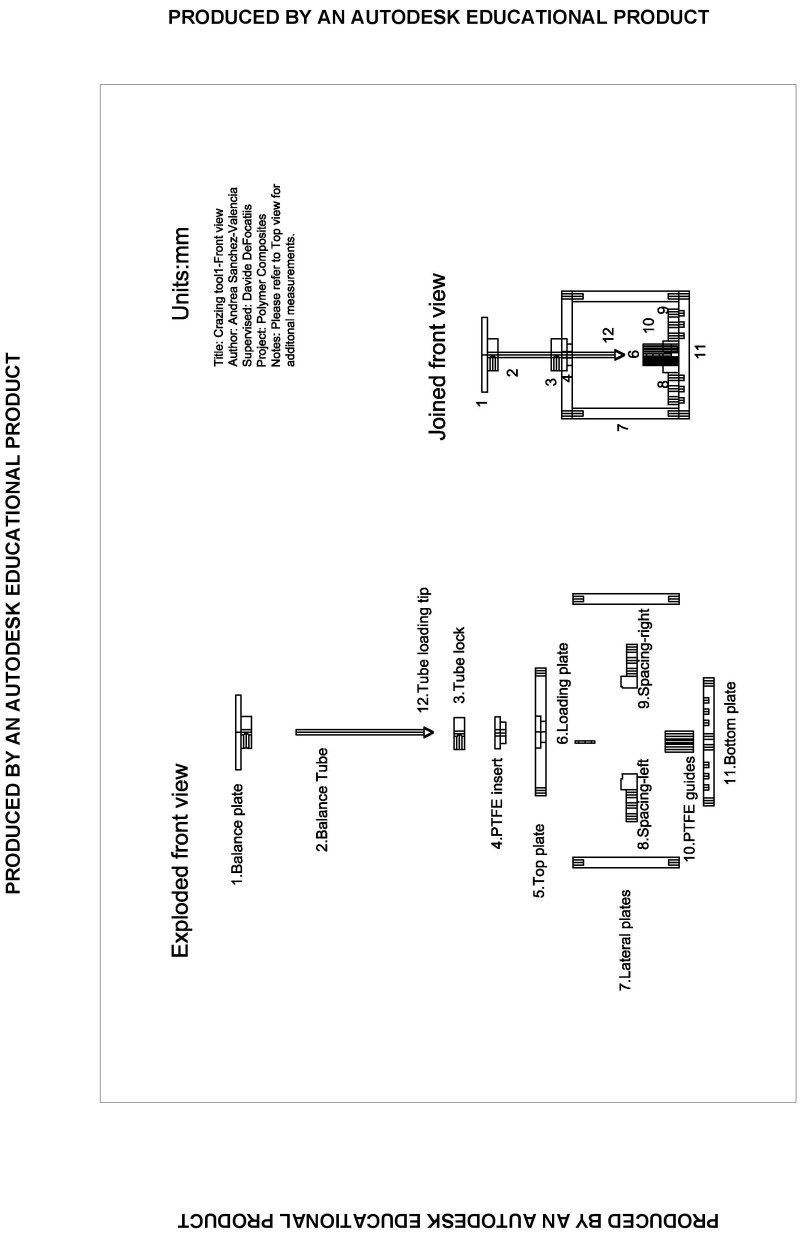


Figure 1: Exploted view of new crazing tool CAD drawings; elements have been labelled and numbered for production purposes.

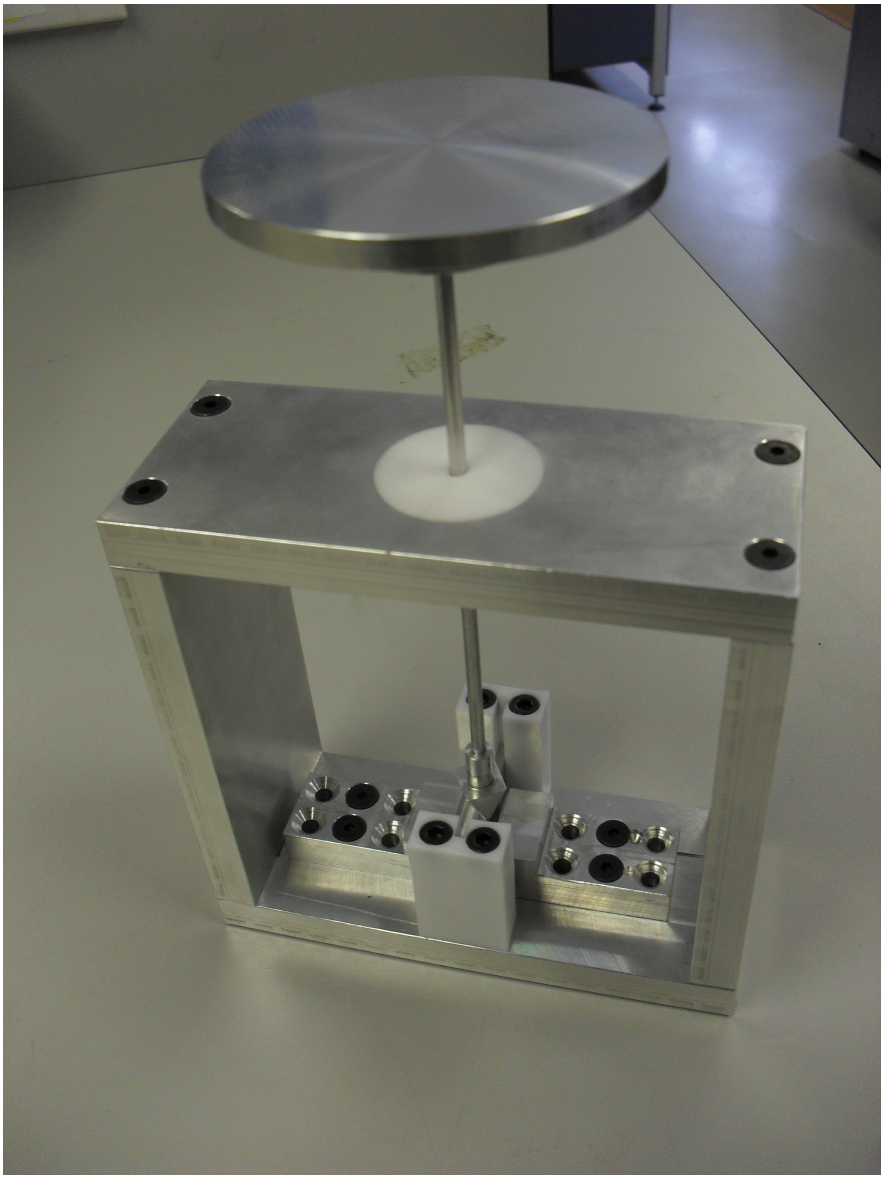


Figure 2: Detail image of new crazing rig as manufactured from CAD drawings shown in figure 1.

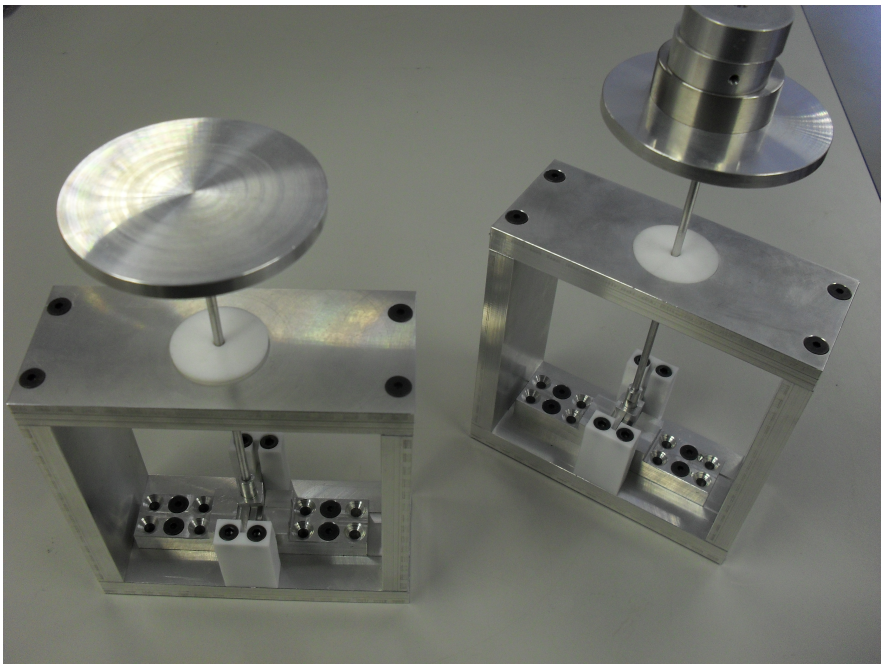


Figure 3: Image of the two sets of crazing rigs produced.

Appendix B: CIS correction

Ischronal three point bending tests were performed in miniature specimens of polydisperse material R, to verify the accuracy of the testing procedure and performance of new manufactured rigs. The material was tested at a series of creep times: 10s, 60s, 300s and 1800s, with the sample soaked in DEG during the test. The results were compared against those reported in [24]. The results have been plotted in figure 4, against the cited literature.

The reported CIS for material R showed an increase of approximately 2-3 MPa compared to De Focatiis data. To evaluate the differences that could arise from using our newly machined set of rigs, it was decided to plot the data obtained for our monodisperse materials against that previously reported by De Focatiis [20]. Figure 5, presents both sets of data in a CIS vs Molar mass plot, exhibiting the 3-step regime for crazing as proposed by De Focatiis,

From figure 5 the discrepancy between De Focatiis data and the data for our monodisperse materials was quantified as ±4-5MPa. To study the source for this disparity it was then decided, to have a closer inspection of the rigs used for the creep bending tests, to discard the possibility of them having differences in geometries (e.g. support spacing, L) that could alter the reported CIS value. The distance between the supports was measured with a caliper, to show a consistent 5±0.03mm in both rigs.

It was then decided to examine the edges of the left (LHS) and right (RHS) hand supports where the specimen was placed. This was done to eliminate the possibility of the curvature found in the edges of the supports modifying in some additional way the support spacing distance L. The supports of both rigs were analysed through an optical microscope in transmission mode, and calibrated

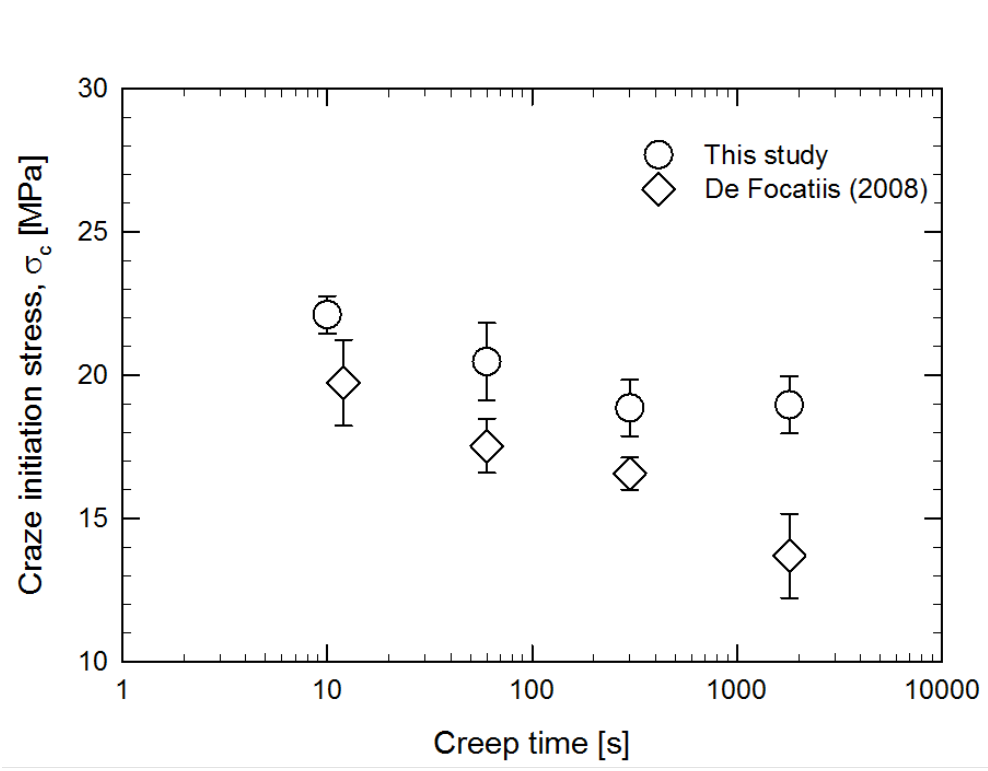


Figure 4: Craze initiation stress for polymer R in DEG, as reported in this study compared to [24].

accordingly with the use of a calibration scale. The obtained micrographs were subsequently processed using ImageJ software to measure the radii found in the edges of the supports of both rigs. Figure 6 presents the micrographs along with the measured radii for: a-b): LHS and RHS supports of the new rig manufactured at our Nottingham workshop, and c-d) the support plates used by[20; 24].

The measured radii in the LHS, r_1 and RHS r_2, supports were added to the previous total support spacing L to obtained a new value for L as is shown in table 1.

By looking at the values in table 1, is possible to show a support spacing difference of ∼0.40mm between one rig and the other, evidencing that this radial distance is in fact altering the spacing distance by 5±0.40mm. In order to account for this difference, it was necessary to correct the data by re-calculating a new corrected craze initiation stress σ_{cn}, by using the expression developed in 1,

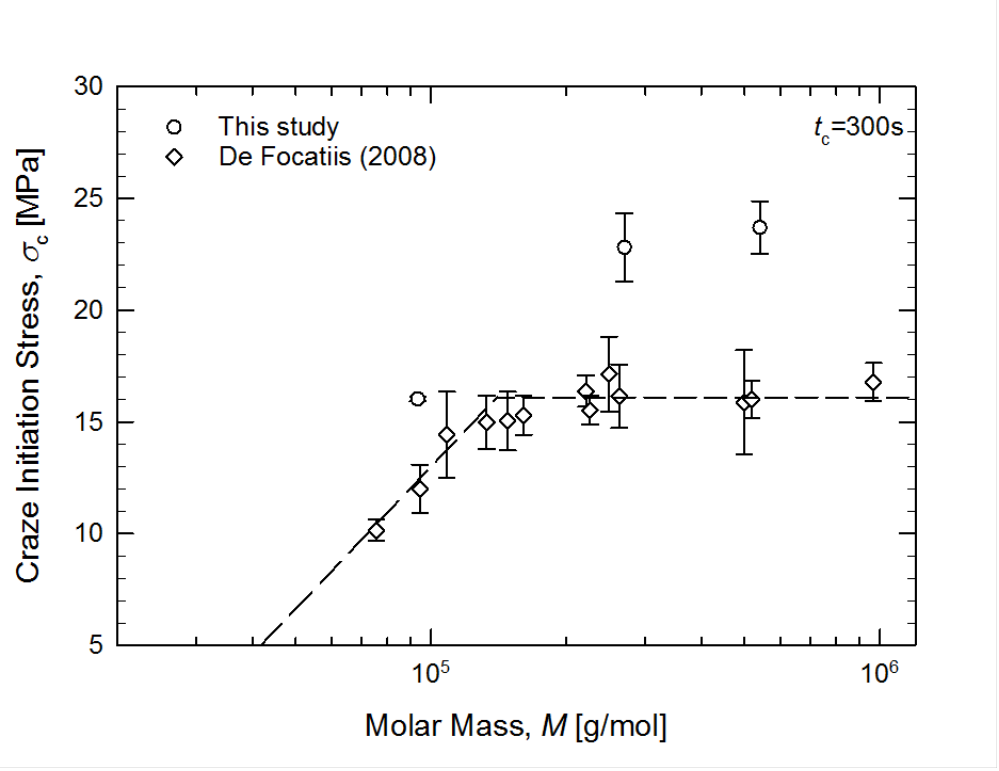


Figure 5: CIS as measured for monodisperse materials BF, BG and BH. Data has been plotted against the monodisperse data and fitting limits for the mechanisms of crazing as reported by [20].

Table 1: Radii measurements of the LHS and RHS supports.

Study	LHS, r_1 [μm]	RHS, r_2 [μm]	Total, r_T [μm]	New L [mm]
De Focatiis	284.17±13.2	250.41±8.12	534.58	5.5346
This study	27.26±2.8	102.13±8.7	129.38	5.1294

$$\sigma_{cn} = \sigma_c \left(\frac{L_u - L_c}{L_n - L_c} \right) \tag{1}$$

where L_u stands for the uncorrected spacing length, while L_n defines the new corrected spacing length, given by $L_u + r_T$, where r_T is the curvature distance of

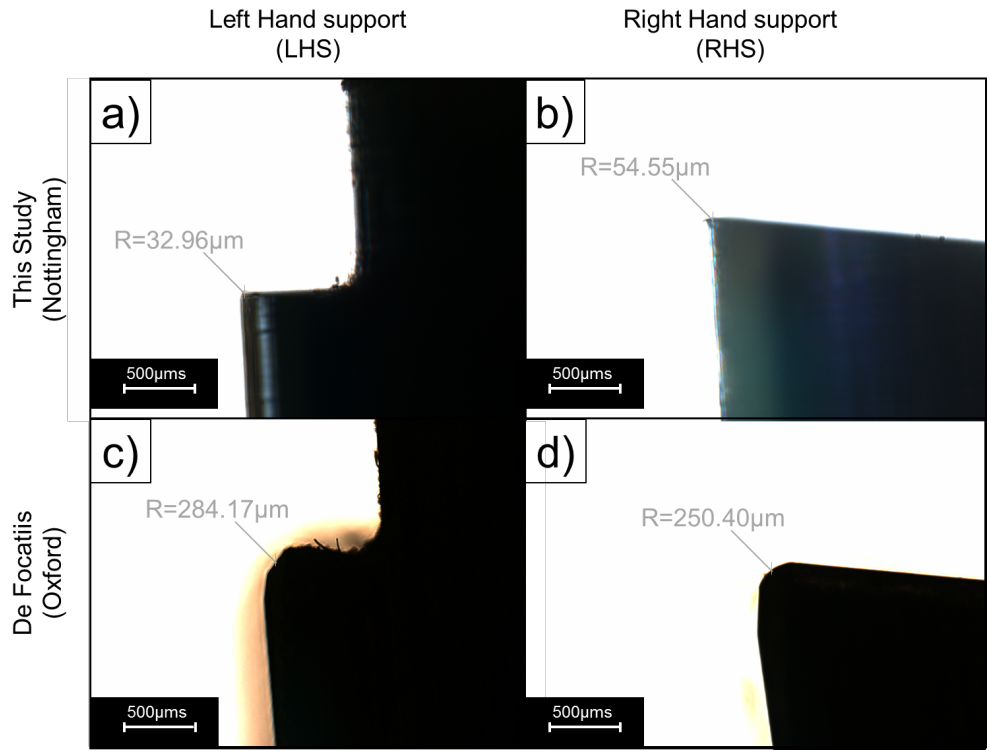


Figure 6: Micrographs showing the radii (R) difference of the edges in the specimen support plates used in this study and by De Focatiis[20; 24].

the radii in the edges of the specimen supports.

The data for both rigs has been corrected to account for the 0.53mm and 0.13mm radii distance into the 5mm spacing in the old and new rigs respectively. Tables for these correction can be found in the appendix section.

The new corrected data is presented in figure 7.

A new linear regression was applied to De Focatiis corrected data to find the corrected values for the disentanglement and chain scission limits. The corrected M_c value at which crazing shift from disentanglement into saturation (at chain scission) was found at 154,000 g/mol, compared to the previous 140,400 g/mol value reported by De Focatiis uncorrected data [20]. Although it is still possible to observe small differences of the order of a few MPa in crazing stress between the De Focatiis' data and the current dataset, thes are attributed to differences in the lighting and microscopy set-ups, which, especially given the discrete nature of the crazes and their spacing in miniature specimens, are consistent with the

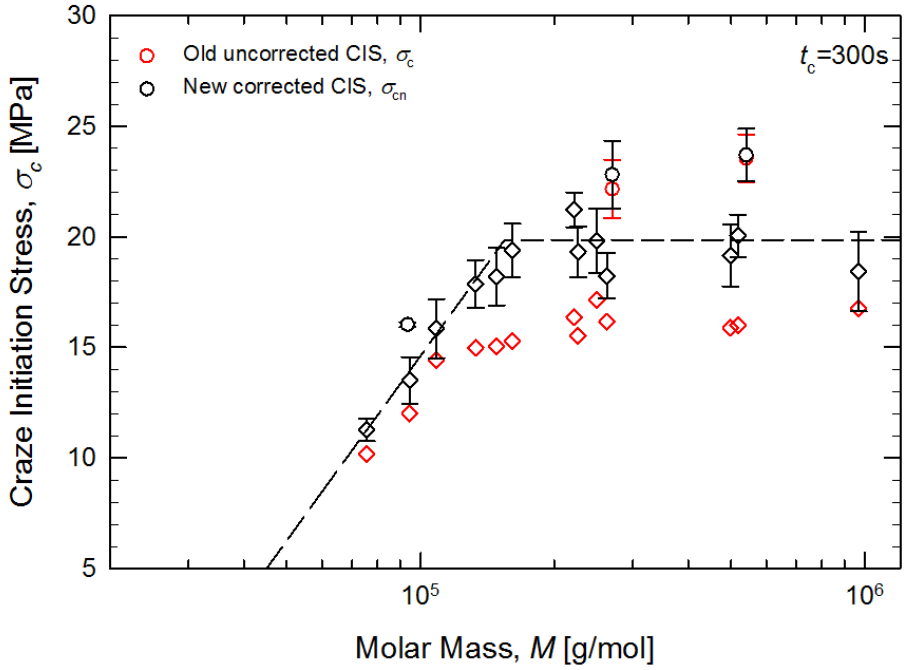


Figure 7: CIS of monodisperse materials using the radii correction, and new modified crazing limits.

systematic differences observed.

All the data produced in this study will consider the effect of r_T to calculate a value for σ_c, and as such the nomenclature for the presented data can be assumed to follow $\sigma_{cn} = \sigma_c$.

References

[1] E.H. Merz, L.E. Nielsen, and Rolf Buchdahl. Influence of molecular weight on the properties of polystyrene. *Industrial and Engineering Chemistry*, 46(6):1396–1401, 1951. ix, 7, 8, 9

[2] Ronald W. Nunes. Influence of molecular weight and molecular weight distribution on mechanical properties of polymers. *Polymer Engineering and Science*, 22(4):205–228, 1982. ix, 8, 10, 12, 148

[3] J.J. Wu and C.P. Bucklely. Plastic deformation of glassy polystyrene: A unified model of yield and the role of chain length. *Journal of Polymer Science Part B: Polymer Physics*, 42:2027–2040, 2004. ix, 2, 14, 16, 17, 18, 75, 194

[4] Thomas G. Fox and Paul J. Flory. Second-order transition temperatures and related properties of polystyrene. i. influence of molecular weight. *Journal of Applied Physics*, 21:581–591, 1950. ix, 18, 19, 75, 132, 194

[5] James Mark, Kia Ngai, William Graessley, Leo Mandelkern, Edward Samulski, Jack Koening, and George Wignall. *Physical properties of polymers*. Cambridge University Press, Cambridge, 3rd edition edition, 2004. ix, 12, 21, 75, 76, 194

[6] E. van Ruymbeke, Chen-Yang Liu, and Christian Bailly. Quantitative tube model predictions for the linear viscoelasticity of linear polymers. *Rheology Reviews*, pages 53–134, 2007. ix, 20, 22, 23, 24, 28, 104, 188, 190, 191, 196, 198, 199, 208, 210

[7] A.E. Likhtman and T.C.B. McLeish. Quantitative theory for linear dynamics of linear entangled polymers. *Macromolecules*, 35:6332–6343, 2002. ix, 21, 26, 27, 31, 35, 188, 190, 198

[8] T. Shahid, Q. Huang, F. Oosterlinck, and E. van Ruymbeke. Dynamic dilution exponent in monodisperse entangled polymer solutions. *Soft Matter*, 2016. ix, 28, 30, 191, 207

[9] R.S. Graham, A.E. Likhtman, and T.C.B. McLeish. Microscopic theory of linear, entangled polymer chains under rapid deformation including chain stretch and convective constraint release. *Journal of Rheology*, 47(5):1171–1200, 2003. ix, 31, 33, 35, 188, 190, 211, 214, 218, 236

[10] Davide S. A. De Focatiis, John Embery, and C. Paul Buckley. Large deformations in oriented polymer glasses: Experimental study and a new glass-melt constitutive model. *Journal of Polymer Science Part B: Polymer Physics*, 48:1449–1463, 2010. ix, xv, 20, 33, 34, 35, 36, 186, 187, 188, 211

[11] Cambridge Polymer Group. The theory of birefringence. Report, Cambridge Polymer Group, Inc., 2004. ix, 37

[12] Davide S. A.; De Focatiis and C. Paul; Buckley. Prediction of frozen-in birefringence in oriented glassy polymers using a molecularly aware constitutive model allowing for finite molecular extensibility. *Macromolecules*, 44:3085–3095, 2011. x, 38, 39, 40, 175, 176, 184

[13] Davide S. A. De Focatiis. Polymer engineering. University Lecture, 2014. x, 41

[14] Larry L. Berger. Relationship between craze microstructure and molecular entanglements in glassy polymers. 1. *Macromolecules*, 22:3162–3167, 1989. x, 43, 49, 52, 155

[15] Edward J. Kramer. Microscopic and molecular fundamentals of crazing. *Advances in Polymer Science*, 52/53:1–56, 1983. x, 2, 41, 42, 43, 44, 45, 49, 141, 160, 184

[16] J.F. Fellers and B.F. Kee. Crazing studies of polystyrene. i. a new phenomenological observation. *Journal of Applied Polymer Science*, 18:2355–2365, 1974. x, 41, 45, 46

[17] A.M. Donald and Edward J. Kramer. Effect of molecular entanglements on craze microstructure in glassy polymers. *Journal of Polymer Science: Polymer Physics Edition*, 20:899–909, 1982. x, 47, 48, 52, 141, 184

[18] C.J.G. Plummer and A.M. Donald. Disentanglement and crazing in glassy polymers. *Macromolecules*, 23:3929–3937, 1990. x, 49, 50, 52, 54, 160, 162, 165, 169, 184

[19] Larry L. Berger and Edward J. Kramer. Chain disentanglement during high-temperature crazing of polystyrene. *Macromolecules*, 20:1980–1985, 1987. x, 50, 51

[20] Davide S. A. De Focatiis, C. Paul Buckley, and Lian R. Hutchings. Roles of chain length, chain architecture, and time in the initiation of visible crazes in polysyterene. *Macromolecules*, 41:4484–4491, 2008. x, xiii, xiv, xix, 42, 55, 57, 63, 139, 142, 143, 155, 156, 158, 160, 166, 181, 185, 250, 251, 252, 253

[21] Davide S. A. De Focatiis and C. Paul Buckley. Craze initiation in glassy polymers: Quantifying the influence of molecular orientation. *Polymer*, 52(18):4045–4053, 2011. x, xv, 58, 59, 60, 63, 127, 178, 179, 180, 182, 183, 184

[22] S.M. Sarge, W. Hemminger, E. Gmelin, H. Höhne, H.K. Cammenga, and W. Eysel. Metrologically based procedures for the temperature, heat and heat flow rate calibration of dsc. *Journal of Thermal Analysis*, 49:1125–1134, 1997. xi, 77, 78

[23] Davide S. A. De Focatiis and C. Paul Buckley. A toolbox for parameter-free predictions of solid-state properties of monodisperse glassy polymers with frozen-in molecular orientation. *Journal of Polymer Science Part B: Polymer Physics*, 50:1748–1756, 2012. xi, 81, 82

[24] Davide S. A. De Focatiis and C. Paul Buckley. Determination of craze initiation stress in very small polymer specimens. *Polymer Testing*, 27(2):136–145, 2008. xi, xii, xix, 42, 53, 54, 63, 82, 87, 89, 90, 93, 141, 158, 184, 250, 251, 253

[25] Uttam Kumar Das. Different variants of microscope. University Lecture, 2014. xii, 97

[26] Faith A. Morrison. *Understanding Rheology*. Oxford University Press, New York, 1st edition edition, 2001. xii, 98

[27] Davide S. A. De Focatiis. Advanced rheology and materials. University Lecture, 2014. xii, 98, 102, 212

[28] Martin Sentmanat. Miniature universal testing platform: from extensional melt rheology to solid-state deformation behavior. *Rheologica Acta*, 2004. xii, 100, 101, 102

[29] Timothy P. Lodge and Thomas C.B. McLeish. Self-concentratinos and effective glass transition temperatures in polymer blends. *Macromolecules*, 33:5278–5284, 2000. xiii, 133, 134, 136, 185

[30] Preetanshu Pandey and Rahul Bharadwaj. *Predictive Modeling of Pharmaceutical Unit Operations*. Woodhead Publishing, 2016. 2

[31] L.R.G Treolar. *The Physics of Rubber Elasticity*. Oxford University Press, London, 1975. 2

[32] John D. Ferry. *Viscoelastic Properties of Polymers*. John Wiley & Sons, United States of America, 1980. 2, 12, 13, 23

[33] Mary C. Boyce, David M. Parks, and Ali S. Argon. Large inelastic deformation of glassy polymers. part i: Rate dependent consitutive model. *Mechanics of Materials*, 7:15–33, 1988. 2, 15

[34] Mary C. Boyce, David M. Parks, and Ali S. Argon. Large inelastic deformation of glassy polymers. part ii: Numerical simulation of hydrostatic extrusion. *Mechanics of Materials*, 7:35–47, 1988. 2

[35] C.P. Buckley and D.C. Jones. Glass-rubber consitutive model for amorphous polymers near the glass transition. *Polymer*, 36:3301–3312, 1995. 2, 15, 16

[36] T.A. Tervoort, R.J.M Smit, W.A.M Brekelmans, and L.E. Govaert. A constitutive equation for the elasto-viscoplastic deformation of glassy polymers. *Mechanics of Time-Dependent Materials*, 1:269–291, 1998. 2, 15

[37] Arnold C.-M Yang, Edward J. Kramer, Chia C. Kuo, and S. Leigh Phoenix. Craze fibril stability and breakdown in polystyrene. *Macromolecules*, 19:2010–2019, 1986. 2, 42, 142, 166

[38] Michael Wendlandt, Theo A. Tervoot, and Ulrich W. Suter. Non-linear, rate-dependent strain-hardening behavior of polymer glasses. *Polymer*, 46:11786–11797, 2005. 2

[39] J. des Cloizeaux. Double reptation vs. single reptation in polymer melts. *Europhysics Letters*, 5:437–442, 1988. 2, 26, 27, 198, 202

[40] N.G. McCrum, C. Paul Buckley, and C.B. Bucknall. *Principles of polymer engineering*. Oxford University Press, Oxford, 2nd edition, 1997. 4, 12, 13, 41, 146

[41] Paul C. Painter and Michael M. Coleman. *Fundamentals of Polymer Science*. Technomic Publishing Company, Switzerland, 1997. 4

[42] Tim A. Osswald and Georg Menges. *Materials Science of Polymers for Engineers*. Hanser/Gardner Publications, Cincinnati, Ohio, 1995. 4

[43] J. Cazes. A question of molecular weight. Report, Waters Associates, Inc. 5, 9

[44] R.F.T. Stepto. Dispersity in polymer science. *Pure Applied Chemistry*, 81:351–353, 2009. 6

[45] E. Foden, D.R. Morrow, and J.A. Sauer. The effect of molecular weight on the fatigue behavior of polystyrene. *Journal of Applied Polymer Science*, 16:519–526, 1972. 7

[46] B.H. Bersted and T.G. Anderson. Influence of molecular weight and molecular weight distribution on the tensile properties of amorphous polymer. *Journal of Applied Polymer Science*, 39:499–514, 1990. 9, 147, 165

[47] R.N. Haward and R.J. Young. *The Physics of Glassy Polymers*. Chapman & Hall, London, 1997. 11, 41

[48] R.J. Young and P.A. Lovell. *Introduction to Polymers*. Chapman & Hall, second edition edition, 1991. 12

[49] N.W. Tschoegl. Time dependence in material properties: An overview. *Mechanics of Time-Dependent Materials*, 1:3–31, 1997. 12, 14

[50] David Roylance. Engineering viscoelasticity. Tech report, Massachusetts Institute of Technology, Cambridge, MA 02139, October 2001. 12

[51] John Dealy and Don Plazek. Time-temperature superposition-a users guide. *Rheology Bulletin*, 2009. 13

[52] P.C. Powell and A.J. Ingen Housz. *Engineering with Polymers*. Stanley Thornes Publishers Ltd, Cheltenham,UK, 1998. 13

[53] Julian Vincent. *Structural Biomaterials*, inbook Basic Elasticity and Viscoelasticity, pages 1–28. Princeton University Press, 3rd edition, 2012. 13

[54] O.A. Hasan and M.C. Boyce. A constitutive model for the nonlinear viscoelastic viscoplastic behavior of glassy polymers. *Polymer Engineering and Science*, 35(4):331–344, 1995. 14

[55] R.N. Haward and G. Thackray. The use of a mathematical model to describe isothermal stress-strain curves in glassy thermoplastics. *Proc. Roy. Soc. A.*, 302:453–472, 1968. 14

[56] P.J. Dooling, C.P. Buckley, S. Rostami, and N. Zahlan. Hot-drawing of poly(methyl methacrylate) and simulation using a glass-rubber constitutive model. *Polymer*, 43:2451–2465, 2002. 16

[57] H.X. Li and C.P. Bucklely. Evolution of strain localization in glassy polymers: A numerical study. *International Journal of Solids and Structures*, 46:1607–1623, 2009. 16

[58] Ellen M. Arruda, Mary C. Boyce, and R. Jayachandran. Effects of strain rate, temperature and thermomechanical coupling on the finiste strain deformation of glassy polymers. *Mechanics of Materials*, 19:193–212, 1995. 20

[59] Rebecca B. Dupaix and Mary C. Boyce. Constitutive modeling of the finiste strain behavior of amorphous polymers in and above the glass transition. *Mechanics of Materials*, 39:39–52, 2007. 20

[60] L.C.E. Struik. Physical aging in plastics and other glassy materials. *Polymer Engineering and Science*, 17(3):165–173, 1977. 20

[61] L.C.E. Struik. On the rejuvenation of physically aged polymers by mechanical deformation. *Polymer*, 38(16):4053–4057, 1997. 20

[62] P.G. de Gennes. Reptation of a polymer chain in the presence of fixed obstacles. *The Journal of Chemical Physics*, 55(2):572–579, 1971. 20, 213

[63] Masao Doi and S.F. Edwards. Dynamics of concentrated polymer systems. *Journal of the Chemical Society, Faraday Transactions 2: Molecular and Chemical Physics*, 74:1789–1801, 1978. 20, 214

[64] M Doi and S.F. Edwards. *The Theory of Polymer Dynamics*. Oxford: Clarendon Press, Oxford, 1988. 20, 202

[65] Kwang Soo Cho, Kyung Hyun Ahn, and Seung Jong Lee. Simple method for determining the critical molecular weight from the loss modulus. *Journal of Polymer Science Part B: Polymer Physics*, 42:2724–2729, 2004. 20, 22, 23

[66] L.J. Fetters, D.J. Lohse, and R.H. Colby. *Chain Dimensions and Entanglements Spacing*. Springer, 2007. 21

[67] Tom C.B. McLeish. Present puzzles of entangled polymers. *Rheology Reviews*, pages 197–233, 2003. 22

[68] Hiroshi Watanabe and Tadao Kotaka. Viscoelastic properties and relaxation mechanisms of binary blends of narrow molecular weight distribution polystyrenes. *Macromolecules*, 17:2316–2325, 1984. 25, 205

[69] Hiroshi Watanabe, Takashi Sakamoto, and Tadao Kotaka. Entanglements in linear polystyrenes. *Macromolecules*, 18:1436–1442, 1985. 25, 205

[70] Hiroshi Watanabe, Takashi Sakamoto, and Tadao Kotaka. Viscoelastic properties of binary blends of narrow molecular weight distribution polystyrenes. 2. *Macromolecules*, 18:1008–1015, 1985. 25, 191, 205

[71] Masao Doi. Explanation for the 3.4-power law for viscosity of polymeric liquids on the basis of the tube model. *Journal of Polymer Science Part B: Polymer Physics*, 21(5):667–684, 1983. 25, 26

[72] Ralph H. Colby. Melt viscosity-molecular weight relationship for linear polymers. *Macromolecules*, 20:2226–2237, 1987. 25

[73] S.T. Milner and T.C.B. McLeish. Reptation and contour-length fluctuations in melt of linear polymers. *Physcial review letters*, 81(3):725–728, 1998. 26

[74] Michael Rubinstein and Ralph H. Colby. Selfconsistent theory of polydisperse entangled polymers: Linear viscoelasticity of binary blends. *The Journal of Chemical Physics*, 89:5291–5306, 1988. 26, 201

[75] Christos Tsenoglou. Molecular weight polydispersity effects on the viscoelasticity of entangled linear polymers. *Macromolecules*, 24:1762–1767, 1991. 27, 198

[76] E. van Ruymbeke, R. Keunings, V. Stphenne, A. Hagenaars, and C. Bailly. Evaluation of reptation models for predicting the linear viscoelastic properties of entangled linear polymers. *Macromolecules*, 35:2689–2699, 2002. 27, 190, 202

[77] G. Marrucci. Relaxation by reptation and tube enlargement: A model for polydisperse polymers. *Journal of Polymer Science B Polymer Physics*, 23:159–177, 1985. 28, 160

[78] G. Marrucci. Dynamics of entanglements: A nonlinear model consistent with the cox-merz rule. *J. Non-Newtonian Fluid. Mech.*, 62, 1996. 31

[79] A.E. Likhtman and R.S. Graham. Simple constitutive equation for linear polymer melts derived from molecular theory: Rolie-poly equation. *J. Non-Newtonian Fluid. Mech.*, 114:1–12, 2003. 31, 35, 214, 218, 236

[80] Alexei E. Likhtman, Scott T. Milner, and Tom C.B. McLeish. Microscopic theory for the fast flow of polymer melts. *Physical Review Letters*, 85(1):4550–4553, 2000. 31, 188

[81] T. Reis and H.J. Wilson. Rolie-poly fluid flowing through constrictions: Two distinct instabilities. *Journal of Non-Newtonian Fluid Mechanics*, 195:77–87, 2013. 32

[82] P.K. Biswas, S. Sengupta, and A.N. Basu. Unified study of the different physical properties of amorphous polymers. *Colloid and Polymer Science*, 266:501–508, 1988. 38

[83] Robert F. Landel and Lawrence E. Nielsen. *Mechanical properties of Polymers and Composites*. CRC Press, 2nd edition, 1993. 38

[84] Werner Kuhn and Hans Kuhn. Rigidity of chain moleculees and its determination from viscosity and flow birefringence in dilute solutions. *J. Colloid Sci*, 3(1):11–32, 1947. 39

[85] A.S. Argon and J.G. Hannoosh. Initiation of crazes in polystyrene. *Philosophical Magazine*, 36:1195–1216, 1997. 41

[86] A.C. Deblieck, D.J.M. van Beek, Klaas Remerie, and Ian Ward. Failure mechanisms in polyolefines: The role of crazing, shear yielding and the entanglement network. *Polymer*, 52:2979–2990, 2011. 42, 51, 155, 160, 172

[87] A.J. Kinloch and R.J. Young. *Fracture Behaviour of Polymers*. Applied Science Publishers, Amsterdam, 2nd edition edition, 1985. 50

[88] A.M. Donald. The effect of temperature on crazing mechanisms in polystyrene. *Journal of Material Science*, 20:2630–2638, 1985. 50

[89] T.C.B. McLeish, C.J.G. Plummer, and A.M. Donald. Crazing by disentanglement: non-diffusive reptation. *Polymer*, 30:1651–1655, 1989. 52, 184

[90] C.J.G. Plummer and A.M. Donald. Craze fibril breakdown in glassy polymers. *Polymer*, 32:409–418, 1991. 52, 156, 169, 184

[91] H.Z.Y. Han, T.C.B. McLeish, R.A. Duckett, N.J. Ward, and A.F. Johnson. Experimental and theoretical studies of the molecular motions in polymer crazing. 1. tube model. *Macromolecules*, 31:1348–1357, 1998. 52, 57, 155, 184

[92] Edward J. Kramer and Larry L. Berger. Fundamental processes of craze growth and fracture. *Advances in Polymer Science*, 91/92:1–68, 1990. 52, 53

[93] K Miyake, N. Satomi, and S. Sasaki. Elastic modulus of polystyrene film from near surface to bulk measured by nanoindentation using atomic force microscopy. *Applied Physics Letter*, 89:89–91, 2006. 53

[94] C. Maestrini and E.J. Kramer. Craze structure and stability in oriented polystyrene. *Polymer*, 22:609–618, 1991. 58, 59, 182

[95] Nigel Clarke, F. Roger Colley, A. Collins, Lian R. Hutchings, and L. Thompson, Richard. Self-diffusion and viscoelastic measurements of polystyrene star polymers. *Macromolecules*, 39:1290–1296, 2006. 65

[96] Olga Smerdova, Richard S. Graham, Urs Gasser, Lian R. Hutchings, and Davide S. A. De Focatiis. A novel method of extraction of blend component structure from sans measurements of homopolymer bimodal blends. *Macromolecular Chemistry and Physics*, 215:859–866, 2014. 66, 118

[97] Andre M. Striegel, Wallace W. Yau, Joseph J. Kirkland, and Donald D. Bly. *Modern Size-Exclusion Liquid Chromatography. Practice of Gel Permeation and Gel Filtration Chromatography*. John Wiley & Sons, Inc., Hoboken, New Jersey, 2nd edition edition, 2009. 68, 70, 71, 118

[98] Associates Waters. Calibration of gpc systems. Report. 68, 71

[99] Matlab optimization toolbox, 2015a. The MathWorks, Natick, MA, USA. 72

[100] Davide S. A. De Focatiis. Tooling for near net-shape compression moulding of polymer specimens. *Polymer Testing*, 31(4):550–556, 2012. 81

[101] C.B. Bucknall. New criterion for craze initiation. *Polymer*, 48:1030–1041, 2007. 87

[102] Jorge Ramirez and Alexei Likhtman. Rheology of entangled polymers: Toolkit for analysis of theory & experiment, 2017. 103, 194, 211

[103] R.H. Boyd. Effective dimensions of oligomers in size exclusion chromatography. a molecular dynamics simulation study. *Macromolecules*, 29:1182–1190, 1996. 113

[104] R.R Chance, S.P. Baniukiewicz, D. Mintz, G. Ver Strate, and N. Hadjichristidis. Characterization of low-molecular weight polymers: failure of universal calibration in size exclusion chromatography. *Int. J. Polymer Analysis and Characterization*, 1:3–34, 1995. 113

[105] Thomas Sun. A study of the separation principle in size exclusion chromatography. *Macromolecules*, 37:4304–4312, 2004. 113

[106] Gabriel Y.H. Choong and Davide S.A. De Focatiis. A method for the determination and correction of the effect of thermal degradation on the viscoelastic properties of degradable polymers. *Polymer Degradation and Stability*, 130:182–188, 2016. 122

[107] A.S. Marshall and S.E.B. Petrie. Rate determining factors for enthalpy relaxation of glassy polymers. molecular weight. *J. Appl. Phys.*, 46(10):4223–4230, 1975. 122

[108] Shadi L. Malhotra, Jean Hesse, and Louis-P Blanchard. Thermal decomposition of polystyrene. *Polymer*, 16:81–93, 1975. 122

[109] Marino Guaita. Thermal degradation of polystyrene. *British Polymer Journal*, 18(4):226–230, 1986. 122

[110] L. Costa, G. Camino, A. Guyot, M. Bert, and A. Chiotes. The role of chain ends in the thermal degradation of anionic polystyrene. *Polymer Degradation and Stability*, 4:245–260, 1982. 122

[111] Qian Huang, Olga Mednova, Henrik K. Rasmussen, Nicolas J. Alvarez, Anne L. Skov, Kristoffer Almdal, and Ole Hassager. Concentrated polymer solutions are different from melts: role of entanglement molecular weight. *Macromolecules*, 46(12):5026–5035, 2013. 123, 221, 235

[112] Jean-Michel Widmaier and Gilles Mignard. Polystyrene-poly α-methylstyrene blends: influence of molecular weight on miscibility. *Physical Review E*, 23(12):989–992, 1987. 124

[113] Vivek Thirtha, Richard Lehman, and Thomas Nosker. Glass transition phenomena in melt-processed polystyrene/polypropylene blends. *Polymer Engineering and Science*, pages 1187–1193, 2005. 124

[114] Sergey Vyazovkin and Ion Dranca. A dsc study of α- and β-relaxations in a ps-clay system. *J. Phys Chem B*, 108:11981–11987, 2004. 124

[115] S. Peter, H. Meyer, and J. Baschnagel. Md simulation of concentrated polymer solutions: structural relaxation near the glass transition. *Eur. Phys. J. E*, 28:147–158, 2008. 126, 127

[116] Suk-fai Lau, Jaya Pathak, and Bernhard Wunderlich. Study of phase separation in blends of polystyrene and poly(α-methylstyrene) in the glass transition region using quantitative thermal analysis. *Macromolecules*, 15:1278–1283, 1982. 126, 133, 136

[117] Evgeny B. Stukalin, Jack F. Douglas, and Karl F. Freed. Plasticization and antiplasticization of polymer melts diluted by low molar mass species. *Journal of chemical physics*, 2010. 127

[118] Lawrence A. Wood. Glass transition temperatures of copolymers. *Journal of polymer science*, 28:319–330, 1958. 129

[119] Thomas G. Fox. Influence of diluent and copolymer composition on the glass temperature of a polymer system. *Bull Am Phys Society*, 1(2):123–135, 1956. 129

[120] Woo Nyon Kim and Charles M. Burns. Thermal behavior, morphology and the determination of the flory-huggins interaction parameter of polycarbonate-polystyrene blends. *Journal of Applied Polymer Science*, 34:945–967, 1987. 130

[121] P.G. Santangelo and C.M. Roland. Molecular weight dependence of fragility in polystyrene. *Macromolecules*, 31:4581–4585, 1998. 132, 133

[122] Kurt Ueberreiter and Gerhard Kanig. Self-plasticization of polymers. *Journal of Colloid Science*, 7.6:569–583, 1952. 132

[123] G.-C. Chung and J.A. Kornfield. Compositional dependence of segmental dynamics in a miscible polymer blend. *Macromolecules*, 27:5729–5741, 1994. 133

[124] Jane E.G. Lipson and Scott. T. Milner. Multiple glass transitions and local composition effects on polymer solvent mixtures. *Journal of Polymer Science: Part B: Polymer Physics*, 44:3528–3545, 2006. 133, 136

[125] D.M. Kulich, S.K. Gaggar, and R. Lowry. Acrylonitrile-butadiene-styrene polymer, 2001. 144

[126] J.A. Sauer and M. Hara. Effect of molecular variables on crazing and fatigue of polymers. *Advances in Polymer Science*, 91/92:69–118, 1990. 145

[127] Jianning Liu, Panpan Lin, Shiwang Cheng, Weiyu Wang, Jimmy W. Mays, and Shi-Qing Wang. Polystyrene glass under compression: Ductile and brittle responses. *Macro letters*, 4:1072–1076, 2015. 145

[128] A.M. Donald and Edward J. Kramer. Craze microstructure and molecular entanglements in polystyrene-poly(phenylene oxide) blends. *Polymer*, 23:461–465, 1982. 148, 160, 162, 165, 166, 184

[129] Herman J.C. Berendsen. *A Student's Guide to Data and Error Analysis*. Cambridge University Press, 2011. 152

[130] J. Rottler and M.O. Robbins. Growth, microstructure and failure of crazes in glassy polymers. *Phys. Rev. E: Stat. Phys., Plasmas, Fluids, Relat. Interdiscip, Top.*, 68:011801, 2003. 155

[131] J.F. Fellers, D.J. Lohse, D. Richter, T.A. Witten, and A. Zirkel. Connection between polymer molecular weight, density, chain dimensions and melt viscoelastic properties. *Macromolecules*, 27(17):4639–4647, 1994. 160

[132] R.N Haward. Strain hardening of high density polyethylene. *Journal of Pol. Sci.: Part B: Pol. Phys.*, 45:1090–1099, 2007. 160, 171

[133] Ralph H. Colby and Michael Rubinstein. Two-parameter scaling for polymers in solvents. *Macromolecules*, 23:2753–2757, 1990. 161

[134] E. van Ruymbeke, Y. Masubuchi, and H. Watanabe. Effective value of the dynamic dilution exponent in bidisperse linear polymers: From 1 to 4/3. *Macromolecules*, 45:2085–2098, 2012. 161, 202

[135] E. van Ruymbeke, V. Shchetnikava, Y. Matsumiya, and H. Watanabe. Dynamic dilution effect in binary blends of linear polymers with well-separated molecular weights. *Macromolecules*, 47:7653–7664, 2014. 161, 206

[136] H.G.H. van Melick, O.F.J.T. Bressers, J.M.J. den Toonder, L.E. Govaert, and H.E.H Meijer. A micro-indentation method for probing the craze-initiation stress in glassy polymers. *Polymer*, 44:2481–2491, 2003. 169

[137] P.J. Mills, J.N. Hay, and R.N Haward. The post-yield behaviour of low-density polyethylenes. *Journal of Materials Science*, 20:501–507, 195. 172

[138] R.N Haward. Strain hardening of thermoplastics. *American Chemical Society*, 26:5860–5869, 1993. 172

[139] Edward J. Kramer. A molecular theory of the fracture toughness of low molecular weight polymers. *Journal of Materials Science*, 14:1381–1388, 1979. 172

[140] R.D. Andrews and J.F. Rudd. Photoelastic properties of polystyrene in the glassy state. i. effect of molecular orientation. *Journal of Applied Physics*, 28(10):1091–1095, 1957. 173

[141] J.F. Rudd and E.F. Gurnee. Photoelastic properties of polystyrene in the glassy state. i. effect of temperature. *Journal of Applied Physics*, 28(10):1096–1100, 1957. 173

[142] John Dealy. Weissenberg and deborah numbers - their definition and use. *Rheology Bulletin*, 2010. 174

[143] Clarisse Luap, Marina Karlina, Thomas Schweizer, and David C. Venerus. Limit of validity of the stress-optical rule for polystyrene melts: Influence of polydispersity. *J. Non-Newtonian Fluid. Mech.*, 138:197–203, 2006. 174, 179

[144] Nigel R. Farrar and Edward J. Kramer. Microstructure and mechanics of crazes in oriented polystyrene. *Polymer*, 22:691–698, 1981. 177

[145] Dusan C. Prevorsek. Tensile strength of oriented polymers below the glass transition temperature. *Journal of Polymer Science Part A-2*, 4:63–88, 1966. 178

[146] Ian M Ward. *Structure and properties of oriented polymers*. Springer Science & Business Media, 2012. 178

[147] S.J. Park and R.G. Larson. Long-chain dynamics in binary blends of monodisperse linear polymers. *J. Rheol.*, 50:21–39, 2006. 190

[148] E. van Ruymbeke, C. Bailly, R. Keuning, and D. Vlassopoulos. A general methodology to predict the linear rheology of branched polymers. *Macromolecules*, pages 6248–6259, 2006. 190

[149] C. Pattamaprom, R. Larson, and T.J. Van Dyke. Quantitative predictions of linear viscoelastic rheological properties of entangled polymers. *Rheological Acta*, 39:517–531, 2000. 190

[150] Chen-Yang Liu, Jiasong He, Roland Keunings, and Christian Bailly. New linearized relation for the universal viscosity-temperature behavior of polymer melts. *Macromolecules*, 39:8867–8869, 2006. 191

[151] Qian Huang, Nicolas J. Alvarez, Yumi Matsumiya, Henrik K. Rasmussen, Hiroshi Watanabe, and Ole Hassager. Extensional rheology of entangled polystyrene solutions suggest importance of nematic interactions. *ACS Macro Letters*, 2:741–744, 2013. 194, 221, 235

[152] J. des Cloizeaux. Relaxation of entangled polymers in melts. *Macromolecules*, 23:3992–4006, 1990. 198, 202

[153] Christian Carrot, Pascale Revenu, and Jacques Guillet. Rheological behavior of degraded polypropylene melts: from mwd to dynamic moduli. *Journal of Applied Polymer Science*, 61:1887–1897, 1996. 198, 199

[154] Frdric Lonardi, Jean-Charles Majest, Ahmed Allal, and Grard Marin. Rheological models based on the double reptation mixing rule: The effects of a polydisperse environment. *J. Rheology*, 44(4):675–692, 2000. 199, 205

[155] Michael Rubinstein and Eugene Helfand. Theory of polydispersity effects on polymer rheology. binary distribution of molecular weights. *Macromolecules*, 20:822–829, 1987. 201

[156] Christos Tsenoglou. Viscoelasticity of binary homopolymer blends. *ACS Polym. Prepr*, 28:185–186, 1987. 202

[157] W.H. Tuminello. Molecular weight and molecular weight distribution from dynamic measurements of polymer melts. *Polymer Engineering and Science*, 26:1339–1347, 1986. 202

[158] Christian Carrot and Jean-Charles Majeste. A modified tube dilatation theory for the relaxation of entangled linear polymer melts. *J. Non-Newtonian Fluid Mechanics*, 129:98–105, 2005. 202, 205, 210

[159] Hiroshi; Watanabe, Satoshi Ishida, Yumi Matsumiya, and Tadashi Inoue. Test of full and partial tube dilation pictures in entangled blends of linear polyisoprenes. *Macromolecules*, 37:6619–6631, 2004. 202

[160] D.W. Mead. Component predictions and the relaxation spectrum of the double reptation mixing rule for polydisperse linear flexible polymers. *Journal of Rheology*, 40:633–661, 1996. 205

[161] D. Maier, A. Eckstein, Chr. Friedrich, and J. Honerkamp. Evaluation of models combining rheological data with the molecular weight distribution. *J. Rheology*, 42(5), 1998. 205

[162] H. Watanabe. Viscoelasticity and dynamics of entangled polymers. *Prog. Polym. Sci.*, 24:1253–1403, 1999. 206

[163] Xiangnan Ye and Tam Sridhar. Effects of the polydispersity on rheological properties of entangled polystyrene solutions. *Macromolecules*, 38(8):3442–3449, 2005. 208, 210, 217

[164] Dietmar Auhl, Pierre Chambon, Tom C.B. McLeish, and Daniel J. Read. Elongational flow of blends of long and short polymers: Effective stretch relaxation time. *Physcial review letters*, 103:1–4, 2009. 210, 220, 236, 245

[165] Shigeharu Onogi, Toshiro Masuda, and Keishi Kitagawa. Rheological properties of anionic polystyrenes. i. dynamic viscoelasticity of narrow-distribution polystyrenes. *Macromolecules*, 3(2):109–116, 1970. 210

[166] T. Sridhar, V. Tirtaatmadja, D.A. Nguyen, and R.K. Gupta. Measurement of extensional viscosity of polymer solutions. *Journal of Non-Newtonian Fluid Mechanics*, 40:271–280, 1991. 212, 235

[167] Anders Bach, Kristoffer Almdal, Henrik Koblitz Rasmussen, and Ole Hassager. Elongational viscosity of narrow molar mass distribution polystyrene. *Macromolecules*, 36:5174–5179, 2003. 213, 235

[168] D. Pearson, E. Herbolzheimer, N. Grizzuti, and G. Marrucci. Transient behavior of entangled polymers at high shear rates. *Journal of Polymer Science: Part B: Polymer Physics*, 29:1589–1597, 1991. 213, 214

[169] P.G. de Gennes. Dynamics of entangled polymer solutions. i. the rouse model. *Macromolecules*, 9(4):587–593, 1976. 213

[170] David W. Mead, Dmitry Yavich, and L. Gary Leal. The reptation model with segmental stretch. ii. steady flow properties. *Rheological Acta*, 34(4):360–383, 1995. 214

[171] Giovanni Ianniruberto and Giuseppe Marrucci. A simple constitutive equation for entangled polymers with chain stretch. *Journal of Rheology*, 45:1305–1318, 2001. 214

[172] D.J. Read. Convective constraint release with chain stretch: Soution of the rouse-tube model in the limit of infinite tubes. *Journal of Rheology*, 48:349–377, 2004. 214, 227

[173] Suzanne M. Fielding. Criterion for extensional necking instability in polymeric fluids. *Phys. Rev. Lett.*, 107:25–16, 2011. 216

[174] M.H. Nafar Sefiddashti, B.J. Edwards, and B. Khomami. Individual chain dynamics of a polyethylene melt undergoing steady shear flow. *Journal of Rheology*, 59:1–35, 2015. 220

[175] Salvatore Costanzo, Qian Huang, Giovanni Ianniruberto, Giuseppe Marruci, Ole Hassager, and Dimitris Vlassopoulos. Shear and extensional rheology of polystyrene melts and solutions with the same number of entanglements. *Macromolecules*, 49(10):3925–3935, 2016. 220, 235

[176] Qian Huang, Ludovica Hengeller, Nicolas J. Alvarez, and Ole Hassager. Bridging the gap between polymer melts and solutions in extensional rheology. *Macromolecules*, 48:4158–4163, 2015. 221, 235

[177] Ludovica Hengeller, Qian Huang, Andriy Dorokhin, Nicolas J. Alvarez, Kristoffer Almdal, and Ole Hassager. Stress relaxation of bi-disperse

polystyrene melts. exploring the interactions between long and short chians in non-linear rheology. *Rheologica Acta*, 2016. 221

[178] Jean Louis Viovy, Michael Rubinstein, and Ralph H. Colby. Constraint release in polymer melts: Tube reorganization versus tube dilation. *Macromolecules*, 24:3587–3596, 1991. 227

[179] D.J. Read. Binary blends of entangled polymers: when two seems many more than one! XXVIIth International Congress of Rheology, 2017. 236